ARTIFICIAL MATERIALS FOR MICROWAVE APPLICATIONS

Syed S. Bukhari

A Doctoral Thesis Submitted in Partial Fulfilment of the Requirements for the Award of Doctor of Philosophy of Loughborough University

November 2016

Abstract

This thesis has focussed on the properties and manufacturing techniques of artificial RF materials. These artificial materials can be divided into two types depending on the whether their individual unit cell is resonant or non-resonant. Both these types have been discussed. It has been shown that the efficiency and bandwidth of a patch antenna using a flexible 3D printed substrate can be improved by using composite materials as heterogeneous substrates. Composite materials with a large range of relative permittivity values were manufactured by combing 3D printing with commercial laminates. An equation to design such composite materials has been presented. The engineering tolerance and repeatability of 3D printing as a manufacturing process to fabricate 'on demand' dielectrics has been presented.

For materials with resonant unit cells, 2D materials known as metasurfaces have been considered. Metasurfaces presented in this thesis have been developed by close coupling of two Babinet's complements. It has been shown that the unit cell of a dipole-slot metasurface can be miniaturized by adding an additional layer of dipoles, making a dipole-slot-dipole metasurface. The response of both these metasurfaces was explained with a qualitative circuit model. Miniaturization has been achieved by using square loops as the building blocks for a Babinet complementary metasurface. A $\lambda/17$ structure was designed, fabricated and measured by using square loops; however the two layers should be shifted with respect to each other to achieve strong inter-layer coupling, thus miniaturization. The width-optimization of a dipole-slot metasurface has been achieved by maximising the coupling co-efficient. The expression for optimum length to width ratio of a dipole-slot metasurface has been derived. A generalised analytical circuit model, for any Babinet complementary metasurface, has been derived based on integral equations. This analytical model has been used to explain the pass band and compact nature of these metasurfaces. The comparison between this analytical model and full wave analysis showed excellent agreement with high numerical accuracy.

Acknowledgements

First of all, I am extremely thankful to the one and only God. I would like to thank my parents for their guidance, help, moral and financial support. I am thankful to my brothers for their support and, insightful and stimulating discussions.

I would like to thank Dr. Will Whittow for not only his patience, extremely quick turnaround time, availability as well as technical help with research, measurements and simulations but also for his personal help and support, for which I will remain grateful. I am also thankful to Professor Yiannis Vardaxoglou for his vision and research guidance. I am indebted to Professor Stefano Maci for his help with physical insight using maths and most of all demonstrating that how fun research is, if done properly and with expertise.

I thank Dr. Shiyu Zhang, Dr. Alford Chauraya and Dr. Chinwe Njoku for their friendship, and help with fabrication and measurements. I would like to mention Peter Awe, Aris Tsolis and Yi Zheng for all their help. I am also thankful to my fellows at CMCR: Dina, Duarte, Elijah, Ignacio, Isaac, John, Seun, Symeon and Tassos.

I would also like to express my gratitude to Dr. Chinthana Panagamuwa and Professor John Batchelor who have taken time out of their busy schedules to examine my thesis.

List of Publications

JOURNAL ARTICLES

1. **S. S. Bukhari**, W. G. Whittow, J. C. Vardaxoglou, S. Maci (2016) “Dipole-slot-dipole Metasurfaces,” IET Microwaves, Antennas and Propagation, ISSN: 1751-8725. (DOI: 10.1049/iet-map.2015.0849). (in press)

2. **S. S. Bukhari**, W. G. Whittow, S. Zhang, J. C. Vardaxoglou, (2016) “Composite materials for microwave devices using additive manufacturing,” Electronics Letters, 52(10), pp.832-833, ISSN: 0013-5194. (DOI: 10.1049/el.2016.0078).

3. **S. S. Bukhari**, W. G. Whittow, J. Joubert, J. C. Vardaxoglou, (2015) “Flexible three-dimensional printed antenna substrates,” The Journal of Engineering. (DOI: 10.1049/joe.2015.0092).

4. W. G. Whittow, **S. S. Bukhari**, L. A. Jones, I. L. Morrow (2014), “Applications and Future Prospects for Microstrip Antennas using Heterogeneous and Complex 3-D Geometry Substrates,” Prog. Electromagn. Res., vol. 144, pp. 271–280. (DOI: 10.2528/PIER13121902).

5. P. A. Catherwood, **S. S. Bukhari**, G. Watt, W. G. Whittow and J. McLaughlin (2016), “Wireless Hospital Patient Monitoring Networks using Body Contoured Flexible Antennas,” IET Microwaves, Antennas and Propagation. (submitted)

6. ***S. S. Bukhari**, W. G. Whittow, J. C. Vardaxoglou, S. Maci (2016), “Analytical Circuit Modelling of Babinet Complimentary Metasurfaces,” IEEE Transactions on Antennas and Propagation. (in preparation)*

7. ***S. S. Bukhari**, W. G. Whittow, J. C. Vardaxoglou, S. Maci (2016), “Optimization of Dipole-slot Metasurfaces,” IEEE Transactions on Antennas and Propagation. (in preparation)*

8. ***S. S. Bukhari**, W. G. Whittow, J. C. Vardaxoglou, S. Maci (2016), "Square Loops Complementary Metasurfaces," IEEE Antennas and Wireless Propagation Letters. (in preparation)*

CONFERENCE PROCEEDINGS / ABSTRACTS

1. **S. S. Bukhari**, W. G. Whittow, J. C. Vardaxoglou, S. Maci (2015), "Dipole and Slot loaded Closely Coupled Complementary Metasurfaces," 2015 Loughborough Antennas and Propagation Conference (LAPC)

2. **S. S. Bukhari**, W. G. Whittow, J. C. Vardaxoglou, S. Maci (2015), "Square Loop Complementary Frequency Selective Surfaces," 2015 IEEE International Symposium on Antennas and Propagation & USNC/URSI National Radio Science Meeting.

3. **S. S. Bukhari**, W. G. Whittow, J. C. Vardaxoglou, S. Maci (2015), "Dipole loaded Complementary Frequency Selective Surfaces," 2015 USNC-URSI Radio Science Meeting (Joint with AP-S Symposium)

6. **S. S. Bukhari**, W. G. Whittow, J. C. Vardaxoglou (2015), "3D printed Bespoke Substrates," 2015 European Conference on Antennas and Propagation Conference (EuCAP)

5. **S. S. Bukhari**, W. G. Whittow, J. C. Vardaxoglou (2014), "3D printed Bespoke Substrates," 2014 Loughborough Antennas and Propagation Conference (LAPC)

7. **S. S. Bukhari**, W. G. Whittow (2014), "Bandwidth Enhancement using Heterogeneous Substrates for Microstrip Antennas," 2014 USNC-URSI Radio Science Meeting

8. **S. S. Bukhari**, W. G. Whittow (2013), "Heterogeneous Substrate Microstrip Antenna with Enhanced Bandwidth," 2013 Loughborough Antennas and Propagation Conference (LAPC)

List of Figures

List of Tables

Table of Contents

Chapter 1 : Introduction

1.1 Research Motivation

Microwaves (300 MHz – 300 GHz), in the modern world, are the primary source of wireless communications. They are the carriers which are responsible for transmitting data when we are using wi-fi; they transfer our voice when we call using our mobile phones; they are also used for sensing using wireless nodes; surveillance of air traffic using radars and to communicate with satellites. Their use is so ubiquitous that it is easy to overlook that it was just in 1888 when Heinrich Hertz showed that waves can travel through space, practically demonstrating the theory of James Clerk Maxwell (1864). Since then, scientists and engineers have endeavoured to exploit the potential of wireless energy transfer in order to enrich and improve human life. These efforts have resulted in an unprecedented growth in the number of wireless communication devices. Currently, there are more mobile phones in the world than people and the number of shipped wi-fi devices will be over 15 billion by the end of year 2016 [1], [2].

It is amazing that with the introduction of commercially available wearable devices and the introduction of internet of things, this trend is set to continue and the decrease in the growth rate of wireless devices is not yet in sight. Current wearable technology market is worth 9 billion dollars and according to the Forbes by 2020, this number will be increased to 34

billion [3]. According to Ericsson, with the advent of the internet of things, the use of wearable devices will extend beyond the areas of health and fitness; they estimate that such devices, in the future, will be used for security, smart clothing, surveillance and non-verbal communications [4].

This rapid increase in the number of wireless devices requires more bandwidth for communications, a demand which is shared by the current consumer market. The modules needed for manufacturing a wireless device are also required to be energy efficient, low cost, conformal, flexible, light weight and low profile. These requirements are usually conflicting in nature, therefore innovation, on the part of the designer, is required in order to satisfy all these demands. One of the most significant areas and the fertile grounds for innovation is in the design of materials which are used to manufacture wireless devices like antennas, lenses and filters. This area has always been given attention since the beginning of 20^{th} century and scientists like Maxwell Garnett, Lorentz and Lewin have developed models to predict the electromagnetic properties of mixtures and other hybrid structures [5]–[7]. However, since the practical discovery of left-handed materials by Pendry and Smith, this area has seen exponential growth [8], [9]. The most promising and intriguing feature of these left-handed materials is that they allow the possibility of existence of negative permittivity and negative permeability at the same frequency, thereby making the refractive index negative for such materials. This anomalous negative refraction does not occur in natural materials therefore artificial (man-made) materials have to be constructed in order to take advantage of this unusual property (which offers complete control of electromagnetic waves) [10]. It should be noted that such materials had previously been theoretically predicted by Veselago in 1967 [11].

Since these artificial materials remove the constraints on the designer imposed by the naturally occurring materials; they not only help the designer improve current devices but

also offer the practical possibility of manufacturing such devices which were considered impossible by using natural materials [12]. Although much interest has been given to developing a cloaking device using metamaterials, a myriad of possibilities like perfect focussing, efficient electrically small antennas, waveguides without diffraction limit become possible using artificial negative indexed materials [13]–[15]. A cloaking device bends the light in such a way that the cloak and the space covered by it become invisible. Conversely by using metamaterials, electromagnetic radiation coming from all directions can be concentrated in a small space which can then be used to design field enhanced sensors or to capture energy coming from every direction in energy scavenging systems. By using negative indexed metamaterials, a hyperlens can be developed which conserves the near field information carried by the evanescent waves (since evanescent waves decay exponentially as they propagate (hence limiting resolution)) [16], [17]. However by using metamaterials, evanescent modes can be converted into propagating ones which can result in the imaging of sub-wavelength features.

Another significant scientific development that enhanced the focus on the development of artificial materials also arose from Pendry's work on cloaking [18], [19]. This is based on the invariance of Maxwell's equations under coordinate transformation and is called transformation optics. Transformation optics converts a given space to target space in such a way that the resulting response (of both spaces) to an incoming electromagnetic wave is identical. This technique can potentially revolutionise the design of traditional devices like energy collimators, polarization convertors; transformation optics can also be used to simplify the physical structure of antennas [20]–[22]. However, there are some practical constraints which arise when a space is transformed with transformation optics. The (new) values for the relative permittivity and relative permeability become anisotropic after this transformation. This requires 'on demand' materials which can be synthesized to tailor the

needs of the designer. As the low loss magnetic materials with varying relative permeability are extremely difficult to manufacture, the focus shifts to varying the dielectric index for controlling the relative permittivity. This can be achieved by the careful design of aforementioned ‘on demand’ dielectric materials. This method is also superior to ‘metamaterials approach for transformation optics’ in terms of bandwidth [23]. Metamaterials are highly dispersive and narrowband; on the other hand, dielectrics possess a wideband response when the individual building blocks are much smaller than the operating wavelength. Such dielectric materials prepared using liquid phase casting, have been used to manufacture a flat hyperbolic and Luneberg lens [23], [24]. The all dielectric approach has been used to structure surface transformation lens antennas and flat reflectors [25], [26]. A flat all-dielectric hyperbolic lens is shown in Figure 1-1.

Figure 1-1: *All dielectric planar hyperbolic lens designed using transformation optics. Different coloured rings indicate a different relative permittivity. The relative permittivity for this planar lens ranges from 3 to 12.6 (redrawn from* [23]*)*

This thesis studies the design of “on demand” dielectrics, also called heterogeneous materials (since such dielectrics are formed as a result of combining existing materials). However, the focus has been on developing these ‘on demand’ heterogeneous materials by using 3D

printing. 3D printing, also known as additive manufacturing, is a very powerful, environmentally friendly technique which uses layer by layer design in order to manufacture the desired material(s). In the future, 3D printing can make the whole process of making electromagnetic devices monolithic [27]. The user friendly and reliable nature of 3D printing also makes it suitable to cope with the increasing demand of heterogeneous materials in the future along with making the process to locally vary the dielectric tensors extremely simple.

The advantage of large bandwidth with heterogeneous dielectrics comes at a cost; since the individual unit cell is non-resonant, the unique advantages (like negative refraction, sub-wavelength imaging, complete phase control of electromagnetic waves) offered by metamaterials (due to their resonant nature) are lost. This thesis, therefore, reports on the development and the properties of both these kinds of materials. However instead of metamaterials, the focus is on their 2d counterparts, metasurfaces. Metasurfaces offer sub-wavelength control owing to their compact nature, and the phase discontinuity across the metasurface can be applied to control and vary the phase of incoming electromagnetic wave over an extremely small distance [28], [29]. Another significant advantage of metasurfaces is that they can be fabricated by traditional techniques. Due to their planar nature, they become very cost effective in contrast to complex 3D metamaterials [30], [31]. The research on metasurfaces is growing at a rapid pace (ranging from microwaves to optical frequencies) and they have been shown to manufacture flat lenses, compact spatial filters, holographic antennas and cavity excited antennas with high aperture efficiency [28], [32]–[35]. Metasurfaces, presented in this thesis, are developed based on the Babinet's principle and fabricated using conventional etching methods. This is because 3D printing still has not managed to successfully print dielectrics and low loss metals as a single process however as the technology evolves, 3D printing can also take over the manufacturing of metasurfaces (in the future). Inkjet printing is another technique which can be used for manufacturing

metasurfaces since it can print on a variety of substrates like paper, fabric etc [36], [37]. Inkjet printing has already been successfully utilised to fabricate frequency selective surfaces and Radio-Frequency Identification (RFID) tags [38], [39]. Consumers and industry demand ever increasing performance in smaller volumes and busier environments. The advent of EM simulations has made it hard to keep optimising just the metallisation shape. Therefore, the next stage of progress is likely to be via materials. These can be either non-resonant or resonant structures. This thesis examines both of these options

1.2 Overview of this Thesis

Chapter 2 starts with the review of various fabrication methods that have been employed to make heterogeneous substrates. This review discusses how heterogeneous substrates have been used to improve antenna performance. Heterogeneous substrates, in this chapter, have been fabricated by using both, Taconic and 3D printed materials [40]. The comparison between a microstrip patch antenna on a homogeneous substrate and a heterogeneous substrate has been presented. The work presented in this chapter exploits the non-uniform nature of a microstrip patch's electric fields and uses heterogeneous substrates to improve the bandwidth and efficiency of a patch using a 3D printed material as its substrate. The measured S_{11} results and radiation patterns of the antennas are presented.

Chapter 3 briefly reviews the classical models for estimating the relative permittivity of heterogeneous materials and the advantages offered by the use of such materials in the areas of transformation optics and lenses. Various methods for measuring the relative permittivity of samples have been discussed. Bi-phase and tri-phase composite heterogeneous materials have been prepared and their relative permittivity has been measured. 3D printing is combined with commercially available laminates in order to manufacture bespoke materials

with a wide (and near continuous) range of relative permittivities. The reliability of 3D printing as a manufacturing technique for making composite heterogeneous materials has been presented.

Heterogeneous materials discussed in Chapter 2 and 3 have non-resonant individual building blocks, Chapter 4 discusses metasurfaces in which the individual unit cell is resonant. Chapter 4 starts with the literature review of metasurfaces covering their salient features and potential applications. Dipole-slot metasurfaces have been designed on the basis of Babinet's principle. The compact and pass band nature of these metasurfaces has been investigated and the effects of various parameters has been presented, using CST and EMPIRE simulations. A qualitative circuit model that describes the response of the dipole-slot metasurface has been developed. The measured response of the dipole-slot metasurface has been presented at the end of this chapter and showed good agreements with simulations.

Chapter 5 presents square loop complementary metasurfaces and multi-layered dipole-slot-dipole metasurfaces. In this chapter square loops are used to achieve miniaturization for Babinet complementary metasurfaces. The coupling between the two complementary square loops layers has been explained using Babinet's principle. The measured response for these square loop metasurfaces has been presented. This chapter also discusses the dipole-slot-dipole metasurface, which is a multi-layered metasurface, where an extra layer of dipoles has been used to miniaturize the unit cell of a dipole-slot metasurface. A qualitative circuit model has been developed to explain the behaviour of the dipole-slot-dipole metasurface. The measured transmission response of the fabricated dipole-slot-dipole metasurface has been presented.

Chapter 6 starts with optimizing the dipole-slot metasurface with respect to its width of its individual elements (i.e. dipoles and slots). An expression has been derived which gives the

optimal width to length ratio (of both individual elements) for the maximum miniaturization. This validity of this ratio for different lengths and relative permittivitties (of the in-between dielectric) has been verified with simulations. The measured results of the optimized dipole-slot metasurface has been presented and compared with non-optimized dipole-slot metasurfaces.

This chapter also presents a derivation of an analytical generalised equivalent circuit model for any Babinet complementary metasurfaces. This model has been derived using integral equations and has been used to explain both, the compact nature and pass band characteristics of the Babinet complementary metasurfaces. A comparison between this analytical circuit model and CST simulations has been presented to verify the model.

Chapter 7 contains the conclusions along with the summary of results of the whole thesis. The suggestions for future work have also been made in this Chapter.

1.3 Research Novelty of this Thesis

i. Chapter 2: The bandwidth and efficiency of a microstrip antenna has been improved using a flexible 3D printed heterogeneous substrate.
ii. Chapter 3: Commercial laminates have been combined with 3D printing to structure composite heterogeneous materials such that the relative permittivity of the sample can be tailored according to the demands of the designer. The fabricated composite materials with a large range of relative permittivity values have been successfully designed. A design equation has been derived and validated with measurements.
iii. Chapter 4 and 5: A dipole-slot metasurface has been miniaturized by adding an additional layer of dipoles to form a dipole-slot-dipole metasurface. The response of

both the dipole-slot metasurface and dipole-slot-dipole metasurface has been described by developing a qualitative equivalent circuit model. The effect of dielectric thickness and its relative permittivity, and the alignment of the dipole and dipole-slot layers, on the behaviour of the dipole-slot-dipole metasurface has been studied and reported.

iv. Chapter 5: An extremely compact metasurface ($\lambda/13.5$) with Babinet complementary square loops, as its individual building blocks has been presented. It has been explained using Babinet's principle that the coupling between the two complementary layers is maximised by shifting one layer by half of the periodicity (with respect to the other layer along both axes).

v. Chapter 6: An expression has been derived for optimizing the width of the dipole-slot metasurface in order to achieve maximum miniaturization. This has been verified using both simulations and measurements. A large ratio between the pass band and stop band of the dipole-slot metasurface has been achieved by optimizing the width of this metasurface.

vi. Chapter 6: An analytical equivalent circuit model has been developed for a generalised Babinet complementary metasurface. The model has been used to combine the two integral equations into a single equation. The compact nature of the Babinet complementary metasurface and its pass band nature has been explained with this circuit model and verified via simulations.

References

[1] http://www.ibtimes.co.uk/there-are-more-gadgets-there-are-people-world-1468947, “Active Mobile Phones Outnumber Humans for the First Time.” .

[2] http://www.wi-fi.org/news-events/newsroom/wi-fi-device-shipments-to-surpass-15-billion-by-end-of-2016, “Wi-Fi® device shipments to surpass 15 billion by end of 2016 _ Wi-Fi Alliance.” .

[3] http://www.forbes.com/sites/paullamkin/2016/02/17/wearable-tech-market-to-be-worth-34-billion-by-2020/#243e75b13fe3, “Wearable Tech Market To Be Worth $34 Billion By 2020.” .

[4] https://www.ericsson.com/thinkingahead/consumerlab/consumer-insights/wearable-technology-and-the-internet-of-things, “Wearable Technology and the Internet of Things - Ericsson.” .

[5] O. Levy and D. Stroud, “Maxwell Garnett theory for mixtures of anisotropic inclusions: Application to conducting polymers,” *Phys. Rev. B*, vol. 56, no. 13, pp. 8035–8046, 1997.

[6] W. R. Tinga, W. A. G. Voss, and D. F. Blossey, “Generalized approach to multiphase dielectric mixture theory,” *J. Appl. Phys. 44*, vol. 3897, 1973.

[7] L. Lewin, “The Electrical Constants Of A Material Loaded With Spherical Particles,” *Electr. Eng. - Part III Radio Commun. Eng. J. Inst.*, vol. 94, pp. 65–68, 1946.

[8] J. B. Pendry, A. J. Holden, D. J. Robbins, and W. J. Stewart, “Magnetism from Conductors and Enhanced Nonlinear Phenomena,” *IEEE Trans. Microw. Theory Tech.*, vol. 47, no. 11, pp. 2075–2084, 1999.

[9] R. A. Shelby, D. R. Smith, and S. Schultz, “Microwave transmission through a two-dimensional , isotropic , left-handed metamaterial,” *Appl. Phys. Lett.*, vol. 78, no. 4, pp.

489–491, 2001.

[10] N. Engheta and R. Ziolkowski, *Metamaterials: Physics and Engineering explaorations*. Wiley-IEEE Press, 2006.

[11] V. G. Veselago, “The Electrodynamics of Substances with Simultaneously Negative Values of And μ,” *Sov. Phys. Upsekhi*, vol. 10, no. 4, pp. 517–526, 1968.

[12] V. M. Shalaev, “Transforming Light,” *Science (80-.).*, vol. 322, no. October, pp. 5–8, 2008.

[13] J. B. Pendry, “Negative Refraction Makes a Perfect Lens,” *Phys. Rev. Lett.*, vol. 85, no. 18, pp. 3966–3969, 2000.

[14] A. Alù and N. Engheta, “Guided Modes in a Waveguide Filled With a Pair of SNG, DNG and/or DPS Layers,” *IEEE Trans. Microw. Theory Tech.*, vol. 52, no. 1, pp. 199–210, 2004.

[15] R. W. Ziolkowski and A. D. Kipple, “Application of Double Negative Materials to Increase the Power Radiated by Electrically Small Antennas,” *IEEE Trans. Antennas Propag.*, vol. 51, no. 10, pp. 2626–2640, 2003.

[16] A. V Kildishev and V. M. Shalaev, “Transformation optics and metamaterials,” *Phys. - Uspekhi*, vol. 54, no. 1, 2011.

[17] H. Lee, Z. Liu, Y. Xiong, C. Sun, and X. Zhang, “Development of optical hyperlens for imaging below the diffraction limit,” *Opt. Express*, vol. 15, no. 24, pp. 15886–15891, 2007.

[18] J. B. Pendry, D. Schurig, and D. R. Smith, “Controlling Electromagnetic Fields,” *Science (80-.).*, vol. 312, no. 2006, pp. 1780–1782, 2009.

[19] P.-G. Luan, “Chapter 2 Metamaterials and Transformation Optics,” in *The Current*

Trends of Optics and Photonics, Springer Netherlands, 2015.

[20] D. Kwon and D. H. Werner, "Transformation optical designs for wave collimators, flat lenses and right-angle bends," *New J. Phys.*, vol. 10, 2008.

[21] D. Kwon and D. H. Werner, "Polarization splitter and polarization rotator designs based on transformation optics," *Opt. Express*, vol. 16, no. 23, pp. 18731–18738, 2008.

[22] R. Yang, W. Tang, and Y. Hao, "A broadband zone plate lens from transformation optics," *Opt. Express*, vol. 19, no. 13, pp. 12348–12355, 2011.

[23] O. Quevedo-Teruel, W. Tang, R. C. Mitchell-Thomas, A. Dyke, H. Dyke, L. Zhang, S. Haq, and Y. Hao, "Transformation optics for antennas: why limit the bandwidth with metamaterials?," *Sci. Rep.*, vol. 3, p. 1903, 2013.

[24] C. Mateo-Segura, A. Dyke, H. Dyke, S. Haq, and Y. Hao, "Flat Luneburg Lens via Transformation Optics for Directive Antenna Applications," *IEEE Trans. Antennas Propag.*, vol. 62, no. 4, pp. 1945–1953, 2014.

[25] R. Yang, W. Tang, and Y. Hao, "Wideband Beam-Steerable Flat Reflectors via Transformation Optics," *IEEE Antennas Wirel. Propag. Lett.*, vol. 10, pp. 1290–1294, 2011.

[26] R. Yang, Z. Lei, L. Chen, Z. Wang, and Y. Hao, "Surface wave transformation lens antennas," *IEEE Trans. Antennas Propag.*, vol. 62, no. 2, pp. 973–977, 2014.

[27] C. C. Njoku, W. G. Whittow, and J. C. Vardaxoglou, "Simulation Methodology for Synthesis of Antenna Substrates With Microscale Inclusions," *IEEE Trans. Antennas Propag.*, vol. 60, no. 5, pp. 2194–2202, 2012.

[28] N. Yu and F. Capasso, "Flat optics with designer metasurfaces," *Nat. Mater.*, vol. 13, no. January, pp. 139 – 150, 2014.

[29] S. B. Glybovski, S. A. Tretyakov, P. A. Belov, Y. S. Kivshar, and C. R. Simovski, "Metasurfaces : From microwaves to visible," *Phys. Rep.*, vol. 634, pp. 1–72, 2016.

[30] G. Yoon, I. Kim, and J. Rho, "Microelectronic engineering challenges in fabrication towards realization of practical metamaterials," *Microelectron. Eng.*, vol. 163, pp. 7–20, 2016.

[31] N. Meinzer, W. L. Barnes, and I. R. Hooper, "Plasmonic Meta-atoms and Metasurfaces," *Nat. Photonics*, vol. 8, pp. 1–22, 2014.

[32] A. Epstein, J. P. S. Wong, and G. V Eleftheriades, "Cavity-excited Huygens' metasurface antennas for near-unity aperture illumination efficiency from arbitrarily large apertures," *Nat. Commun.*, vol. 7, pp. 1–10, 2016.

[33] G. Minatti, F. Caminita, M. Casaletti, and S. Maci, "Spiral leaky-wave antennas based on modulated surface impedance," *IEEE Trans. Antennas Propag.*, vol. 59, no. 12, pp. 4436–4444, 2011.

[34] S. Pandi, C. A. Balanis, and C. R. Birtcher, "Design of Scalar Impedance Holographic Metasurfaces for Antenna Beam Formation With Desired Polarization," *IEEE Trans. Antennas Propag.*, vol. 63, no. 7, pp. 3016–3024, 2015.

[35] S. Maci, G. Minatti, M. Casaletti, and M. Bosiljevac, "Metasurfing : Addressing Waves on Impenetrable Metasurfaces," *IEEE Antennas Wirel. Propag. Lett.*, vol. 10, pp. 1499–1502, 2012.

[36] B. M. Turki, E. T. A. Parker, S. Wünscher, U. S. Schubert, R. Saunders, V. Sanchez-romaguera, M. A. Ziai, S. G. Yeates, and J. C. Batchelor, "Significant Factors in the Inkjet Manufacture of Frequency-Selective Surfaces," *IEEE Trans. Components, Packag. Manuf. Technol.*, vol. 6, no. 6, pp. 933–940, 2016.

[37] R. D. Seager, A. Chauraya, J. Bowman, M. Broughton, R. Philpott, and N. Nimkulrat,

"Fabric based frequency selective surfaces using weaving and screen printing," *Electrnoic Lett.*, vol. 49, no. 24, pp. 1507–1509, 2013.

[38] J. C. Batchelor, E. A. Parker, J. A. Miller, and S. G. Yeates, "Inkjet printing of frequency selective surfaces," *Electrnoics Lett.*, vol. 45, no. 1, pp. 1–2, 2009.

[39] V. Sanchez-romaguera, S. Wünscher, B. M. Turki, R. Abbel, S. Barbosa, D. J. Tate, D. Oyeka, J. C. Batchelor, E. A. Parker, U. S. Schubert, and S. G. Yeates, "Inkjet printed paper based frequency selective surfaces and skin mounted RFID tags : the interrelation between silver nanoparticle ink , paper," *J. Mater. Chem. C*, vol. 2132, no. 3, pp. 2132–2140, 2015.

[40] Taconic - Advanced Dielectric Division, http://www.taconic-add.com/, [last accessed 01/02/2017].

Chapter 2 : Heterogeneous Substrates for Microstrip Antennas

Abstract

This chapter illustrates the advantages which can be achieved by using a heterogeneous substrate for a microstrip patch antenna. A substrate is categorised as a heterogeneous substrate when its relative dielectric index is varied as a function of location. Section 2.1 reviews various fabrication techniques used for making heterogeneous substrates and application of these substrates to improve antenna performance. Such techniques include drilling holes in a slab; removal of a part of the substrate through etching or using a multi-layered structures in which the dielectric constant is varied with each layer. In Section 2.2 heterogeneous substrates are prepared by 3D printing which simplifies the manufacturing process along with bringing in extra degrees of freedom for the designer. This heterogeneous substrate was prepared by incorporating sub-wavelength slots of different electromagnetic properties in the printed dielectric slab thus altering the dielectric index locally. The 3D printed material used in this section is flexible but very lossy therefore antennas employing it as a homogeneous substrate had low radiation efficiency. The radiation efficiency of those antennas has been improved significantly by using heterogeneous substrates. The antennas have been fabricated and measured results are included in Section 2.3.4. For the

heterogeneous substrate, the patch was fed diagonally in order to increase the impedance bandwidth by combining TM_{10} and TM_{01} modes. The novelty of this chapter is using heterogeneous substrates to improve the efficiency of 3D printed patch antennas for wearable applications.

2.1 Literature Review of Heterogeneous Substrates

Microstrip patch antennas are half wavelength resonating structures, which can be characterised as a dielectric filled parallel plate waveguide radiating at the discontinuities. The transmission line model defines it as an array of two aperture radiators connected via a half wavelength microstrip [1]. This aperture array is expected to have a broadside radiation pattern such that the radiated power decreases as we move away from the maximum [2]. Microstrip patch antennas are inexpensive, low profile structures and can easily be integrated with other electronics systems. Monolithic microwave integrated circuits technology (MMIC) allows the fabrication of the antennas and the circuits in a single process [3]. MMICs generally use materials like silicon, gallium arsenide and indium phosphide for fabrication. These materials possess high values of relative permittivity which leads to a degradation in the performance of microstrip antennas which employ them as a substrate. High permittivity substrates inherently reduce the bandwidth of the antenna. Increasing the thickness of the substrate increases the bandwidth but it also increases the energy trapped inside the substrate in the form of trapped surface modes. This results in an increased interference with other circuit elements. This trapped energy also radiates from the edges of the substrate hence causing a detrimental effect on the antenna radiation pattern. Using a material with a low relative permittivity as the antenna substrate reduces the interference by trapping negligible amount of energy. The low indexed material can also increase the bandwidth of the antenna but having a low indexed substrate requires a hybrid integration scheme for the circuit fabrication which not only makes the process very intricate but also increases the cost [4]–[6].

2.1.1 Micromachined Heterogeneous Substrate Antennas

This problem was resolved by utilising heterogeneous substrates. Micromachining was applied to the substrate present below the radiator as shown in Figure 2-1 in order to synthesize the heterogeneous substrate. Part of silicon was removed from the wafer, effectively replacing it with air. 50% to 80% of the silicon from this portion was removed by chemical etching, which led to a lower value for the effective dielectric constant. The value of effective permittivity for this mixture was calculated by using the cavity model. The capacitance of patch was computed by making use of equation 2.1 [4].

$$C = \frac{\varepsilon_{eff} A}{t} \tag{2.1}$$

$$\varepsilon_{reff} = \varepsilon_{cavity}\left(\frac{L + 2\Delta L\left(\frac{\varepsilon_{fringe}}{\varepsilon_{cavity}}\right)}{L + 2\Delta L}\right)$$

$$\frac{\varepsilon_{fringe}}{\varepsilon_{cavity}} = \frac{\varepsilon_{air} + (\varepsilon_{sub} - \varepsilon_{air})x_{air}}{\varepsilon_{air} + (\varepsilon_{sub} - \varepsilon_{air})x_{fringe}}$$

$$\varepsilon_{cavity} = \frac{\varepsilon_{air}\varepsilon_{sub}}{\varepsilon_{air} + (\varepsilon_{sub} - \varepsilon_{air})x_{air}}$$

$$\varepsilon_{eff} = \varepsilon_{reff}\varepsilon_0$$

C represents the capacitance in this quasi-static model with *A* being the area and *t* the thickness of dielectric. $\varepsilon_{\text{fringe}}$ is the relative permittivity in the region of fringing fields while x_{fringe} is the ratio of air to the total thickness in that region. L represents the length of the patch while the change in length ΔL due to the fringing fields can be calculated from [41]. ε_{cavity} is the relative permittivity of the slab excluding the fringing fields with x_{air} being the ratio of the substrate to the air cavity thickness. The relative permittivity was reduced from 11.7 to 2.2 when the mixture had a ratio of 3 to 1 (air to silicon). The inclusion of the fringing fields in the calculation for the effective dielectric constant was reported to be very important

as neglecting them in the computation, yielded inaccurate results. This antenna with the proposed air-silicon mixture showed an increase in bandwidth, which indicates a decrease in Q-factor [4].

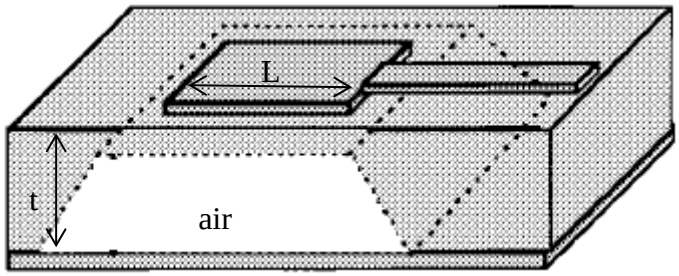

Figure 2-1*: Micromachined patch antenna with chemical etching. Chemical etching is inherently anisotropic, which is the reason for slanted edges* [4]

The effect of the air-silicon mixture on antenna efficiency and radiation pattern was also compared by the fabrication of an antenna on a high permittivity substrate ($\varepsilon_r = 10.8$), a low permittivity substrate ($\varepsilon_r = 2.2$) and a micromachined substrate, as described above on a high indexed material. The relative permittivity of 2.3 was attained by removal of 75% of silicon. This micromachined antenna also showed an increase in bandwidth indicating an increase in its efficiency. The radiation pattern of the micromachined antenna was very similar to the low indexed substrate antenna, hence providing a considerable improvement on the high valued substrate. The averaged measured efficiency (including the mismatch, feedline and connector losses) of the three antennas showed an increase in the efficiency through micromachining. It is also worth mentioning that the micromachined antenna with half of the silicon removed, showed the same efficiency as that of the antenna with the high value of relative permittivity, indicating no improvement. However the efficiency of this antenna was increased by 13% after extending the air-silicon mixture beyond the radiating edges by a factor which was twice the height of the substrate [4].

Heterogeneous substrates, with silicon as the base material, have been fabricated using micromachining. These substrates were also used to reduce the coupling among various antenna elements of a patch array and were found superior in performance to conventional patches, especially over a wideband range. The resonant frequency was calculated using finite element method (FEM) which takes into account the fringing fields and higher order effects for calculation and its results were found out to be very close to the measured values [3]. The accurate value of effective dielectric constant for multi-layered substrates can be computed by equation 2.2

$$\varepsilon_{effective} = \left(\frac{c}{2Lf_r}\right)^2 \tag{2.2}$$

where *L* is the length of the patch and '*c*' is the speed of light in free space.

Another way to fabricate a heterogeneous silicon substrate is to combine micromachining with two layered silicon . Both layers in the substrate of the antenna possessed the same height with the patch being printed on one layer and the other layer containing an air cavity below the patch. The placement of this cavity decreased the permittivity from 9.7 to 2.8 and improved the bandwidth to 12.4% in comparison to a conventional patch (whose typical values are 4.4% and 2% for a relative permittivity of 2.2 and 10 respectively) [7].

Backside etching has also been used to manufacture heterogeneous substrates [5]. Trenches were introduced at the edges of the radiating element with a part of conductor extending beyond the edges of the etched substrate. Backside etching was used as the fields from the edge are less attached to the substrate in comparison with front side etching. The introduction of these cantilevered edges with trenches caused an increase in the resonant frequency of the structure indicating a decrease in the effective value of the permittivity. For the antenna to radiate at the same frequency as without trenches, its area needed to be increased by 79%. The bandwidth also increased from 515 MHz to 720 MHz and a more uniform radiation

pattern was obtained with 1.2dB increase in the radiated power, which was an indication of an improvement in antenna efficiency. This improvement was attributed to the fact that the radiating edges were immersed in air instead of being attached to a lossy dielectric [5].

In another approach, an antenna was designed with an inverted substrate i.e. the radiator was placed at the interface of dielectric slab and micromachined air cavity. The antenna was designed with Taconic CER-10 and silicon for ISM band (24 - 24.25 GHz), and compared with a coplanar fed antenna having a micromachined air cavity in the substrate. Both antennas yielded a high gain; the gain was higher for the inverted substrate antenna due to superstrate effects of the dielectric [8].

The conductive properties of silicon (especially low resistive silicon), when it is used as a substrate, lower the efficiency of the antenna [9]. A SiO_2 layer can therefore be used to mitigate the substrate loss hence improving the antenna efficiency [10]. Such a structure is illustrated in Figure 2-2. An antenna placed on a layer of SiO_2 has been presented in [14] in which a very high efficiency of 92% and relatively larger bandwidth were achieved by reducing the effective permittivity through micromaching. A major portion of silicon homogeneous block below the SiO_2 layer was removed with the resulting ratio of air to silicon being 26:1. This decreased the effective relative dielectric constant to 1.41 [9].

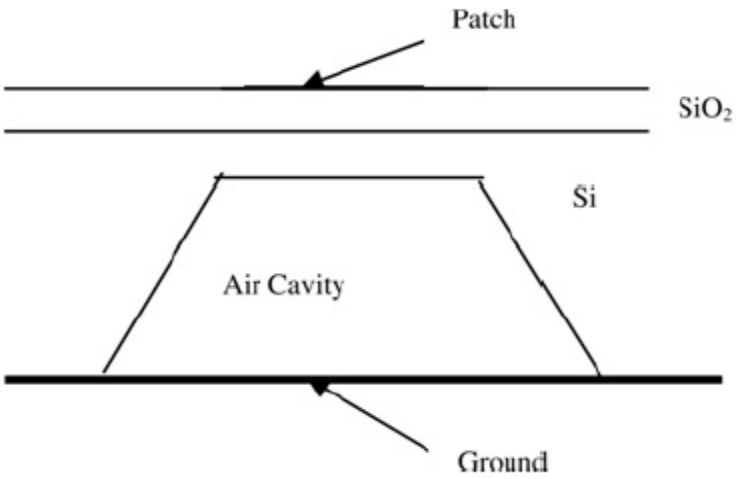

Figure 2-2*: Micromachined patch antenna with SiO2 layer [9]*

Another antenna where micromaching was used to reduce the effective dielectric index and improve antenna performance is given in [11]. Meandering was utilised to reduce the size of the antenna. Antenna was then placed on a layer of SiO_2 for reduction of loss due to substrate conductivity. As a result antenna bandwidth and gain was improved [11].

Surface micromaching with copper metal plating was used for construction of a heterogeneous substrate patch, with a substrate thickness of 300µm [12]. The patch had the ground plane on its one side and 4-pillars at the non-radiating edges of the radiator on the other side. The radiator was 300µm away from the top of the high resistivity silicon substrate and was supported by the pillars structure. This antenna resonated at 41.5 GHz and had a bandwidth of 6 GHz, with a size of $2.12 \times 2.12 mm^2$. Antenna size was reduced to $1.78 \times 1.78 mm^2$ by removal of two pillars from non-radiating edges and adding a pillar to the radiating edge. The bandwidth was also reduced to 4 GHz. It was also reported that increasing the thickness of the pillar at the radiating edge further reduced the size to $1.41 \times 1.41 mm^2$. The bandwidth of the structure was also reduced further by 1 GHz. The electroplating of copper and gold suffered from Kirkendall effect since both metals have a

different diffusion rate, leading to a porous fragile structure with poor conductivity. To avoid this nickel was added between copper and gold layers [12].

A disadvantage of using micromachining to reduce the effective dielectric index is that it adds fragility to the structure. This drawback has been eliminated by using a heterogeneous substrate in which the etched part of the low resistive silicon is filled with SU8 photoresist (ε_r = 4.1) for a differential fed dipole. The silicon is etched in such a way that middle part is completely removed, dividing it into two halves separated by SU8. This SU8 layer supported the 500nm silicon nitride layer on which the antenna was situated. This approach increased the efficiency from 0.96% to 20.5% with a high bandwidth exceeding 43% at a resonant frequency of 5.8 GHz. The original extremely small efficiency was due to low resistive silicon being used as a substrate, which ended up connecting both arms of the dipole before the addition of SU8 [13].

Heterogeneous substrates were also synthesized by etching a small portion of silicon below the patch antenna and filling the resulting cavity with SiO_2 or polyimide. The antenna was fed by a coplanar waveguide. The resonant frequency for SiO_2 and polyimide filled cavity was 9.07 GHz and 9.24 GHz respectively. The higher frequency was due to the fact that polyimide's permittivity is 3.2 whereas the value of permittivity for SiO_2 is 3.5. The bandwidth for these antennas was 2.2% and 2% respectively. A double C patch antenna on a traditional micromachined high permittivity substrate produced by anisotropic etching was also presented. The resulting patch had a resonant frequency of 3.23 GHz with 2% bandwidth [14].

Heterogeneous substrates have also been applied to improve the performance of reconfigurable antennas. The antenna geometry of such reconfigurable antennas was controlled by making use of MEMS switches. Instead of high permittivity silicon, a substrate

was prepared with silicon and glass having the ratio 1:2 resulting in the index being lowered to 5.8. Switching between 2.4 and 5.8 GHz was controlled by RF-MEMS [10].

2.1.2 Heterogeneous Substrates with Partial Substrate Removal

Heterogeneous substrates have been prepared by using partial substrate removal. This technique was mostly utilised to reduce the surface waves radiated by the microstrip antennas. Surface waves cause power loss thus decreasing the radiation efficiency of the antenna. The finite length of the substrate also results in the diffraction of these waves from the edges. These diffracted waves cause interference which distorts the radiation pattern of the antenna. Surface waves effects are more pronounced when the employed antenna substrate has a higher relative permittivity. For thin substrates, the TM mode is the chief cause of surface wave radiation. This mode is completely supressed when the radius of the magnetic current ring is equal to the radius of the radiator [15]. By making use of the equivalence principle and the cavity model, the radiation pattern of an antenna can be computed by modelling it as a magnetic current ring. However, the magnetic current ring is larger in size when compared to a circular microstrip antenna on a homogeneous substrate; therefore in order to meet this condition, the effective dielectric constant can be reduced by introducing an inhomogeneity in the substrate. A portion of the substrate is removed from the core of the patch in order to increase its size by lowering of the effective dielectric constant. This newly formed hollow cavity is responsible for lowering the effective permittivity as it can also be viewed as replacing a portion of the substrate by a material whose relative permittivity is unity. A high valued dielectric is preferred because a comparatively smaller portion of the substrate needs to be removed in contrast to a lower permittivity value, where the newly formed cavity would have to be extended very close to the edge of the patch [16]. Such a structure has been demonstrated in Figure 2-3.

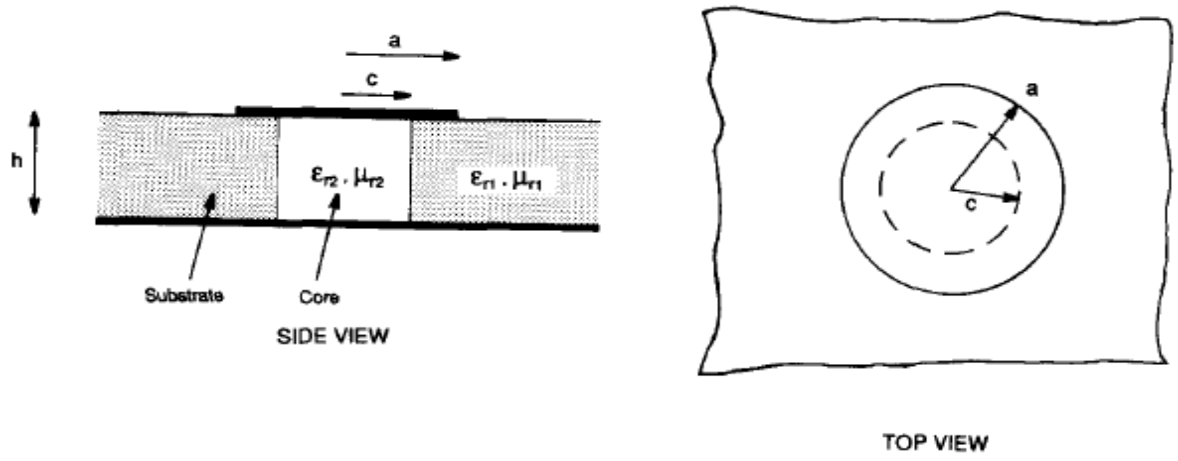

Figure 2-3: *A cored patch design with 'c' and 'a' being the radii of core and the circular patch and h the height of substrate ($\mathcal{E}_{r2} < \mathcal{E}_{r1}$)* [16]

This method does not cater for the waves radiated from the feed and other higher order modes, hence does not completely eliminat the surface waves; however there is a significant reduction which is useful for improving the radiation pattern of the antenna [16].

The same theory was then applied to a rectangular microstrip antenna being operated at 23 GHz on a 0.635mm thick substrate of relative permittivity 10.8 for surface wave reduction. The rectangular magnetic current loop was also found to be larger in size than the conventional patch, so the permittivity was lowered by removing some of the substrate from below the patch leading to an increase in its resonant length [17].

The cored patch design was also proposed to reduce the surface waves for vehicle toll collection systems. The core was filled with a relatively lower dielectric index material in a substrate of higher permittivity, causing a reduction in the effective dielectric constant thus enabling the antenna to meet size restriction indicated by the equivalent magnetic loop model [18].

The cored patch design was also applied to a microstrip antenna array and side lobe level (SLL) was successfully reduced [19]. This SLL is very much desired for radar applications and it was achieved by eliminating the surface waves and therefore decreasing the mutual coupling among the array elements.

Partial substrate removal has also been applied to increase the gain of a microstrip patch by reducing the surface waves. A portion of a substrate is removed from the sides of the patch resulting in the formation of an air cavity surrounding the patch. This is shown in Figure 2-4. The gain of the patch was increased depending on the portion of the substrate removed; the large amount of removal led to a higher gain. The removal of substrate also led to a decrease in the effective dielectric constant thus the size of the antenna was increased to keep the resonant frequency constant. An antenna with a homogeneous substrate, having the same effective dielectric constant (as obtained from substrate removal) was compared to affirm that the partial substrate removal was successful in reducing the surface wave effects, which led to an increase in the antenna gain [20].

Since surface waves are stronger along the radiating edges, it was also reported that removal of substrate along the non-radiating edges produced a much smaller increase in the gain of the antenna. Partial substrate removal was also used to reduce the mutual coupling between array elements due to its characteristic of surface wave suppression [20].

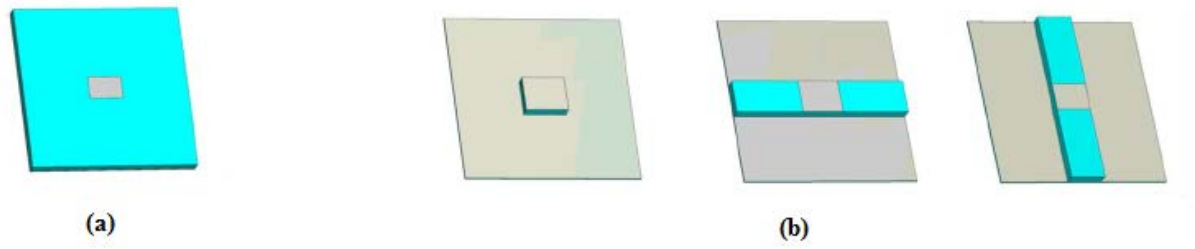

Figure 2-4*: (a) Patch without substrate removal (b) Various configurations of substrate removal [20]*

Substrate removal has been applied to improve the characteristics of a cavity-backed slot antenna which inherently suffers from low efficiency and has a small bandwidth for substrates with small thickness [21]. The substrate is removed below the slot which causes a decrease in the capacitance of the structure resulting in lowering of the q-factor thus increasing the bandwidth. The replacement of the lossy substrate with air decreased the substrate losses, which increased the efficiency of the antenna. The effect has been studied for partial substrate removal which increased the bandwidth and efficiency of the antenna. It was observed that substrate near the slot had more significant effects on the behaviour of the cavity-backed slot antenna [21].

A different idea for improving the radiation pattern was proposed in [2], where an antenna was designed on a heterogeneous substrate. The antenna was designed in such a way that the radiator was suspended in the air with the dielectric substrate surrounding it. The radiation pattern of this structure was compared against a homogeneous substrate antenna. The pattern with the suspended patch showed a significant improvement over the homogeneous substrate antenna. The radiation pattern was improved further when this idea was extended to a patch on a GaAs substrate with a supporting layer of SiO_2/SiN_x. For fabrication, the suspended patch structure was changed and the heterogeneous substrate was used to provide support to the antenna. This heterogeneous substrate was prepared by etching holes in the homogeneous slab. The resonant frequency of the patch also changed from 11.1 to 13.2 GHz due to the heterogeneous substrate prepared by etching holes [2].

2.1.3 Heterogeneous Substrates Prepared by Drilling Holes

The effective dielectric index of the substrate, for antennas designed on high indexed materials like silicon and gallium-arsenide, can also be lowered by drilling small periodic holes in the dielectric slab [22]. The periodicity is small in comparison to the operating

wavelength so that quasi-static techniques calculate the effective value of permittivity accurately. The effective permittivity was measured by placing the newly synthesized substrate between the two parallel metallic layers and the capacitance was measured. This capacitance was then used to calculate the permittivity. Another method used for calculation was designing a microstrip antenna with this synthesized substrate; its resonant frequency was then measured and used to find the effective relative permittivity. Both practical methods produced similar results. The synthesized lower indexed dielectric was then used to improve to the efficiency and bandwidth of an antenna (designed on high indexed dielectric with drilled holes). The behaviour of the synthesized low dielectric substrate was found similar to a substrate having low homogeneous permittivity [22].

Microstrip antenna designers usually employ materials of relative permittivity around 10 (like Taconic CER-10) for high indexed substrates in order to achieve antenna miniaturization. Heterogeneous substrates (also referred to as textured dielectrics) have also been utilised for increasing the relative permittivity of the substrate for miniaturization. The substrates of relative permittivity even higher than 40 were synthesized by perforating a slab of Barium titanate ($\varepsilon_r = 30$) and filling the holes with Bi-Ba-Nd-Titanate (BBNT; $\varepsilon_r = 100$) and utilized for antenna miniaturization. The evaluation of the exact relative permittivity was difficult to ascertain, so an aperture coupled antenna was synthesized on this substrate and its resonant frequency and bandwidth were measured. A method of moments (MoM) program was then used to calculate the permittivity and loss tangent. The resulting values for these quantities were 46.2 and 0.0004 respectively. These values were then used to design an antenna capable of operating at 1.243 GHz with a bandwidth of 13.75 MHz. The measured resonant frequency deviated by about 1% for this design; the deviation however was found to be 8% if permittivity was calculated through the volumetric ratio [23].

In another design, heterogeneous substrates with a lower valued dielectric index were used to surround the antenna with the purpose of improving its radiation pattern [11]. These dielectrics were manufactured by drilling holes in the substrate to lower its permittivity. This process (of surrounding the antenna with a substrate having a lower effective permittivity) caused a reduction in the energy trapped inside surface waves hence decreasing the amount of energy radiated from the edges of the finite ground plane causing a significant reduction in the dip at boresight in the radiation pattern, without compromising the bandwidth of the antenna for a thicker substrate [6]. An example of heterogeneous substrates prepared by drilling holes in a slab is shown in Figure 2-5.

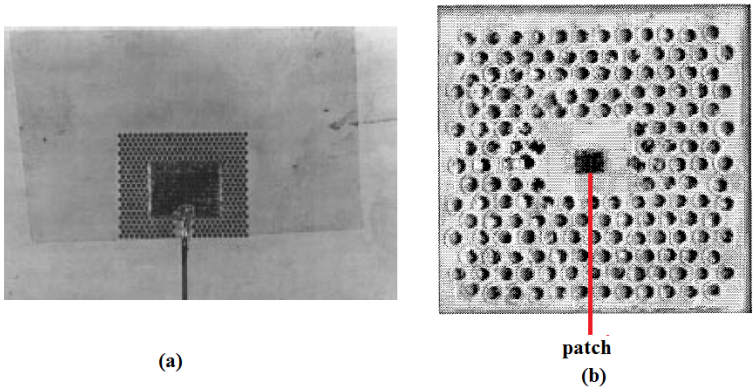

Figure 2-5*: Fabricated patched antenna (a) synthesized substrate below the patch* [22] *(b) synthesized substrate surrounding the patch* [6]

Stacked patches are utilized to achieve wide bandwidth and in three layered stacked patches, the middle layer's relative permittivity is expected to be very close to 1, hence this layer comprises of foam or air, making the structure fragile. Textured dielectrics are created by drilling of holes in the substrate to achieve low dielectric index and provide mechanical stability. Because of the electrically small holes, the substrate behaved as a block having an effective relative permittivity given by the equation 2.3 [24],

$$\varepsilon_{r(av)} = \frac{\varepsilon_r(d^2 - \pi a^2) + \pi a^2}{d^2} \tag{2.3}$$

Where d is the distance between the holes, $\mathcal{E}_r$ is the effective relative permittivity of the substrate and a is the radius of a hole. For triangular lattice, the permittivity is even lower for the same values as the proportion of air in this textured structure increases [24].

Textured dielectrics are applied to tapered slot antennas (TSA) [25]. These antennas are very sensitive to the effective electrical thickness of the substrate given by the equation 2.4 [25].

$$t_{eff} = t(\sqrt{\varepsilon_r} - 1) \tag{2.4}$$

The maximum effective thickness needs to be $0.03\lambda_0$ which shows that for a sturdy structure, the dielectric constant needs to be very small. This can be achieved by drilling holes inside the substrate. The effective dielectric constant using a Duroid substrate ($\varepsilon_r = 2.2$) was lowered to a value of 1.46 through perforation. This allowed an increase in the thickness of the substrate. For constant width TSA to be operated at 94 GHz, the effective thickness needs to be 200μm, which makes the structure very fragile. The permittivity was reduced to 1.46 by drilling of holes and about 40% of the substrate was replaced with air. The substrate thickness of the new antenna was increased to 380 μm, which provided mechanical sturdiness to the structure. The radiation pattern of the machined antennas was compared with the traditional antenna of the same substrate thickness and a considerable improvement was observed [25].

Heterogeneous materials have also been employed to improve a Rotman lens. Rotman lenses [26] are an important component of many beam forming networks and have been utilised in various applications like multi-beam receivers, beam steering antenna systems and automotive radar systems [27], [28]. A Rotman lens has three focal points which result in enhancing the scanning capabilities. On a homogeneous substrate the lens suffers from energy loss, which can be improved by using textured dielectrics. A gradient of dielectric

permittivities is employed to bend the rays within the lens which leads to better focussing of power, thus alleviating the losses due to imperfect focussing. The relative permittivity is changed gradually in order to minimise the reflections at the interface and the lens is placed closer to the beam port end so that relatively more energy is confined within its structure instead of being wasted. The value of dielectric constant for a substrate was varied by drilling holes inside the structure. Substrates of five different permittivities were prepared by varying the number of holes per unit area as shown in Figure 2-6 .

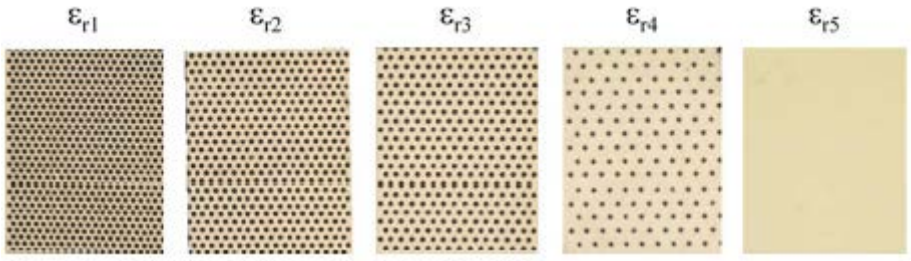

Figure 2-6: *Heterogeneous materials with different dielectric index for Rotman lens (permittivity is varied by changing the density of holes)* [27]

A lens with varying local dielectric index was fabricated. The dielectric index increased and the contour angle decreased when moving towards the array port side. This kind of structure led to better focussing of the beam. The graded lens showed an improved insertion loss when it was compared with a Rotman lens having a homogeneous substrate. The difference in peak power also decreased, at extreme scan angles. The loss of power due to spill-over to the side ports was also reduced by making use of synthetic dielectrics [27].

2.2 Antennas on Additively Manufactured Heterogeneous Substrates

Additive manufacturing (or 3D printing) is one of the most exciting technologies of the 21st century and research on this area is being carried out at a rapid rate. The technology is becoming less expensive with time and its popularity and usefulness is increasing rapidly so

much that NASA has sent a 3D printer into space [38]. Additive manufacturing uses layer by layer material deposition thus offering a wide range for customisation as each layer can have a distinct shape and material; also digital fabrication removes the need for a mask therefore every printed sample can be different and for example, that is one of the reasons that most hearing aids are now additively manufactured.

Current manufacturing techniques used in the microwave industry use subtractive processes like milling and etching; where the structure of the desired shape and properties are created by partial removal of the available materials. However by using additive manufacturing materials are deposited only where required and therefore comparatively less material is wasted which can potentially have cost-saving and environmental advantages. Also when additive manufacturing becomes able to print both conductive and non-conductive materials in a single process then the whole process of fabricating antenna circuitry can be monolithic. 3D printing uses a CAD file for manufacturing different structures thus making it possible to make the geometries which were considered too intricate or too expensive previously. Recently 3D frequency selective surfaces have been manufactured by using 3D printing [36], [37].

2.2.1 Analysis and Design

A 3D printed heterogeneous substrate was prepared by locally changing the dielectric properties in specific areas of an additively manufactured substrate using a Connex 500 3D printer. The base material used is DM9760 and the dielectric properties of the substrate were altered by placing air-filled gaps at the radiating edges of the antenna. DM9760 is flexible and lends itself to wearable antennas, for which flexibility is a requirement on most occasions. DM9760 has a relative permittivity of 3 and a loss tangent of 0.051. These values were measured by using a split-post dielectric resonator at 1.9 GHz. The higher loss is because the

DM9760 is not designed for electromagnetic applications. If a homogeneous DM9760 substrate were to be used the high value of the loss tangent will have an adverse effect on the efficiency of the patch antenna.

2.2.2 Efficiency Improvement

First, a homogeneous substrate antenna was designed using EMPIRE XCcel, full wave electromagnetic analysis software which uses the finite-difference-time-domain (FDTD) algorithm. This antenna was 36mm long and 34mm wide. It is placed on a 70 × 70mm^2 homogeneous slab of DM9760 of thickness 3.2mm. It is probe-fed along the x-axis at a position 9mm from the centre of the patch. This antenna is shown in Figure 2-7. It resonates at 2.4 GHz and has a fractional bandwidth of 6.25%. The substrate for this antenna shown was 3D printed. A thin sheet of copper was used to act as a ground plane on one side by gluing it to the substrate and the patch was affixed on the other side. A 0.7mm hole was drilled for the feed. An SMA connector was used as a probe feed and then soldered on to the patch. The fabricated antenna is shown in Figure 2-8. The measured and simulated results for this antenna are shown in Figure 2-9.

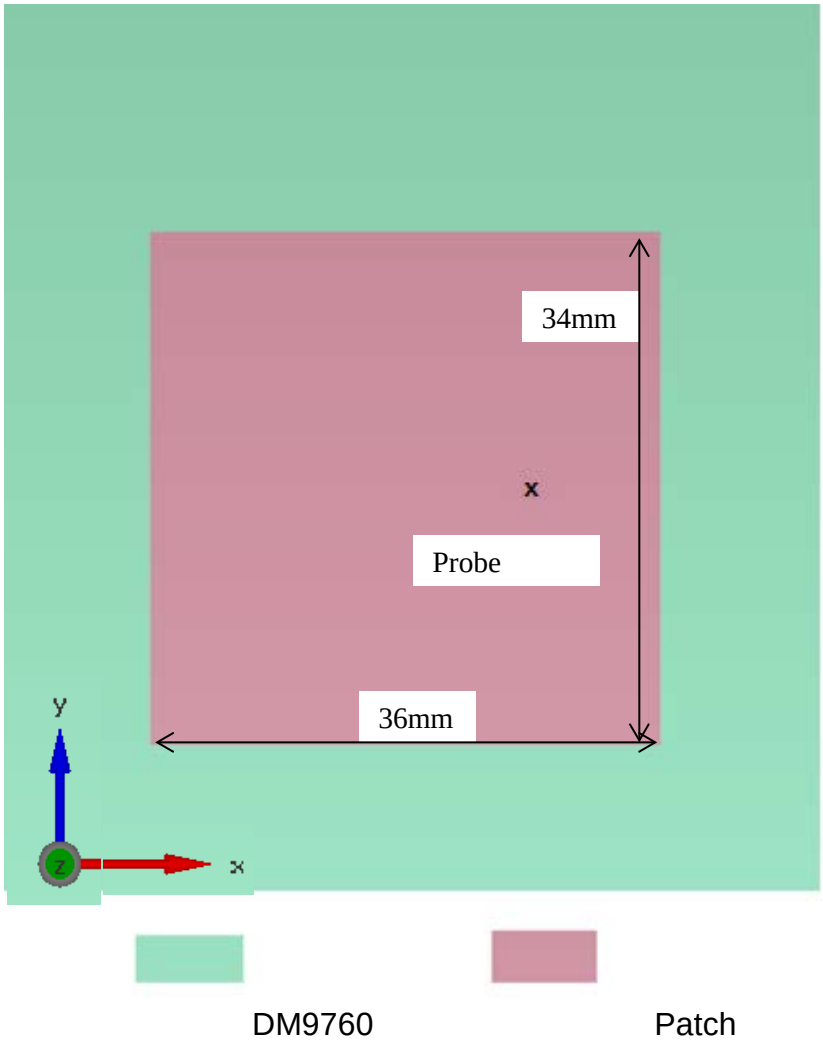

Figure 2-7: *Homogeneous Substrate Antenna on a 70 x 70mm^2 ground plane*

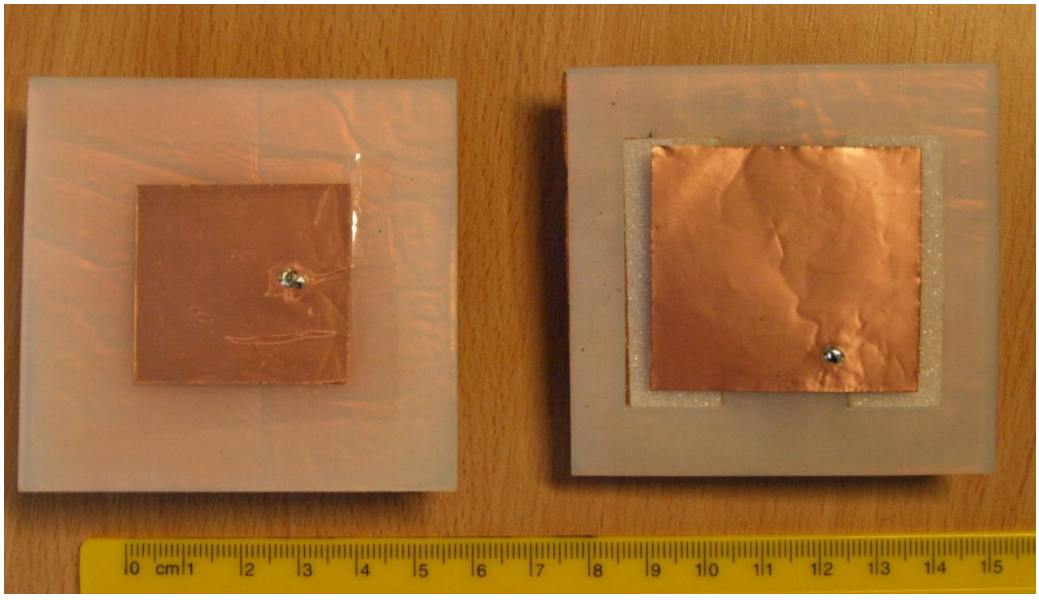

Figure 2-8: *Fabricated homogeneous and heterogeneous substrate microstrip antennas*

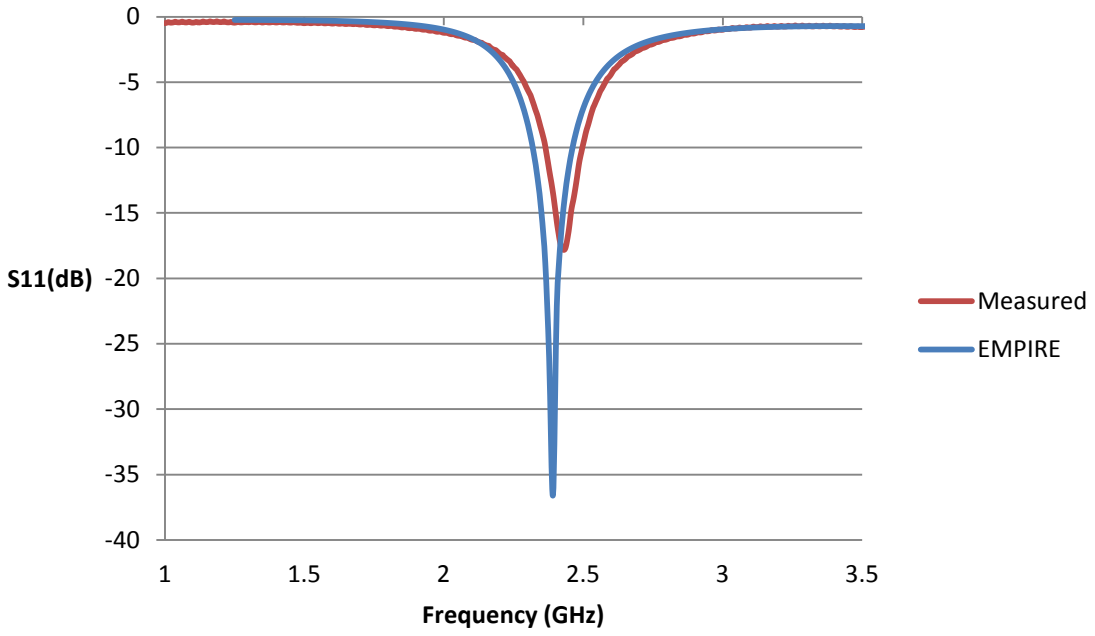

Figure 2-9: *Measured and simulated S11 results for homogeneous substrate antenna*

The homogeneous substrate antenna (Figure 2-7) had a simulated radiation efficiency of 42%. This low value is because DM9760 is a very lossy substrate. By using a heterogeneous substrate, the radiation efficiency was improved up to 74percent because a lossless material (air) is introduced.

The heterogeneous substrate antenna has been shown in Figure 2-10. The air-filled slots extended 4mm beyond the edges of the patch and were 16mm long and 46mm wide. Since a conventional microstrip antenna is a narrowband structure thus various other methods have been reported in literature to improve its bandwidth; these methods include stacked patches, defected ground planes, use of parasitic elements and planar inverted-F antennas (PIFA) [29]–[34],[37]. For the heterogeneous substrate antenna presented in this section, TM_{10} and TM_{01} modes have been combined to enhance its bandwidth. The radiating edges for the two modes are perpendicular to each other and by controlling the location and size of the air-filled

slots the resonant frequencies of the two modes can be brought together and the impedance bandwidth of the structure increased by combining the TM_{10} and TM_{01} mode resonances. The antenna on the heterogeneous substrate was 44mm long and 42mm wide. The manufactured antenna heterogeneous antenna is shown in Figure 2-8. The antenna was fed with a probe. Since both modes need to be matched well below -10dB (for this antenna) in order to achieve a large impedance bandwidth, the probe was off-set with respect to both the axes as indicated in Figure 2-10.

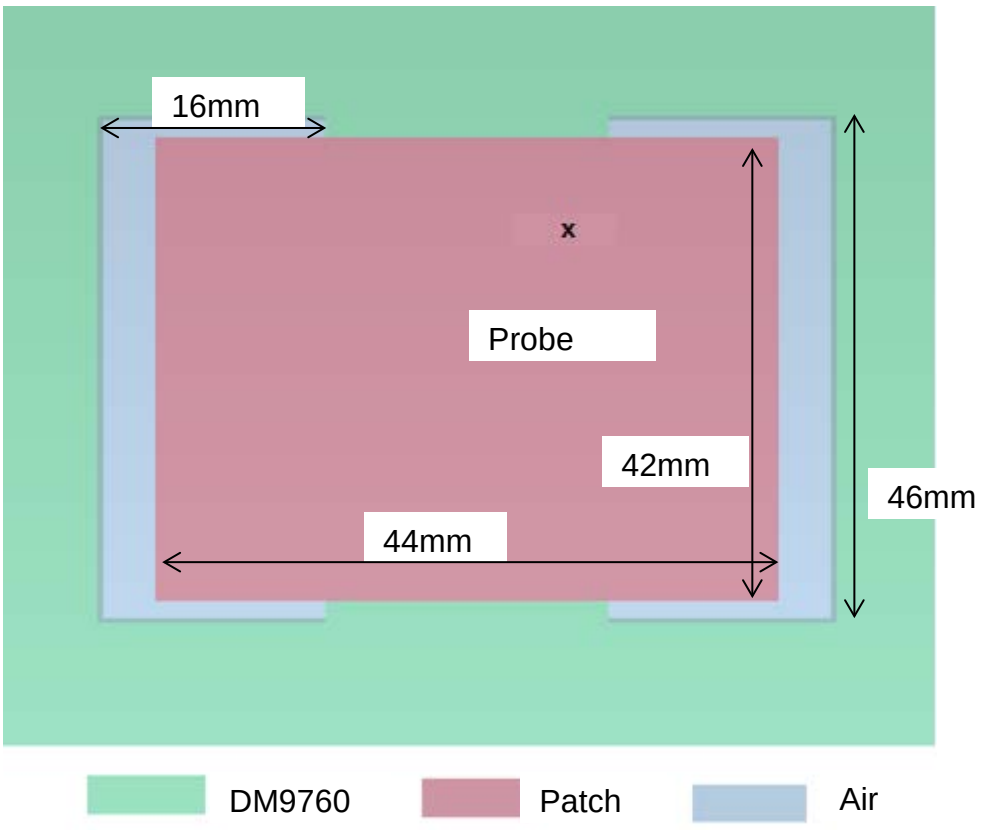

Figure 2-10*: Heterogeneous substrate antenna on a 70 x 70mm^2 substrate*

The size of the antenna was increased in order to keep the frequency constant as the air filled slots reduce the dielectric loading. The substrates for the antenna (shown in Figure 2-8) was 3D printed and the fabrication process is identical to the one described for the homogeneous

substrate antenna earlier in this section; however for the heterogeneous substrate antenna, the slots were filled with Rohacell ($\varepsilon_r \sim 1$) to ensure that the patch remained flat. S11 values were measured using an Anritsu network analyser. The measured and simulated S11 results for the heterogeneous substrate antennas are shown in Figure 2-11.

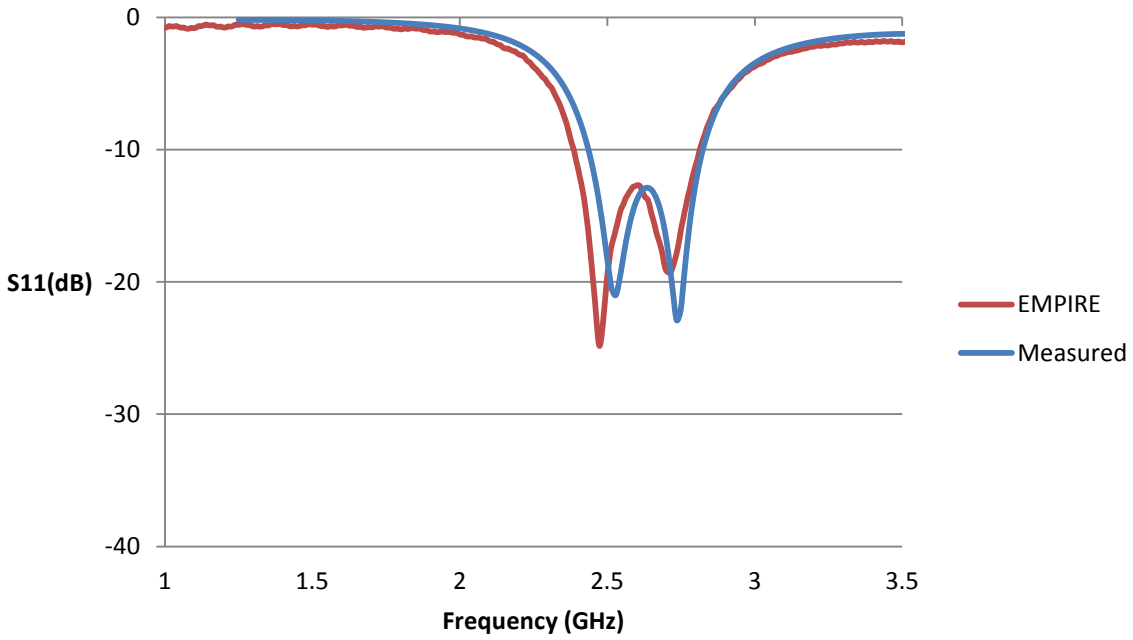

Figure 2-11*: Measured and Simulated S11 results for a 3D printed heterogeneous substrate antenna*

The first resonance occurs at 2.52 GHz and the second resonance is at 2.74 GHz. The impedance bandwidth of this antenna was found to be 14% which is 380 MHz with respect to the second resonance. Contour plots of the electric field magnitude are shown at the two resonances due to TM_{10} and TM_{01} modes, shown in Figure 2-12 and Figure 2-13 respectively. (Heterogeneous substrate antennas whose bandwidth has been increased by combining the two modes have been attached as Appendix A.)

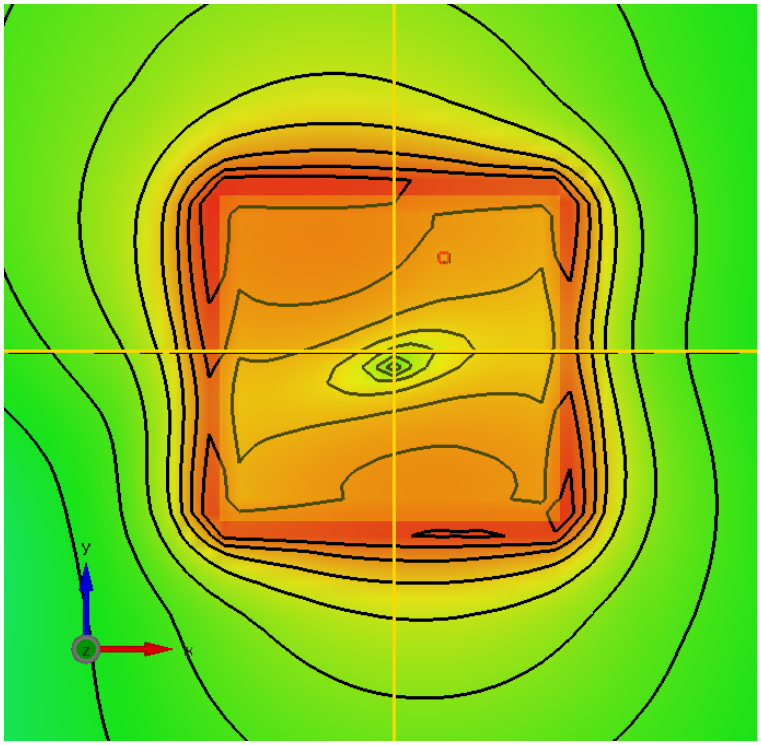

Figure 2-12: *Electric fields at first resonance (2.52 GHz) for heterogeneous substrate antenna showing high electric field values at the radiating edges.*

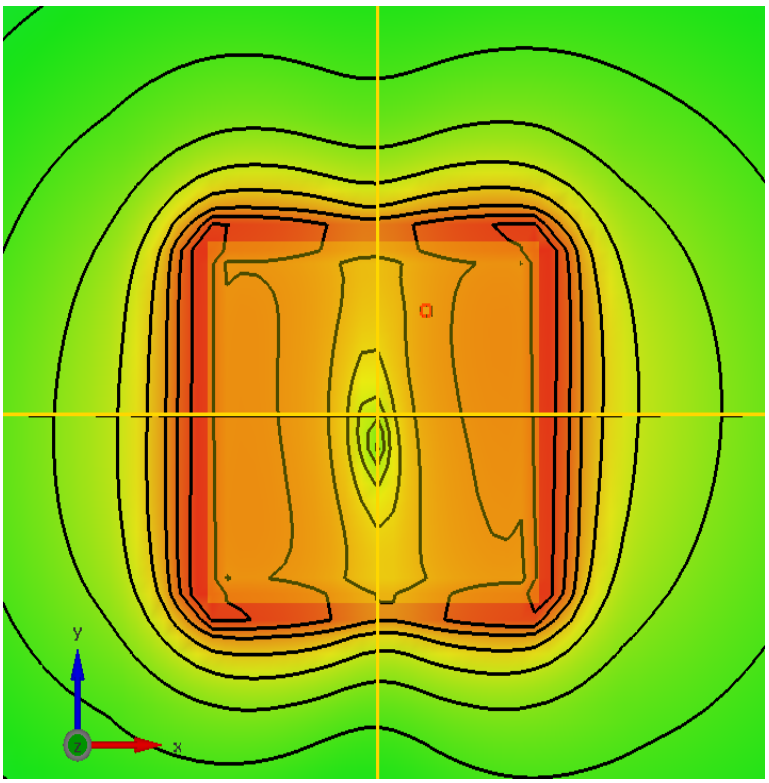

Figure 2-13: *Electric fields at second resonance (2.73 GHz) for heterogeneous substrate antenna showing the concentration of electric fields at the radiating edges placed along y-axis*

The simulated value for the radiation efficiency of the heterogeneous substrate antenna at the first resonance (2.52 GHz) is 60% and at the second resonance (2.76 GHz) is 78%. The radiation efficiency, at the frequency point which is at local maximum between the two resonant frequencies, is 63% at 2.63 GHz. The radiation efficiency of the heterogeneous substrate antenna is higher at the second resonance frequency as compared to the first resonant frequency because for the second resonance the radiating edges are present along the y-axis and are completely immersed in air. At 2.63 GHz, both modes tend to combine so the value for the radiation efficiency lies in between the two resonant values. It is worth noting that the efficiency for the heterogeneous antenna, at both resonant frequencies is greater than the efficiency of the homogeneous substrate antenna.

The effect of the position of these slots on radiation efficiency has also been analysed and summarised in Table 2-1. These slots were 46mm wide and 10mm long. The dimensions of the substrate were $70 \times 70 mm^2$ and the antenna was $44 \times 42 mm^2$. The position of the slots in the heterogeneous substrate is shown in Figure 2-14. This antenna had a simulated resonant frequency of 2.04 GHz and exhibited a radiation efficiency of 38%. By moving slots 8mm from the centre, the resonant frequency of the antenna was changed to 2.34 GHz and the simulated radiation efficiency was 54%. When the slots were moved 7mm further towards the edges, these slots extended 3mm beyond the edges of the patch which resonated at 2.43 GHz and demonstrated a simulated radiation efficiency of 58%. This shows that placing the slots at the edge of the patch has a greater influence on the antenna performance. The increase in the efficiency is due to two reasons: (i) the introduction of the air-filled slots cause a decrease in the losses of the substrate and since the electric fields of a patch antenna are highly concentrated in the substrate, this effect becomes significant and leads to an improvement in the radiation efficiency; (ii) the secondary effect is a decrease in effective permittivity of the

material with the introduction of air-filled slots which leads to an increase in the resonant frequency (for a patch antenna).

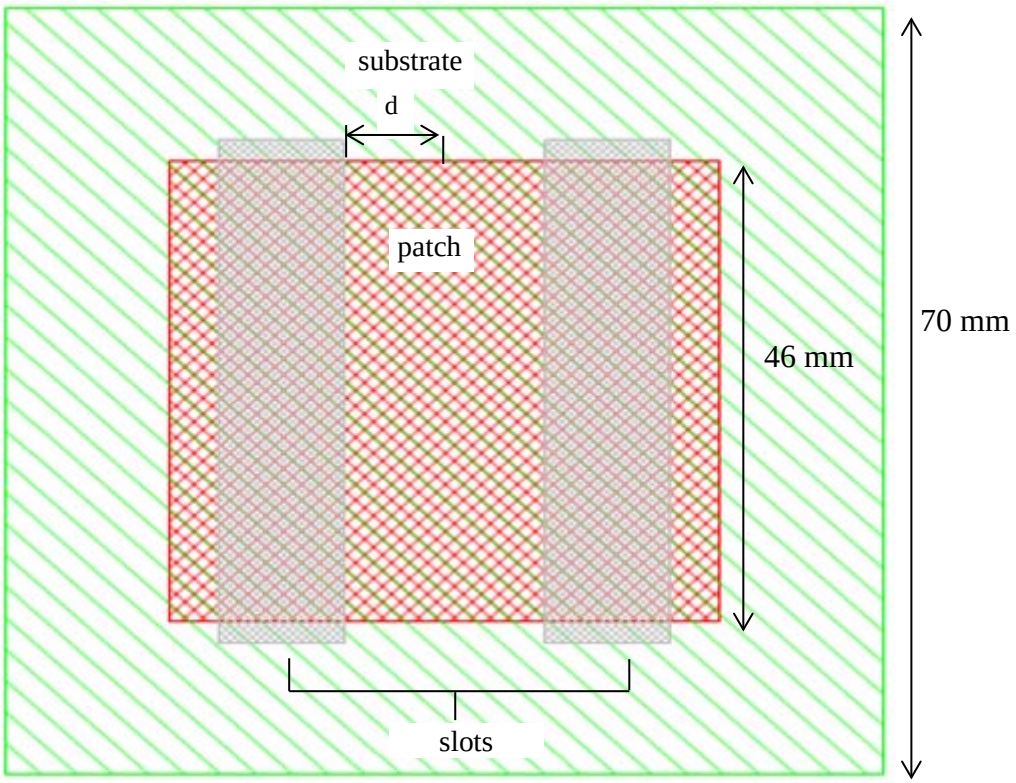

Figure 2-14: Distance *d* of the slots (grey) from the centre of the substrate (green) and the patch (red)

Table 2-1: *Variation in simulated resonant frequency and radiation efficiency with respect to the location of slots for a heterogeneous substrate antenna*

Distance *d* of slots from the centre (mm)	Resonant Frequency (GHz)	Radiation Efficiency (%)
1	2.04	38
8	2.34	54
15	2.43	58

To investigate how the heterogeneous substrate caused a decrease in the losses of the structure (which significantly improves the radiation efficiency); a larger 44 × 42mm^2

antenna was simulated on a homogeneous DM9760 substrate. This antenna exhibited a resonant frequency of 1.96 GHz and a radiation efficiency of 37%. The same patch was then simulated on a substrate of a relative permittivity 1.9 and loss tangent 0.051. This simulation was carried out to make this antenna resonant at 2.43 GHz without changing its dimensions. This antenna exhibited a radiation efficiency of 47%. This shows that the increased efficiency is due to both the reduction in losses and the increase in size.

2.2.3 Measured Radiation Patterns and Efficiency

The radiation patterns of both antennas (shown in Figure 2-8) in both principle planes and their radiation efficiencies were measured using spherical measurement in the far-filed in an Anechoic Chamber. The comparison of measured and simulated radiation patterns for the homogeneous antenna is shown in Figure 2-15. For the heterogeneous substrate antenna, Figure 2-16 and 2-18 demonstrate the simulated and measured radiation patterns at first and second resonance respectively while Figure 2-17 compares the simulated and measured radiation pattern at the local maximum between the two resonances.

The measured radiation efficiency for the homogeneous substrate antenna was 44% and the measured and simulated radiation patterns also showed good agreement. The radiation patterns in both planes show a broadside main beam and the beamwidth is similar in both E- and H-planes with linear polarisation as expected from a traditional patch. For the heterogeneous substrate the measured radiation efficiency at the first resonance was 60% and the shape of the patterns resembled that of the homogeneous substrate antenna. Since the feed was offset with respect to both axes therefore large cross polarisation values was observed. For the second resonance the pattern shape remained the same and the pattern again shows cross polarisation. The measured radiation efficiency at the second resonance was 74%. For

the local maximum at 2.63 GHz between the cross polarisation becomes higher without any noticeable change in the pattern shape. This is due to the fact that at this point both orthogonal modes TM_{10} and TM_{01} tend to combine with each other. The measured radiation efficiency for this frequency was found out to be 64%. The measured values for radiation efficiencies show agreement with the simulated results. The comparison between the measured and the simulated results is summarised in Table 2-2.

Table 2-2: *Comparison between the measured and simulated radiation efficiency for the heterogeneous substrate antenna*

Frequency (GHz)	Simulated Radiation Efficiency (%)	Measured Radiation Efficiency (%)
2.52	60	60
2.63	63	64
2.76	78	74

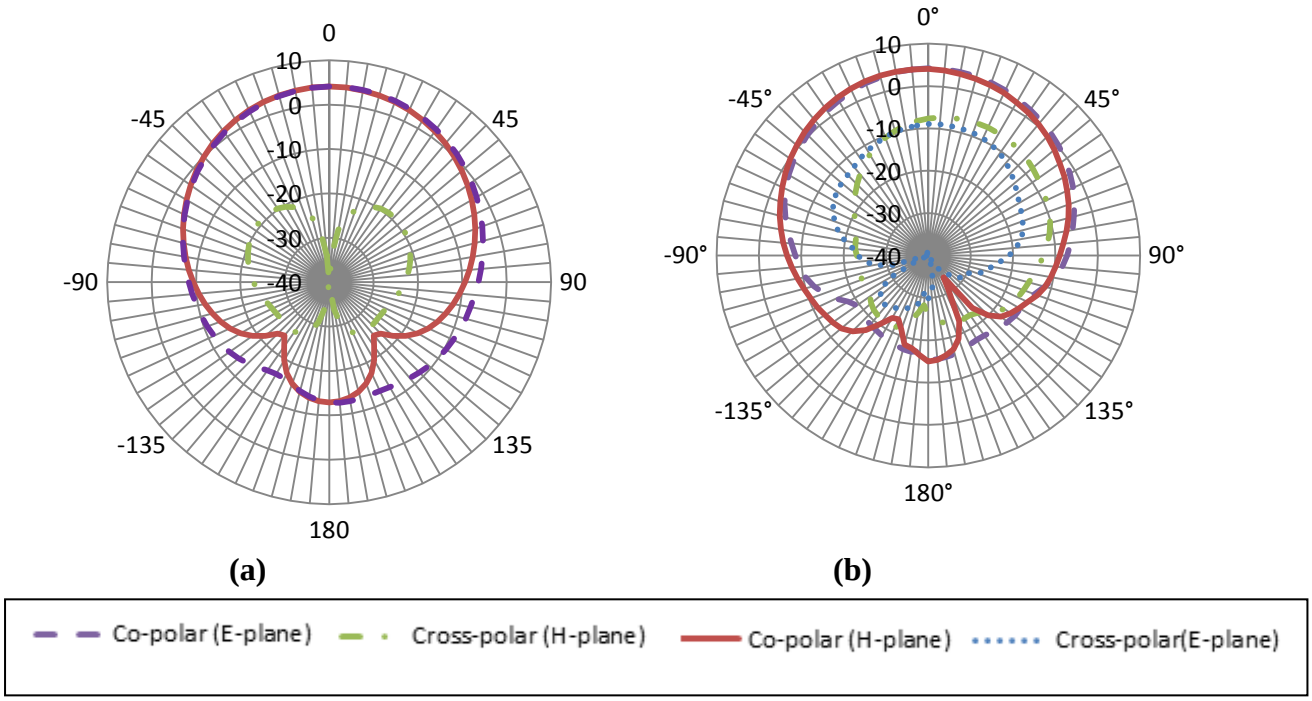

Figure 2-15: *(a) Simulated and (b) measured radiation patterns for homogeneous substrate antenna*

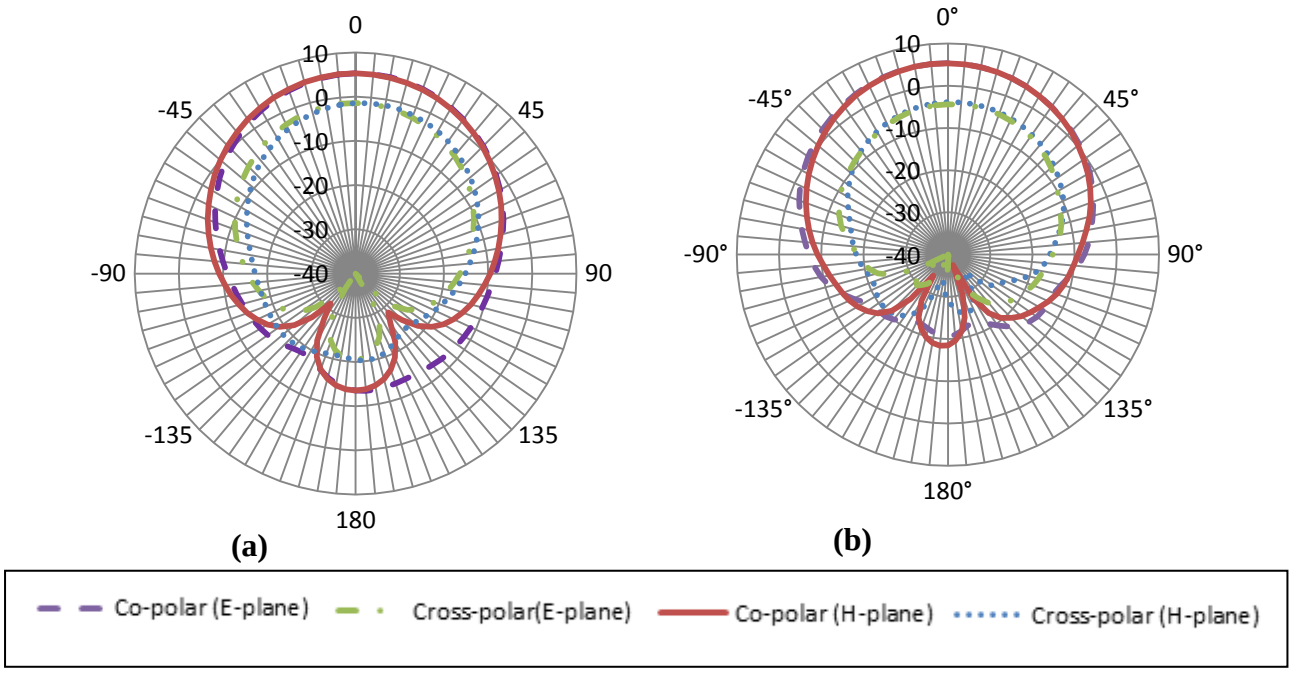

Figure 2-16: *(a) Simulated and (b) measured radiation patterns for heterogeneous substrate antenna at first resonance*

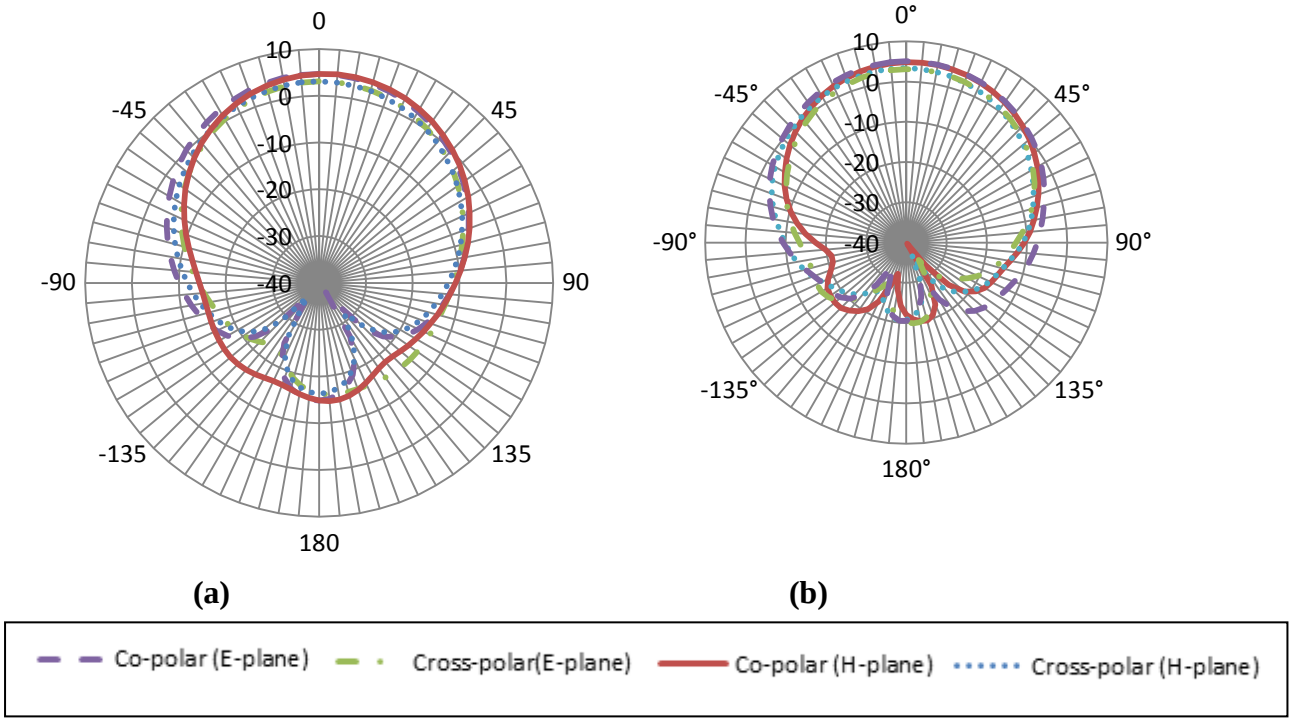

Figure 2-17: *(a) Simulated and (b) measured radiation patterns for heterogeneous substrate antenna at the maximum between first and second resonance*

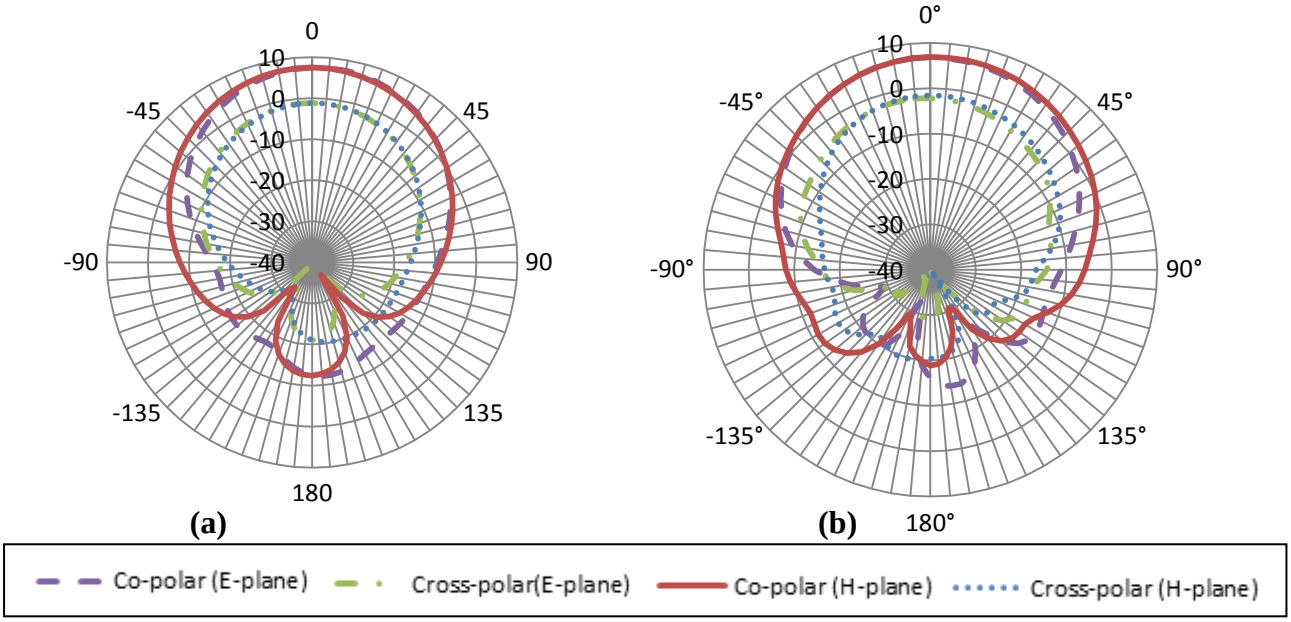

Figure 2-18**:** *(a) Simulated and (b) measured radiation patterns for heterogeneous substrate antenna at the second resonance*

The polarisation for the second resonance of heterogeneous substrate antenna was orthogonal to the first resonance which is not deemed to be an issue for mobile and wearable antennas in rich multipath environments as the antenna may be flexed when attached to the arm or a leg of a person and its orientation is changed with the movement of the person.

2.3 Conclusions

Heterogeneous substrates with air slots have been employed to improve the efficiency of a microstrip patch antenna using a flexible 3D printed substrate. These substrates were manufactured by using additive manufacturing. Since the value of loss tangent for the additively manufactured flexible substrate is high, it caused the homogeneous substrate antenna to have low radiation efficiency. With air filled slots in the heterogeneous substrate the dielectric losses were considerably lowered which caused an improvement in the radiation efficiency of the antenna. The air filled slots caused a decrease in the effective permittivity of the substrate which also increased the radiation efficiency. It was also demonstrated that the effects of the heterogeneity on the radiation efficiency were more pronounced when it was present in the region where electric fields were high. The bandwidth of the heterogeneous substrate antenna was increased by combining TM_{01} and TM_{10} modes occurring at the perpendicular edges of the rectangular patch. The slots were placed at the two vertical edges of the patch which caused them to influence one mode more than the other. The probe feed for heterogeneous substrate antenna is offset with respect to both the axes so that the antenna was well matched for both modes. This caused an increase in the cross polar component of the heterogeneous substrate antenna. The manufacturing flexibility of 3D printing allows future researchers to design substrates with more complex permittivity maps. 3D printing

could replace the Rohacell in the structure with a mesh structure which is predominantly air by volume (i.e. low infill fraction).

References

[1] K. Carver and J. Mink, “Microstrip antenna technology,” *IEEE Trans. Antennas Propag.*, vol. 29, pp. 2–24, 1981.

[2] M. J. Vaughan, K. Y. Hur, and R. C. Compton, “Improvement of Microstrip Patch Antenna Radiation Patterns,” *IEEE Trans. Antennas Propag.*, vol. 42, no. 6, pp. 1980–1983, 1994.

[3] L. P. B. Katehi, “Micromachined microstrip patch antenna with controlled mutual coupling and surface waves,” *IEEE Trans. Antennas Propag.*, vol. 49, no. 9, pp. 1282–1289, 2001.

[4] I. Papapolymerou, R. F. Drayton, and L. P. B. Katehi, “Micromachined Patch Antennas,” *IEEE Trans. Antennas Propag.*, vol. 46, no. 2, pp. 275–283, 1998.

[5] Q. Chen, V. F. Fusco, M. Zheng, and P. S. Hall, “Micromachined Silicon Antennas,” in *Microwave and Millimeter Wave Technology Proceedings, ICMMT ’98. 1998 International Conference on*, pp. 289–292.

[6] J. S. Colburn and Y. Rahmat-Samii, “Patch antennas on externally perforated high dielectric constant substrates,” *IEEE Trans. Antennas Propag.*, vol. 47, no. 12, pp. 1785–1794, 1999.

[7] M. Zhang, Q. Chen, P. S. Hall, and V. F. Fusco, “Broadband microstrip patch antenna on micromachined silicon substrates,” *Electron. Lett.*, vol. 34, no. I, pp. 8–9, 1998.

[8] S. Aditya, C. K. Sim, D. Wu, W. T. Chua, Z. X. Shen, and C. L. Law, “High-Gain 24-GHz CPW-Fed Microstrip Patch Antennas on High-Permittivity Substrates,” *IEEE Antennas Wirel. Propag. Lett.*, vol. 3, pp. 30–33, 2004.

[9] V. K. Singh, “Ka-band micromachined microstrip patch antenna,” *IET Microwaves, Antennas Propag.*, vol. 4, no. July 2008, pp. 316–323, 2010.

[10] D. Phan and G. Chung, “Design and Optimization of Reconfigurable Inset-Fed Microstrip Patch Antennas with High Gain for Wireless Sensor Networks,” in *Computing and Communication Technologies, 2009. RIVF ’09. International Conference on*, 2009, no. 2, pp. 5–8.

[11] A. Ibrahim and D. R. S. Cumming, “A Micromachined 10 GHz Meander Dipole Antenna On High Resistivity Silicon Substrate For Remote Sensing Applications,” in *Loughborough Antennas and Propagation Conference*, 2009, no. November, pp. 345–347.

[12] M. Ha, Y. Cho, and C. Wo, “Q-band Micro-patch Antennas implemented on a High Resistivity Silicon substrate using the Surface Micromachining Technology,” in *Microwave Symposium Digest, 2004 IEEE MTT-S International*, 2004, pp. 1189–1192.

[13] J. Yan and R. D. Murch, “Fabrication of a Wideband Antenna on a Low-Resistivity Silicon Substrate Using a Novel Micromachining Technique,” *IEEE Antennas Wirel. Propag. Lett.*, vol. 6, pp. 476–479, 2007.

[14] W. Pan, S. Wu, and Y. Chen, “Micromachined Patch Antennas on Synthesized Substrates,” in *International Conference on Mirowave and Milimeter Wave Technology Proceedings*, 2004, pp. 58–61.

[15] A. K. Bhattacharyya, “Characteristics of Space and Surface Waves in a Multilayered Structure,” *IEEE Trans. Antennas Propag.*, vol. 38, no. 8, pp. 1231–1238, 1990.

[16] D. R. Jackson, J. T. Williams, A. K. Bhattacharyya, R. L. Smith, S. J. Buchheit, and S. A. Long, “Microstrip Patch Designs That Do Not Excite Surface Waves,” *IEEE Trans. Antennas Propag.*, vol. 41, no. 8, pp. 1026–1037, 1993.

[17] I. Papapolymerou, R. F. Drayton, and L. P. B. Katehi, “Surface wave mode reduction for rectangular microstrip antennas,” *IEEE Antennas Propag. Soc. Int. Symp. 1995*

Dig., vol. 3, pp. 1494–1497, 1995.

[18] Y. Xia, A. Li, and Q. Huang, "Cored Circle Patch Antenna for Automotive ETC System," in *Microwave, Antenna, Propagation and EMC Technologies for Wireless Communications, 2009 3rd IEEE International Symposium on*, 2009.

[19] N. Bayat, H. R. Hassani, and S. Mohammad, "Sidelobe Level Reduction In Microstrip Patch antenna array," in *Loughborough Antennas and Propagation Conference*, 2011, no. November, pp. 3–6.

[20] S. B. Yeap and Z. N. Chen, "Microstrip Patch Antennas With Enhanced Gain by Partial Substrate Removal," *IEEE Trans. Antennas Propag.*, vol. 58, no. 9, pp. 2811–2816, 2010.

[21] S. Yun, D. Kim, and S. Nam, "Bandwidth and Efficiency Enhancement of Cavity-Backed Slot Antenna Using a Substrate Removal," *IEEE Antennas Wirel. Propag. Lett.*, vol. 11, pp. 1458–1461, 2012.

[22] G. P. Gauthier, A. Courtay, and G. M. Rebeiz, "Microstrip Antennas on Synthesized," *IEEE Trans. Antennas Propag.*, vol. 45, no. 8, pp. 1310–1314, 1997.

[23] D. Psychoudakis, Y.-H. Koh, J. L. Volakis, and J. H. Halloran, "Design Method for Aperture-Coupled Microstrip Patch Antennas on Textured Dielectric Substrates," *IEEE Trans. Antennas Propag.*, vol. 52, no. 10, pp. 2763–2765, 2004.

[24] E. A. Navarro, I. J. Craddock, and D. L. Paul, "Synthetic dielectrics for planar antenna," *Electron. Lett.*, vol. 36, no. 6, pp. 491–493, 2000.

[25] J. B. Muldavin and G. M. Rebeiz, "Millimeter-Wave Tapered-Slot Antennas on Synthesized Low Permittivity Substrates," *IEEE Trans. Antennas Propag.*, vol. 47, no. 8, pp. 1276–1280, 1999.

[26] W. Rotman and R. Turner, "Wide-angle microwave lens for line source applications,"

IEEE Trans. Antennas Propag., vol. 11, no. 6, pp. 623–632, Nov. 1963.

[27] L. Schulwitz and a. Mortazawi, "A New Low Loss Rotman Lens Design Using a Graded Dielectric Substrate," *IEEE Trans. Microw. Theory Tech.*, vol. 56, no. 12, pp. 2734–2741, Dec. 2008.

[28] D. H. Archer and M. J. Maybell, "Rotman lens development history at raytheon electronic warfare systems 1967–1995," in *Antennas and Propagation Society International Symposium*, 1995, pp. 31–34.

[29] T. Taga and K. Tsunekawa, "Performance Analysis of a Built-In Planar Inverted F Antenna for 800 MHz Band Portable Radio Units," *IEEE J. Sel. Areas Commun.*, vol. SAC-5, pp. 921–929, 1987.

[30] C. Wood, "Improved bandwidth of microstrip antennas using parasitic elements," *Microwaves, Opt. Antennas, IEE Proc. H*, vol. 127, no. 4, pp. 231–234, 1980.

[31] S. Egashira and E. Nishiyama, "Stacked microstrip antenna with wide bandwidth and high gain," *IEEE Trans. Antennas Propag.*, vol. 44, no. 11, pp. 1533–1534, 1996.

[32] M. J. Ammann and M. John, "Some Techniques To Improve Small Groundplane Printed Monopole Performance," in . *IEEE Antennas and Propagation International Symposium, Honolulu*, 2007, pp. 2825–2828.

[33] M. J. Ammann and M. John, "Optimum Design of the Printed Strip Monopole," *IEEE Antennas Propag. Mag.*, vol. 47, no. 6, pp. 59–61, 2005.

[34] S. D. Targonski, R. B. Waterhouse, and D. M. Pozar, "Design of Wide-Band Aperture-Stacked Patch Microstrip Antennas," *IEEE Trans. Antennas Propag.*, vol. 46, no. 9, pp. 1245–1251, 1998.

[35] http://www.bbc.co.uk/news/technology-24329296, "BBC News - Nasa plans first 3D printer space launch in 2014." .

[36] B. J. Banks, “Adding Value in Additive Manufacturing,” *Pulse, IEEE*, vol. 4, no. 6, pp. 22–26.

[37] E. A. Parker and B. Sanz-Izquierdo, “3D printing technique for fabrication of frequency selective structures for built environment,” *Electron. Lett.*, vol. 49, no. 18, pp. 1117–1118, Aug. 2013.

Chapter 3 : Heterogeneous Composite Materials

Abstract

The focus of Chapter 2 concerned heterogeneous substrates and their impact on the microstrip antenna performance. 3D printing was introduced as a novel way of making such substrates. Chapter 3 combines 3D printing with commercially available laminates to develop and manufacture heterogeneous composite materials. These composite materials constitute two or more materials with distinct electromagnetic properties. The relative permittivity of these composite materials can be controlled in order to achieve values that are not readily available “off the shelf”. This effective dielectric constant of the composite material depends on the properties of its constituent materials and their volumetric ratio. The dielectric constant of composite materials can be estimated by using effective medium theory. Section 3.1.1 summarises some important effective medium approximations. Section 3.1.2 gives the potential electromagnetic advantages which can be attained by using composite materials. In Section 3.2, bi-phase composite materials have been manufactured using two commercially available laminates or homogeneous 3D printed slabs. Section 3.3 creates tri-phase materials by 3D printing meshed structures with a commercial laminate, therefore the three constituents are: PLA, laminate and air. Section 3.3 also shows that by combining additive manufacturing with commercially available laminates, composite materials with a large and near continuous range of dielectric constants can be manufactured. Section 3.4 investigated the reliability of

3D printing as a manufacturing technique by investigating its engineering tolerance. Finally Section 3.5 presents the conclusions. The novelty of this chapter is in combining 3D printing with commercial laminates in order to manufacture ‘on demand’ dielectrics with a near continuous wide range (relative permittivity = 1.4 to 8.7). A design equation to predict the relative permittivity of these composite materials has been derived using Weiner bounds.

3.1 Literature Review of Composite Materials

Composite materials are made up of constituents with distinct dielectric properties. Since low loss magnetic materials at microwave frequencies are very difficult to find and manufacture, therefore the work in this chapter is limited to the relative permittivity of the composite materials. The refractive index of the composite materials can be controlled by only varying the relative permittivity of the constituent materials.

The mixture of the constituent materials yields composite materials with dielectric properties different than their constituents. The dielectric constant of the composite materials can be analytically calculated by effective medium theory [1], [2]. It is worth noting that the effective medium approach requires the periodicity or the lattice constant of the structure to be much smaller than the wavelength of operation [3]. Generally in the literature the lattice constant is one-tenth of the wavelength or even smaller [4]. This allows the characterisation of the composite materials as a single effective medium whose properties can be controlled by varying the properties and volumetric ratios of its constituents.

3.1.1 Review of Effective Medium Theory

One of the earliest and widely used approximations for ascertaining the effective dielectric constant of heterogeneous composite materials is the Clausius-Mossotti relation. In

the non-homogeneous materials, this approximation has been applied to study the Hall effect [5].

The Clausius-Mossotti equation relates the macroscopic properties of a mixture to the microscopic properties of its constituents [6]. It is also known as Lorentz-Lorenz relation in refractivity where it gives the relation between the refractive index and the molecular polarizability. The Clausius-Mossotti equation defines the relation between the molecular polarizability and the dielectric constants of the parent material and the heterogeneity. The parent material is assumed to be uniform and isotropic. The Clausius-Mossotti relation is given in Equation 3.1

$$\frac{\varepsilon_r - 1}{\varepsilon_r + 2}\left(\frac{M}{d}\right) = \frac{N}{3\varepsilon_0 \alpha} \tag{3.1}$$

Where ε_r is the relative permittivity of the material, M is the molar mass, N represents Avogadro's number, d represents the density, ε_0 represents the permittivity of vacuum and α is the molecular polarizability of the heterogeneity. It should be noted that this relation considers the vacuum (free space) to be the parent/host material [7].

The key assumption in Clausius-Mossotti relation is that the electric field present between the two poles of a dipole can only be neglected when the density of heterogeneity is extremely low like that of a dilute gas [8]. For a relatively denser medium, the electric field among the poles of the molecular dipole, represented by a delta function, needs to be accounted for. In a dense medium at a microscopic level, the effect of the dipole itself and that of the other dipoles delta electric fields has a significant effect [6], [9]. This term can also be observed when the static Green's tensor of an electric field is calculated [7].

Another way to explain this phenomenon is by considering the discrete nature of the lattice. The discrete nature of a spherical heterogeneity is shown in Figure 3-1. When a hypothetical

region containing a number of molecules is considered, the electric field inside this region will be dependent on the polarizability of the uniform space surrounding it and the effects of the dipole itself and the other surrounding dipoles. Since the polarization divergence over the uniform region is zero thus there occurs a discontinuity at the surface of this hypothetical region. This discontinuity thus makes the term related to the individual dipole moment appear when calculating the electric field [6]. It is also worth mentioning that the molecular polarizability is directly related to the induced dipole moment of a molecule in the presence of an electric field.

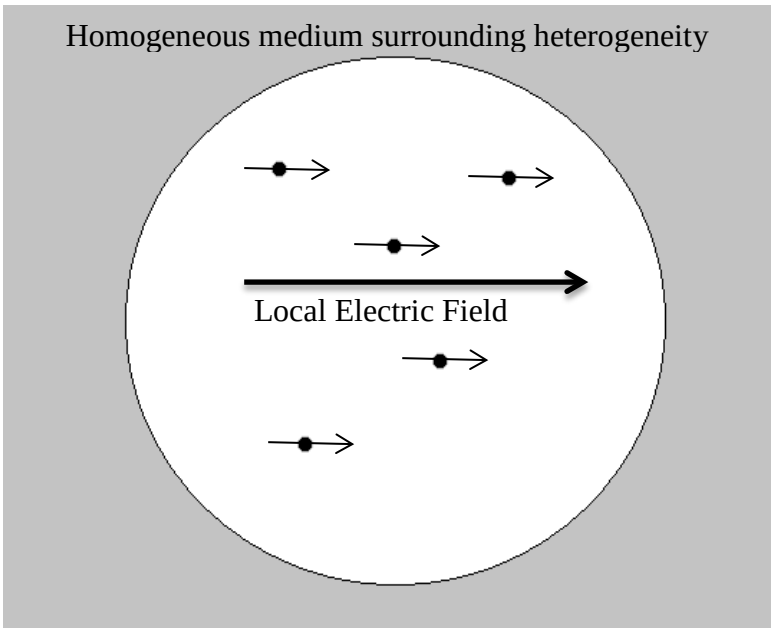

Figure 3-1: *A spherical heterogeneity placed in a homogeneous medium. The discrete nature of the heterogeneity and local electric field is illustrated (redrawn from* [6]*)*

The Clausius-Mossotti equation can directly be used to derive the Maxwell Garnett approximation. Maxwell Garnett equation predicts the effective relative permittivity of the composite material [5], [7]. By substituting the value of polarizability in Equation 3.1, the equation is transformed in to the Maxwell Garnett approximation for composite materials

$$\varepsilon_{eff} = \frac{1 + \frac{(1+2f)(\varepsilon_r - 1)}{3}}{1 + \frac{(1-f)(\varepsilon_r - 1)}{3}}$$

(3.2)

where ε_{eff} is the relative permittivity of the composite material, ε_r is the relative permittivity of the heterogeneity and f is the volume fraction ratio. This equation assumes that the host/parent material is vacuum and the inclusions (heterogeneity) are assumed to spherical in shape [7]. The Equation 3.2 needs to be rewritten for a parent material having relative permittivity other than 1 [7]. This is very important because for the most cases the parent material in a composite material is not air/vacuum. Equation 3.2 can be rewritten for a parent material having an arbitrary value for its relative permittivity [7].

$$\varepsilon_{eff} = \varepsilon_p \frac{1 + \frac{(1+2f)(\varepsilon_r - \varepsilon_p)}{3\varepsilon_p}}{1 + \frac{(1-f)(\varepsilon_r - \varepsilon_p)}{3\varepsilon_p}}$$

(3.3)

ε_p is the relative permittivity of the host/parent material. Maxwell Garnett relation shows that the dielectric constant of a composite material is dependent on the relative permittivity of the parent material, the relative permittivity of the host material and the ratio between their volumes.

Bruggeman's formula for estimating the effective relative permittivity of a composite material is also widely cited [10]. The formula is valid for the composite materials in which the periodicity of the structure is very small as compared to the wavelength. This condition allows the assumption that the electric field remains constant across the unit cell/heterogeneity [11]. The formula also assumes that the heterogeneity introduced is spherical in shape [12]. It is given by Equation 3.4.

$$(1-f)\left(\frac{\varepsilon_{eff}^{b}-\varepsilon_{p}}{\varepsilon_{eff}^{b}+2\varepsilon_{p}}\right)+(f)\left(\frac{\varepsilon_{eff}^{b}-\varepsilon}{\varepsilon_{eff}^{b}+2\varepsilon}\right)=0$$

(3.4)

where ε_{eff}^{b} is the Bruggeman effective relative permittivity of the composite material, ε_p is the relative permittivity of the host/parent material and f is the volume fraction. Lichtenecker's formula and power-law models have also been utilised for analysis and estimation for composite materials [13]. Composite structures come in a variety of shapes with the heterogeneity distributed arbitrarily among the parent material. This aperiodic distribution of the heterogeneity can lead to different effective permittivity values for the composites having the same volumetric ratios. There is also a difference between the estimated values calculated from different formulae; therefore it is a common practice to define the bounds on the relative permittivity of the composite structures [10].

Hashin-Shritkman bounds place the strictest limit on the effective relative permittivity for the composite materials. These bounds were originally presented for the relative permeability but are also applicable to dielectric constants. Hashin-Shritkman bounds are derived for those composite materials which are bi-phase, isotropic and macroscopically uniform [14], [15]. For a composite material with the parent material having the relative permittivity ε_p and the heterogeneity with relative permittivity ε_r, these bounds are given by 3.5a and 3.5b

$$\varepsilon_{min}^{HS}=\varepsilon_{p}+\frac{f}{\frac{1}{\varepsilon_{r}-\varepsilon_{p}}+\frac{1-f}{3\varepsilon_{p}}}$$

(3.5a)

$$\varepsilon_{max}^{HS}=\varepsilon+\frac{f}{\frac{1}{\varepsilon_{p}-\varepsilon_{r}}+\frac{1-f}{3\varepsilon_{r}}}$$

(3.5b)

where f is the volume fraction of the heterogeneity, ε_{min}^{HS} is the lowest bond for the composite material; ε_{max}^{HS} is the highest bound and $\varepsilon_p > \varepsilon_r$.

Another kind of bounds known as Wiener bounds is also very significant for estimating the effective dielectric constant of a composite material. Wiener bounds give the absolute limits on the effective dielectric constant [16], [17]. These bounds were derived when the electric field was applied to a layered composite material. In order to calculate the absolute upper and lower limit, the structure of the layers were parallel and perpendicular to the applied electric field vector respectively [18]. Wiener bounds are also applicable for anisotropic materials. These bounds have also found applications in pharmaceutical industry where in conjunction with pulsed terahertz waves, they have been proposed for tablet quality inspection [19]. The upper and lower Wiener bounds can be calculated using Equations 3.6a and 3.6b.

$$\varepsilon_{max}^{W} = f\varepsilon_r + (1-f)\varepsilon_p \tag{3.6a}$$

$$\varepsilon_{min}^{W} = \frac{f}{\varepsilon_r} + \frac{(1-f)}{\varepsilon_p} \tag{3.6b}$$

ε_{max}^{W} is the maximum effective relative permittivity and $\varepsilon_{min}^{W}$is the minimum effective relative permittivity predicted by Wiener bounds.

3.1.2 Advantages of Composite Materials

Composite materials are artificially manufactured therefore their properties can be controlled. This allows the manufacturer to fabricate the materials specially tailored to the demands of the designer. Materials whose relative permittivity can be controlled by the designer have the potential to be employed as antenna substrates to enhance antenna performance [20]. Composite materials can be used to synthesize dielectrics with dielectric constants not readily available.

Such materials are also an integral part of graded index (GRIN) devices. Graded index materials have their relative permittivity locally varied in order to achieve the desired electromagnetic response. Graded index materials combined with field transformation have been successfully demonstrated for the design of a five layer flat lens with its performance superior to that of a similar designed lens using ray optics [21].

Transformation optics is another area in which composite materials are of paramount importance. Transformation optics is a potentially revolutionary discovery of this century and can be used to design novel microwave devices which were considered impractical in the past. Transformation optics is based on the principle of transforming the original coordinate system of an electromagnetic device in such a way that its electromagnetic behaviour remains unaltered. This is achieved by changing the refractive index (relative permittivity and permeability) in the coordinate space by using metamaterials and various other artificially designed materials [22]. The technique has been successfully applied to design a flat hyperbolic lens without compromising the performance of the original lens, using only isotropic artificially manufactured materials. These isotropic artificial materials were designed using micro and nanoparticles of titanates using vacuum casting and maintain a discrete profile of relative permittivity [23]. Composite materials, designed on the principle of transformation optics, have also been utilised for a wideband transmission through a sub-wavelength aperture [24].

Another significant advantage of composite materials lies in the manufacture of Luneberg lenses. A Luneberg lens is a spherically symmetric object with two foci, one lying at infinity and the other at the surface of the lens [25]. A perfect Luneberg lens should have a refractive index which varies radially. The refractive index decreases radially from the centre and is given by $n(r)^2 = \varepsilon_r(r) = 2 - \frac{r^2}{R^2}$, where r is the distance from the centre, $n(r)$ is the refractive index as a function of r, $\varepsilon_r(r)$ is the relative permittivity and R is the radius of the

lens. Although a continuously varying relative permittivity is impossible to achieve, a discrete profile with sub-wavelength thick concentric shells using composite materials has been used to practically manufacture such lenses [26]. Another technique for manufacturing a Luneberg lens is 3D polymer jetting rapid prototyping. This technique makes the process of manufacturing very simple by combining arbitrarily shaped polymers with air voids. By controlling the volumetric ratios of both materials, a Luneberg lens (with discrete dielectric profile) has been realised and presented [27], [28]. By making use of the transformation optics concept, a flat Luneberg lens for directive antennas has been fabricated with the required composite materials prepared by vacuum casting [29]. Composite materials can also be used for wideband designing flat reflectors and surface wave transformation lens antennas [30], [31]. Composite materials made from epoxy resin and multi-wall carbon nanotubes have been used to manufacture microwave absorbing structures [32].

3.2 Hybrid Composite Materials with Two Constituent Materials

In this section it will be shown that by combining commercial laminates; a resulting composite can be manufactured whose relative permittivity is different from its constituent laminates. The constituent materials are Arlon AD-1000, Taconic RF-60, Taconic RF-45 and Polylactic acid (PLA) which is very commonly used in 3D printing.

A large number of composites having different volumetric ratios were manufactured by gluing the two pieces of different laminates. All the pieces were 80mm long and 80mm wide. These materials are non-magnetic; therefore they have a relative permeability equal to 1. The properties of the resulting hybrid composite material can be estimated by using the upper Wiener bounds (volumetric ratios) of the materials making up that composite.

3.2.1 Measuring Effective Dielectric Constant of Composite Materials

Various techniques have been reported in the literature for measuring the relative permittivity of a structure. A structure's relative permittivity can be measured by using the Nicolson Ross Weir (NRW) approach [33], [34]. This technique is based on measuring the transmission and reflection coefficients when the material is placed between two flanges of a waveguide. These parameters are then utilised to ascertain the dielectric constant of the material. However, the thickness of material is required to be less than quarter of the wavelength because it can lead to ambiguity in the ascertained values. Another approach involves measuring the parallel plate capacitance of the material [35]. The material is placed between two perfectly conducting plates and the resulting capacitance of the structure is measured. This can then be used to measure the relative permittivity since the capacitance of the material is directly proportional to it.

In this study, the dielectric constant is measured by employing the composite material as a substrate of a microstrip antenna. This technique has been employed in [35]–[37]. Since the

resonant frequency of the antenna is a function of the relative permittivity of the substrate therefore the change in the resonant frequency of the antenna can be used as a measure to calculate the relative permittivity of the material.

Taconic, Rogers and Arlon laminates are anisotropic in nature thus the relative permittivity of the material is also dependant on its orientation [38], [39]. The values quoted by the manufacturer represent the relative permittivity in the direction perpendicular to its plane (parallel to its thickness). The microstrip antenna has a ground plane on one side of the substrate and the patch antenna on its other side. The electric fields inside the substrate are perpendicular to the plane of the substrate, the antenna and the ground plane. The ascertained value of the relative permittivity is thus the same as provided by the manufacturer. This is one of the reasons for using a microstrip antenna as a measuring device instead of the NRW method (as the NRW method measures the dielectric constant parallel to the plane of the laminate). It can be argued that the resonant frequency of the antenna is dependent on the refractive index given by $n = \sqrt{\varepsilon_r \mu_r}$, where n is the refractive index, ε_r is the relative permittivity of the material and μ_r is the relative permeability. Since the relative permeability remains unity, the change in the refractive index is independent of it and is completely controlled by the relative permittivity (dielectric constant) of the substrate. Another requirement of using the NRW method is that the material should be cut so that it completely fills the waveguide aperture. This requirement is unnecessary when the material is utilised as a microstrip antenna substrate thus slightly simplifying the dielectric constant measurement process.

The effective relative permittivity of the composite was measured by using Full wave analysis. The microstrip patch antenna was simulated in EMPIRE XCcel using a homogeneous substrate and the resonant frequency of this patch was compared to the measured value. Since these two resonant frequency values will differ initially, the dielectric

constant of the substrate is changed until the two values are exactly the same or lie within 1% of each other; and then this value of the dielectric constant has been taken to represent the relative permittivity of the composite material. This iterative process is repeated for each sample of the composite material. It should be noted that the electric fields of a microstrip antenna are confined in the region in which the antenna is placed. This region can be thought of as the sample space. In this study, the substrate extended beyond this region thus ensuring that there is no leakage of electric fields (A small substrate can possibly have fringing fields beyond its physical dimension which can introduce error in the dielectric constant measurement of the sample).

The measurement process was started by using each individual material as the patch antenna substrate to ascertain its exact dielectric constant (the patch had dimensions of 25×10 mm^2).

This is done because the dielectric values for each material provided by the manufacturer has a tolerance linked to it and the actual value of the dielectric constant of the laminate lies within this range. The quoted value for Arlon AD-1000 is 9.1 with a tolerance of 0.35. Its measured value was 8.7 (which is very close to the tolerance range).Using the measured value helps reduce the errors in the formula since this value represents the actual value for the sample being used. This error is however reduced when the measured value is inserted into this equation. The measured value for the relative permittivity of Taconic RF-60A was 6 while the value provided by the manufacturer was 6.15 with a tolerance range of 0.25. The measured value of Taconic RF-45 was 4.5 which were exactly the same as provided by the manufacturer. A comparison of the measured value and the manufacturer's quoted value is shown in Table 3-1.

Table 3-1: *Measured and quoted values (from the datasheet) of the commercial laminates used*

Material	Quoted value of dielectric constant	Measured value of dielectric constant
Arlon AD-1000	9.1	8.7
Taconic RF-60A	6.15	6.0
Taconic RF-45	4.5	4.5

3.2.2 Measured Results for Composite Hybrid Materials with Two Constituent Materials

Composite materials with two parent materials are called two phase or bi-phase materials. In this section, they are prepared by combining slabs of Arlon AD-1000, Taconic RF-60A, Taconic RF-45 and PLA. These laminates are shown in Figure 3-2. The slabs of two of these materials are glued together to form a composite. The relative permittivity or dielectric constant of a composite material is measured by using it as a substrate for a microstrip patch antenna. The patch was 25×10 mm^2 with the ground plane on its opposite side.

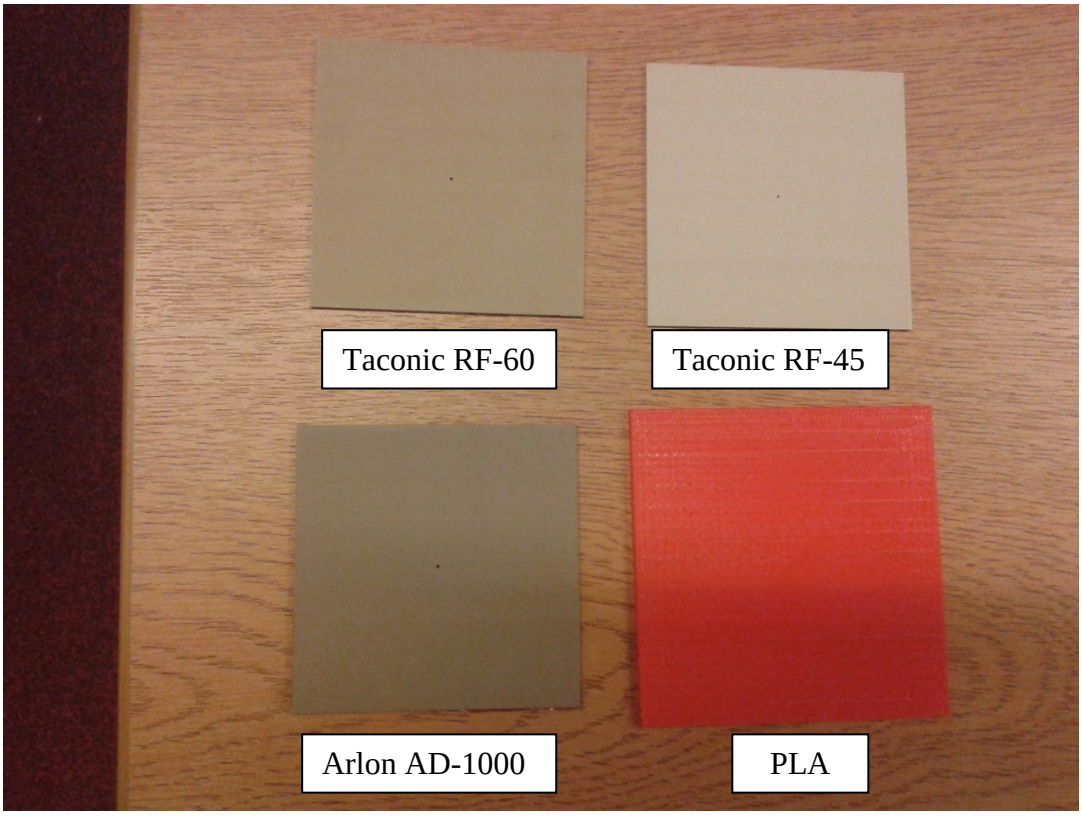

Figure 3-2: *Arlon Ad-1000, Taconic RF-60, Taconic RF-45 laminates and PLA*

A large number of these samples were prepared with different combinations of the four basic constituent materials. A 0.7mm diameter hole was drilled in every sample so that a SMA connector can be attached to it. The antenna is then fed via this connector and its resonant frequency is measured by using Anritsu vector network analyser (VNA). The total thickness of the composite material was also recorded. The microstrip antenna configuration used for measuring the dielectric constant of composite materials is shown in Figure 3-3.

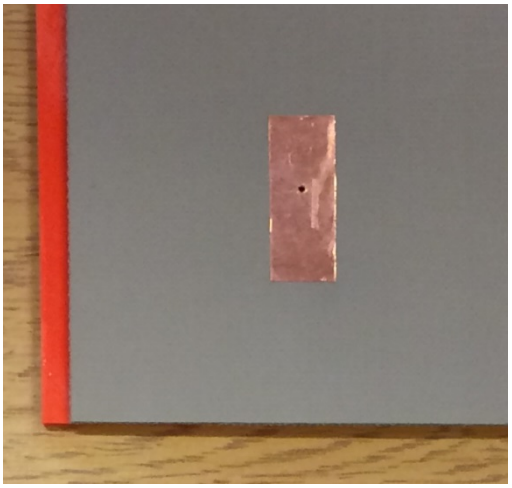

Figure 3-3: *Microstrip antenna used to measure the dielectric constant of a composite material consisting of PLA (orange) and Taconic RF-60 (grey)- The PLA slab is shifted towards the right in order to make it visible*

The thickness of the composite material is the sum of thickness of its constituents. Since these composite materials are made from commercial laminates, the range of the chosen thickness is limited. The volumetric ratio of the constituent materials in this case was the ratio of their thickness. This was due to the fact that the area of both the slabs used to construct the composite material is the same.

The volumetric ratio combined with the dielectric constant (which is the upper limit of the Weiner bounds) provides a very good approximation for the estimation of the relative permittivity of this composite material. By varying the thickness of the constituent material we can alter the volumetric ratio therefore varying the dielectric constant of the composite. This however is not easily possible for the commercially available laminates since they come with a specific thickness and a dielectric constant. To circumvent this issue, we can make use of 3D printing where the designer controls the properties and the thickness of the constituents. The results for the composite bi-phase materials are summarised in Table 3-2. By using four different materials as constituents, bi-phase composites having the dielectric constant ranging from 3.6 to 8.7 have been structured.

Table 3-2: *Measured relative permittivity of different composite materials*

Constituent Materials (Upper/Lower)	Materials Volume Ratio	Relative Permittivity of Constituents	Patch Resonant Frequency (GHz)	Measured Effective Permittivity
Arlon AD1000	100	8.7	2.03	8.7
Arlon AD1000; RF-60	60, 40	8.7, 5.9	2.19	7.5
Arlon AD1000; RF-60	50, 50	8.7, 5.9	2.24	7.2
Arlon AD1000; RF-45	60, 40	8.7, 4.5	2.29	7.0
Arlon AD1000; RF-45	50, 50	8.7, 4.5	2.35	6.6
Arlon AD1000; PLA	75, 25	8.7, 2.7	2.45	6
Taconic RF-60	100	5.9	2.47	5.9
Arlon AD1000; PLA	60, 40	8.7, 2.7	2.54	5.5
Arlon AD1000; PLA	40, 60	8.7, 2.7	2.6	5.3
RF-60; RF-45	50, 50	5.9, 4.5	2.63	5
RF-45	100	4.5	2.82	4.5
RF-60; PLA	65, 35	5.9, 2.7	2.87	4.3
RF-45; PLA	60, 40	4.5, 2.7	3.05	3.6

3.3 Three Phase Composite Materials Using Additive Manufacturing

Section 3.2 used homogeneous PLA with laminates; this section uses meshed PLA geometry to exploit an extra degree of design freedom. Effective medium theory dictates that for a structure to behave as a homogeneous material the wavelength of operation should be much longer than the lattice constant. A reasonable rule of thumb is to have the lattice of order $\lambda/10$ which is the case for these measurements. The rationale behind this approach is that when the individual unit cell of the structure is very small as compared to the wavelength, the variations in the electric fields of an electromagnetic wave over a unit cell is also small; this allows the material to be treated as a quasi-static medium. For a quasi-static medium, the period of a unit cell does not affect the dielectric constant of the composite. This is not the case when the unit cell is of comparable size to the wavelength, for example a half wavelength periodic structure will resonate making the response highly dependent on the periodicity and the interactions between the unit cells. Another phenomenon which occurs with resonance is that it brings losses with it; metamaterials having negative index of refraction bring bespoke properties to reality but since each individual unit cell is generally resonant, the resulting material exhibits considerable losses [40]. This will not be the case for the structures presented in this section; since their periodicity is very small as compared to the wavelength, therefore their behaviour can be described by the effective medium approach. Additive manufacturing has been combined with the commercial laminates to manufacture these composite materials. Since additive manufacturing allows the introduction of air in the lattice of the 3D printed materials, it becomes very easy to manufacture three phased composite materials. Another advantage of using additive manufacturing is that the limit on the thickness of the constituents is relaxed. These advantages allow for a larger range of

relative permittivities that can be designed and synthesized, along with a smooth and near continuous permittivity gradient.

Fused deposition modelling (FDM) technique was used for additive manufacturing. FDM is a very flexible and user friendly technique. It uses a stereolithography file (.stl) for manufacturing the desired structure, layer by layer. The material, in molten state, is extruded from the hot nozzle which then solidifies quickly after extrusion. This section shows that by using FDM, additively manufactured structures can be combined with commercial laminates in order to achieve a wide range of permittivities. The resulting composite materials are three phase structures because three materials with different electromagnetic properties have been used for their synthesis.

Composite materials were manufactured using a Makerbot Replicator 2x shown in Figure 3-4. The printer has a dual nozzle and a resolution of 100 microns. The material used for construction was PLA, it has a relative permittivity of 2.7 and its loss tangent value is 0.008. The two non-printed materials used for manufacturing composite materials presented in this section are Taconic RF-60A (relative permittivity 6.15, loss tangent 0.0038) and air. RF-60A was fixed to the bed of the printer with Kapton thermal tape which also improves the adhesion of PLA to the RF-60A laminate. The bed was heated to 105˚C and PLA was printed directly onto the laminate. Air was introduced in the composite materials in the form of a square lattice in the printed PLA structure as illustrated in Figure 3-5.

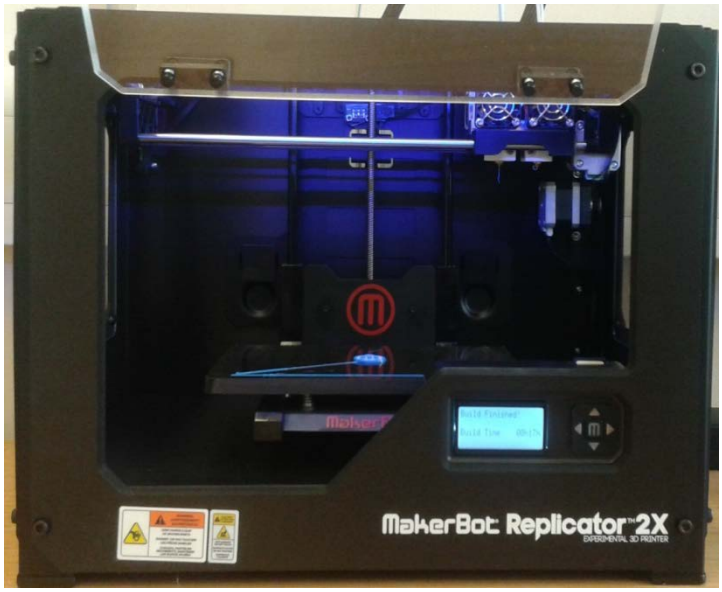

Figure 3-4: A Makerbot Replicator 2X 3D printer

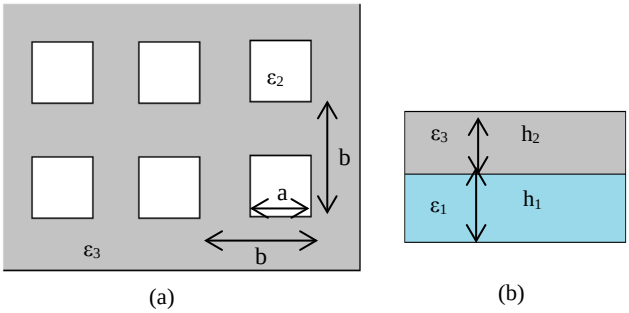

Figure 3-5: (a) *Square lattice showing a, length of the side of each square and the lattice constant b. In this figure, grey indicates PLA while the white colour in the lattice shows the presence of air;* **(b)** *Cross sectional view, grey shows PLA and blue shows Taconic, h_2 and h_1 are their respective thicknesses (top layer has the square lattice)*

The relative permittivity of these composite materials was controlled by varying the ratio and the individual electromagnetic properties of the constituent materials. The relative permittivity of the composite material, shown in Figure 3-6, can be calculated by using Equation 3.7. This equation has been derived by using Weiner bounds for a mixture of dielectrics [41]. It calculates the relative permittivity of the composite material by weighting the volumetric ratios of the constituent materials with their respective dielectric constants.

$$\varepsilon_{r(eff)} = \frac{(h_2)(\varepsilon_1) + k(h_1)(\varepsilon_2) + (1-k)(h_1)(\varepsilon_3)}{h_1 + h_2} \tag{3.7}$$

$$k = \left(\frac{a}{b}\right)^2$$

Where *a* is the length of the side of a square, *b* is the lattice constant/periodicity as shown in Figure 3-5. h_1 and h_2 are the thickness of the constituent materials (in this section h_1 is the thickness of the additively manufactured structure while h_2 is the thickness of the RF laminate). ε_1, ε_2 and ε_3 are the relative permittivity of the constituent materials. $\varepsilon_{r(eff)}$ is the effective permittivity of the composite material. As indicated by the equation 3.7, the relative permittivity of these composite materials can be controlled by varying the volumetric ratios of these three materials.

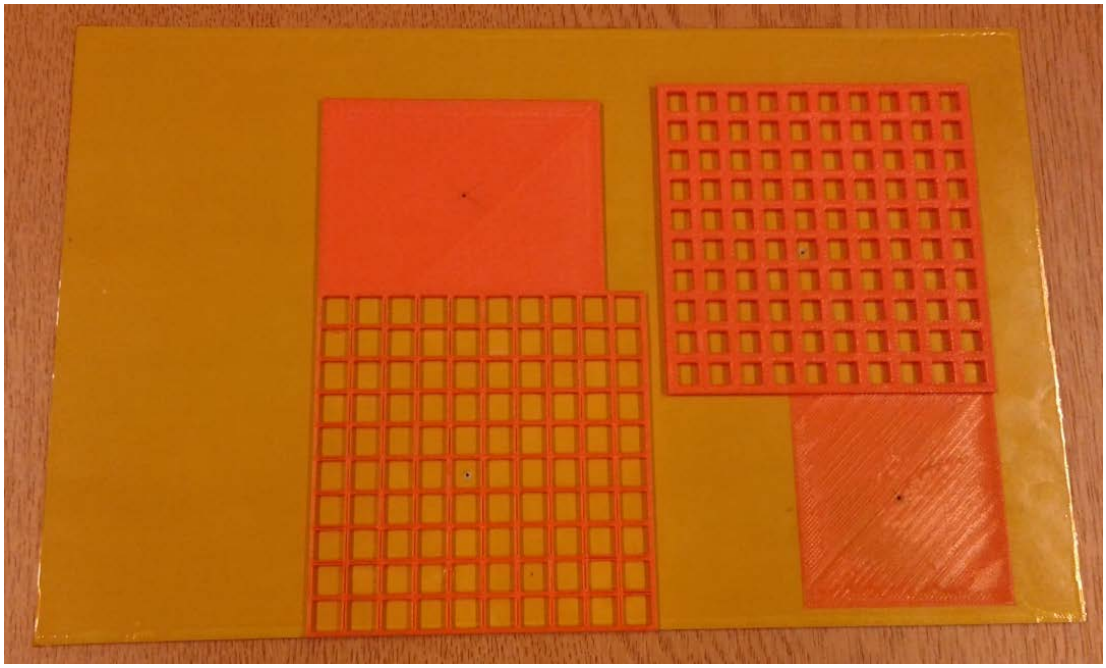

Figure 3-6: *Three phase additively manufactured composite material using a single commercial laminate (RF-60A), PLA and air*

It has been demonstrated, as illustrated in Table 3-3, that by using three phase composite materials, with relative permittivity values ranging from 1.47 to 6, have been manufactured. It is worth mentioning that in Section 3.2 (as indicated by Table 3-2), in order to achieve the dielectric constants ranging from 3.6 to 8.7, four different types of commercial laminates were required. Also it was not possible to achieve a dielectric constant below 1.5 without adding another commercial laminate (such as Rogers 5880) and drilling holes in its slab. Furthermore it would be impossible to achieve a near continuous range of dielectric constants as commercial materials are produced with certain thicknesses.

Since all the materials used for the manufacturing of composite materials are very low loss the resulting composite materials were also low loss. Very good agreements among the measured and calculated values of relative permittivity have been found, as shown in Table 3-3.

The measurements for the first four samples, in Table 3-3, have also been taken with the lattice size of $\lambda/7$ and it was observed that the composite material still behaves as a homogeneous structure at this size. This was achieved by using relatively smaller microstrip antennas for these samples (which resonate at higher frequency therefore having a shorter wavelength). These antennas resonated at a higher frequency while the lattice properties were kept constant. Negligible variations in the measured relative permittivity were found for these composite materials for both lattice sizes (with respect to wavelength). This is summarised is Table 3-4 which shows the comparison between two measured relative permittivity values.

Table 3-3: *Estimated and measured relative permittivity values for composite materials. h_1 is the thickness of the additively manufactured structure which consists of air and PLA, h_2 is the thickness of Taconic RF-60A laminate. The estimated relative permittivity has been calculated by using equation 3.7 with $\varepsilon_1 = 6$, $\varepsilon_2 = 1$ and $\varepsilon_3 = 2.7$. The measured relative permittivity of Taconic RF-60A was 6 which is within the specified tolerance range [42]. All lengths are in mm. Freq. is the measured resonant frequency of the patch.*

Parameters for Eq. 3.7				**ε_r from (3.7)**	**Meas. ε_r**	**Freq. (GHz)**	**Patch Size (mm^2)**
a	***b***	***h1***	***h2***				
7	8	1.6	0	1.40	1.47	2.52	48.5 × 10
5.6	8	2	0	1.87	1.83	2.51	44 × 10
4	8	2	0	2.28	2.24	2.62	38.5 × 9.5
0	1	2.4	0	-	2.70	2.58	35.5 × 10
5.6	8	2.3	1.3	3.36	3.20	3.18	25 × 20
7.0	8	1.3	1.3	3.70	3.65	3.77	19.5 × 15.5
0	1	2.2	1.3	3.92	3.80	2.93	24.5 × 19
2.5	5	0.55	1.3	4.89	5.10	3.19	20.5 × 16
0	1	0	1.3	-	6.00	2.55	24.5 × 10

Table 3-4: *Comparison between the relative permittivity measured for a lattice size of λ/7 and λ/10; (λ/10 values were presented in Table 3-3)*

Material(s)	**Patch Size (mm × mm)**	**Resonant Frequency (GHz)**	**ε_r from (3.7)**	**Measured ε_r**	**Measured ε_r in Table 3-3**
PLA, Air (75%)	23 × 10	5.07	1.40	1.43	1.47
PLA, Air (50%)	19 × 9.5	5.42	1.87	1.85	1.83
PLA, Air (25%)	24.5 × 10	3.93	2.28	2.27	2.24

It would be possible in the future to obtain an even wider range of values of relative permittivity for composite materials, by using dual nozzle 3D printing, and suitably choosing the constituent materials with distinct electromagnetic properties.

3.4 Repeatability of Additively Manufactured Materials

A significant advantage of using 3D printing as a manufacturing process for composite materials is its high engineering tolerance, which can be used to determine the reliability of a manufacturing technique. A higher tolerance indicates that the manufactured material will have (physical, electrical or mechanical) properties which are very close to the desired requirements of the designer. In this case, it indicates that the dielectric constant of the composite material manufactured by 3D printing is extremely close to the input (desired) values.

This was examined by manufacturing numerous 3D printed samples and measuring their dielectric constants and loss tangents. In this section, the dielectric constants of the bi-phase composite materials were measured by using a Split Post Dielectric Resonator (SPDR) [43]. These resonators operate in TE_{01} mode; and the Rayleigh Ritz method has been employed to calculate the resonant frequency and the Q-factor which is then used to measure the loss tangent values [44]. When a dielectric sample is placed in the resonator cavity, the dielectric loading causes a shift in the resonant frequency and the Q-factor of the SPDR which is then used to ascertain the dielectric constant and the loss tangent of the material [45].

In this study, there are four different kinds of lattices depending upon the volumetric ratio of PLA to air. At least four samples were prepared for each lattice, which have the same volumetric ratios. The volumetric ratio of PLA was varied from 25 percent to 100 percent

with equidistant intervals and for every sample, the dielectric constant and the loss tangent was measured and recorded at least three times. The results are summarised in Table 3-5. It should be noted that for each type of lattice, the thickness of the manufactured samples has also been varied. This extra degree of variation has been introduced to test repeatability of 3D printing as a manufacturing process. A Makerbot Replicator 2X was used to 3D print all these samples and PLA was used as the parent material. A 3D printed sample from each lattice is shown in Figure 3-7.

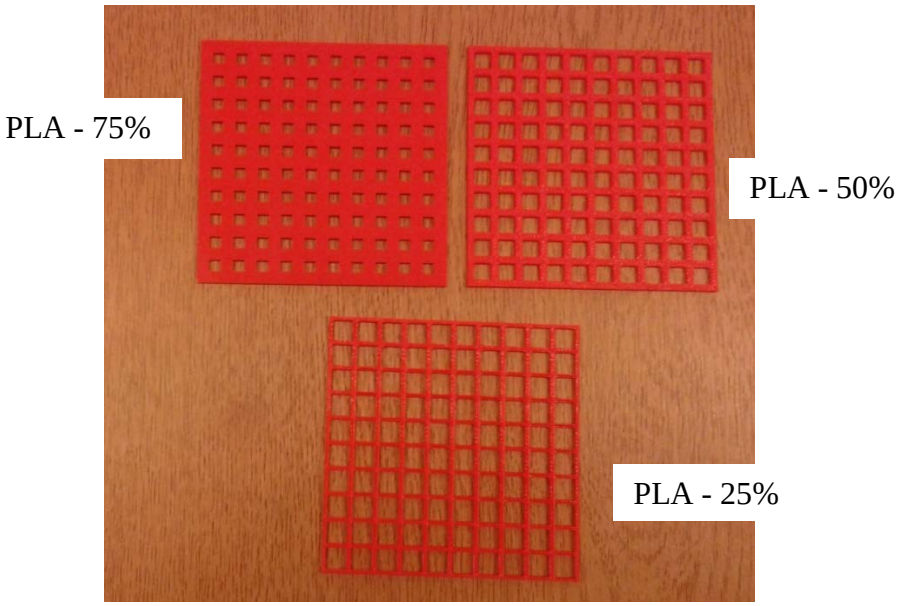

Figure 3-7: 3D printed samples of different lattices

The results shown in Table 3-5 clearly demonstrate the reliability of 3D printing as a manufacturing process. The variation between the measured dielectric constant was negligible for the same thickness. Even for different thicknesses, the difference between the maximum and minimum value measured was less than 0.1 for all four kinds of lattices. The thickness of each sample was measured with a micrometre and a difference of less than 0.1mm was observed between the input value and the actual thickness of all the 3D printed samples. The dielectric constant values were measured with the help of a SPDR which

resonated at 1.9 GHz. It is clear from the loss tangent values that these composite materials are extremely low loss structures.

Table 3-5: *Measured relative permittivity (maximum/minimum) of samples of four different lattices with different thickness using a 1.9 GHz SPDR (Thickness is measured in mm. The volumetric ratio of PLA to air is quoted in the first column)*

Name	Thickness (mm)	Measured Permittivity		Loss Tangent
		Maximum	Minimum	
PLA - 25%	0.41	1.306	1.297	0.0018
PLA - 25%	0.75	1.323	1.312	0.0024
PLA - 25%	1.56	1.299	1.291	0.0021
PLA - 25%	1.95	1.296	1.293	0.0016
PLA - 25%	1.3	1.293	1.291	0.002
PLA - 50%	0.82	1.729	1.712	0.004
PLA - 50%	1.5	1.762	1.743	0.004
PLA - 50%	0.45	1.608	1.585	0.004
PLA - 50%	1.89	1.761	1.756	0.0049
PLA - 50%	1.4	1.647	1.627	0.005
PLA - 75%	2.34	2.166	2.139	0.0059
PLA - 75%	0.86	2.095	2.069	0.010
PLA - 75%	1.99	2.164	2.129	0.005
PLA - 75%	1.65	2.17	2.113	0.006
PLA - 100%	2.31	2.751	2.734	0.004
PLA - 100%	0.72	2.708	2.723	0.008
PLA - 100%	1.48	2.765	2.753	0.007

The dielectric constant and the loss tangent of these four lattices were also measured with a 2.4 GHz SPDR. These measured values were also in very close agreement with their 1.9 GHz measured values counterparts (the largest deviation was for the lattice PLA-25% but these values still fall within a 0.15 tolerance range). The results are shown in Table 3-6. (A comparison between composite materials with square lattice and a stratified structure is presented in Appendix B.)

Table 3-6: *Measured relative permittivity (maximum/minimum) of samples of four different lattices using a 2.4 GHz SPDR (Thickness is measured in mm)*

Name	Thickness	Measured Permittivity		Loss Tangent
		Maximum	Minimum	
PLA - 25%	0.45	1.434	1.413	0.003
PLA - 50%	0.5	1.754	1.711	0.004
PLA - 75%	0.53	2.14	2.11	0.006

3.5 Conclusions

Composite materials in this chapter have been synthesized by combining two or more different types of materials with distinct electromagnetic properties. As the dielectric constants of these composite materials were estimated by using effective medium theory. The dielectric constant of these composite materials is different from its constituents thus making it possible to manufacture materials with dielectric constants not readily available in the market. Two phase composite materials have been manufactured by combining commercially available laminates and composite materials with a range of relative permittivity from 3.6 to 8.7 were engineered. However in order to achieve such a wide range four different kinds of laminates were required; also since commercial laminates are produced with a limited range

of thickness profile, it is impossible to achieve a nearly continuous range of relative permittivities over a wide range. This issue was resolved by using additive manufacturing for constructing composite materials. By using additive manufacturing the designer can not only control the thickness profile but also add air in the structure thus forming three phase composite materials. Fused deposition modelling has been successfully used to 3D print directly on to a Taconic RF-60A laminate. It has been demonstrated that the three phase low loss composite materials with a nearly continuous and wide range of relative permittivity values (from 1.47 to 6) can be manufactured. The relative permittivity of these materials was measured by using the material as a substrate for patch antennas. By using the Weiner bounds, an equation to predict the effective relative permittivity of these three phase composite materials has been derived. The measured values show a very good agreement with the ones analytically calculated. The relative permittivity was controlled by varying the height and the lattice parameters of the additively manufactured structures. It has also been demonstrated that additive manufacturing possesses a high engineering tolerance. A large number of samples for four different kinds of lattices (with PLA as the parent material) have been constructed and their dielectric constants were measured using 1.9 GHz and 2.4 GHz split post dielectric resonators. These samples also had variable thicknesses. However less than 0.1 deviation has been found in the measured dielectric constants for all the samples having the same lattice thus showing the reliability of additive manufacturing for constructing composite materials.

References

[1] W. R. Tinga, W. A. G. Voss, and D. F. Blossey, “Generalized approach to multiphase dielectric mixture theory,” *J. Appl. Phys. 44*, vol. 3897, 1973.

[2] M. Wang and N. Pan, “Predictions of effective physical properties of complex multiphase materials,” *Mater. Sci. Eng.*, vol. R 63, pp. 1–30, 2008.

[3] M. Y. Koledintseva, R. E. Dubroff, and R. W. Schwartz, “Mixtures Containing Conducting Particles At Optical Frequencies,” in *Progress In Electromagnetics Research, PIER 63*, 2006, pp. 223–242.

[4] L. Lewin, “The Electrical Constants Of A Material Loaded With Spherical Particles,” *Electr. Eng. - Part III Radio Commun. Eng. J. Inst.*, vol. 94, pp. 65–68, 1946.

[5] O. Levy and D. Stroud, “Maxwell Garnett theory for mixtures of anisotropic inclusions: Application to conducting polymers,” *Phys. Rev. B*, vol. 56, no. 13, pp. 8035–8046, 1997.

[6] D. E. Aspnes, “Local-field effects and effective-medium theory: A microscopic perspective,” *Am. J. Phys. 50*, vol. 704, 1982.

[7] V. Markel, “A tutorial on Maxwell Garnett approximation 2016,” *HAL Id hal-01282105*, 2016.

[8] J. H. Hannay, “The Clausius-Mossotti equation : an alternative derivation,” *Eur I. Phls. 4*, pp. 141–143, 1983.

[9] A. P. Vinogradov, “On the Clausius-Mossotti-Lorenz-Lorentz formula,” in *Physica A: Statistical Mechanics and its Applications*, 1997, pp. 2498–2501.

[10] K. K. Kärkkäinen, A. H. Sihvola, and K. I. Nikoskinen, “Effective Permittivity of Mixtures : Numerical Validation by the FDTD Method,” *IEEE Trans. Geosci. Remote*

Sens., vol. 38, no. 3, pp. 1303–1308, 2000.

[11] T. G. Mackay and A. Lakhtakia, "A limitation of the Bruggeman formalism for homogenization," *Opt. Commun. 234*, pp. 1–16, 2004.

[12] D. Stroud, "The effective medium approximations : Some recent developments," *Superlattices Microstruct.*, vol. 23, no. 3, pp. 567–573, 1998.

[13] K. Lichtenecker and K. Rother, "Die herleitung des logarithmischen mischungsgesetzes aus allgemeinen prinzipien der stationären strömung," *Phys. Zeitschr*, vol. 34, pp. 255–260, 1931.

[14] Z. Hashin and S. Shtrikman, "A Variational Approach to the Theory of the Effective Magnetic Permeability of," *J. Appl. Phys. 33*, vol. 3125, 1962.

[15] R. Sawicz and K. Golden, "Bounds on the complex permittivity of matrix – particle composites," *J. Appl. Phys. 78*, vol. 7240, 1995.

[16] E. Tuncer, Y. V Serdyuk, and S. M. Gubanski, "Dielectric mixtures – electrical properties and modeling," *IEEE Trans. Dielectr. Electr. Insul.*, vol. 9, no. 5, pp. 809–828, 2002.

[17] C. S. Daily, W. Sun, M. R. Kessler, X. Tan, and N. Bowler, "Modeling the Interphase of a Polymer-based Nanodielectric," *IEEE Trans. Dielectr. Electr. Insul.*, vol. 21, no. 2, pp. 488–496, 2013.

[18] S. M. Holik, "Empirical Mixing Model for the Electromagnetic Compatibility Analysis of On-Chip Interconnects," *Chapter 9, Dielectric Material*, 2012 (Publisher: Intech).

[19] H. Tuononen, K. Fukunaga, M. Kuosmanen, J. Ketolainen, and K.-E. Peiponen, "Wiener Bounds for Complex Permittivity in Terahertz Spectroscopy : Case Study of Two- Phase Pharmaceutical Tablets," *Appl. Spectrosc.*, vol. 64, no. 1, pp. 127–131,

2010.

[20] C. C. Njoku, W. G. Whittow, and J. C. Vardaxoglou, “Simulation Methodology for Synthesis of Antenna Substrates With Microscale Inclusions,” *IEEE Trans. Antennas Propag.*, vol. 60, no. 5, pp. 2194–2202, 2012.

[21] S. Jain, M. Abdel-Mageed, and R. Mittra, “Flat-lens design using field transformation and its comparison with those based on transformation optics and ray optics,” *IEEE Antennas Wirel. Propag. Lett.*, vol. 12, pp. 777–780, 2013.

[22] B. N. B. Kundtz, D. R. Smith, and J. B. Pendry, “Transformation Optics,” *Proc. IEEE*, vol. 99, no. 10, p. 1623, 2011.

[23] O. Quevedo-Teruel, W. Tang, R. C. Mitchell-Thomas, A. Dyke, H. Dyke, L. Zhang, S. Haq, and Y. Hao, “Transformation optics for antennas: why limit the bandwidth with metamaterials?,” *Sci. Rep.*, vol. 3, p. 1903, 2013.

[24] D. Bao, K. Z. Rajab, W. Tang, Y. Hao, D. Bao, K. Z. Rajab, W. Tang, and Y. Hao, “Experimental demonstration of broadband transmission through subwavelength aperture,” *Appl. Phys. Lett. 97*, vol. 134105, 2010.

[25] S. P. Morgan, “Generalisations of Spherically Symmetric Lenses,” *IRE Trans. Antennas Propag.*, vol. 29, pp. 342–345, 1958.

[26] O. Noriomi, “Shell-type luneberg lens,” US Patent 3465362A, 1969.

[27] M. Liang, W. Ng, K. Chang, K. Gbele, M. E. Gehm, and H. Xin, “A 3-D Luneburg Lens Antenna Fabricated by Polymer Jetting Rapid Prototyping,” *IEEE Trans. Antennas Propag.*, vol. 62, no. 4, pp. 1799–1807, 2014.

[28] K. Gbele, M. Liang, W.-R. Ng, M. E. Gehm, and H. Xin, “Millimeter Wave Luneburg Lens Antenna Fabricated by Polymer Jetting Rapid Prototyping,” in *2014 39th*

International Conference on Infrared, Millimeter, and Terahertz waves (IRMMW-THz), 2014, vol. 1.

[29] C. Mateo-segura, A. Dyke, H. Dyke, S. Haq, and Y. Hao, "Flat Luneburg Lens via Transformation Optics for Directive Antenna Applications," *IEEE Trans. Antennas Propag.*, vol. 62, no. 4, pp. 1945–1953, 2014.

[30] R. Yang, W. Tang, and Y. Hao, "Wideband Beam-Steerable Flat Reflectors via Transformation Optics," *IEEE Antennas Wirel. Propag. Lett.*, vol. 10, pp. 1290–1294, 2011.

[31] R. Yang, Z. Lei, L. Chen, Z. Wang, and Y. Hao, "Surface wave transformation lens antennas," *IEEE Trans. Antennas Propag.*, vol. 62, no. 2, pp. 973–977, 2014.

[32] D. Micheli, C. Apollo, R. Pastore, R. B. Morles, S. Laurenzi, and M. Marchetti, "Nanostructured composite materials for electromagnetic interference shielding applications," *Acta Astronaut.*, vol. 69, pp. 747–757, 2011.

[33] A. M. Nicolson and G. F. Ross, "Measurement of the intrinsic properties of materials by time-domain techniques," *IEEE Trans. Instrum. Meas*, vol. IM–19, no. 4, pp. 377–382, 1970.

[34] B. Weir, "Automatic measurement of complex dielectric constant and permeability at microwave frequencies," *Proc. IEEE*, vol. 62, pp. 33–36, 1974.

[35] G. P. Gauthier, A. Courtay, and G. M. Rebeiz, "Microstrip Antennas on Synthesized Low Dielectric-Constant Substrates," *IEEE Trans. Antennas Propag.*, vol. 45, no. 8, pp. 1310–1314, 1997.

[36] D. Psychoudakis, Y.-H. Koh, J. L. Volakis, and J. H. Halloran, "Design Method for Aperture-Coupled Microstrip Patch Antennas on Textured Dielectric Substrates," *IEEE Trans. Antennas Propag.*, vol. 52, no. 10, pp. 2763–2765, 2004.

[37] E. A. Navarro, A. Luximon, I. J. Craddock, D. L. Paul, and M. Dean, “Multilayer and Conformal Antennas Using Synthetic Dielectric Substrates,” *IEEE Trans. Antennas Propag.*, vol. 51, no. 4, pp. 905–908, 2003.

[38] S. Normyle, “The Anisotropy of Dielectric Constant in TLY-5A Material by Bereskin,” *https://www.4taconic.com/uploads/ADD%20Technical%20Articles/1453224717_The%20Anisotropy%20of%20Dielectric%20Constant%20in%20TLY-5A%20Material%20Technical%20Article.pdf*.

[39] P. I. Dankov, “Dielectric Anisotropy of Modern Microwave Substrates.”

[40] N. Engheta and R. W. Ziolkowski, *Metamaterials: Physics and Engineering Explorations*. Wiley-IEEE Press, 2006.

[41] K. K. Karkkainen, “Effective permittivity of mixtures: numerical validation by the FDTD method,” *IEEE Trans. Geosci. Remote Sens.*, vol. 38, no. 3, pp. 1303–1308, 2000.

[42] “RF-60A,” http://www.taconic-add.com/pdf/rf60a.pdf

[43] “Split post dielectric resonators (SPDR),” *http://www.qwed.com.pl/resonators_spdr.html*. [last accessed 01/02/2017]

[44] “Agilent Split Post Dielectric Resonators for Dielectric Measurements of Substrates,” *Technologies, Agilent*.

[45] J. Krupka, R. Clarke, O. Rochard, and A. Gregory, “Split Post Dielectric Resonator Technique for Precise Measurements of Laminar Dielectric Specimens - Measurement Uncertainties,” in *Microwaves, Radar and Wireless Communications. 2000. MIKON-2000. 13th International Conference on*, no. 1, pp. 305–308.

Chapter 4 : Dipole-Slot Metasurfaces

Abstract

In Chapter 3 additive manufacturing was utilised to fabricate artificial materials with non-resonant inclusions. In this chapter, we consider the class of materials in which the individual inclusions are allowed to resonate. Such materials are called metamaterials. This chapter focusses on their two dimensional equivalents called metasurfaces. Section 4.1 starts with a review of metamaterials and metasurfaces. Metasurfaces offer superior performances to metamaterials by being less lossy structures and their planar nature also allows simple manufacturing. Metasurfaces can be used to make ultrathin lenses, control the phase of electromagnetic waves over extremely small thickness profile and improve the performance of spatial filters. These advantages are discussed in detail in Section 4.1.4. Section 4.1.5 defines the complementary metasurfaces designed on the basis of Babinet's principle. Section 4.2 investigates the dipole-slot metasurfaces via simulations and investigates the nature of its behaviour. A dipole-slot metasurface was designed by placing an array of apertures on one side of a very thin dielectric and an array of dipoles on the other side. The effects of the thickness of the dielectric are discussed in Section 4.2.3 and the transmission loss profile of a dipole-slot metasurface is considered in Section 4.2.4. Section 4.2.5 shows the effects of the change in the individual elements length and their placement (in the unit cell) on this

metasurface. A qualitative equivalent circuit has been developed to describe the compact and pass band nature of the dipole-slot metasurface in Section 4.3. The dipole-slot metasurface was fabricated and the comparison between the simulated and measured transmission response is presented in Section 4.4. The novelty of this chapter lies in; (i) the analysis and explanation of the behaviour of the dipole-slot metasurface and the effect of the in-between dielectric and geometry; (ii) developing a qualitative equivalent circuit model to explain the behaviour and the inter-layer coupling of a dipole-slot metasurface.

4.1 Literature Review of Metamaterials and Metasurfaces

Chapter 3 discussed composite materials. The response of these materials can be adequately described by effective medium approximations as the size of the inhomogeneity and the periodicity of the material was very small in comparison to the operating wavelength. The individual particles were not resonant and such a medium can be categorised as quasi-static medium. This Chapter focusses on a new class of artificial materials. In these artificial materials even though the periodicity of the structure is still small as compared to the operating wavelength, the individual scatterer is resonant. These materials are generally classified as metamaterials and they possess very intriguing and interesting phenomena like double negative refractive index (DNG) and near zero index. The focus of this chapter is on their two dimensional counterparts called metasurfaces. The behaviour of metamaterials and metasurfaces can be analytically explained by expansion of Floquet modes [1]. It also needs to be mentioned that when the periodicity of these individual scatterers becomes closer in size to the wavelength of operation, higher order propagating Floquet modes need to be taken into account to accurately describe their behaviour; such structures, therefore are not classified as metamaterials or metasurfaces [1].

4.1.1 Metamaterials

It is a widely established fact that when an electromagnetic wave strikes a composite medium, it induces electric and magnetic dipole moments in the inclusions. These dipole moments, as discussed in Chapter 3, are closely related to the effective permittivity and permeability of the composite medium. Since the size, density, shape and orientation of the inclusions can be controlled by the designer, materials with specific electromagnetic response can be synthesized. These artificially designed materials are called metamaterials. When the individual elements are resonant, such materials can possess negative values for both, relative permittivity and permeability. It needs to be emphasized that the negative refractive index is only possible with the resonant individual elements. This is due to the fact that "resonances have the characteristic that their phase response reverses as frequency changes around the resonance" [2]. Such materials are referred to in the literature as double negative media (DNG), left handed media and backward wave media [3]–[5].

The electromagnetic properties of the metamaterials can be described by using the Lorentz classical theory. In this theory the electron is treated like a damped harmonic oscillator in an electromagnetic field [6], [7]. When the restoring force is negligible, the Lorentz model is reduced to the Drude model. The Drude model allows the negative values of permittivity and permeability over a wide frequency range (unlike the Lorentz model). Due to this property, the Drude model is sometimes preferred to the narrowband Lorentz model for simulations [7].

Metamaterials with resonant individual elements can possess negative permittivity and permeability values. Negative permittivity and permeability values, then according to Snell's law of refraction, make the refracted angle negative thus causing the incident and refracted wave to lie on the same side of normal. This phenomenon is called negative refraction. Negative refraction allows the complete control of electromagnetic waves (including light), in

all four quadrants of a cartesian plane. Due to this unusual characteristic, metamaterials offer potential applications which would have not been possible by only using the naturally occurring materials [7]. One of these numerous applications of the metamaterials is the phase compensation medium. DNG and positive indexed materials are combined together in such a way that the phase difference across the slab of this medium is zero.

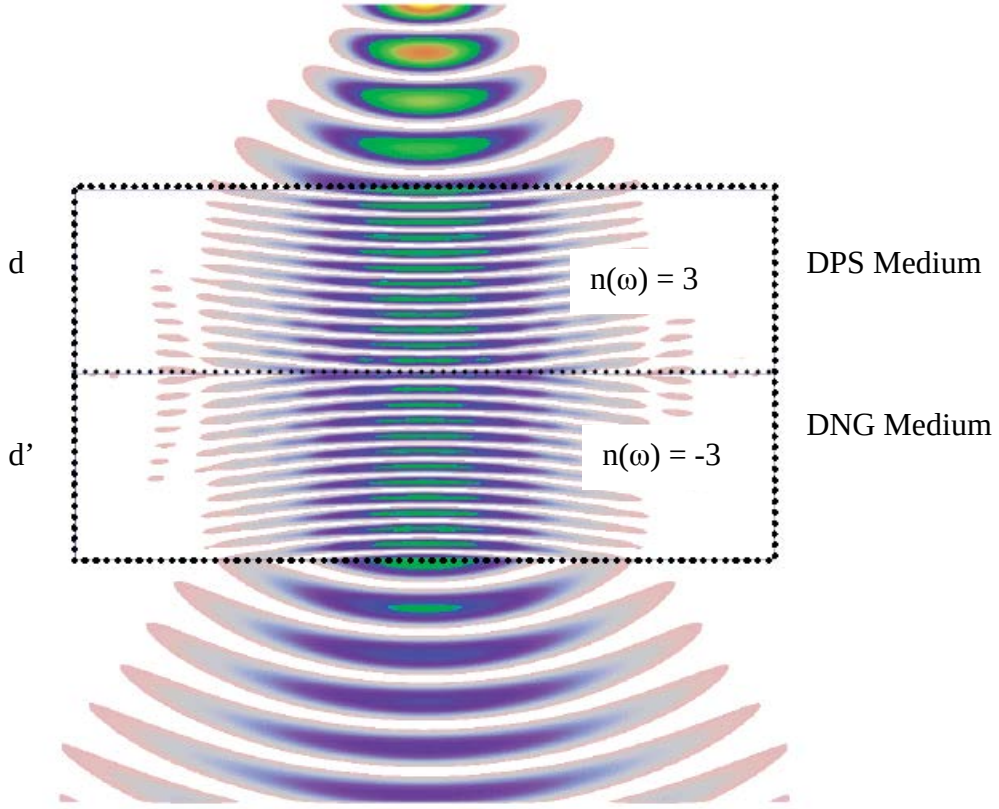

Figure 4-1: *A simulation showing a phase compensation medium [7]*

As shown in Figure 4-1, a DPS and DNG medium have thickness equal to d and d' and their respective refractive indices are n and $-n'$. When a normal monochromatic beam illuminates the slab the phase difference across the DPS part of the slab is $n \times k \times d$, where k represents the wavenumber; while the phase difference across the DNG slab is $-n' \times k \times d'$. Therefore the total phase difference across the slab is $n \times k \times d - n' \times k \times d'$. This shows that the negative index part of the slab compensates for the phase propagation in the positive index

part. By equating the total phase difference to zero, we can arrive at the relation $n/|n'| = d'/d$. This relation indicates that it is the ratio of the thicknesses and the refractive index, which cause the phase difference across the medium to be zero and not the total thickness $(d+d')$ [8]. Another interesting phenomenon which can be observed by combining the positive and negative index materials is the concentrated resonance which occurs at the interface of such two materials [9]. This interface resonance (also known as a surface wave plasmon) can replace the aperture related resonance in a traditional waveguide thus making possible the existence of sub-wavelength thin waveguides. The dispersion relation for such waveguides is also related to the thicknesses ratio d'/d and is independent of the total thickness [10], [11].

Metamaterials, with a negative refractive index equal to -1, can also be used to make a superlens [12]. A superlens (also called a perfect lens) breaks the limitations imposed on focussing by wave optics (for a traditional lens an absolute limit on the area for focussing energy, is a square of wavelength). This is due to the fact that the amplitude of the evanescent waves decays exponentially in a naturally occurring medium whereas DNG materials enhance their amplitude. The structure still obeys the law of conservation of energy as evanescent waves do not carry any energy. It also needs to be noted that even though the refractive index is negative, the characteristic impedance (being the ratio between the permittivity and permeability) is still positive, thus there are no reflections at the interfaces and no (mismatch) energy is lost during the whole phenomenon [12], [13].

4.1.2 Metasurfaces

Metasurfaces are two-dimensional or surface counterparts of metamaterials. Just like metamaterials, it is possible to characterise their response through their electric and magnetic polariziabilities. They are also referred in literature as metafilms [14]. Metamaterials control

the propagation of light due to their bespoke permittivity and permeability values; however they still use the propagation effect to manipulate the electromagnetic waves. This can result in a complicated relatively bulky structure whereas metasurfaces try to manipulate the wave over a single extremely thin layer [15], [16]. The two dimensional nature of metasurfaces, therefore makes them less bulky and offers the possibility of lower loss structures [1]. Due to their 3D nature, it is also difficult to fabricate metamaterials. Metasurfaces offer an extremely promising alternative. Due to their planar structure, metasurfaces can be easily fabricated using planar fabrication tools [17], [18]. The planar fabrication process is also very cost-effective in comparison to the manufacturing of the complex 3D metamaterials [19]. Metasurfaces, being two dimensional materials, can therefore be easily integrated into other devices which can make them a salient feature for nanophotonic circuits; this property will also allow them to be a part of "lab on chip" photonics [20].

The negative index of the metamaterials is due to the resonance of the individual meta-atoms. This property makes the metamaterials inherently dispersive thus the electromagnetic properties of such materials are highly sensitive to the changes in the operating frequency thus making such materials bandwidth limited. It has been shown in [21] that by using extremely thin metasurfaces with deep sub-wavelength notches in a two layered fishnet structure, the dispersion characteristics can be engineered. This technique was then used to make a broadband metasurface filter. The (in band) transmission and (out of band) rejection was achieved by respectively matching and mis-matching the impedance of this metasurface (to the free space). The dispersion characteristics were controlled by tailoring the primary (and secondary) magnetic resonances, and the plasma wavelengths for permittivity. Both these properties (of the metasurface) were highly dependent on the design of the sub-wavelength deep notches. The design was optimized by the help of a genetic algorithm. This broadband metasurface also had a very low insertion loss in the transmission band [21].

Due to the variety of advantages offered by metasurfaces over metamaterials, the scientific community has shown a keen recent interest in this area. This has led to rapid development in the underlying physics which govern the behaviour of metasurfaces and their potential applications.

4.1.3 Definition and Salient Characteristics of Metasurfaces

Metasurfaces are defined as the periodic structures where the thickness and periodicity of the individual elements (scatterer) is small in comparison to the wavelength of operation. These two dimensional periodic structures can also be sub-classified further; an array of apertures in a reflective screen are classified as metascreens while separate individual scatterers are called metafilms [1]. However this classification has not been usually adopted in the published literature. Metasurfaces can also be defined as a (symmetric or asymmetric) array of sub-wavelength resonant scatterers which control the electromagnetic response of the surface [16]. This is the also the property which differentiates the metasurfaces from traditional frequency selective surfaces (FSS). A traditional FSS has individual elements (periodicity) which are of the order of the operating wavelength (generally ~ $\lambda/2$). Another difference between metasurfaces and FSSs is also closely related to the sub-wavelength nature of the individual elements of a metasurface. Since the response of the metasurface sheet is dependent on the localized behaviour of each unit, therefore each individual unit cell is allowed to be spatially varied [16]. Such variations can be used to design metasurface lenses and shape wavefronts; the applications of the metasurfaces will be discussed in Section 4.1.4. The miniaturized individual "meta-atoms" of the metasurfaces allow the sub-wavelength resolution of the wave fronts ranging from microwave to optical

scale. This property of metasurfaces also allows them to behave like homogeneous or nearly homogenous sheets [22].

Another perspective to define a metasurface goes via Huygen's principle [23]. Huygen's principle states that "each point on a wavefront acts as a secondary source" thus allowing the control of wavefronts beyond the source. When an electromagnetic wave strikes a surface, it induces electric and magnetic dipole moments. These moments generate surface currents. According to Schelkunoff's principle, these surface currents are equivalent to the tangential electric and magnetic fields which control the electromagnetic response of a surface [24]. A surface can then be only characterised as a metasurface when its each individual element is polarizable and sub-wavelength. This is achieved by a careful design of the individual element(s) [22].

Metasurfaces can have the ability to tailor both the electric and magnetic field component of the electromagnetic waves; therefore metasurfaces can have negligible mismatch losses as their impedance can be matched by tailoring the electric and magnetic polarizabilities [25], [26]. Metasurfaces without reflection losses are characterised as Huygens metsurfaces [25]. In [25], two layered metasurfaces were used to eliminate the reflection losses; the top layer was employed to temper the electric polarizability while the bottom layer was used to control the magnetic polarizability. A Huygen’s metasurface is shown in Figure 4-2.

(a)

(b)

Figure 4-2: *Top (a) and bottom (b) periodic layers of a Huygen's metasurface [25]. The top layer is used to controlled the electric while bottom layer is used to control the magnetic polarizability of metasurface*

An entirely different paradigm to structure metasurfaces is presented in [27], [28]. Highly absorptive dielectrics and metals have been employed to construct a sub-wavelength thin metasurface. This metasurface achieves the desired phase shift over a nano-scale and is made with highly absorptive dielectrics and metals with finite conductivity. Since the reflection from the interface is no longer perfect, the phase can be tailored and desired phase shifts can be achieved over a much smaller distance. This is in contrast to traditional optical layers which employed extremely low loss metals and dielectrics, and exploit Fabry-Perot type interference for the phase shifts; however unlike metasurfaces, the thickness of such (traditional) films is comparable to the operating wavelengths [28]. Such metasurfaces are not the topic of this thesis and the work presented is limited to the first class of metasurfaces which employ resonant scatterers for their behaviour.

4.1.3.1 Phase Jumps and Generalized Law of Refraction

Conventional devices (eg. lenses, holograms etc) shape the wavefronts over a distance larger than the operating wavelength [29], [30]. Lenses make use of their shape and the material properties (refractive index) to focus energy by gradually varying the phase of an electromagnetic wave; holograms generate images in the far-field through constructive interference [30]. The same is also true in the case of DNG materials which also gradually temper the phase over a distance. Metasurfaces provide an alternative to this approach because an electromagnetic wave passing through a metasurface undergoes a phase jump. This is due to the fact that the phase is discontinuous at a metasurface [31]. This anomalous behaviour decreases the reliance on wave propagation and allows the shaping of wavefronts and focussing of energy over sub-wavelength distance. Metasurfaces can potentially also replace the bulky and heavy devices used traditionally for such purposes.

This phase discontinuity (or jump) owes its existence to the resonant behaviour of the miniaturized (sub-wavelength) metasurface building blocks. When an electromagnetic wave strikes an individual element of a metasurface, it induces a surface electromagnetic wave. This causes the charge present in this element to oscillate. This whole phenomenon is known as surface plasmon [16]. The interaction of the impinging electromagnetic wave and the surface plasmon leads to the phase discontinuity across the metasurface. Due to this discontinuity the Snell's law has been replaced by a "generalized law" for metasurfaces [32].

The generalized law has been derived on the basis of Fermat's principle of least time [32]. Fermat's principle states that out of all the possible paths between two points, light travels on the path which takes the least amount of time [33]. Consider a plane wave at an incidence angle of θ impinging on a metasurface. Two possible paths that the wave can take are shown in Figure 4-3. Since the metasurface causes an abrupt change in the phase (phase

discontinuity), this change at point A is shown by φ, while on A' is it is represented by $\varphi + d\varphi$. The distance between A and A' is assumed to be dx. It is also assumed that φ is a continuous function of x. It is assumed that the two paths are infinitesimally close such that the phase difference between them to reach point A is zero. This leads to the following relation in Equation 4.1 [32]

$$[n\,(k_0)\,\sin(\theta)\mathrm{d}x + (\Phi + \mathrm{d}\Phi)] - [n'(k_0)\,\sin(\theta')\mathrm{d}x + (\Phi)] = 0 \qquad (4.1)$$

where k_0 is the propagation constant and $k_0 = \lambda_0/2\pi$ with λ_0 being the free space wavelength, n and n' are the refractive indices of medium 1 and medium 2 as shown in Figure 4-3.

Equation 4.1 can be rewritten as

$$n\sin(\theta) - n'\sin(\theta') = \frac{\lambda_0}{2\pi}\frac{dx}{d\varphi} \qquad (4.2)$$

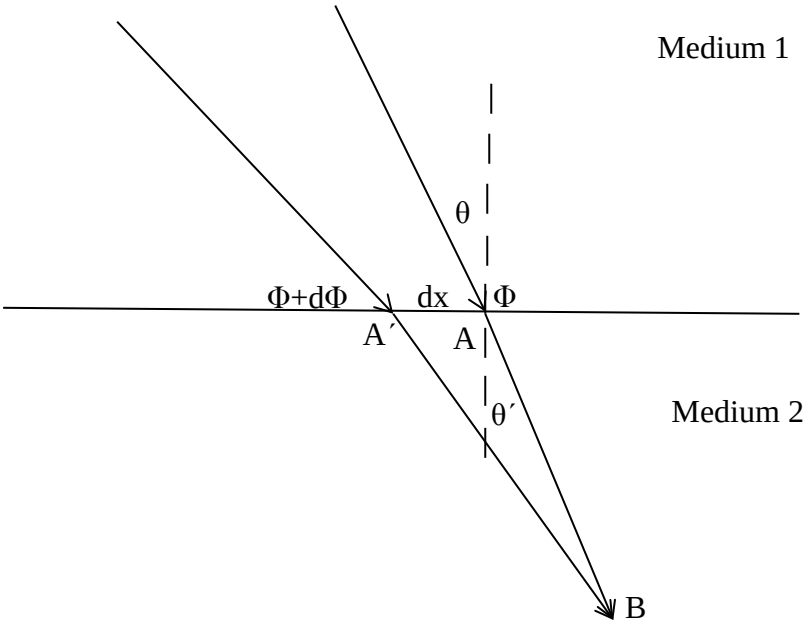

Figure 4-3: *An illustration of generalised law of refraction. Φ and Φ+dΦ are phase discontinuities at A´ and A while dx is the distance between them. θ´ and θ represent the angles of incidence and refraction to the normal (dotted line) (redrawn from* [32]*)*

Similarly the generalised law of reflection for metasurfaces is given by Equation 4.3.

$$\sin(\theta) - \sin(\theta_{refl}) = \frac{\lambda_0}{2\pi n}\left|\frac{dx}{d\varphi}\right| \tag{4.3}$$

where θ_{refl} is the angle of reflection. The non-linear relation between the incidence and the reflection is worth noting since the angle of incidence and reflection are no longer equal for a metasurface.

Equation 4.2 and 4.3 can be easily reduced to the original Snell's law of refraction and reflection if there is no phase discontinuity across the surface *(dΦ/dx = 0)*. The generalised laws of reflection and refraction have been demonstrated by reflectarrays and v-shaped antennas respectively [32], [34], [35].

4.1.4 Applications of Metasurfaces

As discussed earlier in this section, the interaction of surface plasmon with the electromagnetic wave leads to a phase discontinuity across the metasurface. Since elements on a metasurface can be spatially varied, this variation can cause the currents on the surface to lead (or lag) depending on the individual resonant element. This localized phenomenon allows us to tailor the wavefronts as they pass through a metasurface and leads to a variety of applications.

4.1.4.1 Wavefront Control / Shaping using Metasurfaces

In the past, wavefront shaping in the microwave regime has been achieved with the help of reflect- and transmit-arrays [36], [37]. Such arrays have used variable element size and rotation (in case of reflect-arrays), and aperture coupled miniaturized delay lines (with a patched ground) for the transmit-array, in order to shape the wavefronts [38], [39]. Such arrays however have a periodicity of the order λ/4 - λ/2, therefore they do not provide sub-

wavelength resolution (sub-wavelength resolution can improve the aperture efficiency of such arrays) [22], [40]. Due to large periodicity, the induced electric and magnetic polarizbilities can no longer completely define their response and they cannot be considered 'homogenised', hence they cannot be classified as metasurfaces.

Metsurfaces allow the 360˚ control of the phase by introducing anisotropy through its individual elements. V-shaped anisotropic elements have been used to obtain a full control of the phase, however reflection losses reduce the efficiency of the structure to 50% and since anisotropy exploits the cross-polar component to achieve a full 360˚ of phase manipulation, the efficiency of the structure is further halved [16], [26]. The metasurface with anisotropic v-shaped scatterers is shown in Figure 4-4. In order to unlock further potential of metasurface design, multi-layered Huygens surfaces have been proposed [41]. These surfaces eliminate the reflection losses completely. Huygen's metasurfaces with efficiency of 86% at 10 GHz have been shown in [25]. This design also showed a wide 3-dB bandwidth of 24%.

Figure 4-4: *A metasurface with sub-wavelength v-shaped anisotropic scatterers. The orientation of the scatterers has been used varied in order to gain a full phase control of the wavefront [32]*

The local phase manipulation by metasurfaces has also been used to shape the wavefronts of the reflected wave. The variation in the dimensions of square patches on a dielectric layer backed by a ground plane has been shown to tailor the reflected wavefront [42]. By carefully controlling the size and response of each sub-wavelength inclusion in along both perpendicular axes, a birefringent metasurface has been successfully constructed in [43]. This metasurface showed an efficiency of 92% with additional advantage of splitting the incoming non-polarised electromagnetic wave into two orthogonal linear polarisations. A similar approach using perpendicular strip dipoles in a triangular lattice in terahertz range has been presented in [44].

4.1.4.2 Metasurface Lenses

Metasurfaces can also be employed to fabricate ultrathin lenses. In order to focus the electromagnetic energy at a distance *d*, a metasurface needs to have a phase profile given by Equation 4.4 [16].

$$\Phi_L(x,y) = \frac{2\pi}{\lambda}(\sqrt{x^2+y^2+d^2} - d^2) \tag{4.4}$$

This profile also alters the shape of the wavefront from planar to spherical, a condition necessary for focussing. High numerical aperture efficiency can be achieved as long as the electromagnetic wave strikes the surface at normal. However when the angle of incidence is not perpendicular, a phenomenon known as 'coma' occurs, which can cause a significant degradation in the numerical aperture efficiency. The effects of ‘coma’ can be reduced by placing the surface on a curved piece of dielectric [16]. Metasurface consisting of v-shaped antennas have been shown to focus energy at telecom frequencies [45]. Another metasurface lens based on reflect-arrays is presented in [46]. The lens was designed for near infrared

region and was designed on metal-insulator-metal structure. Gold bricks were deposited on silicon dioxide and the individual elements were optimized in order to engineer the desired reflection response. This lens showed a theoretical efficiency of 78%. Ametasurface lens based on rectangular dielectric resonators (RDRs) has been shown to focus energy at a single focus for three different frequencies. This was made possible by making the sum of the phase transversed by the wave and the phase jump imparted by the metasurface constant at three distinct frequencies. The resulting metasurface ended up being completely aperiodic [47].

4.1.4.3 Non-Linear Metasurfaces

Non-linear metasurfaces have been deployed to protect sensitive electronics and reduce interference on a shared platform. Non-linearity was introduced using diodes and capacitors which were incorporated in the design process and controlled the response of the metasurface. This surface absorbed the high powered radio frequency signals while causing a minimal distortion to the low powered ones [9]. In non-linear electrodynamics, metsurfaces and metamaterials can be used to enhance the magnitude of the non-lineary; they also allow targeting of the magnetic non-linear phenomenon and also combine it with the electric non-linearity [48]. One of the most important aspects of non-linearity is the second harmonic generationwhich is the process where two photons combine to form a single photon. This new photon has twice the energy and its frequency is also double in comparison to the original photon(s). This phenomenon happens when two photons interact with a non-linear material [49], [50]. Metasurfaces have been deployed to enhance this process. Using fishnet metasurfaces in near infrared region, an enhancement in the resonance of second harmonic generation spectrum was observed using spectroscopy [50]. It needs to be noted that if a

medium is inversion symmetric, it cannot generate the second harmonic and thus breaking the symmetry is imperative in order to observe the second harmonic generation.

4.1.4.4 Frequency Selective Surfaces Based on Metasurfaces

A typical frequency selective surface (FSS) is a periodic structure having each individual element resonant at the resonance frequency. FSSs typically have periodicity equal to half the wavelength of the resonant frequency [51]. They have been frequently employed to provide spectral filtering in signal communications. Moreover they are also used as diplexers, beam splitters and to make antenna radomes [52]. Metasurfaces can replace FSS due to the resonant nature of "meta-atoms". Since a metasurface's building blocks are sub-wavelength in nature they also bring additional advantages in comparison to a traditional FSS. The sub-wavelength periodicity allows to pack a large number of unit cells in a constrained space which is highly useful for radomes with limited space [53]. The small size of the unit cell also allows metasurfaces to have a stable response with respect to the changes in the angle of incidence of the illuminating electromagnetic wave. Such a structure has been presented in [54], where a layer of patches is backed by a wire grid on the other side of dielectric. The capacitance of patches coupled with the inductance of the wire grid formed an LC resonant structure with the resonant frequency much smaller than the wavelength at the resonant frequency.

In addition to structural design, lumped circuit elements have also been used to miniaturize the size of a unit cell of a periodic metasurface [55]. By using capacitors, the size of the individual element presented in [54] has been successfully decreased [56]. Convoluted elements with a reduced unit cell size have been presented in [57]. Metamaterials are usually designed with the help of split ring resonators (SRRs) [58]. SRRs have sub-wavelength physical dimensions and their Babinet's complement has been used to design and tailor the properties of metasurfaces [59]. Non-reciprocal bianisotropic elements have been used to

design "one way transparent" metasurfaces [60]. Active spatial filters (FSSs) designed using PIN and varactor diodes with complementary SRRs as their building blocks have been successfully employed for tuning and dual band operation [61].

Once a metasurface is fabricated, its response is fixed. Its reflection and transmission response cannot be changed. However since metasurface response is based on localized control, reconfigurable metasurfaces are very much desired in order to use a single metasurface for a wide range of applications. This has been addressed by a variety of designs presenting tunable/reconfigurable metasurfaces. There are three major ways in which a metasurface can be tuned (i) mechanical tuning (ii) material state change under a stimulus (iii) use of varactor diodes (in microwave domain) [62]. Mechanical tuning in all dielectric metasurfaces has been used in [63] and a shift in both resonances was recorded by rotating the individual elements. MEMS have also been applied for mechanical tuning in [64]. By shifting an engineered ground plane, beam steering from a reflector has also been achieved [65]. The capacitance of varactor diodes can be controlled by varying the voltage across them which make them an excellent candidate for electrically tuning the metasurfaces [66]. These diodes have been used for beam steering and switching the states (modes) of metasurfaces [67], [68]. A tuneable metasurface with varactor diodes is shown in Figure 4-5. Metasurfaces with dispersive refractive index have been proposed for THz domain since the modulators at THz frequency usually work at extremely low (cryogenic) temperatures [69].

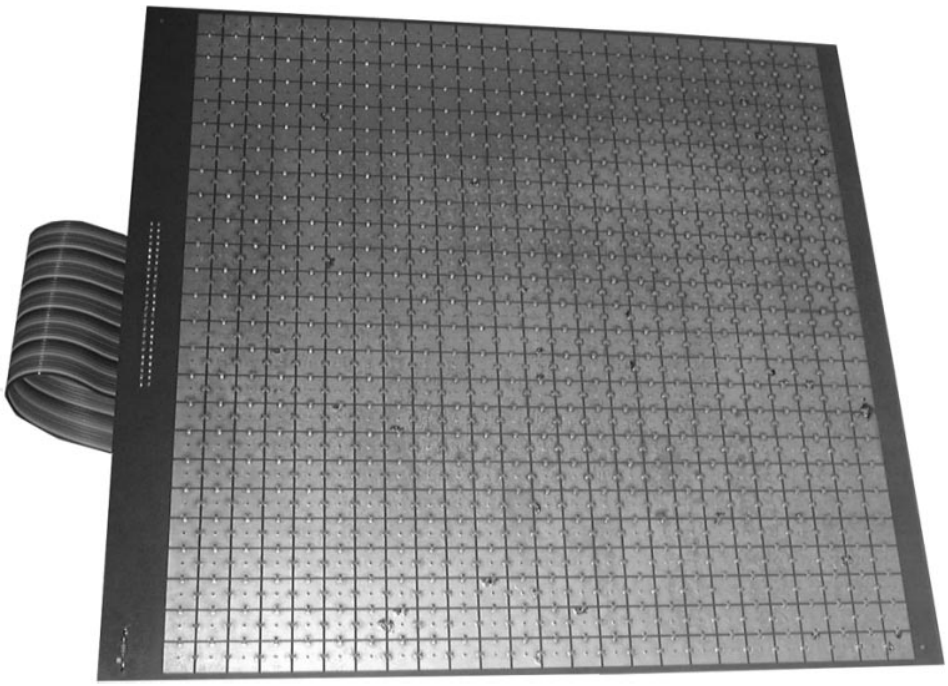

Figure 4-5: *A tunable metasurface (impedance surface) used as a steerable reflector with 1125 varactor diodes* [67]

Metasurfaces can also improve the performance of horn antennas. In [70], a metasurface designed using a genetic algorithm has been used as an inner surface for a conical horn and the cross polar levels and the side lobe levels have been improved over the entire Ku band. A similar approach was applied to improve the performance of a hybrid mode square horn antenna using metasurfaces [71]. Metasurfaces have been proposed for medical body area networks (MBAN) as well, by improving the performance of a low profile monopole antenna. This truncated metasurface, in contrast to artificial magnetic conductors (AMCs), also contributed to the radiation from the antenna thus increasing the gain and the front to back ratio [72]. Two layered metasurfaces loaded with resistors have been demonstrated to reduce the radar cross section (RCS) of a stacked antenna array thus offering an alternative to radar absorbing material. The antenna was sandwiched between these two metasurfaces; the metafilm above the antenna reduced the RCS for out of band frequencies while the one below reduced the RCS for the in band frequencies [73]. Metasurfaces have also been successfully

used to design and manufacture high gain holographic antennas [74], [75]. In [76], multi layered metasurfaces with sub-wavelength profile, were used as partial reflective surfaces to design a high gain antenna with an enhanced bandwidth.

4.1.5 Complementary Metasurfaces

Complementary metasurfaces are designed when two or more arrays of periodic elements are placed in close proximity of each other in such a way that there is a strong coupling among the complimentary surfaces. The resulting complementary metasurface then, becomes a pass band structure. The complementary nature of two periodic arrays is governed by the Babinet's principle.

4.1.5.1 Babinet's principle

Babinet's principle was originally defined in optics. It states that the radiation from a source in a plane without any obstruction is equal to the vector sum of the radiation caused by two complementary surfaces (by the same source in the same plane). Consider an opaque sheet with some holes inside it in front of a screen. Another surface is said to be its complementary surface, only when the transparent and opaque areas from the original surface are entirely interchanged. The sum of radiation patterns due to the complementary surfaces on the screen is equal to the radiation pattern in the absence of any surface. Two complementary Babinet's complementary surfaces are shown in Figure 4-6.

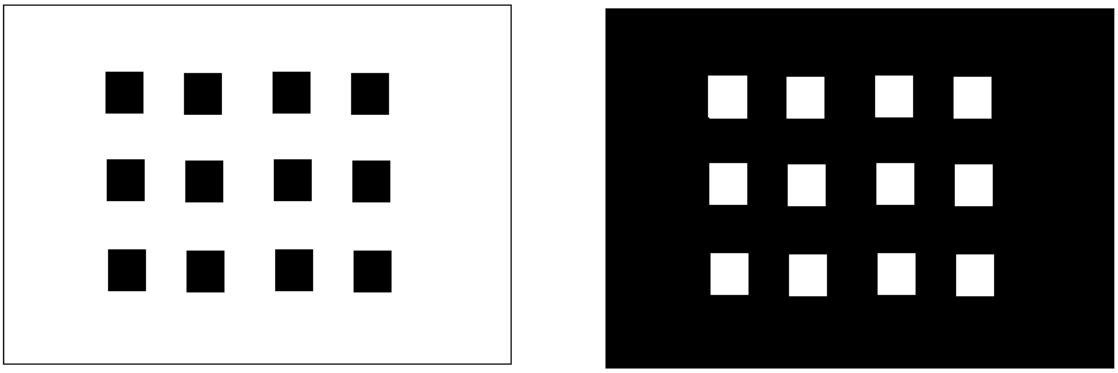

Figure 4-6: *Two complementary Babinet's surfaces. Black indicates the presence of absorber (in optics) or perfect reflector (in microwaves region)*

The translation of this principle from optics to electromagnetic radiation requires some additional work due to two reasons; (i) The opaque screens gets replaced by a thin reflecting metallic screen; (ii) The resonant behaviour of the two complementary structures needs to be taken into account [77]. An array of half-wave long dipoles acts a reflector to the impinging electromagnetic wave. By the virtue of Babinet's principle, the complementary surface of dipole i.e. slots should transmit the energy at that frequency. This is true albeit for a small deviation. The slots are required to be rotated by 90˚. This is due to the fact that when an electromagnetic wave strikes an array of dipoles, each element develops a voltage across its arms. For a slot to be transparent at this frequency, it needs to develop the same voltage across the slot. Thus the electric field needs to be parallel to the orientation of the dipole while perpendicular to the slots.

Mathematically, Babinet's principle can be defined in terms of admittances (or surface impedances). Consider two complimentary sheets with admittances Y_1 and Y_2. Let the medium surrounding the both sheets having admittance equal to Y. When a plane wave with Electric field E is normally incident on the screen, then the relationship between the transmitted and the incident electric field is given by Equation 4.5 [77] :

$$\frac{E}{2Y + Y_1} = \frac{E_1}{2Y}$$

(4.5)

Similarly for the complimentary sheet

$$\frac{E}{2Y + Y_2} = \frac{E_2}{2Y}$$

(4.6)

where E_1 and E_2 represent the transmitted electric field.

These two quantities can be related to each other by using Babinet's principle [77]. Since the sum of the field due to two complimentary surfaces is equal to the field in the absence of any surface, it can be written that

$$t_1 + t_2 = 1 \quad (4.7)$$

where t_1 and t_2 are the transmitted fields which are normalized with respect to the field in the absence of any surface.

Combining Equations 4.5, 4.6 and 4.7, a relationship between equivalent surface admittances of the complementary surfaces and admittance of the medium is obtained

$$Y_1 Y_2 = 4Y^2$$

For equivalent impedances, Equation can be rewritten as

$$4Z_1 Z_2 = 4Z^2$$

where Z_1 and Z_2 are the impedances of the complimentary surfaces ($Y_2 Z_2$ = 1).

If the medium surrounding the sheets is free space, then Z = 377 Ω and the Babinet principle can be rewritten as

$$Z_1 Z_2 = 35477\ \Omega^2$$

A complementary frequency selective surface (CFSS) is constructed when a thin sheet of dielectric has a periodic array of slots on one side while its other side contains an array of its Babinet's complement i.e. dipoles. When these two layers are very close, the strong coupling between the dipoles and the slots considerably decreases the resonant frequency of the CFSS as presented in [78]. This causes a reduction in the size of the individual unit cell and the resulting CFSS is inherently a pass band structure. The small individual scatterer size also introduces locality in the structure and makes its response insensitive to the changes in the incidence angle for the illuminating plane wave. Surface waves can be supported on self-complementary metasurfaces. If the vertices are connected, the TM wave is supported and a TE wave is supported when they are disconnected [79]. Metasurfaces with complementary split ring resonators in different orientations exhibited either a band stop or band pass behaviour [80]. Checkerboard metasurfaces with adjacently connected patches have been shown to support a quasi TEM mode [81].

4.2 Dipole-Slot Metasurfaces

A dipole-slot metasurface, also referred to as a CFSS, is shown in Figure 4-7. This section investigates the nature of the coupling among the two complementary elements in order to explain the interesting behaviour of the dipole-slot metasurface. The effects of the various parameters on the resonant frequency and the insertion loss of the dipole-slot metasurface were also studied in conjunction.

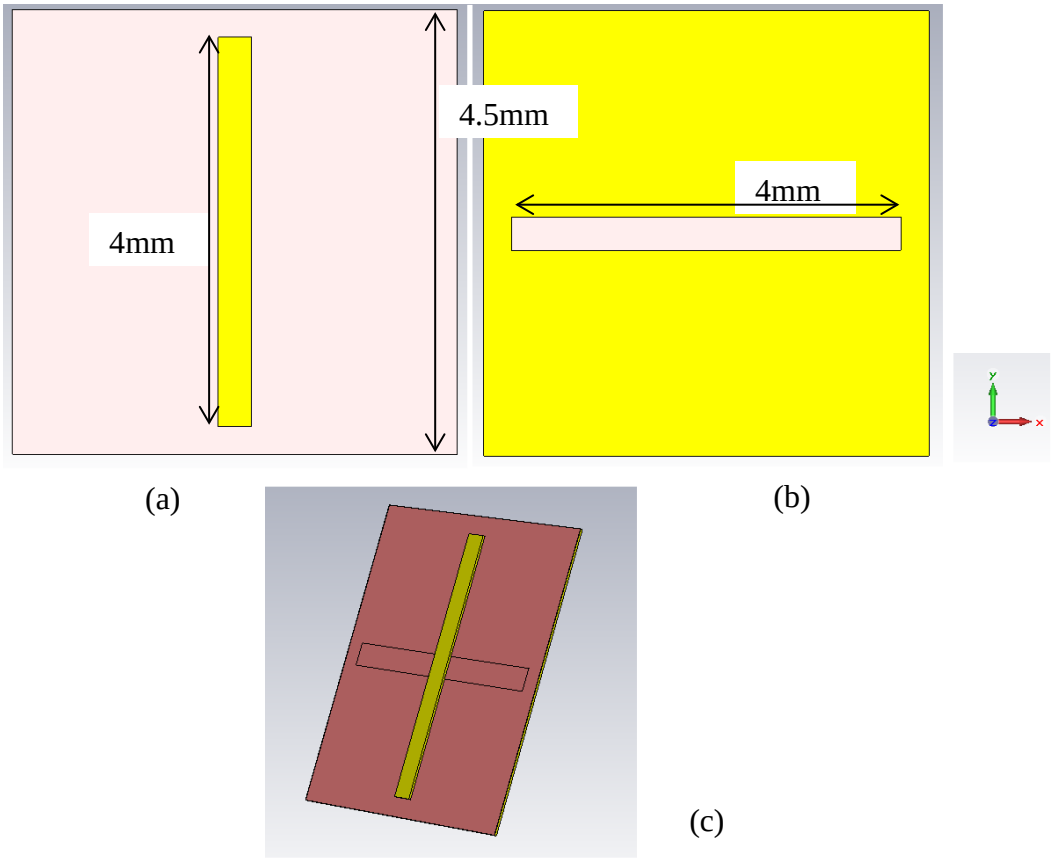

Figure 4-7: *A basic unit cell of a dipole slot metasurface (a) Front view showing the dipole; (b) Back view showing the slot; (c) A 3-dimensional tilted view showing the dipole, the dielectric and the slot in the background*

In this section typical dipole-slot metasurfaces have been simulated in CST Microwave Studio [82]. The unit cell (of the metasurface) is simulated by using the periodic boundary conditions. A TE polarised plane wave is incident normally on the dipole-slot metasurface. The simulation results are calculated by using the Frequency domain solver. The unit cell has a periodicity of 4.5mm. The dipoles and slots are 4mm long and 0.4mm wide. The dielectric between the dipoles and slots is Arlon-3000. The dielectric is 0.05mm thick and has a relative permittivity of 3 and a loss tangent 0.003. The comparison of this dipole-slot metasurface with dipoles and slots array in isolation (but backed by the same thin dielectric) is shown in Figure 4-8.

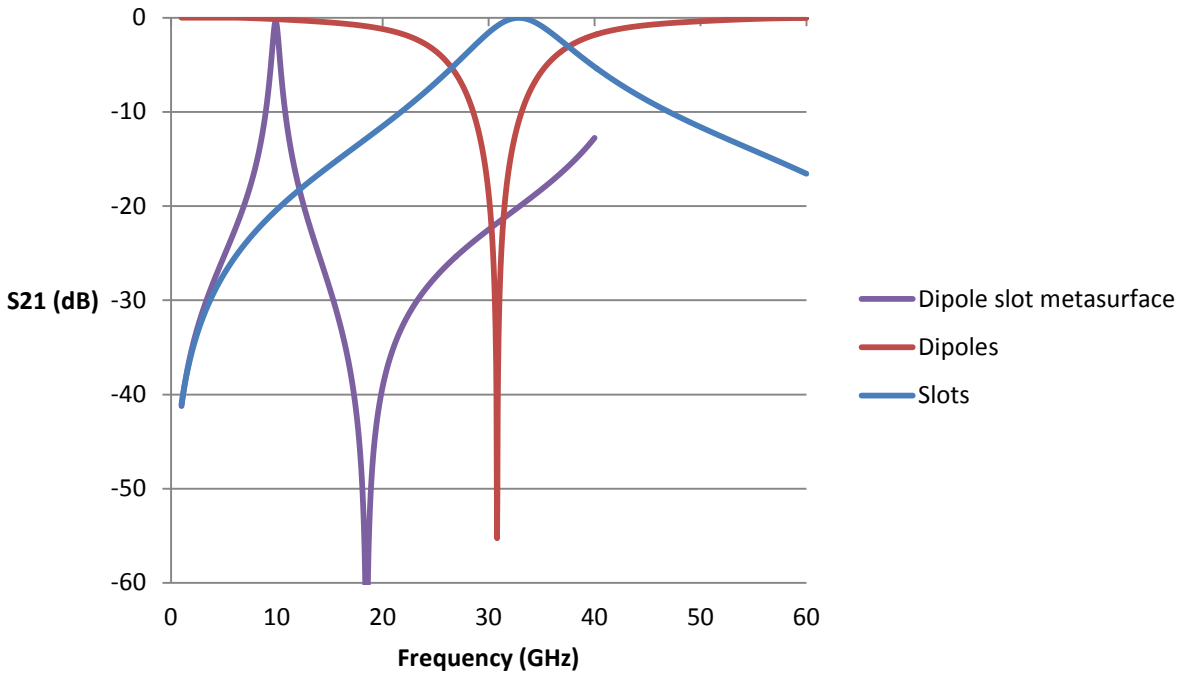

Figure 4-8: *Transmission co-efficient comparison between an array of dielectric backed dipoles, dielectric backed slots and the dipole-slot metasurface (simulated)*

The resonant frequency of the dielectric backed dipoles array was 30.8 GHz while the dielectric backed slots resonated at 32.8 GHz. When these two Babinet's complementary structures are combined together to form a dipole-slot metasurface, the resulting structure shows a pass band resonance at 9.9 GHz which is a significant decrease in the resonant frequency. The period of this structure is now ~λ/7, where λ is the free space wavelength at the resonant frequency and all the scatterers are now sub-wavelength. The dipole-slot metasurface also has a good insertion loss of 0.39dB.

The same structure has also been simulated in the Finite-difference time domain (FDTD) software EMPIRE XCcel [83]. In order to replicate the periodic structure, the perfect electric and magnetic boundary conditions are used along x- and y-axis of the unit cell. The electromagnetic wave strikes the unit cell of the dipole-slot metasurface normally. The results from both software, are compared and they show very good agreement as shown in

Figure 4-9. The simulated resonant frequency of the pass band in CST and EMPIRE is 9.9 GHz and 10.3 GHz respectively.

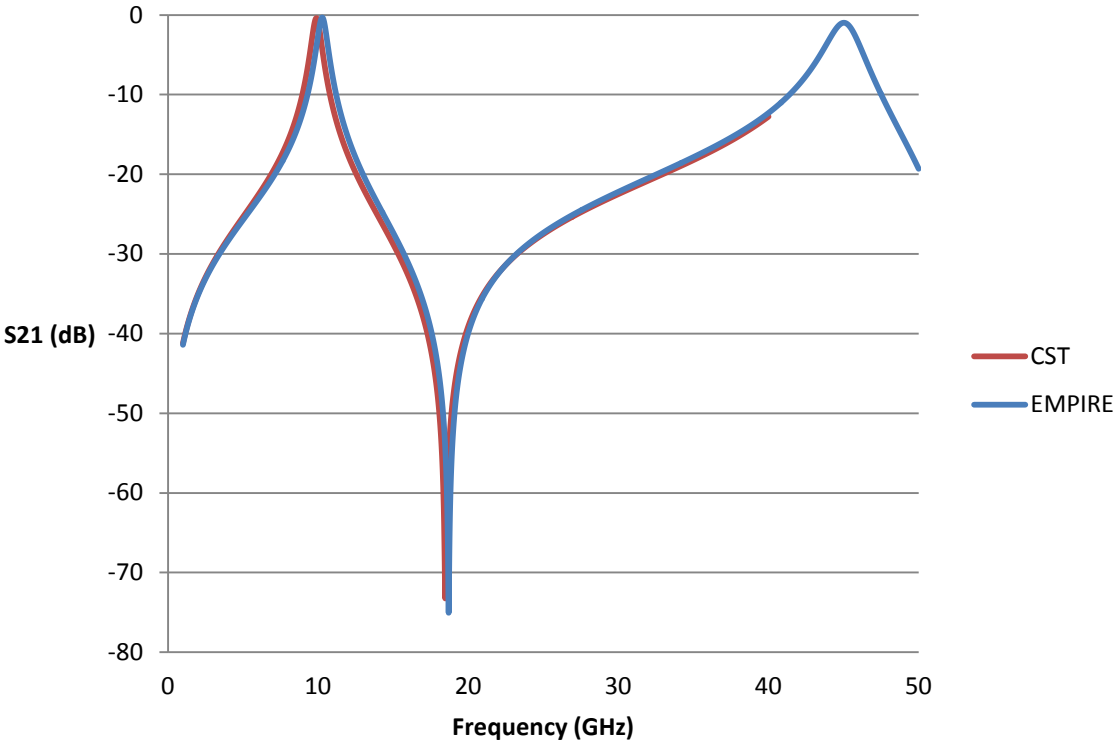

Figure 4-9: *Simulation comparison of the dipole- slot metasurface with CST and EMPIRE*

Figure 4-8 and Figure 4-9 show that the fundamental response of the dipole-slot metasurface is band pass, resembling that of an aperture array (albeit at a much lower resonant frequency). This shows that the dominant/driving element of this metasurface are slots (apertures) while the dipole is the supporting/sub-dominant element. Naturally, a dipole array is capacitive therefore it is expected that it adds an extra capacitance to the dipole-slot metasurface thus causing a decrease in the resonant frequency. As the capacitance is directly proportional to the dielectric constant (relative permittivity) of the dielectric, so increasing the dielectric constant of the material should increase the capacitance added to the structure by the dipoles and therefore causing a further decrease in the resonant frequency of the metasurface.

4.2.1 Effects of Relative Permittivity of the Dielectric on the Dipole-Slot Metasurface

The effect of the relative permittivity (also known as the dielectric constant) of the material, sandwiched between the two complementary layers of a dipole-slot metasurface, on its response is shown in Figure 4-10. The relative permittivity of the material was varied from 1 to 2, 3 and 5. The length and width of the dipoles and slots are still 4mm and 0.4mm respectively. The thickness of the sandwiched dielectric for these simulations is 0.05mm. The thickness of the dielectric layer is kept constant for all the values of the dielectric constants in order to obtain a clear picture of the effect of the relative permittivity on the resonant frequency of the dipole-slot metasurface. It can be easily observed from the Figure 4-10, that the resonant frequency decreases with an increase in the relative permittivity. The simulated resonant frequencies for these dielectric constants are 15.5 GHz, 12.1 GHz, 9.9 GHz and 8.1 GHz respectively. This result clearly demonstrates that the coupling among the two layers is increased with an increase in the dielectric constant. It also points to the fact that the capacitance added to the apertures (slots) layer, due to close proximity of the dipole layer, is an integral part of this coupling.

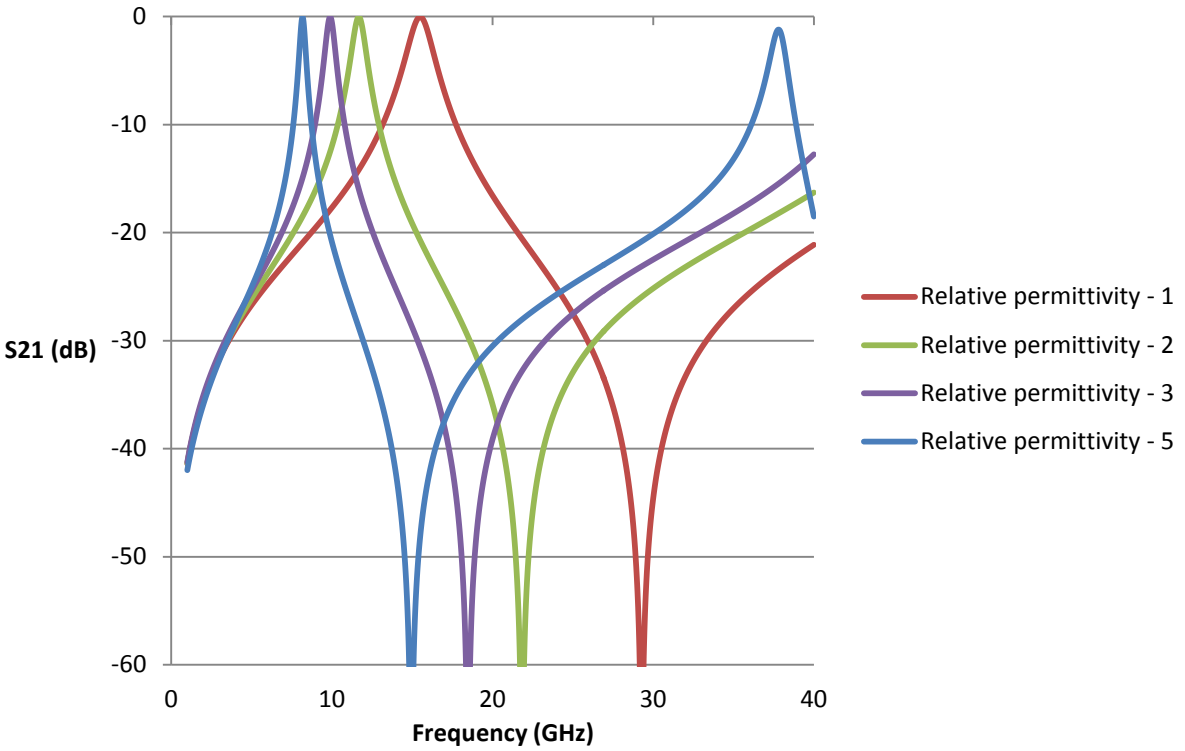

Figure 4-10: *Effects of change in the dielectric constant of the material on the dipole-slot metasurface pass band resonance frequency(simulated)*

It is worth noting that even when the simulated relative permittivity of the dielectric was 1 (i.e. the dielectric was assumed to be free space between the two layers), the resonant frequency of the dipole-slot metasurface was 15.5 GHz. This value is still considerably below the resonance of the dipole and slots in isolation (~33.3 GHz for λ/2 resonance), indicating that the coupling among the two layers is still extremely strong (for a relative permittivity of 1). The presence of dielectric enhances this coupling further as it increases the capacitance due to the dipole layer therefore causing a further decrease in the resonant frequency.

4.2.2 Dipole-slot Metasurface with an Anisotropic Dielectric

The strongest evidence which demonstrates that it is indeed the capacitive coupling among the two complementary arrays which is the main reason for the decrease in resonant

frequency and that, the capacitance of the dipole is the main driving factor of this coupling comes from using anisotropic materials. Unlike isotropic materials (whose electromagnetic properties are independent of direction), we consider uniaxial anisotropic materials. The relative permittivity matrix of such a material is a diagonal matrix. If xyz-coordinates are considered then the permittivity matrix is given as

$$\begin{bmatrix} \varepsilon_x & 0 & 0 \\ 0 & \varepsilon_y & 0 \\ 0 & 0 & \varepsilon_z \end{bmatrix}$$

where ε_x, ε_y and ε_z is the relative permittivity along each of the orthogonal axis. Another condition for the uniaxial medium is that two of these tensors are equal.

As shown in Figure 4-7 (a) and (b), the dipole and slot are placed in the xy-plane while the thickness of the dielectric is along the z-axis. If the coupling among the two layers is the main reason for the peculiar behaviour of the dipole-slot metasurface, a comparatively large change in its response is expected when the tensor along z-axis is altered. On the other hand, if altering ε_x and ε_y leads to a more pronounced change, it will point to the fact that it is the intra-layer coupling which plays a major role (instead of the inter-layer coupling).

The results shown (for a dipole-slot metasurface) in Figure 4-10 are used as a reference. The resonant frequency of the structure is 15.5 GHz when the relative permittivity of the dielectric material is 1. Now the same structure was simulated on a uniaxial isotropic material. CST Microwave Studio allows defining the relative permittivity of the material with respect to orthogonal axes, thus making possible the modelling of uniaxial anisotropic materials. Three different uniaxial anisotropic materials were considered. The first material had $\varepsilon_x = 3$, similarly the second material had $\varepsilon_y = 3$, and the third material had $\varepsilon_z = 3$ (both other permittivity tensors were equal to 1).

The results for these experiments and their comparison with a dipole-slot metasurface simulated on a material with an isotropic permittivity of 1 is shown in Figure 4-11. Negligible difference between the resonant frequency of the first and the second material was observed. The simulated resonant frequency for first material ($\varepsilon_x = 3$) was 15.28 GHz while the simulated resonant frequency for the second material ($\varepsilon_y = 3$) was 15.32 GHz. The resonant frequency for third material ($\varepsilon_z = 3$) however showed a marked difference. Its value was 10 GHz. As shown in Figure 4-9 (at the start of the Section 4.2), the dipole-slot metasurface with an isotropic dielectric, having a relative permittivity of 3, exhibited resonance at 9.9 GHz. The comparison between the isotropic material and the anisotropic material ($\varepsilon_z = 3$) is shown in Figure 4-12. Figure 4-11 and Figure 4-12 demonstrate that it is indeed the inter-layer coupling which is chiefly responsible for the compact nature of the dipole-slot metasurface and that the capacitance added to the apertures layer by the dipole layer causes this decrease in the resonant frequency of this structure. This has been concluded because, the difference between the response of the dipole-slot metasurface when an isotropic material (of relative permittivity = 3) was used (as the dielectric) was extremely close the response (of the same metasurface) when a uniaxial anisotropic material with $\varepsilon_z = 3$ was used. This also shows that it is indeed the coupling along z-axis which is the major factor in determining the resonant frequency of the dipole-slot metasurface. Similarly the response for anisotropic materials with $\varepsilon_x = 3$ and $\varepsilon_y = 3$ showed a very small deviation (~0.2 GHz) in the resonant frequency in comparison to when free space is employed (as the dielectric). This shows that relative permittivity along x- and y-axis indeed plays a very minor role. (The relative permeability of all the materials is considered isotropic thus the only varying factor is the relative permittivity).

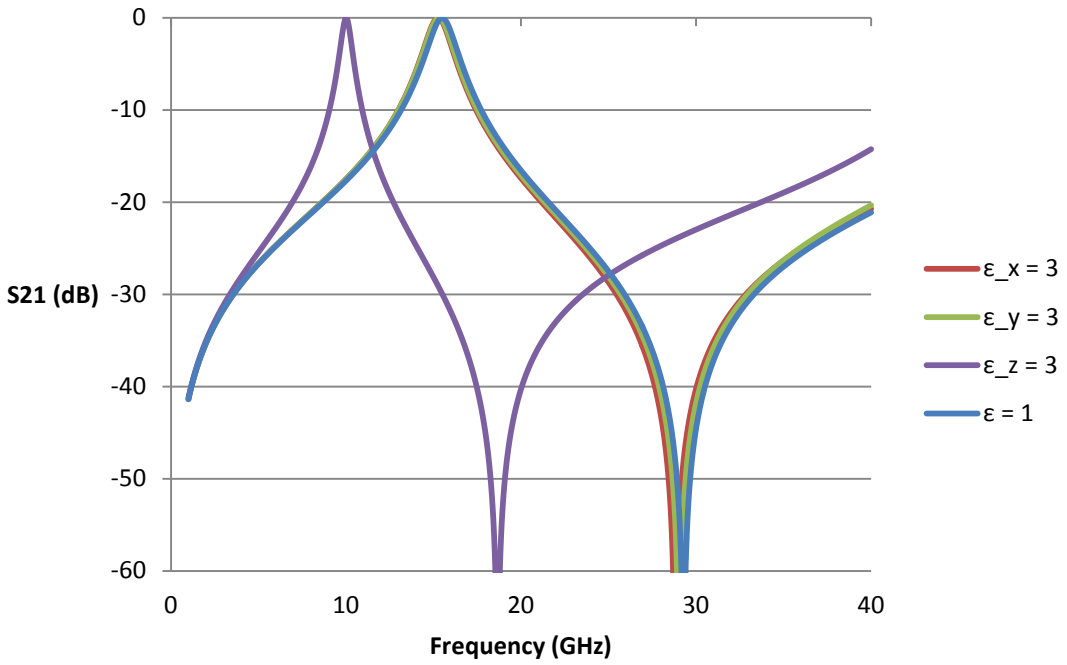

Figure 4-11: *Comparison between the uniaxial anisotropic and isotropic materials is shown. ε stands for the isotropic material. The thickness of the material for all the simulations is equal to 0.05mm (simulated)*

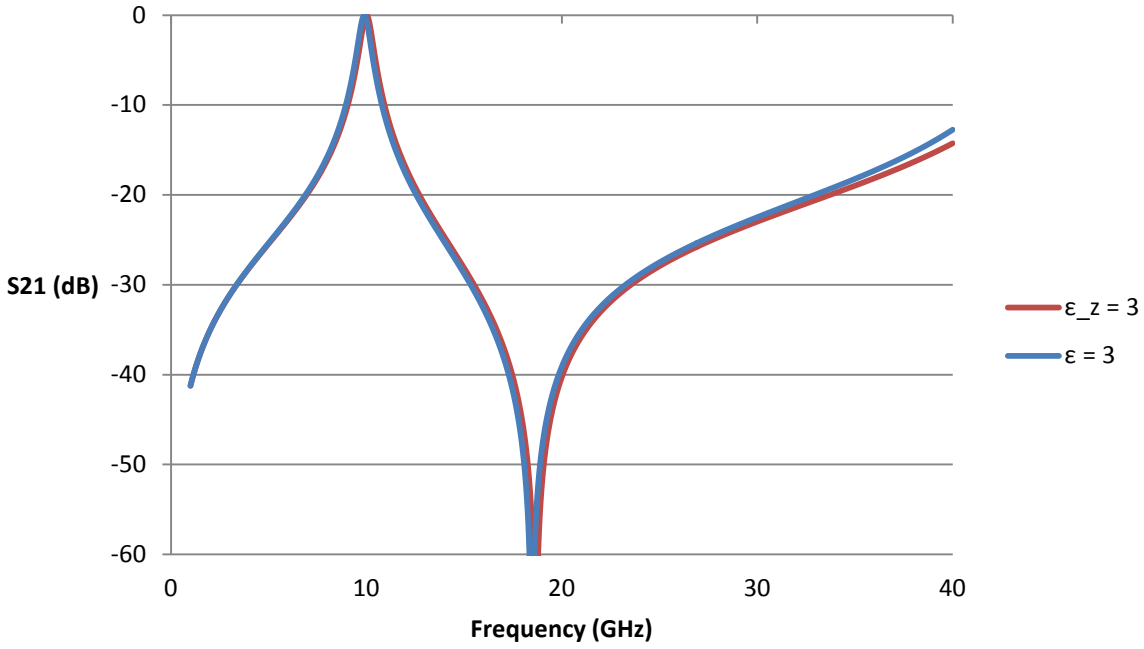

Figure 4-12: *Comparison between the uniaxial anisotropic and the isotropic material (with relative permittivity 3) l is shown. ε stands for the isotropic material. The thickness of the material for all the simulations is equal to 0.05mm.*

The nature of the capacitance added by the dipole layer has also been investigated. As discussed in Chapter 2, the electric fields along a patch adjacent to a ground plane vary as a function of location. However if this capacitance resembles that of a parallel plate then the electric fields remain nearly constant along the metallic area. This was investigated by two different configurations shown in Figure 4-13. In Figure 4-13 (a), the dielectric was placed at the edges of the dipole while in Figure 4-13 (b) the same dielectric was placed in the middle. The transmission co-efficient of these two configurations were then compared with the structure shown in Figure 4-7 (when the dielectric was placed along the whole area of the unit cell). The relative permittivity of the dielectric was assumed to be 3 and its thickness was 0.05mm.

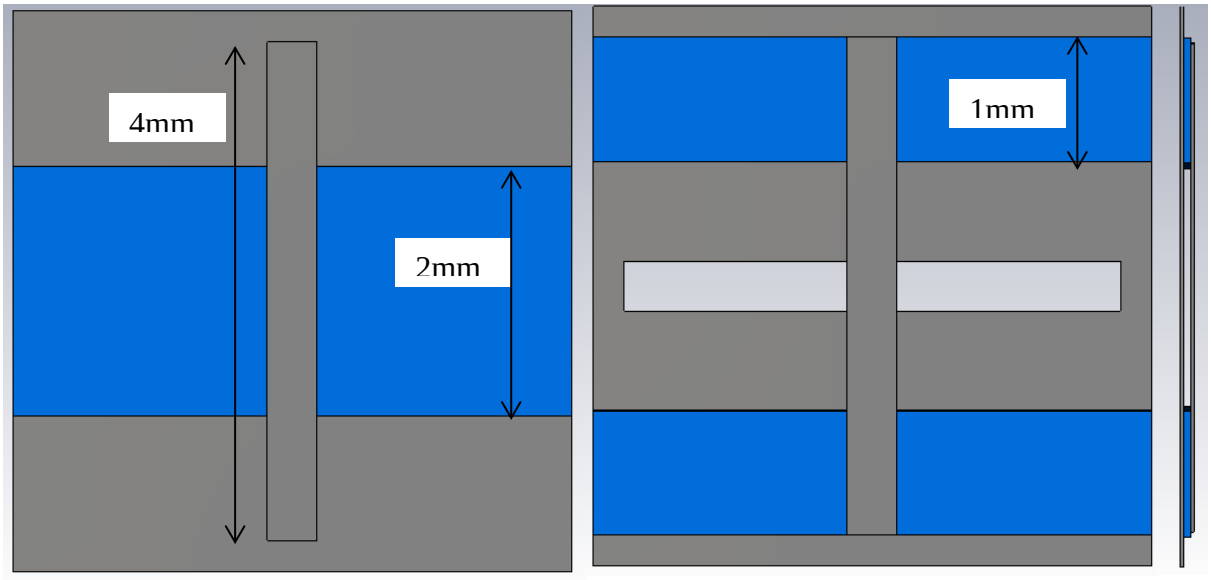

Figure 4-13: (a) *The dielectric (blue) is placed along the middle of the dipole;* **(b)** *dielectric (blue) is placed along the edges of the dipole;* **(c)** *side view showing that the distance between the slot and the dipole is constant and the absence of dielectric means free space*

The resonant frequency for the configuration, shown in Figure 4-13 (a) was 12.1 GHz while the structure in Figure 4-13 (b) resonated at 11.5 GHz. The comparison between the response

of these two structures and that of a dipole-slot metasurface is shown in Figure 4-14. This shows that the capacitance added by the dipole layer is not of the parallel plate nature (for parallel plate capacitance, the values for both configurations should have been extremely close) and that the electric fields are indeed stronger at the edges in comparison to the centre of the dipoles. This is indeed conformed by electric fields plot of the dipole-slot metasurface (shown in Figure 4-7). The electric fields are shown in Figure 4-15.

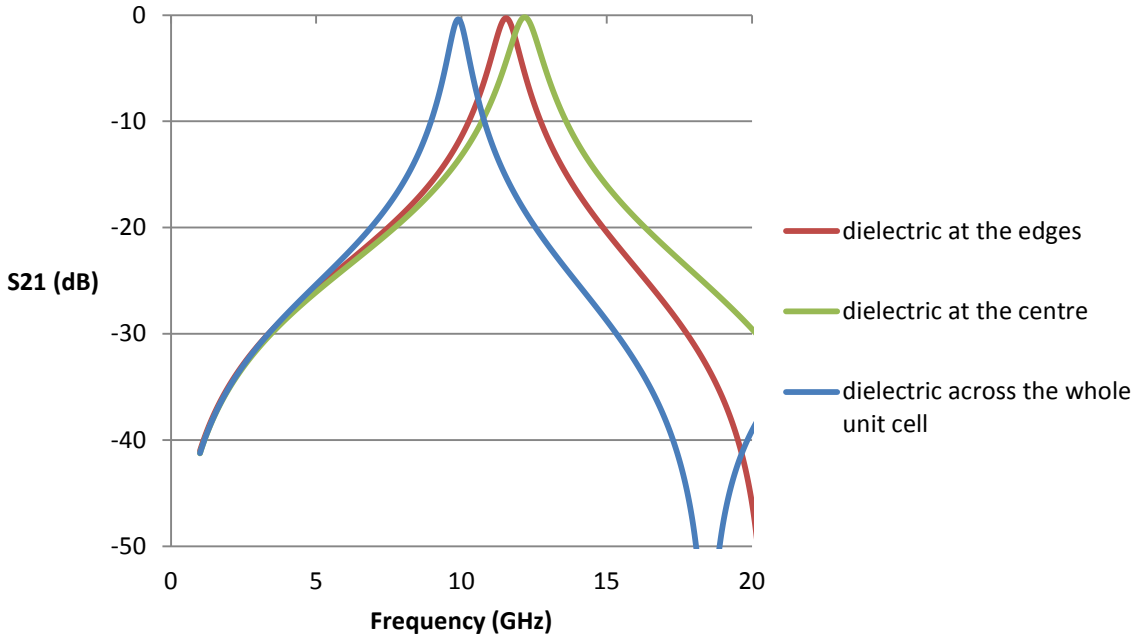

Figure 4-14: *Simulated transmission co-efficient comparison when dielectric is placed at the edges(red line) as shown in Figure 4-13(a) at the centre(green line) as shown in Figure 4-13(b) and across the whole unit cell as shown* in Figure 4-7.

The electric fields are plotted at the resonant frequency of the dipole-slot metasurface (9.9 GHz) in Figure 4-15. The arrows of the electric fields plot point in the direction of the z-axis (perpendicular to the plane of the dielectric). This is due to the capacitance added to the slots layer by the dipole (through the dielectric). The electric fields are negligible at the centre of the dipole. This is due to the presence of the slot (as the absence of metal does not allow the

dipole (capacitance) to be coupled). It is also evident from Figure 4-15 that the magnitude of the electric fields is maximal at the edges of the dipole and it decreases towards the centre.

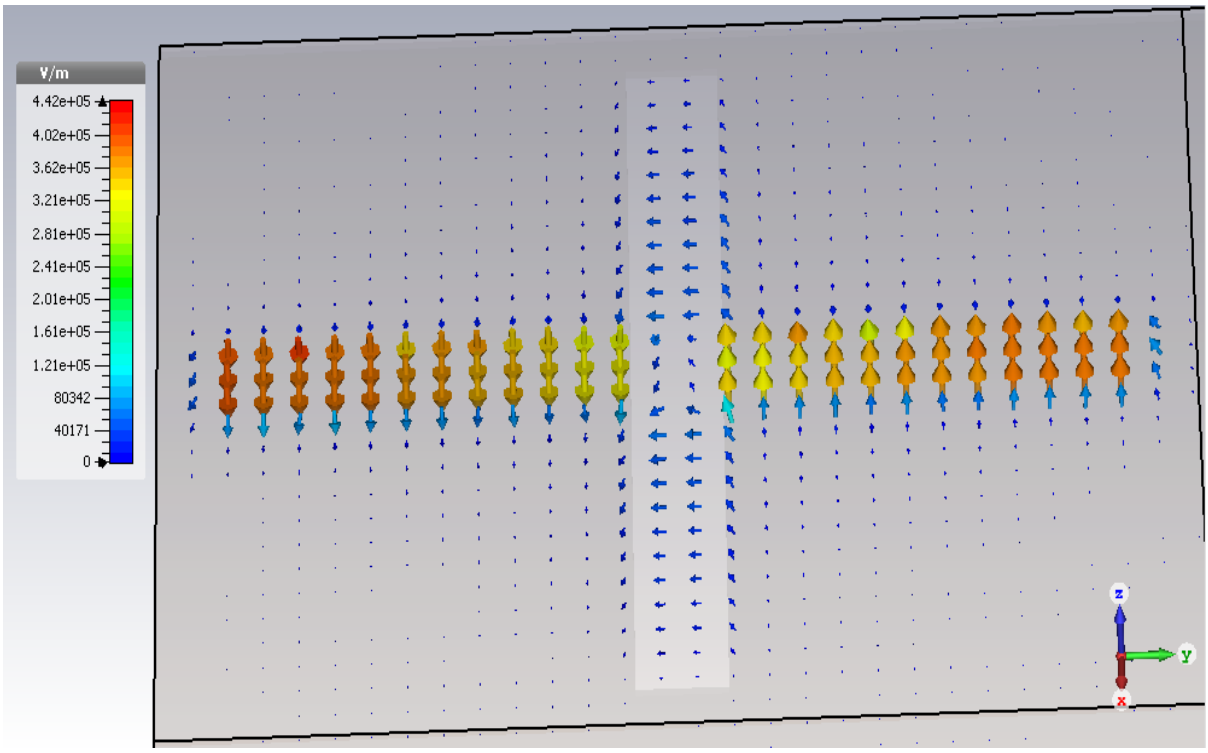

Figure 4-15: *Electric fields plot of a dipole slot metasurface at 9.9 GHz. The electric fields are simulated in Microwave Studio CST (at the centre of the dielectric)*

4.2.3 Effects of Thickness of Dielectric on the Dipole-Slot Metasurface

The effect of changing the thickness of the dielectric on the resonant frequency of the dipole-slot metasurface has also been studied via CST simulations. The purpose of these simulation experiments was to observe how the coupling among the two complementary layers was affected with an increase in the thickness of the dielectric. Since the thickness of a dielectric is inversely proportional to the capacitance, it is expected that increasing the thickness of the dielectric would lead to an increase in the resonant frequency. This is indeed what was observed and shown in Figure 4-16 (a) and (b). As the thickness was varied from

0.03mm to 0.05, 0.07, 0.11 and 0.15mm; the resonant frequency increased from 8.1 to 9.9, 11.2, 12.8 and 13.8 GHz respectively. Another interesting observation is that as the thickness increased further, the change in the resonant frequency was reduced, for example, by changing the thickness from 0.03mm to 0.07mm caused an increase in the resonant frequency equal to 3.1 GHz (from 8.1 GHz to 11.2 GHz) however the same change in thickness from 0.11mm to 0.15mm caused only an increase of 1GHz (12.8 GHz to 13.8 GHz). This shows that the rate of decoupling decreases with an increase in the thickness.

This observation leads to another interesting question: *can the two layers decouple completely?* To test this, the dipole-slot metasurface was simulated using a thick dielectric between the two layers. The thickness was varied from 5mm to 9mm and 13mm. The results are shown in Figure 4-16 (b). The simulated resonant frequencies are 19.3, 19.9 and 20.3 GHz respectively. The unit cell size at these resonant frequencies is now greater than $\lambda/4$ and the dipole-slot structure can no longer be classified as a metasurface (for this thick interim dielectric). Another phenomenon to be noticed is related to the transmission co-efficient in Figure 4-16 (b). The insertion loss at these frequencies has also increased beyond 1.5 dB (worst case is at 19.3 GHz when insertion loss is 2.5dB). This shows that the thick dielectric which was low loss (and simulated with a loss tangent of 0.003), now dissipated a significant amount of energy (which is to be expected from a bulky material). This experiment concludes that the two complementary layers do not decouple completely even when a thick dielectric is placed between them however the effect of the change in the thickness, on the resonant frequency is certainly reduced when the gap between the two complimentary layers is wide. The relative permittivity of the dielectric for all these simulations was 3.

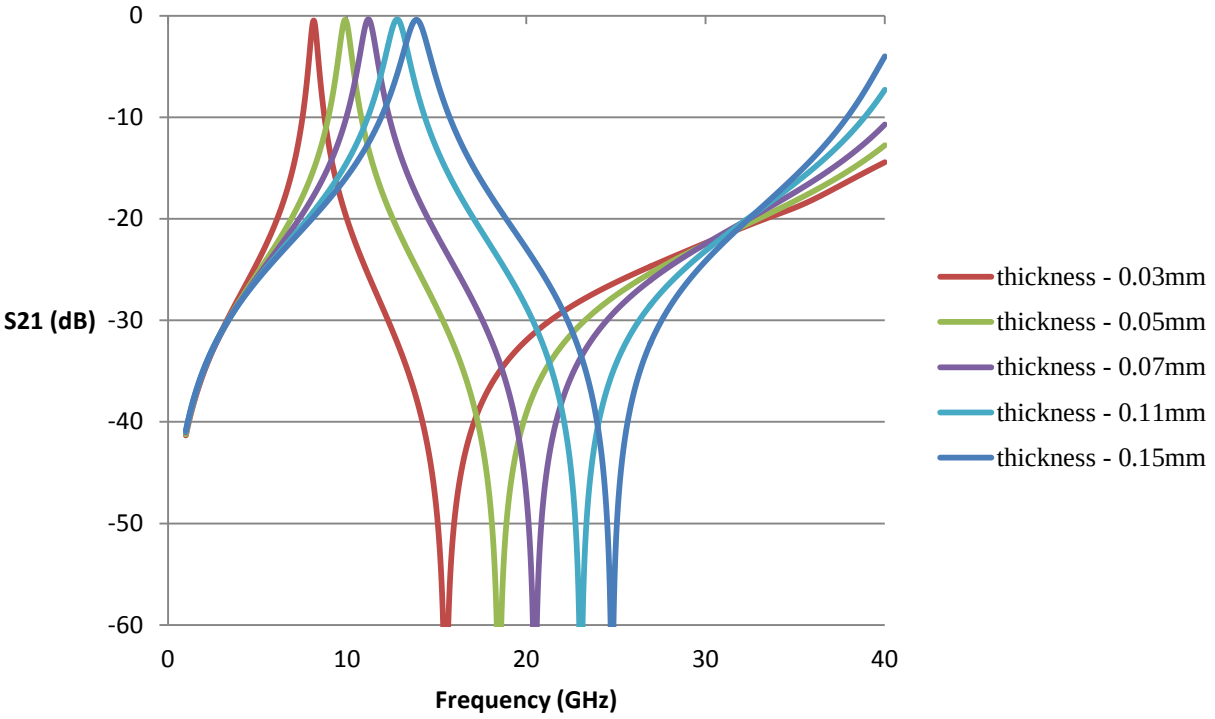

(a)

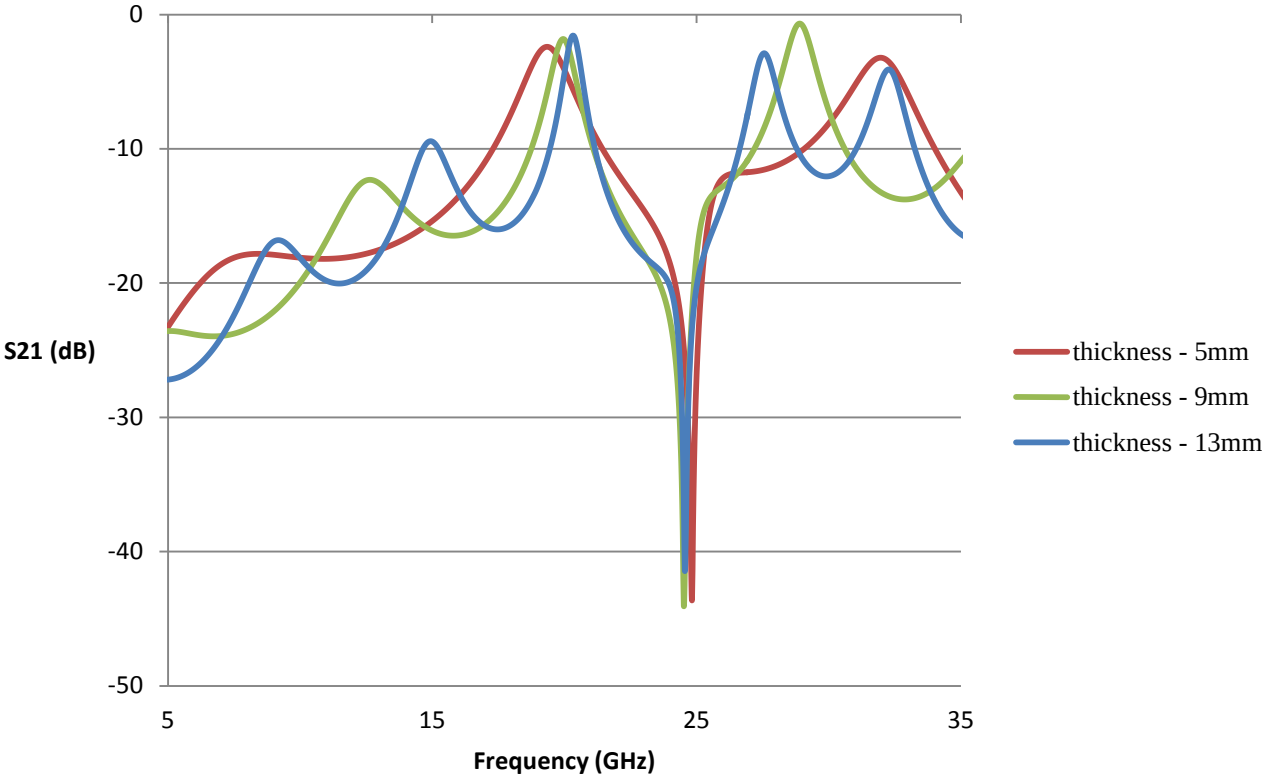

(b)

Figure 4-16: *Simulated effect of thickness on the resonant frequency of the dipole-slot metasurface (a) thickness (0.03 – 0.15 mm) (b) thickness (5 – 13mm)*

4.2.4 Effect of Dielectric Loss Tangent on the Transmission Loss of a Dipole-Slot Metasurface

One of the distinguishing features of the dipole-slot metasurface is that its response can be scaled by changing the relative permittivity of the dielectric material. Section 4.2.1 showed that increasing the dielectric constant of the material leads to a considerable change in its resonant frequency. This is in contrast to the traditional frequency selective surfaces which do not exhibit such a strong response to the relative permittivity change of the supporting dielectric. This extremely useful characteristic of the dipole-slot metasurface is due to the strong capacitive coupling between the two layers across the dielectric. Since the added capacitance is dependent on the relative permittivity (and it plays a key part in evaluating the response of the dipole-slot metasurface) therefore the dielectric constant is a significant factor in determining the resonant frequency of such a structure. It was shown in Section 4.2.3 that the transmission losses for a dipole-slot metasurface increased for thick dielectric materials thus indicating that there is a strong relationship between the properties of the dielectric and the transmission loss. This was investigated further by varying the loss tangent of the dielectric material while keeping all other parameters constant.

The loss tangent value was varied from 0 (loss-less) to 0.005, 0.010 and 0.100. The results are shown in Figure 4-17. The loss-less material (as expected) showed negligible transmission loss. The transmission loss increased with an increase in the loss tangent value. For loss tangent of 0.005, the loss was about 0.5dB. Further increasing the loss tangent value (to 0.010) increased this loss to 1.1dB. For an extremely lossy material (loss tangent value equal to 0.1), the transmission loss was 7.3dB. This is to be expected since the coupling through the dielectric is the main reason for the anomalous transmission response of the dipole-slot metasurface. It also presents a caution for choosing the dielectric material in order

to design a dipole-slot metasurface. A low loss material ought to be selected in order to avoid significant transmission loss.

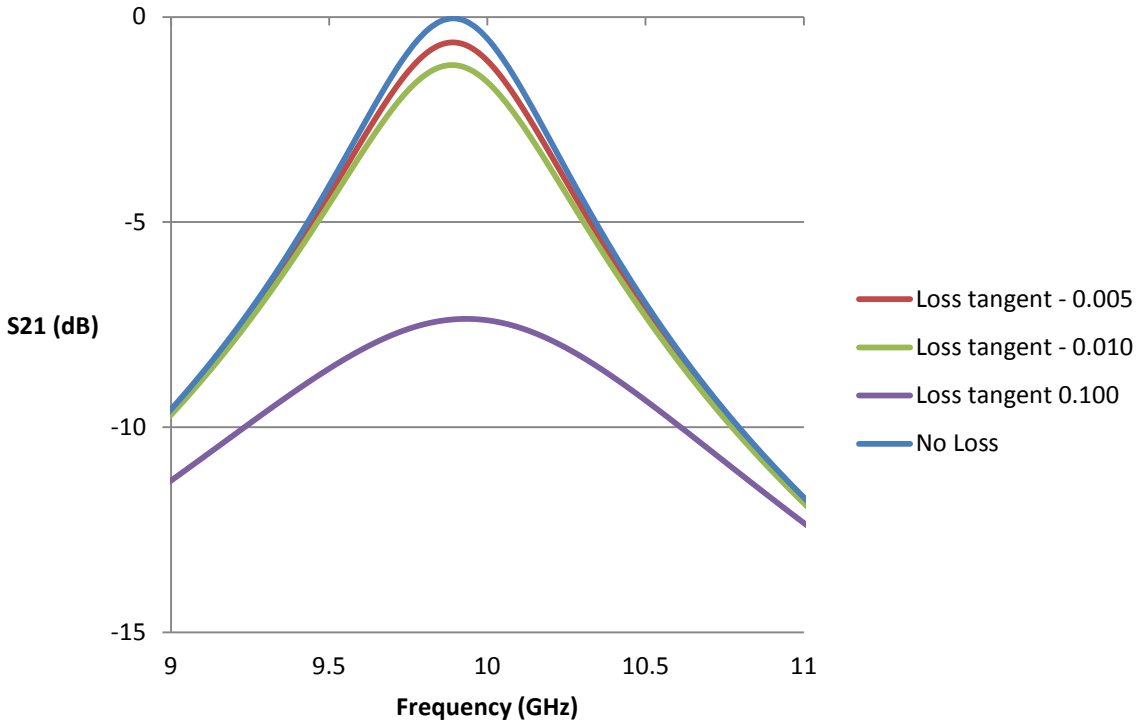

Figure 4-17: *Transmission loss dependency on the loss tangent of the dielectric (simulated)*

4.2.5 Effect of Size of Elements on the Dipole-Slot Metasurface

Another distinguishing feature of a dipole-slot metasurface is the effect of the length of elements on its resonant frequency. Since the inter-layer coupling is the chief reason for the extraordinary behaviour of the dipole-slot metasurface therefore the resonance of such a surface is less sensitive to the change in element length unlike a typical FSS. This can be viewed as follows: the behaviour of a typical FSS requires the elements to be resonant at the frequency of operation in order to engineer the desired response from such a surface and the resonance of these elements is closely related to their length. For a dipole-slot metasurface, it is the coupling which is the main perpetrator in determining the resonance therefore the

change in the elements length should alter the coupling and lead to a change in the resonant frequency; however this change will not be as significant as it should be for a typical FSS. A typical FSS resonates when the elements are of order λ/2 therefore increasing or decreasing the length (of an element) by a factor 2 leads to the similar change in the resonant frequency. However for a dipole slot metasurface this should not be the case. Figure 4-18 shows the effect of the length of the dipoles on the resonance of a dipole slot-slot metasurface. The dielectric in between was 0.05mm thick and had a relative permittivity of 3. The periodicity of the structure was 4.5mm.

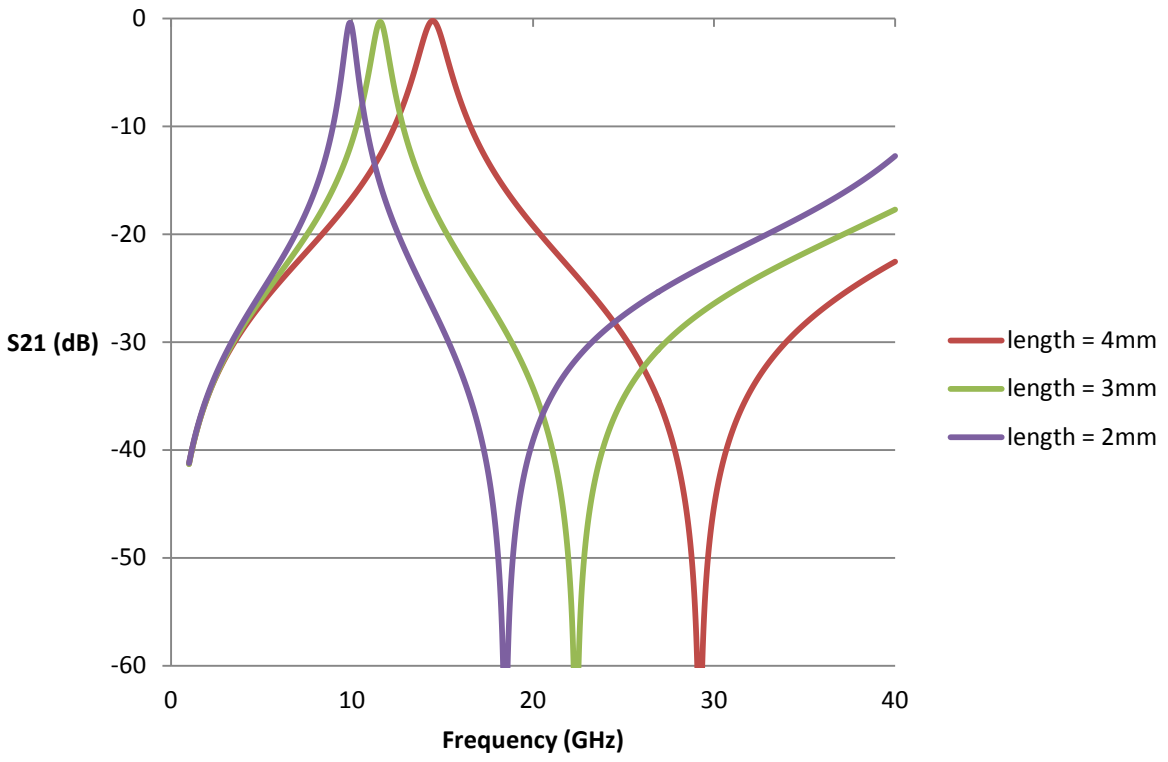

Figure 4-18: *Simulated effect of the length of the dipoles on the dipole-slot metasurface*

As the length of the dipoles was varied from 4mm to 3mm and 2mm; the resonance of the structure shifted from 9.9 to 11.6 and 14.5 GHz respectively. The effect of changing the

lengths of the slots had also been reported. As the lengths of the slots was varied from 4 to 3, 2mm, the resonance of the structure moved from 9.9 to 11.1 and 12.6 GHz respectively. These results are shown in Figure 4-19. Since the dipoles add capacitance to the slot and are the major reason for the inter-layer coupling therefore the variations in the lengths of the dipoles has a greater effect on the resonant frequency of the dipole-slot metasurface. It should be noted that even though the length of the dipoles and slots have been halved, the frequency of the structure has not been doubled.

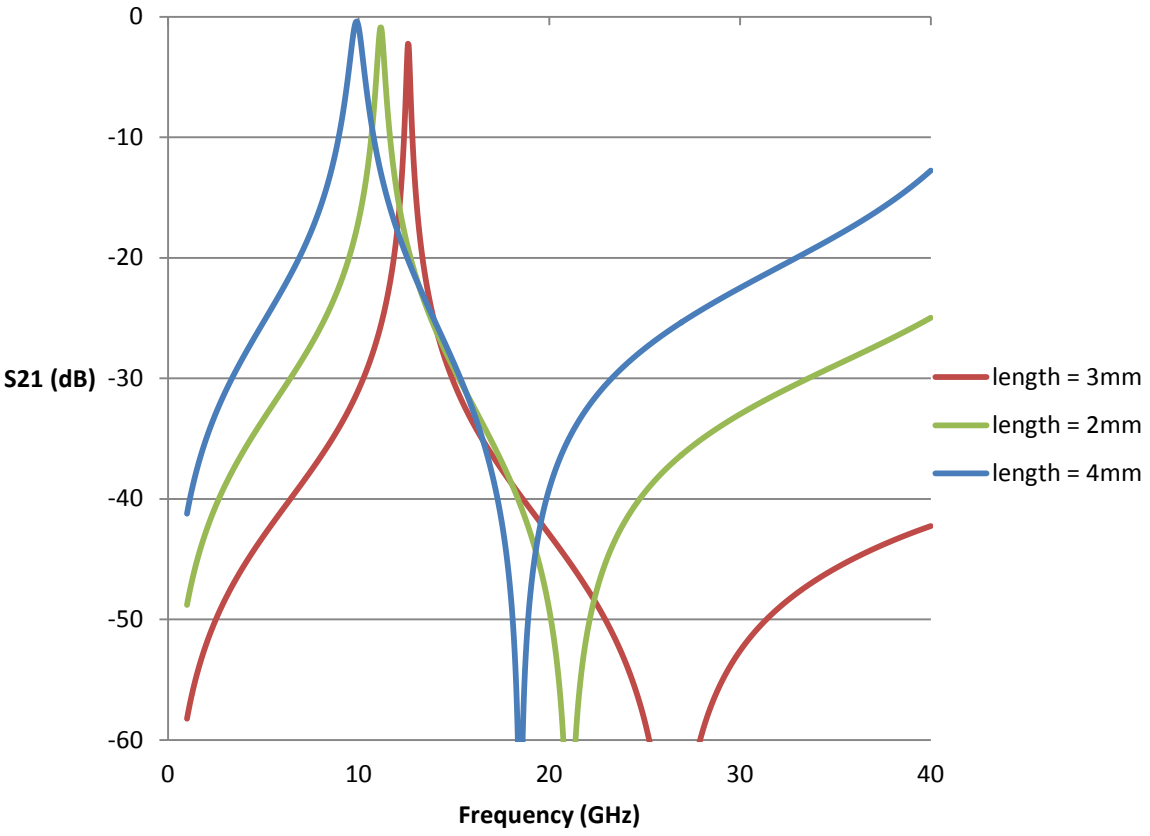

Figure 4-19: *Effect of the change in the slot length on the dipole-slot metasurface resonance (Simulated)*

The effect of shifting of the dipoles and the slots with respect to each other has also been studied. The movement of these elements has been illustrated in Figure 4-20. The effect of

these movements on the dipole-slot resonance has been shown in Figure 4-21 and Figure 4-22. As the dipoles were moved away from the centre, the resonant frequency moved away from 9.9 GHz (when the dipoles were at the centre) to 10.2, 11.1 and 13.2 GHz (when the distance of the dipoles from the centre was 1mm, 2mm and 3mm respectively. Similarly as the slot were moved away from the centre at these aforementioned distances, the simulated resonant frequency was observed to be 10.4, 11.5 and 15.4 GHz respectively.

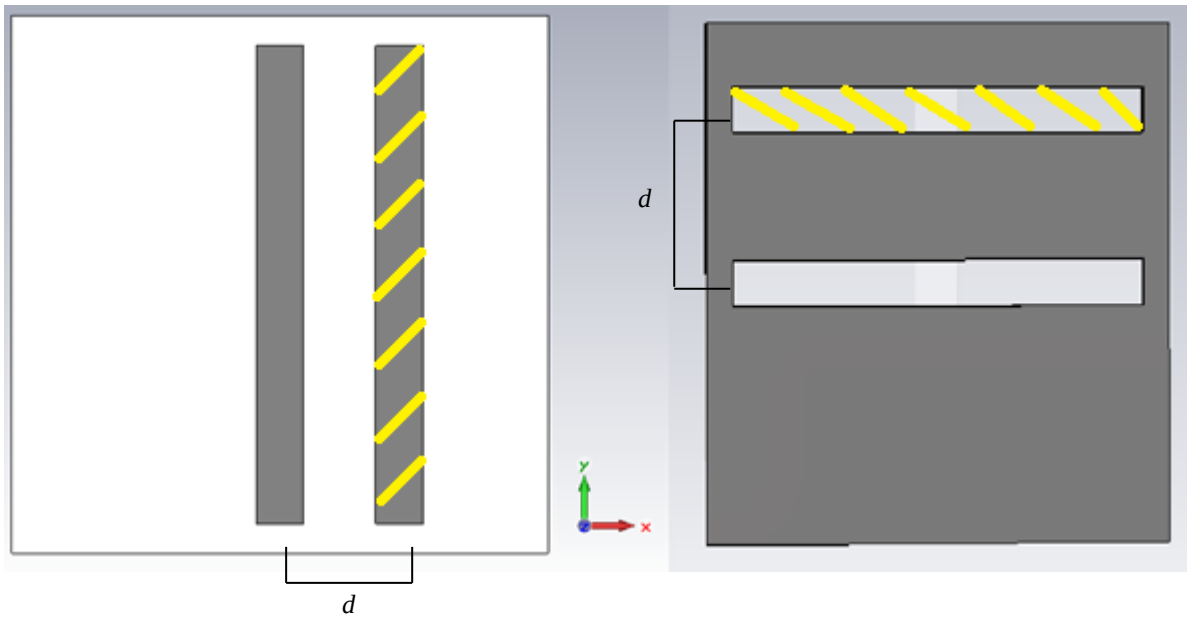

Figure 4-20: (a) *Movement of the dipole away from centre;* **(b)** *movement of the slot away from the centre – d measures the distance from the centre – (the hatched portion indicates the position after movement)*

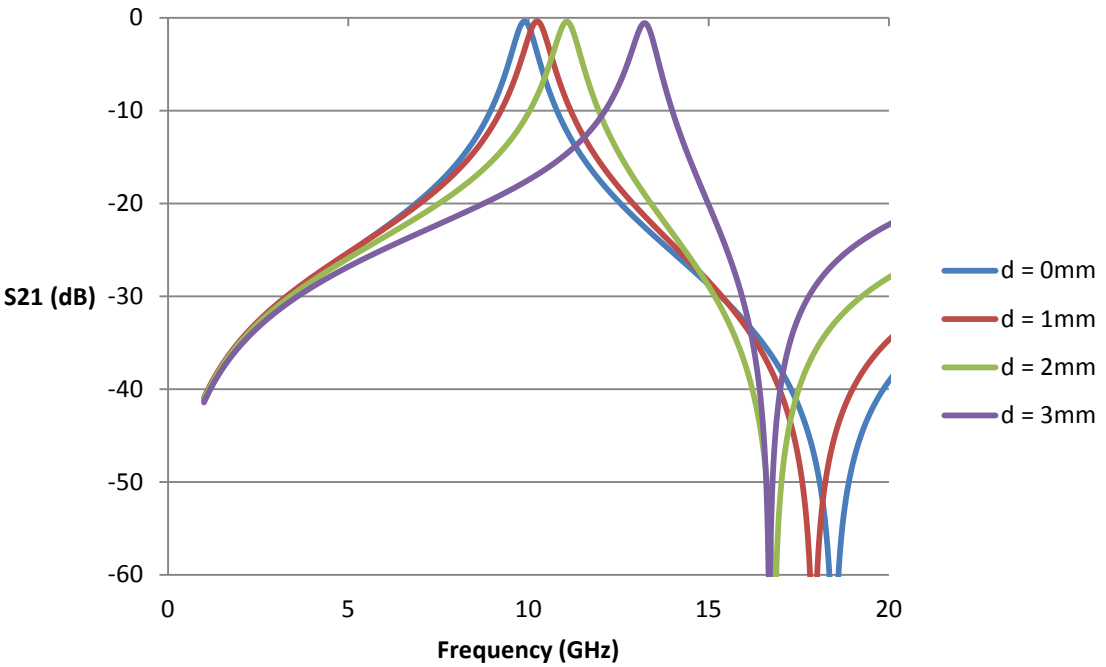

Figure 4-21: *Simulated effects of the movement of the dipole (as shown in Figure 4-20(a)) on the dipole-slot metasurface (d is the distance of the centre of the dipole from the centre)*

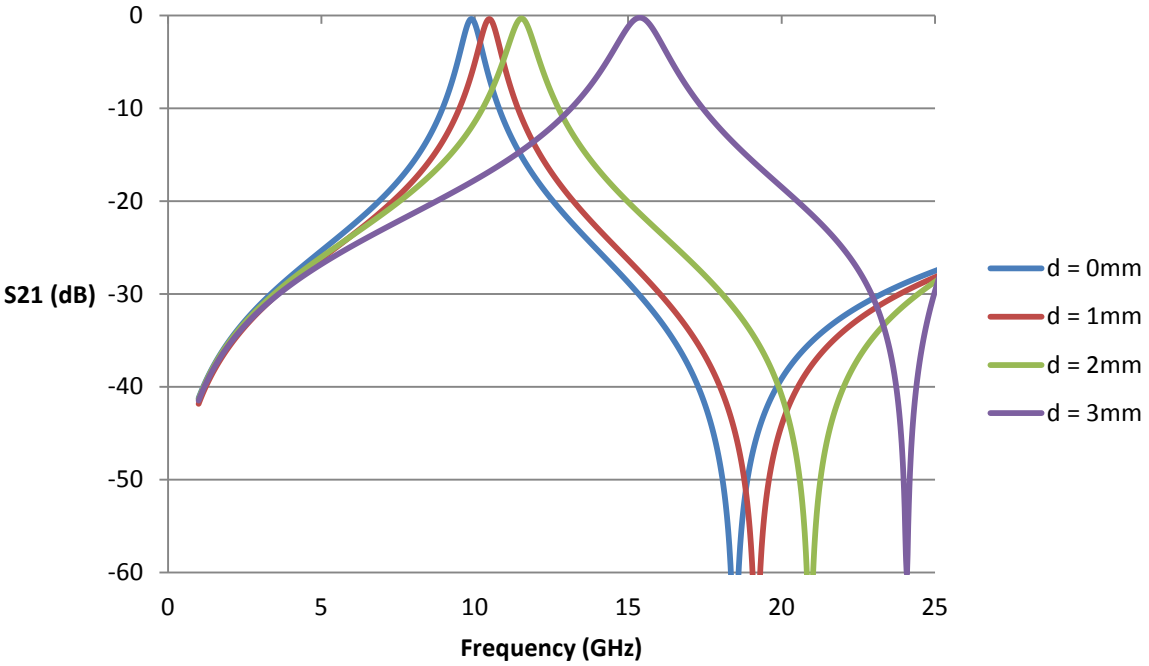

Figure 4-22: *Simulated effects of the movement of the slot (as shown in Figure 4-20(a)) on the dipole-slot metasurface (d is the distance of the centre of the dipole from the centre)*

When both the dipole and the slots were at the centre, the coupling among the layers is maximal. The maximal electric fields of the slots overlap the minima of the electric fields of

the dipole. When the dipole is moved away from the centre, the minimal electric fields of the dipoles no longer overlap the maximal electric fields of the slot. Similar effects were seen when the slot is moved along the y-axis, away from the centre. The maximal electric fields of the slots no longer overlap the minimal electric fields from the dipoles thus the resonant frequency of the structure is increased.

4.3 Equivalent Circuit Modelling of a Dipole-Slot Metasurface

A qualitative equivalent circuit model has been developed to explain the behaviour of a dipole-slot metasurface. This model is shown in Figure 4-23. The slot layer (being a pass band structure) is represented by a parallel LC circuit, while the dipole layer (which is a stop band structure) is represented by a series LC circuit. $C_{dipole,}$ L_{dipole}, C_{slot} and L_{slot} are their respective capacitance and inductance values. The coupling between the two layers is represented by a shunt capacitance C_1. It is the presence of this capacitance which causes a decrease in the resonant frequency of the individual dipole-slot structure, in comparison with the resonant frequency of a single layer of either the dipoles or the slots. Because the resulting response of the dipole-slot metasurface is that of a band pass (spatial filter), therefore the low-frequency dominant part of the dipoles circuit (capacitance) can be used to represent the couplings between the layers. The values of C_{dipole} can be calculated from the relations given in [79], [84], [85], see Equation 4.8.

$$C_{dipole} = \frac{2\varepsilon_0 p}{\pi} ln\left(\frac{1}{\sin\frac{\pi p}{2d}}\right) \tag{4.8}$$

Where C_{dipole} is the capacitance for the layer of dipoles in isolation in free space, ε_0 is the permittivity of free space, p is the periodicity of the structure and d is the distance between two dipoles. Since the thickness of the dielectric between the elements is extremely small therefore it can be accounted for in the additional equivalent circuit element C1.

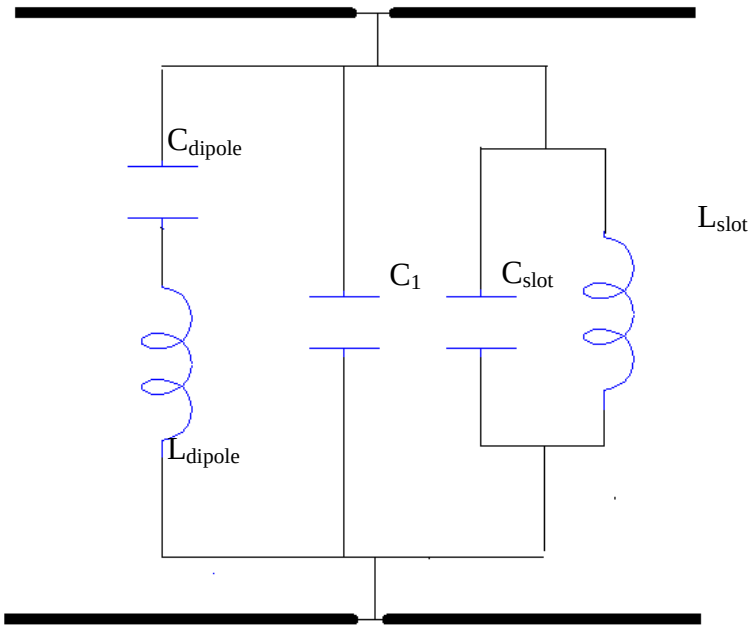

Figure 4-23: *Equivalent Circuit Model of a dipole-slot Metasurface*

The value for the inductance of the slot can then be ascertained by using the Babinet's principles, as shown in Equation 4.9 [79],

$$\sqrt{\frac{L_{slot}}{C_{dipole}}} = \frac{Z_0}{2} \tag{4.9}$$

with L_{slot} being the inductance of the layer of the slots in free space and Z_0 is the free space impedance. The effect of the dielectric is negligible on the inductance [54], [79]. The sub-dominant components of the circuit, namely C_{dipole} and L_{slot} can be estimated by adding the resonance condition $\sqrt{C_{dipole}L_{dipole}} = 1/\omega_0$, where ω_0 is the angular frequency at which a

single layer of dipoles or slots resonates in free space, occurring when the length of the individual element is approximately half the wavelength. The value of C_1 plays a fundamental role in coupling and it is responsible for down-shifting the resonant frequency. Its value can be determined by numerical matching of the obtained final resonance. As a reference, the value of this capacitance can be obtained from equation 4.8; including the effect of the dielectric $C_{ref} = \frac{\varepsilon_0(\varepsilon_r+1)p}{\pi} ln\left(\frac{1}{\sin\frac{\pi p}{2d}}\right)$ where ε_r is the relative permittivity of the dielectric. This capacitance can then be written as, $C_1 = n^2 C_{ref}$, where n can be interpreted as a winding ratio of a transformer that reports capacitance at the slot level.

The equivalent circuit response qualitatively predicts the one of the full wave analysis with a value of C_1 = 0.3pF, which corresponds to $n \sim 2$; showing that the dipole capacitance has been quadrupled. This increase of capacitance is due to the strong concentration of electric fields around the zone of the slot-dipole crossing, which considerably increases the voltage across the slot (and then the winding ratio n) with respect to the voltage in isolation. The circuit has been simulated in AWR Microwave office [86]. The values for the individual elements of the circuit are: C_{slot}= 0.0193pF, L_{slot}= 1.17nH, C_{dipole}= 0.033pF, L_{dipole} = 0.688nH. This model predicts the resonance of the dipole-slot metasurface to be 7.6 GHz, which is very close to the simulated (7.4 GHz) and measured value (7.5 GHz). An analytical equivalent circuit model of a dipole-slot metasurface derived using the electric and magnetic field integral equations will be presented in Chapter 6.

4.4 Measured Results of a Dipole-Slot Metasurface

A dipole-slot metasurface was fabricated by using a 0.044mm thick GTS material. The individual length of the dipoles and slots is 4.5mm. Both are 0.5mm wide and the unit cell has a periodicity of $5 \times 5mm^2$. A $26 \times 26cm^2$ sample was used to measure the transmission response of the dipole-slot metasurface by placing the sample in a radar absorbing material, having a $25 \times 25cm^2$ aperture. The measurement setup is explained in detail in chapter 5. The sample has been shown in Figure 4-24. The comparison between the CST simulations and measured results is shown in Figure 4-25. A very good agreement between the measured and simulated values is shown.

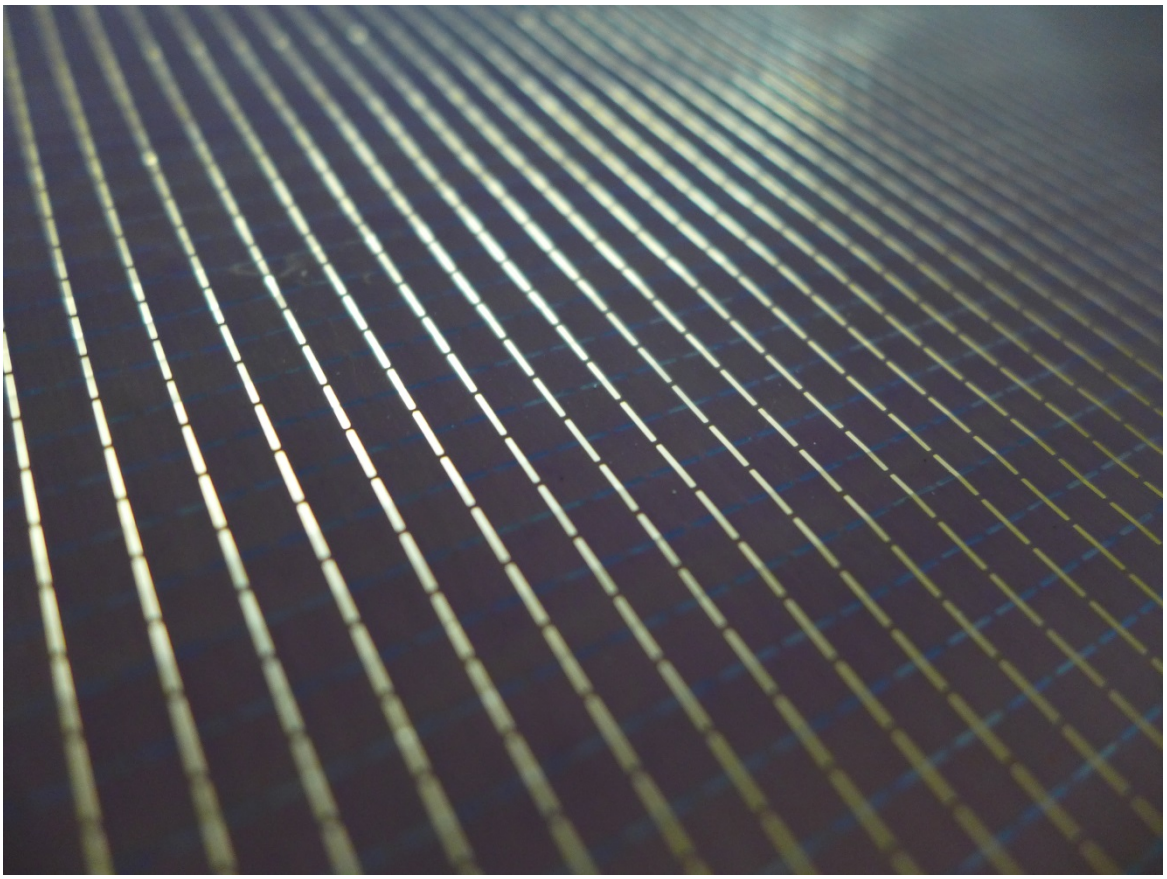

Figure 4-24: *Fabricated sample of a dipole-slot metasurface on the GTS material*

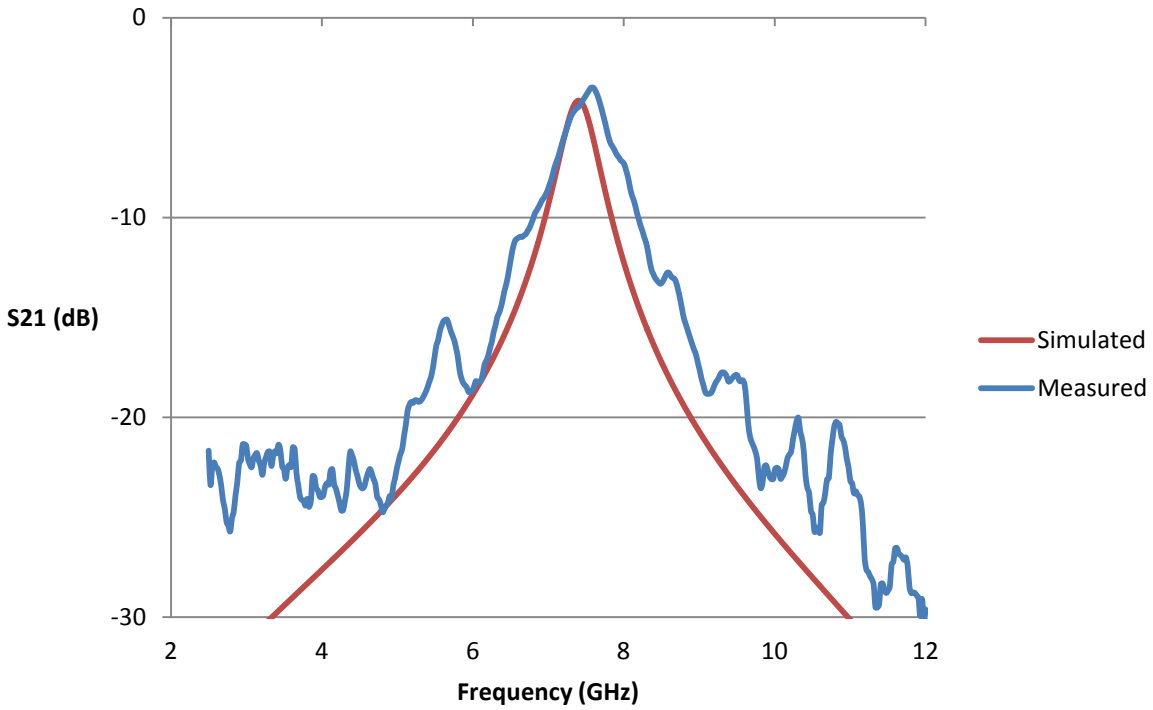

Figure 4-25: *Comparison between the measured and simulated results of a dipole-slot metasurface*

The resonant frequency of the dipole-slot metasurface is very stable to the changes in the angle of incidence. The two major reasons for this stability are: (i) the inter-layer coupling among the two complementary elements plays a major role in determining the resonant frequency of this structure (ii) the unit cell of the dipole-slot metasurface is much smaller in comparison to the wavelength.

4.5 Conclusions

A dipole-slot metasurface, designed on the basis of Babinet's principle, constitutes an array of dipoles and an array of slots separated by a very thin dielectric. The coupling between these two arrays makes the individual unit cell sub-wavelength and is the reason of shrinking its size to ~$\lambda/7$. Simulation experiments using anisotropic dielectric elements clearly showed

that the major phenomenon responsible for this coupling is the capacitance added to the slots array by the close proximity of the dipoles. This resonance can be further lowered by increasing the relative permittivity or decreasing the thickness of the dielectric since that will increase the capacitance offered by the dipoles layer. A dipole-slot metasurface with a unit cell size of 4.5mm and the individual dipole and slots length of 4mm exhibited a band pass resonance at 9.9 GHz. Since the coupling among these two layers is very strong and occurs through the dielectric, the properties of the dielectric govern the transmission losses offered by a dipole-slot metasurface. It has been shown that as the loss tangent of the dielectric increased from 0 (loss-less) to 0.01, the transmission loss also increased to 1.1 dB. The effect of changing the length of each individual element was also reported. It was demonstrated that decreasing the lengths of the individual elements led to a decrease in the resonance of the dipole-slot metasurface. However this change was considerably reduced in comparison with a typical FSS, indicating that it is indeed the inter layer coupling between the layers which is responsible for the peculiar behaviour of the dipole-slot metasurface. It has also been shown that the coupling between the layers is maximal when the two Babinet's complement centres align as the shifting of the layers with respect to each other led to an increase in the resonant frequency of the dipole-slot metasurface. The behaviour of the dipole-slot metasurface was explained with the help of a qualitative equivalent circuit. A series LC circuit branch represented the dipole layer while the parallel LC circuit branch was used to represent the slot layer. The interlayer coupling, which is responsible for decreasing the resonance of the dipole-slot metasurface, was represented by a shunt capacitance in the equivalent circuit model. A comparison between the simulated and measured response of the dipole-slot metasurface has also been presented. This chapter has shown good agreement between two software packages (CST and EMPIRE) and measurements.

References

[1] C. L. Holloway, E. F. Kuester, J. A. Gordon, J. O'Hara, J. Booth, and D. R. Smith, "An overview of the theory and applications of metasurfaces: The two-dimensional equivalents of metamaterials," *IEEE Antennas Propag. Mag.*, vol. 54, no. 2, pp. 10–35, 2012.

[2] J. B. Pendry, "Metamaterials and the Control of Electromagnetic Fields," *OSA Tech. Dig. Conf. Coherence Quantum Opt., 2007 [Online]*. *Available CD-ROM, Pap. C.*, pp. 1–11.

[3] C. Caloz, H. Okabe, T. Iwai, and T. Itoh, "Transmission line approach of left-handed materials," in *IEEE AP-S International Symposium and USNC/URSINational Radio Science Meeting, San Antonio, TX, abstract, URSI Digest*, 2002, p. 39.

[4] I. V. Lindell, S. A. Tretyakov, K. I. Nikoskinen, and S. Ilvonen, "BW media—Media with negative parameters, capable of supporting backward waves," *Microw. Opt. Tech. Lett.*, vol. 31, no. 2, pp. 129–133, 2001.

[5] E. Heyman and R. W. Ziolkowski, "Wave propagation in media having negative permittivity and permeability," *Phys. Rev. E*, vol. 34, no. 5, 2001.

[6] T. Lorentz, "Lorentz Dispersion Model," 1878, (Technical Note) Spectroscopic Ellipsometry. http://www.horiba.com/fileadmin/uploads/Scientific/Downloads/OpticalSchool_CN/TN/ellipsometer/Lorentz_Dispersion_Model.pdf.

[7] N. Engheta and R. Ziolkowski, *Metamaterials: Physics and Engineering explaorations*. Wiley-IEEE Press, 2006.

[8] N. Engheta, "*Ideas for potential applications of metamaterials with negative*

permittivity and permeability," Advances in Electromagnetics of Complex Media and Metamaterials. 2002.

[9] N. Engheta, "An Idea for Thin Subwavelength Cavity Resonators Using Metamaterials With Negative Permittivity and Permeability," *IEEE Antennas Wirel. Propag. Lett.*, vol. 1, pp. 10–13, 2002.

[10] N. Engheta and R. W. Ziolkowski, "A Positive Future for Double-Negative Metamaterials," *IEEE Trans. Microw. Theory Tech.*, vol. 53, no. 4, pp. 1535–1556, 2005.

[11] A. Alù and N. Engheta, "Guided Modes in a Waveguide Filled With a Pair of SNG, DNG and/or DPS Layers," *IEEE Trans. Microw. Theory Tech.*, vol. 52, no. 1, pp. 199–210, 2004.

[12] J. B. Pendry, "Negative Refraction Makes a Perfect Lens," *Phys. Rev. Lett.*, vol. 85, no. 18, pp. 3966–3969, 2000.

[13] V. G. Veselago, "The Electrodynamics of Substances with Simultaneously Negative Values of And μ," *Sov. Phys. Upsekhi*, vol. 10, no. 4, pp. 517–526, 1968.

[14] E. F. Kuester, M. A. Mohamed, M. Piket-may, and C. L. Holloway, "Averaged Transition Conditions for Electromagnetic Fields at a Metafilm," *IEEE Trans. Antennas Propag.*, vol. 51, no. 10, pp. 2641–2651, 2003.

[15] W. Cai and V. M. Shalaev, *Optical metamaterials : Fundamentals and Applications*. Springer, 2009.

[16] N. Yu and F. Capasso, "Flat optics with designer metasurfaces," *Nat. Mater.*, vol. 13, no. January, pp. 139 – 150, 2014.

[17] G. Yoon, I. Kim, and J. Rho, "Microelectronic engineering challenges in fabrication

towards realization of practical metamaterials," *Microelectron. Eng.*, vol. 163, pp. 7–20, 2016.

[18] C. M. Soukoulis and M. Wegener, "Past achievements and future challenges in the development of three-dimensional photonic metamaterials," *Nat. Photonics*, no. July, pp. 1–8, 2011.

[19] N. Meinzer, W. L. Barnes, and I. R. Hooper, "Plasmonic Meta-atoms and Metasurfaces," *Nat. Photonics*, vol. 8, pp. 1–22, 2014.

[20] "Planar Photonics with Metasurfaces," *http://www.nanometatech.com/Nano-Meta-Technologies*. .

[21] Z. H. Jiang, S. Yun, L. Lin, J. A. Bossard, D. H. Werner, and T. S. Mayer, "Tailoring Dispersion for Broadband Deep-subwavelength Inclusions," *Sci. Rep.*, vol. 3, p. 1571, 2013.

[22] S. B. Glybovski, S. A. Tretyakov, P. A. Belov, Y. S. Kivshar, and C. R. Simovski, "Metasurfaces : From microwaves to visible," *Phys. Rep.*, vol. 634, pp. 1–72, 2016.

[23] C. Huygens, *Traite´ de la Lumie`re (A treatise on light), Leyden*. 1690.

[24] S. R. Rengarajan and Y. Rahmat-Samii, "The Field Equivalence Principle: Illustration of the Establishment of the Non-Intuitive Null Fields," *Antennas Propag. Mag.*, vol. 42, no. 4, 2000.

[25] C. Pfeiffer and A. Grbic, "Metamaterial Huygens ' Surfaces: Tailoring Wave Fronts with Reflectionless Sheets," *Phys. Rev. Lett.*, vol. 197401, no. May, pp. 1–5, 2013.

[26] F. Monticone, N. M. Estakhri, and A. Alu, "Full Control of Nanoscale Optical Transmission with a Composite Metascreen," *Phys. Rev. Lett.*, vol. 203903, no. May, pp. 1–5, 2013.

[27] M. A. Kats, D. Sharma, J. Lin, P. Genevet, R. Blanchard, Z. Yang, M. Mumtaz, D. N. Basov, S. Ramanathan, F. Capasso, M. A. Kats, D. Sharma, J. Lin, P. Genevet, R. Blanchard, Z. Yang, M. M. Qazilbash, D. N. Basov, and S. Ramanathan, "Ultra-thin perfect absorber employing a tunable phase change material," *Appl. Phys. Lett.*, vol. 221101, no. 2012, 2014.

[28] M. A. Kats, R. Blanchard, P. Genevet, and F. Capasso, "Nanometre optical coatings based on strong interference effects in highly absorbing media," *Nat. Mater.*, vol. 12, no. 1, pp. 20–24, 2012.

[29] S. Cornbleet, "Geometrical Optics Reviewed:," *Proc. IEEE*, vol. 71, no. 4, 1983.

[30] J. W. Cathey, "Three-Dimensional Wavefront Reconstruction Using a Phase Hologram," *J. Opt. Soc. Am.*, vol. 1295, no. April, p. 457, 1965.

[31] Y. Zhang, L. Liang, Y. Jing, Y. Feng, B. Zhu, Z. Junming, and T. Jiang, "Broadband diffuse terahertz wave scattering by flexible metasurface with randomized phase distribution," *Sci. Rep.*, no. February, pp. 1–8, 2016.

[32] F. Capasso and Z. Gaburro, "Light Propagation with Phase Discontinuities: Generalized Laws of Reflection and Refraction," *Science (80-.).*, vol. 334, pp. 333–337, 2011.

[33] R. Feynman, R. Leighton, and M. Sands, *The Feynman Lectrures on Physics I*. 1963.

[34] X. Ni, N. K. Emani, A. V Kildishev, A. Boltasseva, and V. M. Shalaev, "Broadband Light Bending with Plasmonic Nanoantennas," *Science 80*, vol. 335, p. 427, 2012.

[35] N. Yu, F. Aieta, P. Genevet, M. A. Kats, and Z. Gaburro, "A Broadband, Background-Free Quarter-Wave Plate Based on Plasmonic Metasurfaces," *N*, vol. 12, pp. 6328–6333, 2012.

[36] D. T. Mcgrath, “Planar Three-Dimensional Constrained Lenses,” *IEEE Trans. Antennas Propag.*, vol. 34, no. 1, pp. 46–50, 1986.

[37] D. M. Pozar, S. D. Targonski, and H. D. Syrigos, “Design of Millimeter Wave Microstrip Reflectarrays,” *IEEE Trans. Antennas Propag.*, vol. 45, no. 2, pp. 287–296, 1997.

[38] J. H. A. Yu, F. Yang, A. Elsherbini, “Experimental Demonstration of a Single Layer Tri-band Circularly Polarized Reflectarray,” in *Antennas and Propagation Society International Symposium, APSURSI*, 2010, no. 1, pp. 1–4.

[39] D. M. Pozar, “Flat lens antenna concept using aperture coupled microstrip patches,” *Electrnoics Lett.*, vol. 32, no. 23, pp. 2109–2110, 1996.

[40] D. M. Pozar, “Wideband reflectarrays using artificial impedance surfaces,” *Electrnoics Lett.*, vol. 43, no. 3, pp. 2–3, 2007.

[41] T. Niemi, A. O. Karilainen, and S. A. Tretyakov, “Synthesis of Polarization Transformers,” *IEEE Trans. Antennas Propag.*, vol. 61, no. 6, pp. 3102–3111, 2013.

[42] J. Ginn, B. Lail, J. Alda, and G. Boreman, “Planar infrared binary phase reflectarray,” *Opt. Lett.*, vol. 33, no. 8, pp. 779–781, 2008.

[43] M. Farmahini-Farahani and H. Mosallaei, “Birefringent reflectarray metasurface for beam engineering in infrared,” *Opt. Lett.*, vol. 38, no. 4, pp. 462–464, 2013.

[44] T. Niu, W. Withayachumnankul, A. Upadhyay, P. Gutruf, D. Abbott, M. Bhaskaran, S. Sriram, and C. Fumeaux, “Terahertz reflectarray as a polarizing beam splitter,” *Opt. Express*, vol. 22, no. 13, pp. 1702–1706, 2014.

[45] Z. Gaburro and F. Capasso, “Aberration-Free Ultrathin Flat Lenses and Axicons at Telecom Wavelengths Based on Plasmonic Metasurfaces,” *Nano Lett.*, 2012.

[46] A. Pors, M. G. Nielsen, R. L. Eriksen, and S. I. Bozhevolnyi, “Broadband Focusing Flat Mirrors Based on Plasmonic Gradient Metasurfaces,” *Nano Lett.*, pp. 829–834, 2013.

[47] F. Aieta and M. A. Kats, “Multiwavelength achromatic metasurfaces by dispersive phase compensation,” *Appl. Opt.*, vol. 347, no. 6228, pp. 1342–1346, 2015.

[48] M. Lapine, I. V Shadrivov, and Y. S. Kivshar, “Colloquium: Nonlinear metamaterials,” *Rev. Mod. Phys.*, vol. 86, no. September, pp. 1093–1123, 2014.

[49] Z. Wang, J. Chen, Z. Wu, and Y. Zhu, “Wave propagation in two-dimensional left-handed non-linear transmission line metamaterials,” *IET Microwaves, Antennas Propag.*, vol. 10, pp. 202–207, 2016.

[50] E. Kim, F. Wang, W. Wu, Z. Yu, and Y. R. Shen, “Nonlinear optical spectroscopy of photonic metamaterials,” *Phys. Rev. B*, pp. 2–5, 2008.

[51] Y. C. Vardaxoglou, *Frequency Selective Surfaces: Analysis and Design*. John Wiley & Sons, 1997.

[52] S. Lee, “Scattering by Dielectric-Loaded Screen,” *IEEE Trans. Antennas Propag.*, vol. AP-19, no. 5, pp. 656–665, 1971.

[53] C. Chiu and K. Chang, “A Novel Miniaturized-Element Frequency Selective Surface Having a Stable Resonance,” *IEEE Antennas Wirel. Propag. Lett.*, vol. 8, pp. 1175–1177, 2009.

[54] K. Sarabandi and N. Behdad, “A frequency selective surface with miniaturized elements,” *IEEE Trans. Antennas Propag.*, vol. 55, no. 5, pp. 1239–1245, 2007.

[55] R. Xu, Z. Zong, and W. Wu, “Low-Frequency Miniaturized Dual-band Frequency Selective Surfaces With Close Band Spacing,” *Microw. Opt. Tech. Lett.*, vol. 51, no. 5,

pp. 1238–1240, 2009.

[56] F. Bayatpur and K. Sarabandi, “A Tunable Metamaterial Frequency-Selective Surface With Variable Modes of Operation,” *IEEE Trans. Microw. Theory Tech.*, vol. 57, no. 6, pp. 1433–1438, 2009.

[57] B. Sanz-izquierdo, E. A. T. Parker, J. Robertson, and J. C. Batchelor, “Singly and Dual Polarized Convoluted Frequency Selective Structures,” *IEEE Trans. Antennas Propag.*, vol. 58, no. 3, pp. 690–696, 2010.

[58] J. B. Pendry, A. J. Holden, D. J. Robbins, and W. J. Stewart, “Magnetism from Conductors and Enhanced Nonlinear Phenomena,” *IEEE Trans. Microw. Theory Tech.*, vol. 47, no. 11, pp. 2075–2084, 1999.

[59] F. Falcone, T. Lopetegi, M. A. G. Laso, J. D. Baena, J. Bonache, M. Beruete, F. Martin, and M. Sorolla, “Babinet Principle Applied to the Design of Metasurfaces and Metamaterials,” *Phys. Rev. Lett.*, vol. 2, no. November, pp. 2–5, 2004.

[60] Y. Ra, V. S. Asadchy, and S. A. Tretyakov, “One-way transparent sheets,” *Phys. Rev. B*, vol. 075109, no. October 2013, pp. 1–7, 2014.

[61] B. Sanz-Izquierdo, E. A. Parker, and J. C. Batchelor, “Dual-Band Tunable Screen Using Complementary Split Ring Resonators,” *IEEE Trans. Antennas Propag.*, vol. 58, no. 11, pp. 3761–3765, 2010.

[62] J. P. Turpin, J. A. Bossard, K. L. Morgan, D. H. Werner, and P. L. Werner, “Reconfigurable and Tunable Metamaterials : A Review of the Theory and Applications,” *Int. J. Antennas Propag.*, 2014.

[63] L. Li, J. Wang, J. Wang, H. Ma, H. Du, J. Zhang, and S. Qu, “Reconfigurable all-dielectric metamaterial frequency selective surface based on high-permittivity ceramics,” *Sci. Rep.*, 2016.

[64] T. Debogovi, J. Bartolic, and J. Perruisseau-Carrier, “Dual-Polarized Partially Reflective Surface Antenna With MEMS-Based Beamwidth Reconfiguratio,” *IEEE Trans. Antennas Propag.*, vol. 62, no. 1, pp. 228–236, 2014.

[65] D. Sievenpiper, J. Schaffner, R. Loo, G. Tangonan, S. Ontiveros, and R. Harold, “A Tunable Impedance Surface Performing as a Reconfigurable Beam Steering Reflector,” *IEEE Trans. Antennas Propag.*, vol. 50, no. 3, pp. 384–390, 2002.

[66] A. E. Bakanowski, N. G. Cranna., and J. A. Uhlir, “Diffused Silicon Nonlinear Capacitors,” *IRE Trans. Electron Devices*, vol. 17, pp. 384–390, 1958.

[67] D. F. Sievenpiper, J. H. Schaffner, H. J. Song, R. Y. Loo, and G. Tangonan, “Two-Dimensional Beam Steering Using an Electrically Tunable Impedance Surface,” *IEEE Trans. Antennas Propag.*, vol. 51, no. 10, pp. 2713–2722, 2003.

[68] F. Bayatpur and K. Sarabandi, “Design and Analysis of a Tunable Miniaturized-Element Frequency-Selective SurfaceWithout Bias Network,” *IEEE Trans. Antennas Propag.*, vol. 58, no. 4, pp. 1214–1219, 2010.

[69] H. Chen, W. J. Padilla, J. M. O. Zide, A. C. Gossard, A. J. Taylor, and R. D. Averitt, “Active terahertz metamaterial devices,” *Nature*, vol. 444 (7119), pp. 597–600, 2006.

[70] Q. Wu, C. P. Scarborough, D. H. Werner, E. Lier, and X. Wang, “Design synthesis of metasurfaces for broadband hybrid-mode horn antennas with enhanced radiation pattern and polarization characteristics,” *IEEE Trans. Antennas Propag.*, vol. 60, no. 8, pp. 3594–3604, 2012.

[71] Q. Wu, C. P. Scarborough, B. G. Martin, R. K. Shaw, D. H. Werner, E. Lier, and X. Wang, “A Ku-band dual polarization hybrid-mode horn antenna enabled by printed-circuit-board metasurfaces,” *IEEE Trans. Antennas Propag.*, vol. 61, no. 3, pp. 1089–1098, 2013.

[72] Z. H. Jiang, D. E. Brocker, P. E. Sieber, and D. H. Werner, “A Compact , Low-Profile Metasurface-Enabled Network Devices,” *IEEE Trans. Antennas Propag.*, vol. 62, no. 8, pp. 4021–4030, 2014.

[73] C. Huang, W. Pan, X. Ma, and X. Luo, “Wideband Radar Cross-Section Reduction of a Stacked Patch Array Antenna Using Metasurface,” *IEEE Antennas Wirel. Propag. Lett.*, vol. 14, no. c, pp. 1369–1372, 2015.

[74] G. Minatti, F. Caminita, M. Casaletti, and S. Maci, “Spiral leaky-wave antennas based on modulated surface impedance,” *IEEE Trans. Antennas Propag.*, vol. 59, no. 12, pp. 4436–4444, 2011.

[75] D. J. Gregoire, “3-D Conformal Metasurfaces,” *IEEE Antennas Wirel. Propag. Lett.*, vol. 12, pp. 233–236, 2013.

[76] K. Konstantinidis, A. P. Feresidis, and P. S. Hall, “Broadband Sub-Wavelength Profile High-Gain Antennas Based on Multi-Layer Metasurfaces,” *IEEE Trans. Antennas Propag.*, vol. 63, no. 1, pp. 423–427, 2015.

[77] H. G. Booker, “Slot Aerials and Their Relation to Complementary Wire Aerials (Babinet’s Principle),” *J. Inst. Electr. Eng. - Part IIIA Radiolocation*, vol. 93, no. 4, pp. 620–626, 1946.

[78] D. S. Lockyer, J. C. Vardaxoglou, and R. A. Simpkin, “Complementary frequency selective surfaces,” *IEE Proc -Microw Antennas Propag* , vol. 147, no. 6, pp. 501–5–7, 2000.

[79] D. González-ovejero, E. Martini, and S. Maci, “Surface Waves Supported by Metasurfaces With Self-Complementary Geometries,” *IEEE Trans. Antennas Propag.*, vol. 63, no. 1, pp. 250–260, 2015.

[80] J. D. Ortiz, J. D. Baena, V. Losada, F. Medina, R. Marques, and J. L. A. Quijano,

"Self-Complementary Metasurface for Designing Narrow Band Pass/Stop Filters," *IEEE Microw. Wirel. Components Lett.*, vol. 23, no. 6, pp. 291–293, 2013.

[81] D. Gonzalez-Ovejero, E. Martini, B. Loiseaux, C. Tripon-Canseliet, M. Mencagli, J. Chazelas, and S. Maci, "Basic Properties of Checkerboard Metasurfaces," *IEEE Antennas Wirel. Propag. Lett.*, vol. 14, pp. 406–409, 2015.

[82] "CST Microwave studio," *https://www.cst.com/products/cstmws*. .

[83] "EMPIRE," *http://www.empire.de/*. .

[84] D. Ramaccia, A. Toscano, and F. Bilotti, "A New Accurate Model Of High-Impedance Surfaces Consisting Of Circular Patches," *Prog. Electromagn. Res. M*, vol. 21, no. May, pp. 1–17, 2011.

[85] O. Luukkonen, C. Simovski, G. Granet, G. Goussetis, D. Lioubtchenko, A. V Räisänen, and S. A. Tretyakov, "Simple and Accurate Analytical Model of Planar Grids and High-Impedance Surfaces Comprising Metal Strips or Patches," *IEEE Trans. Antennas Propag.*, vol. 56, no. 6, pp. 1624–1632, 2008.

[86] "Microwave Office." http://www.awrcorp.com/products/ni-awr-design-environment/microwave-office.

Chapter 5 : Square Loops and Multi-layered Metasurfaces

Abstract

This chapter starts with the discussion on the structure and behaviour of complementary metasurfaces having rotationally symmetric Babinet's complements as the basic individual building blocks. Section 5.1 reports the behaviour of square loop complementary metasurfaces. It is shown that for manufacturing such metasurfaces, one layer has to be shifted by half the periodicity (along both axes) for maximal coupling and therefore miniaturization. The reasoning behind this behaviour is explained with the help of Babinet's principle. The measured results of the fabricated samples of square loop complementary metasurfaces and their comparison with the simulations is shown in Section 5.2. Section 5.3 presents a short review of multi-layered metasurfaces. The pass band resonance of a dipole-slot metasurface is decreased by adding an additional layer of dipoles. This dipole-slot-dipole metasurface is discussed in Section 5.4. An equivalent circuit model has been used to explain the behaviour of dipole-slot-dipole metasurfaces. The effect of the alignment of the dipole and the dipole-slot layer has been discussed in 5.4.1. Section 5.5 presents the measured

results of the dipole-slot-dipole metasurfaces. The conclusions drawn from this chapter are reported in Section 5.6. The novelties of this chapter are: (i) designing a square loop complementary metasurface which is an extremely compact ($\lambda/13.5$) structure and explaining the reason for shifting of the layers by half the periodicity in the light of Babinet's principle; (ii) designing multi-layered complementary metasurfaces by adding a separate dipole layer to a dipole-slot metasurface leading to miniaturization of the structure; and explaining the behaviour and the nature, of dipole-slot-dipole metasurface with a qualitative equivalent circuit model.

5.1 Square Loop Complementary Metasurfaces

The band-pass nature of a Babinet complementary dipole-slot metasurface has been explained in Chapter 4 with the help of a qualitative equivalent circuit model . However as shown in [1], the dipole and slot form a Babinet couple when they are rotated by 90 degrees with respect to each other. This section discusses a rotationally symmetric Babinet couple, the square loops. Due to their compact structure and simple fabrication, square loops, as a resonant element, have attracted a considerable amount of attention [2]–[6]. They have been used in FSSs for radar absorbers and switchable arrays [7]–[9]. Square loop antennas have also been proposed for ultra-wideband, beam steering and energy harvesting [10]–[13].

A square complementary structure has a periodic array of metallic square loops on one side of a very thin dielectric and a second array of aperture square loops on its other side. The individual unit cell is shown in Figure 5-1.

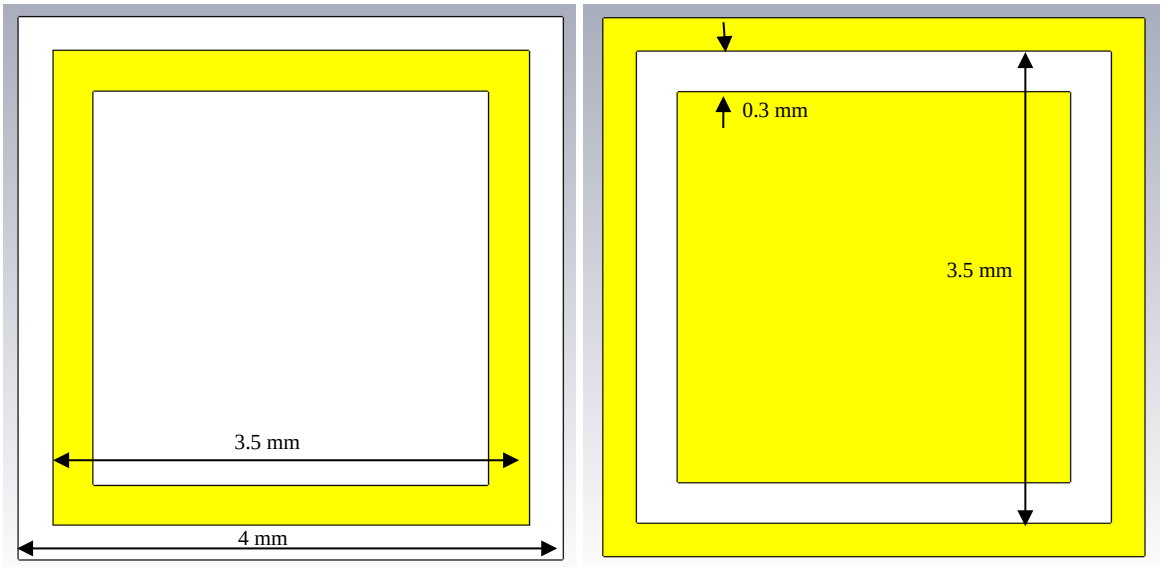

Figure 5-1: *The basic structure of complementary square loops – (yellow is metal) (a) metallic array; (b) apertures array*

Two distinct structures geometries are defined with same basic individual building blocks, as in Figure 5-1. For the first structure (aligned), the apertures array is placed directly behind the metallic array; the second structure (offset) has the apertures array shifted by half the periodicity of the unit cell, with respect to the metallic array (along both axes as shown in Figure 5-2). Both structures have a periodicity of 4mm. The dielectric used has the relative permittivity of 3 and a loss tangent value of 0.003. The thickness of the dielectric is 0.07mm. The length of the individual segment of the square loops is 3.5mm. Both structures were simulated using CST Microwave Studio and were illuminated by a TE polarised plane wave striking at the normal angle of incidence. The simulation results of both structures are shown in Figure 5-3.

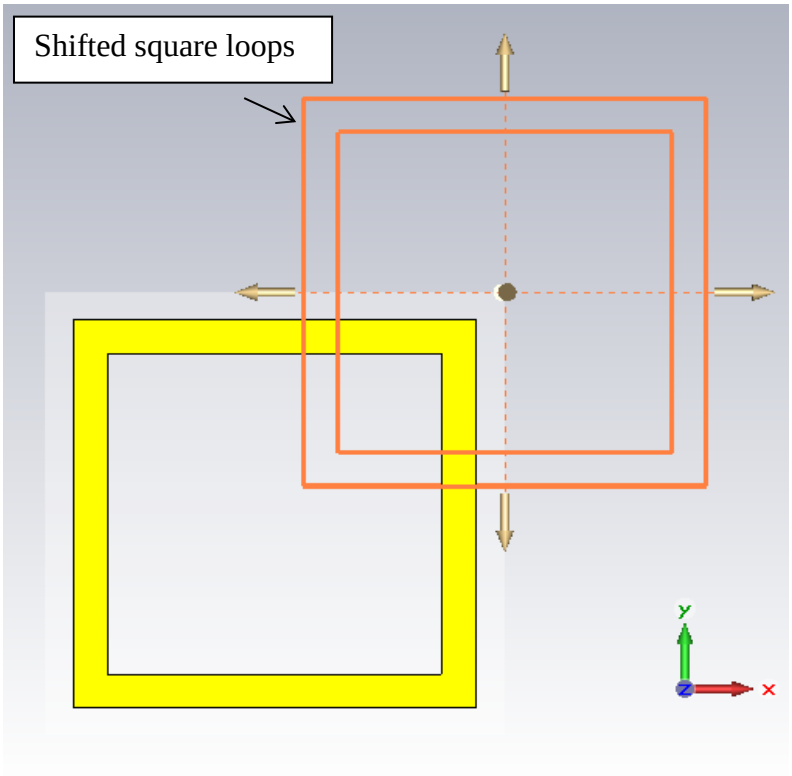

Figure 5-2: *The shifting of square loop along both x- and y-axes*

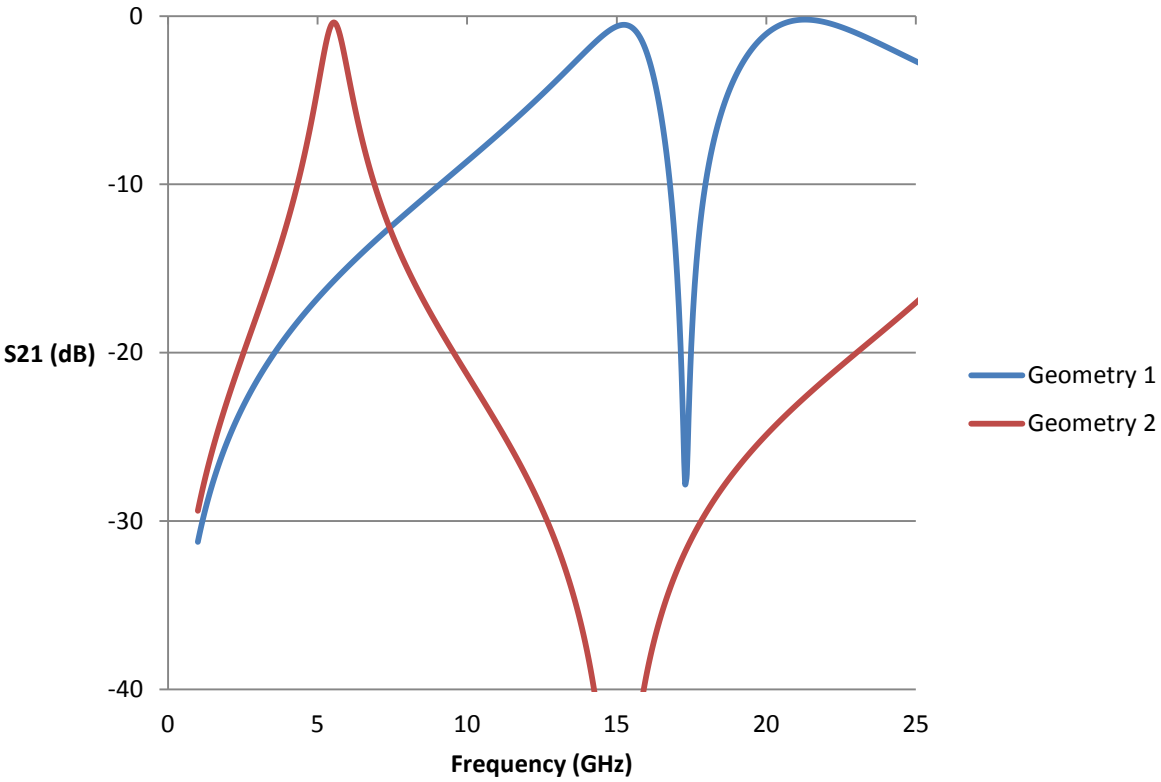

Figure 5-3: *Comparison between the transmission response of two square loop geometries (Geometry 2 has one layer shifted by half the periodicity)*

The first structure (aligned) exhibited the first pass band resonance at 15.2 GHz; this structure has a null at 17.3 GHz with a second pass band resonance occurring at 21.3 GHz. The second structure (offset) resonated at 5.5 GHz, which makes this structure extremely compact. This periodicity of this structure is ~λ/13.5 (where λ is the free space wavelength at the resonant frequency) and it is classified as a square loop complementary metasurface. It is worth mentioning that a single layer square metallic loop backed by the same 0.07mm thick dielectric resonated at 23.4 GHz.

The decrease in the pass band resonant frequency for both structures (compared to the single layer square loop) is due to strong coupling between the two complementary layers. The lower resonant frequency for the square loop complementary metasurface is due to the shifting of the aperture layer by half the periodicity, along both x- and y-axis, which places the metallic loops opposite to the metal of the complementary apertures layer thus leading to a strong interaction among the layers (in the first geometry the metallic square loops are adjacent to the apertures so there is relatively less coupling between the two layers).

A rigorous way to explain the decrease in the pass band resonance, after shifting the square loops by half the periodicity goes via the Babinet principle. Consider two Babinet complementary surfaces T and T'. These surfaces are placed between the observer and the light source. When the two surfaces are placed on top of each other, no light (visible frequencies) reaches the observer. However as one surface is shifted with respect to the other, light begins to pass through (as the transparent holes which were completely covered by the complementary surface earlier will now be partially covered therefore transmitting light). Since the individual element of the complementary metasurface is resonant and the structure is small as compared to the wavelength of operation, so the behaviour of this surface must be explained in terms of electric fields [1]. The maximum coupling between the two layers now becomes analogous to the condition when no light was transmitted to the observer through

the surfaces T and T'. Similarly, the maximum of the electric fields are analogous to the transparent part of these surfaces (T and T').

Since for no light to pass through, the transparent and opaque parts of the surfaces T and T' need to overlap therefore for the maximum coupling to occur, the maximum of the electric fields of the metallic array needs to be adjacent to the minimum of the electric fields of the apertures array. In order to satisfy this condition of maximum coupling in a complementary metasurface, when the individual building block forms a closed loop (like in the case of square loops); one layer needs to be shifted by half the periodicity so that the maximum and minimum electric field points of the two layers are directly above. Therefore the pass band resonance of the geometry 2 (offset) (5.4 GHz) is very low as compared to the pass band resonance of the geometry 1 (aligned) (15.5 GHz). The electric fields plot which shows the locations of the nulls for a single layer square loop periodic structure is shown in Figure 5-4.

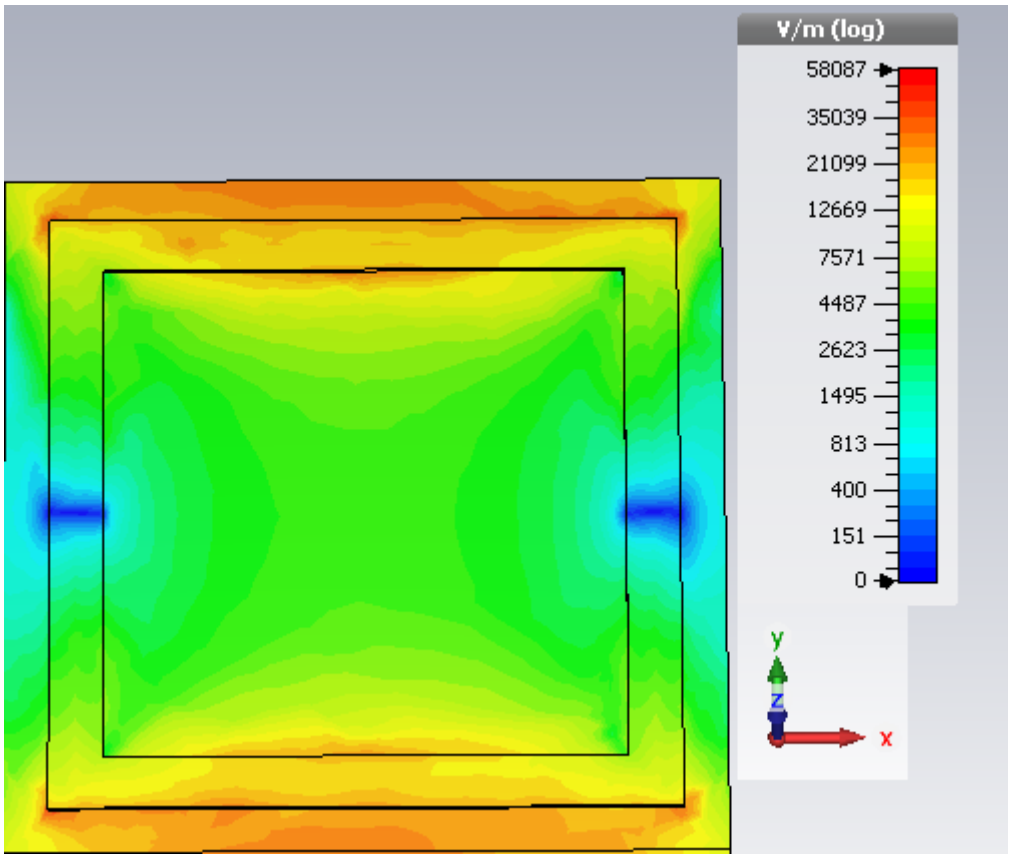

Figure 5-4: *Electric fields plot for a single layer square loop at its resonant frequency*

5.1.1 Effect of Dielectric Thickness on Square Loop Complementary Metasurface

The effect of thickness of the dielectric layer was also studied for a square loop complementary metasurface. As expected, it was observed that an increase in the dielectric thickness led to an increase in the pass band resonant frequency. For a 0.03mm thick dielectric, pass band resonant frequency was observed to be 4.1 GHz. These results are shown in Figure 5-5. The pass band resonance was increased to 8.6 GHz and 8.9 GHz when the thickness was increased to 0.5mm and 0.9mm respectively.

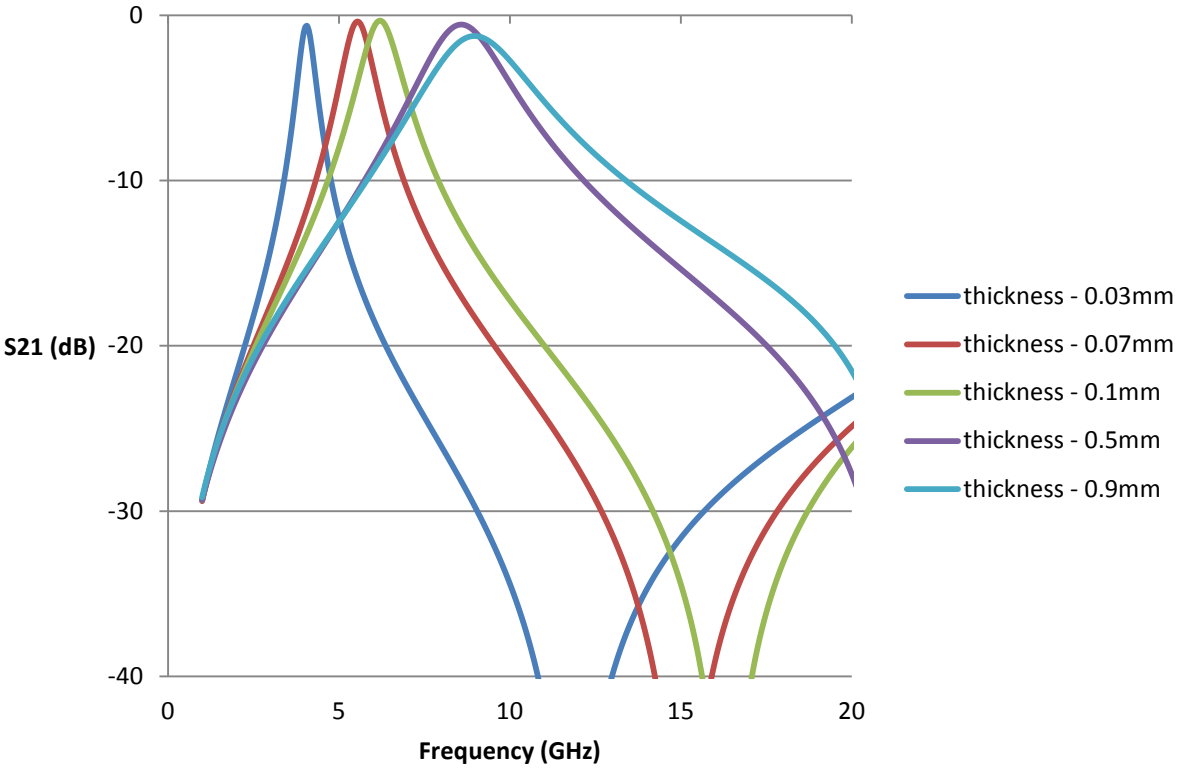

Figure 5-5: *Effect of varying the thickness on square loop complementary metasurface (offset) (simulated)*

5.2 Experimental Verification of Square Loop Complementary Metasurface

5.2.1 Measurement Setup

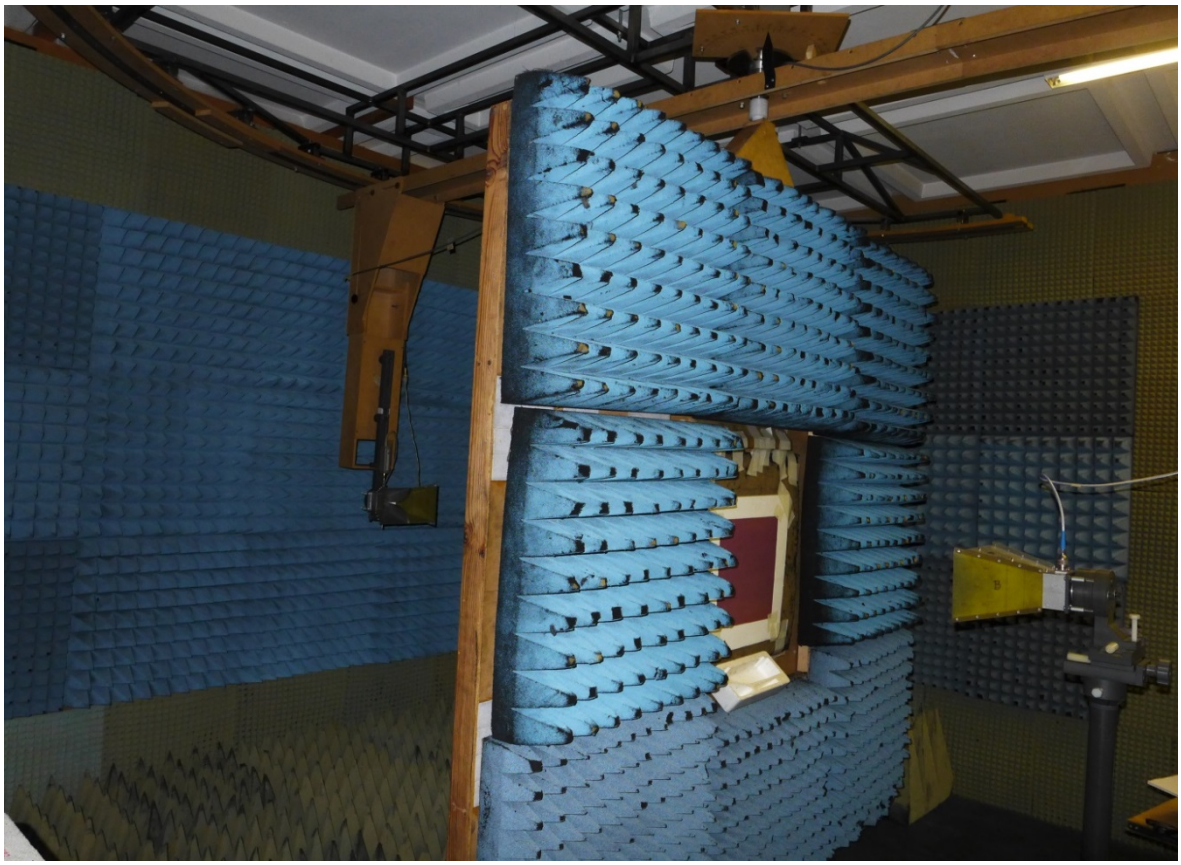

Figure 5-6: *Loughborough University anechoic chamber for measurement of transmission response of metasurfaces*

The measurement setup for fabricated metasurfaces has been shown in Figure 5-6. Two pyramidal horns antennas were used as the receiver and transmitter. These horns were placed at a distance of 3.5m from each other. The path from the transmitter to the receiver has been blocked by using the radar absorbing material in order to prevent transmission, except through the 250 × 250mm^2 aperture. The signal was generated using an 8350B HP signal generator. The magnitude of the S-parameters was measured using an 8757D HP scalar network analyser, see Figure 5-7. The height of the both horns was adjusted and they were

aligned so that the power can be transferred through the square aperture in the radar absorbing wall. The transmitted power over a frequency range (2.5 – 10 GHz) was measured. This power was normalised compared to the case without the metasurfaces.

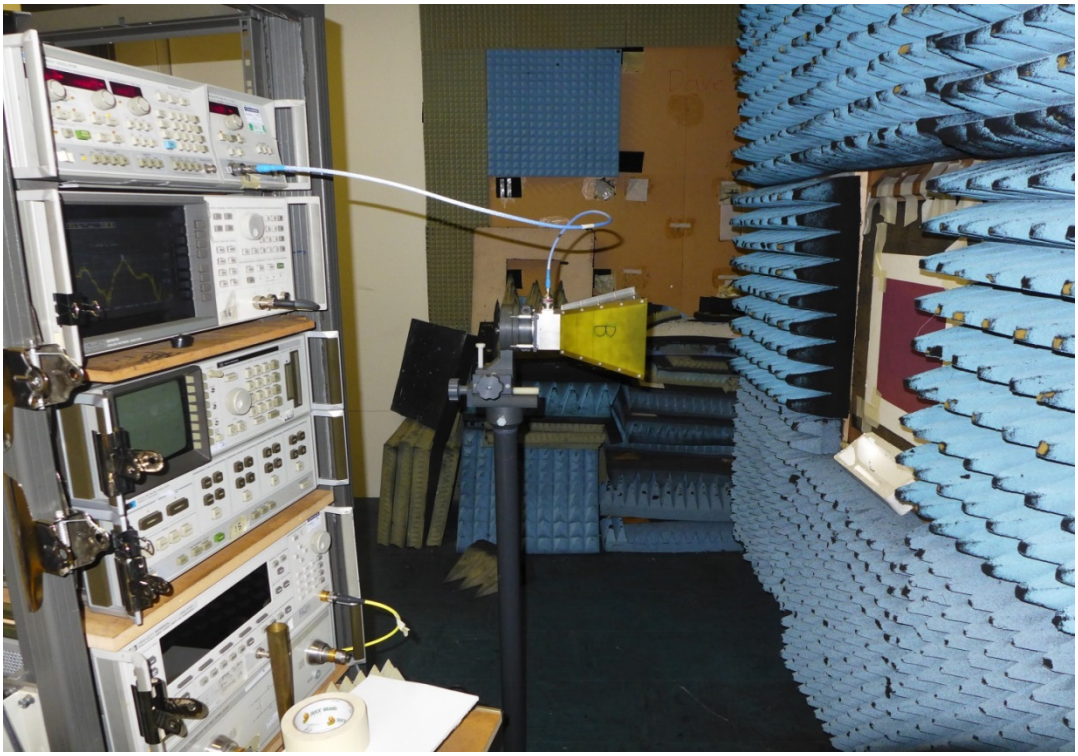

Figure 5-7: *The transmitter horn connected to the 8350B HP signal generator and 8757D HP scalar network analyzer*

5.2.2 Measured Results

Both structures, first one with the apertures layer directly behind the metallic layer (geometry 1 - aligned) and the second one in which one layer is shifted by half the periodicity (square loop complementary metasurface – geometry 2 - offset), were fabricated. They are shown in Figure 5-8. The transmission response of these metasurfaces was measured by placing them in a 25 × 25 cm^2 aperture in a radar absorbing material, placed between a transmitting and a receiving horn. The periodicity for geometry 1 (aligned - when the two complementary layers

are adjacent to each other) is 10mm. The length of the individual element is 9mm with 0.3mm width.

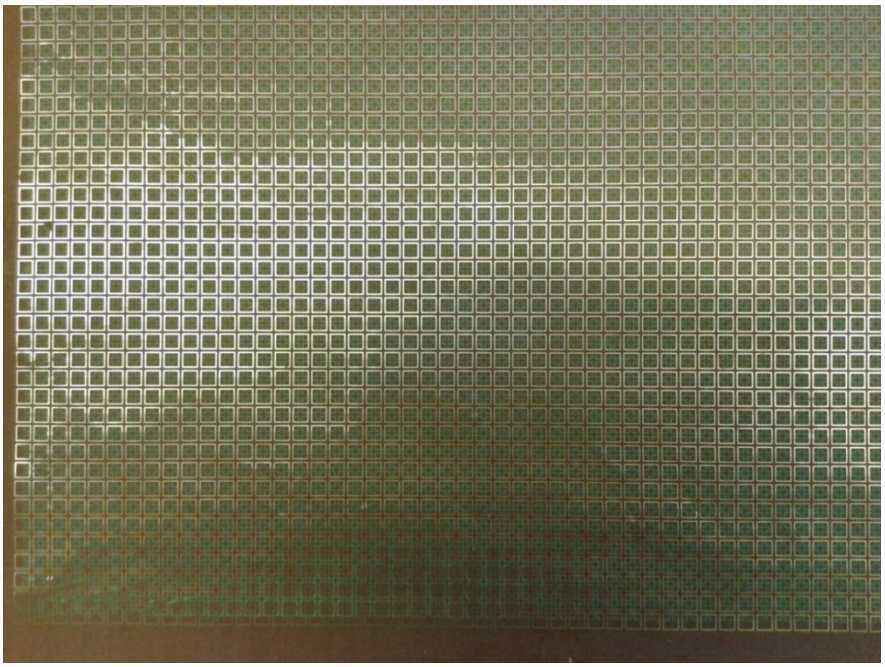

(a)

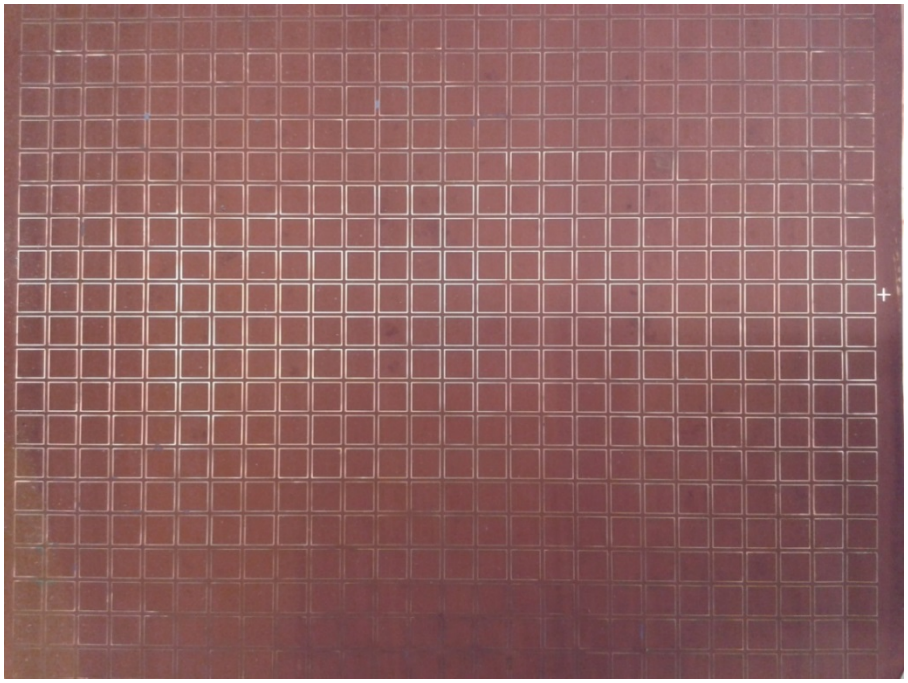

(b)

Figure 5-8: *Fabricated samples for Geometry 2 (offset) (square loop complementary metasurface) – unit cell 4mm (a); and Geometry 1(aligned) unit cell – 10mm (b)*

The periodicity of the square loop metasurface (geometry 2 - offset) is 4mm, with the length of the square loop equal to 3.5mm and width of the individual being 0.3mm as shown in Figure 5-1. The comparison between the simulated and measured results is shown in Figure 5-9. A very good agreement between the simulated and the measured value was recorded. The simulated resonance is 4.7 GHz with an insertion loss of 0.5dB while the measured value of resonance occurs at 4.4 GHz. The measured insertion loss is 0.8dB.

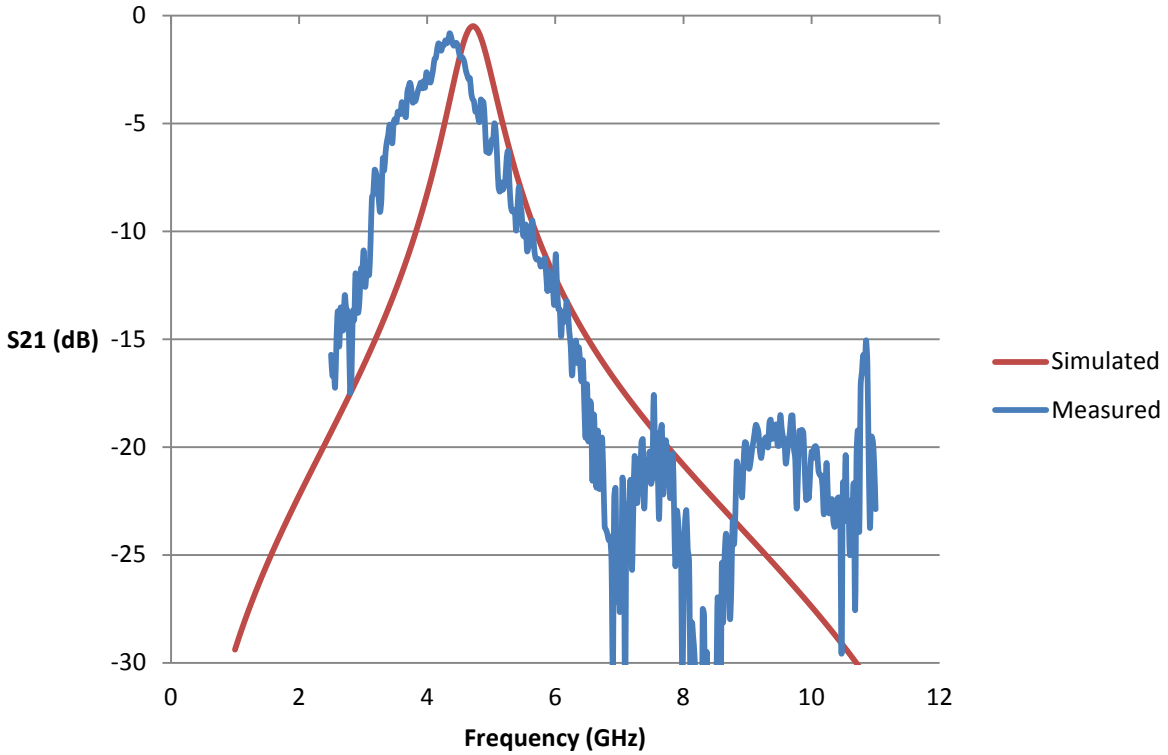

Figure 5-9: *Comparison between the measured and simulated transmission response of a square loop metasurface (geometry 2)*

The periodicity was increased in order to keep the resonance in the frequency range of the transmitting and receiving horns. The comparison between the simulated and measured results is shown in Figure 5-10. The first pass band resonant frequency for the measured and simulated results was 5.9 and 6.0 GHz respectively. An excellent agreement is observed between the two results as indicted by Figure 5-10.

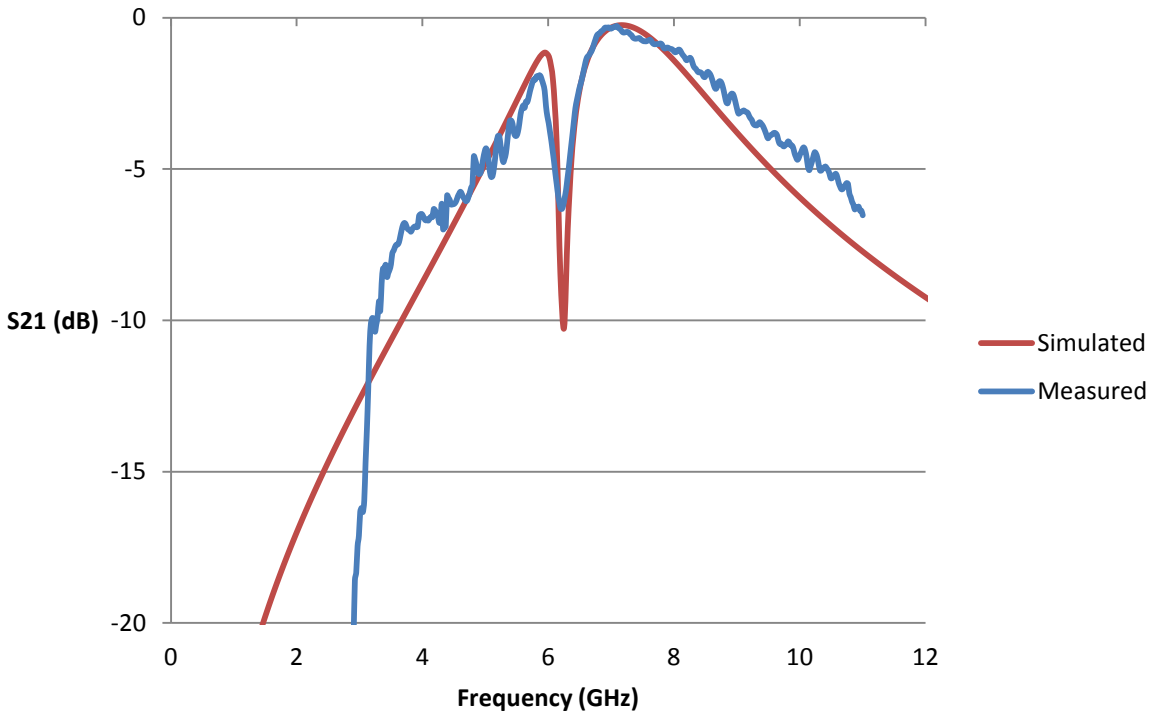

Figure 5-10: *Comparison between the measured and simulated transmission response for geometry 1(aligned)*

It needs to be noted that even though the periodicity of the Geometry 1 (aligned) is 2.5 times that of the Geometry 2 (offset), the resonant frequency of the geometry 2 (square loop metasurface) is still considerably lower, thus emphasizing the effect of the shifting of the layer (thus increasing the inter-layer coupling) on the miniaturization of the structure.

5.3 Review of Multi-layered Metasurfaces

The use of multi layers to improve the response of a FSS has been well documented [14]. Multi-layered FSSs, formed by cascading two or more layers of the periodic structures and carefully aligning them, has led to an increase in the operational bandwidth of the structure and improve the filter's roll-off rate; thus making them available to be used for de-multiplexing in multiband radiometers [15]. Multi-layered structures have also been demonstrated to reduce the size of the individual elements of FSSs; an inductive grid of wires fabricated on one side of the substrate with the other side having a loop grid in which every element is connected to its neighbours with a capacitor. This structure also showed a relatively stable frequency response to the changes in the angle of incidence [16]. A multi-layered square patch complementary structure has been utilized to improve the gain of an antenna over a wide bandwidth by using Fabry-Perrot resonance [17]. Multi-layered periodic structures designed using a genetic algorithm have been used to construct an artificial magnetic conductor [18]. A similar approach has also been employed in the area of metasurfaces. Since metasurfaces can be characterised by their electric admittances and magnetic impedances therefore multi-layered metasurfaces are designed in order to achieve nearly complete transmission [19]. These metasurfaces are called Huygen's metasurfaces. A three layered efficient metasurface for controlling the phase and magnitude of the transmitting beam using horizontally and vertically aligned split-rings has been presented in [20]. In [21], Huygen's metasurfaces have been proposed to convert a non-directive beam from an arbitrary source to a directive one. Such metasurfaces have been utilised to construct a low profile antennas with high aperture efficiency by employing them as a partial reflective surface fed by a cavity [22]. The use of multi-layered Huygen's metasurfaces to structure a bianisotropic metasurface has been proposed in [23].

5.4 Dipole-Slot-dipole Metasurfaces

In this section, multi-layered metasurfaces were used to achieve further miniaturization of a dipole-slot metasurface. The resonant frequency of a dipole-slot metasurface was decreased by adding an additional layer of dielectric backed dipoles. Since a periodic array of complementary metasurface shows a band pass behaviour with strong inter-layer coupling therefore adding an additional layer of dipole, which is naturally a capacitive element, adds extra capacitance to the slot layer which significantly lowers its resonant frequency. The new structure has the configuration of dipole-slot-dipole. A dipole-slot-dipole metasurface is shown in Figure 5-11. Each layer of the slot and the dipole is separated by a thin sheet of a dielectric material.

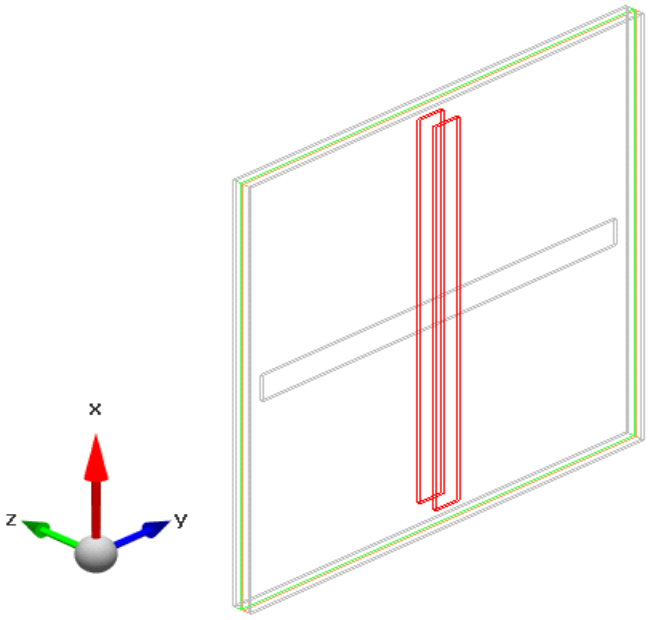

Figure 5-11*: A dipole-slot-dipole metasurface unit cell showing grey slot placed among two red dipoles, each layer of dipoles and slot is separated by a thin dielectric*

The comparison between a dipole-slot-dipole metasurface with a dipole-slot metasurface is shown in Figure 5-12. Both structures were simulated in CST Microwave Studio using

periodic boundary conditions and were illuminated by a TE polarised plane wave at normal incidence. They have a periodicity of 5mm; the dipoles and slots are 0.5mm wide and 4.5mm long. The dielectric used in the simulations is 44microns thick, with a dielectric constant of 3 and a loss tangent of 0.01. The dipole-slot metasurface showed a resonance at 7.41 GHz. The dipole-slot-dipole metasurface, as shown in Figure 5-11, showed a resonance at 5.96 GHz. This decrease in the resonant frequency is due to the additional capacitance added to the dipole-slot metasurface by the newly added dipole layer (third layer). It should be noted that, for the results shown in Figure 5-12, the dielectric on which the new layers of dipoles are placed was exactly the same as the one used for the dipole-slot metasurface.

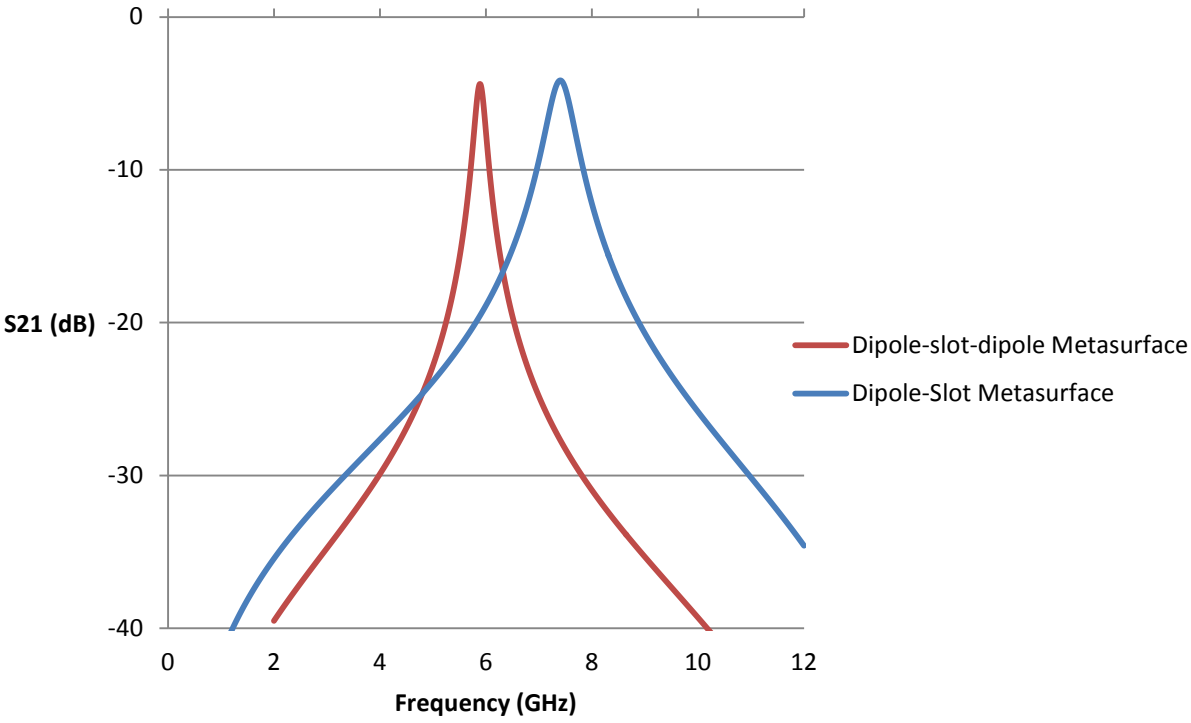

Figure 5-12*: Simulated comparison between the dipole-slot-dipole metasurface and the dipole-slot metasurface*

A qualitative equivalent circuit model has been developed to explain the behaviour of the dipole-slot-dipole metasurface. Figure 5-13 show the equivalent circuit for the dipole-slot-dipole metasurface. The first series LC branch of the equivalent circuit represents the first

dipole layer, with C_{dipole} and L_{dipole} being the capacitive and inductive part of the dipoles. The slot layer, in Figure 5-13, is represented by the parallel LC circuit. L_{slot} and C_{slot} are the inductive and the capacitive parts of the slot layer. Since a periodic layer of dipoles is band stop so it is represented by a series LC circuit; while a slot layer is band pass, thus represented by a parallel LC circuit.

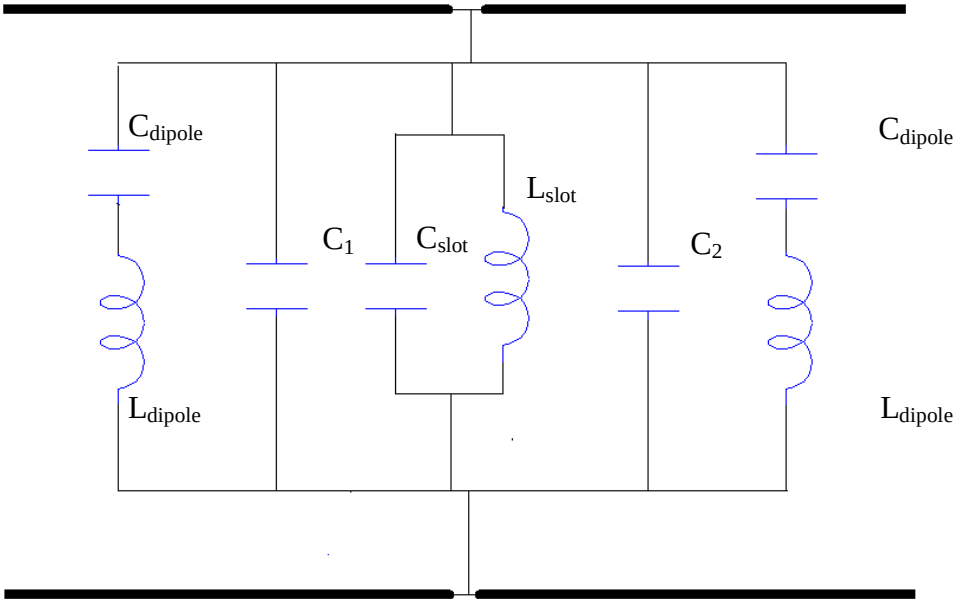

Figure 5-13*: Equivalent circuit model for dipole-slot dipole metasurface*

The equivalent circuit of the dipole-slot-dipole metasurface (in comparison to the equivalent circuit of dipole-slot metasurface in Figure 4-23), contains an extra coupling capacitance C_2, equal to C_1, and another series LC circuit representing the other dipole layer. This extra capacitance increases the overall capacitance of the structure therefore causing a further decrease in the resonant frequency of the structure. Both equivalent circuits were compared by simulating them in AWR Microwave Office [24]. The simulation results are shown in Figure 5-14. The equivalent circuit predicts the resonant frequency of dipole-slot

metasurface to be 7.8 GHz and that of dipole-slot-dipole metasurface to be 5.6 GHz. These values are extremely close to the results from the Full wave simulations of the both structures (CST simulations show the resonance value for dipole-slot metasurface and dipole-slot-dipole metasurface to be 7.4 and 5.9 GHz respectively). The values for the individual elements of the circuit are: C_{slot}= 0.0193pF, L_{slot}= 1.17nH, C_{dipole}= 0.033pF, L_{dipole} = 0.688nH. The equivalent circuit model assumes no losses in system. The values for the coupling capacitances ($C_1 = C_2$) is 0.3nF. These values were calculated by using the method described in Section 4.3 with the help of equations 4.8 and 4.9.

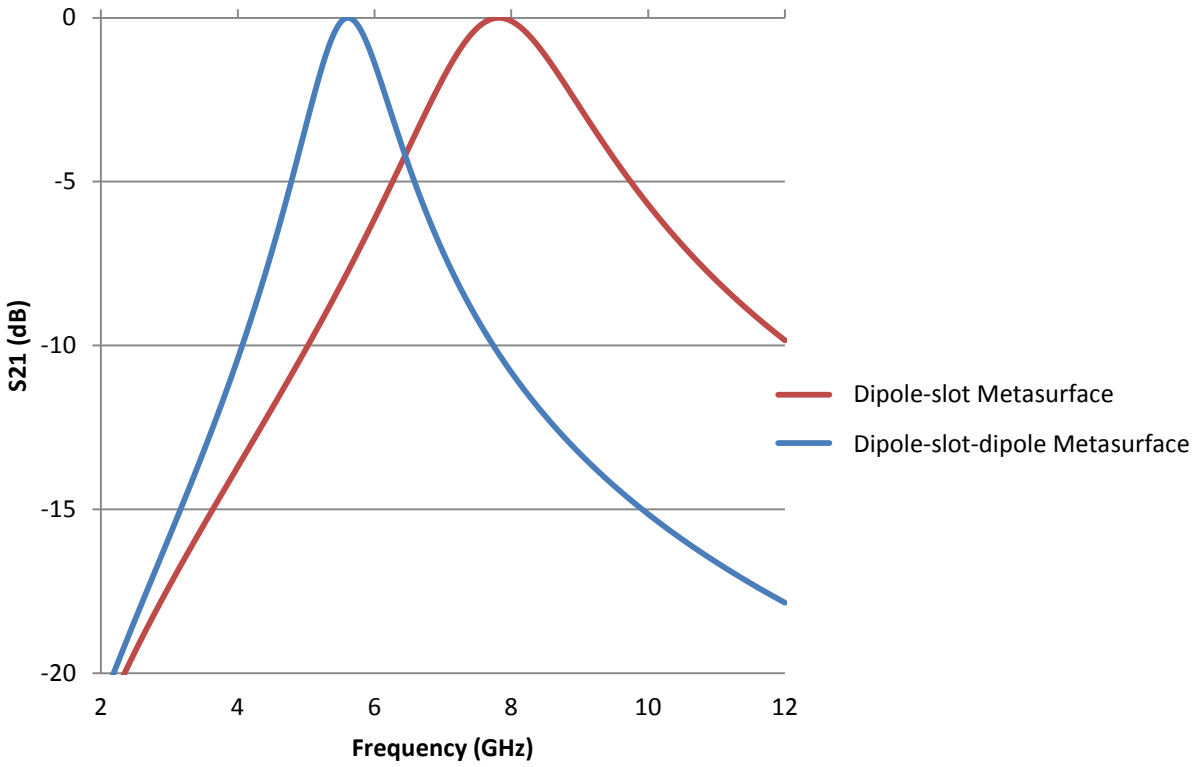

Figure 5-14*: Equivalent circuit comparison between the dipole-slot-dipole metasurface and the dipole-slot metasurface*

Since the added capacitance, which arises due to the close proximity of the extra dipole layer, is the main reason for lowering the resonant frequency; the relative permittivity of the dielectric supporting the extra dipole layer has a significant effect on the coupling. A higher

value of the relative permittivity increases the added capacitance thus decreasing the resonant frequency. This was illustrated by varying the permittivity of the 44micron thick dielectric (supporting the third layer) in the simulations. The results for the simulations with different permittivities of the in-between dielectric are shown in Figure 5-15 and summarised in Table 5-1.

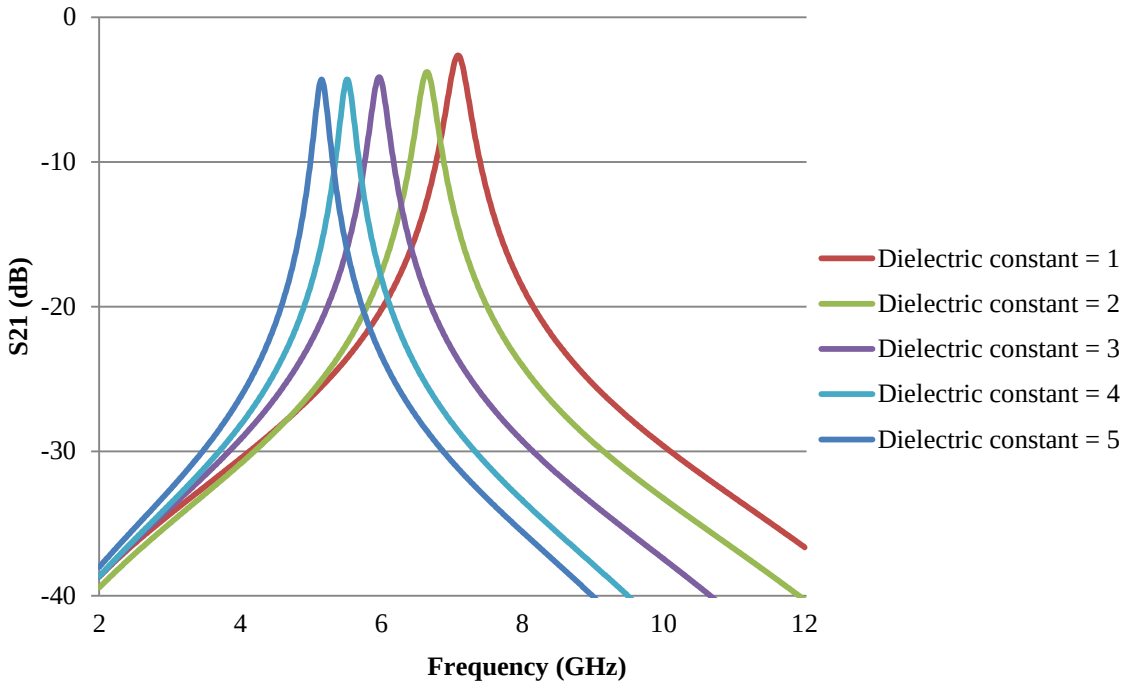

Figure 5-15*: The effect of changing the relative permittivity of the dielectric supporting the added dipole layer on the transmission response of dipole-slot-dipole metasurface (simulated)*

The pass band resonance of the dipole-slot-dipole metasurface decreased nearly linearly, from 7.09 GHz to 5.15 GHz as the relative permittivity of the dielectric sheet supporting the layer of dipoles was increased from 1 to 5. This means that even when the simulated material had a relative permittivity of 1 (equal to vacuum), the resonant frequency of dipole-slot-dipole metasurface is still lower than the original resonant frequency of the dipole-slot metasurface.

Table 5-1: *Simulated change in the pass band resonance of dipole-slot-dipole metasurface as the relative permittivity of the dielectric on the added dipole layer is varied*

Relative permittivity of dielectric supporting the dipole layer	Pass band Resonant Frequency (GHz)
1	7.09
2	6.64
3	5.96
4	5.51
5	5.15

5.4.1 Alignment of Dipole Array

The electric fields on a slot vary as function of sine and are maximal at the centre of the slot. Because the coupling between the slot and the added dipole layer is the most significant reason for the lowering of resonant frequency of a dipole-slot-dipole metasurface, so the added dipole array was gradually moved away from the centre of the slot and the effect of this movement on the resonant frequency was recorded. It was observed that as the dipole array (third layer) was moved away from the centre (horizontally along x-axis), the resonant frequency of dipole-slot-dipole metasurface increased. These results are shown in Figure 5-16. When the centre of the dipole array was aligned with the centre of the slot array, the resonant frequency of the slot-dipole-slot metasurface was 5.96 GHz but as it was moved 0.5mm away, the resonant frequency increased to 6.33 GHz. The resonant frequency was 6.73 GHz and 7.18 GHz when the distance between the centre of the dipole and the centre of the slot was 1mm and 1.5mm respectively. This shows that the maximum coupling takes place when the centre of the dipoles and the slots are aligned.

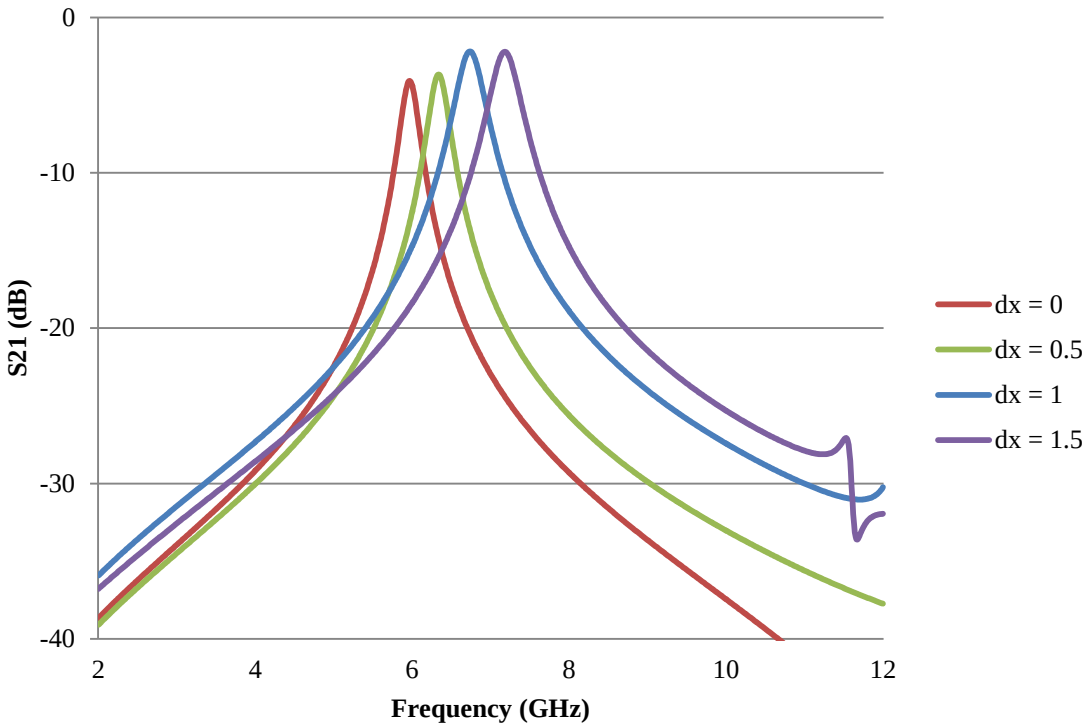

Figure 5-16*: The simulated pass band resonance of the dipole-slot-dipole metasurface as the function of the relative position (dx (mm)) of the added dipole with respect to the dipole-slot metasurface*

For practical purposes, this highlights the fact that the alignment of the both layers is very important and must be given careful consideration, as a slight movement of 0.5mm of the dielectric backed dipole layer away from the centre can cause an upward shift in the pass band resonance of the slot-dipole-slot metasurface.

5.4.2 Effects of Varying Dipole Length on Dipole-slot-dipole Metasurfaces

The dipole-slot-dipole metasurface is a λ/10 structure which makes it extremely compact as compared to a traditional frequency selective surface. This makes the stand-alone dipole layer transparent at the resonant frequency while a stand-alone layer of slots behaves

like a reflector. This also shows that the response of the dipole-slot-dipole metasurface is mainly governed by the coupling among the elements present on different layers, therefore the extra capacitance added to the original dipole-slot metasurface leads to a pronounced decrease in its resonant frequency. The thickness of the whole structure is very small as compared to the wavelength while the coupling among the adjacent layers is very strong; this makes the dipole-slot-dipole metasurface behave like a single pass band structure. The response of the dipole-slot-dipole metasurface to changing the length of the dipole placed on the added dielectric backed layer (third layer) has also been investigated. The length of the dipole, placed on the added layer, was varied from 1.5mm to 4.5mm. As the length was decreased the resonant frequency of the structure increased. This is attributed to the fact that as the size of the dipole is decreased, the added capacitance also decreases which reduces the coupling between the added dipole layer and the dipole-slot metasurface. The results are shown in Figure 5-17. As the length increased from 1.5 to 4.5mm, with an increment of 1mm, the frequency increases from 5.96 GHz to 6.33, 6.77 and 7.16 GHz respectively.

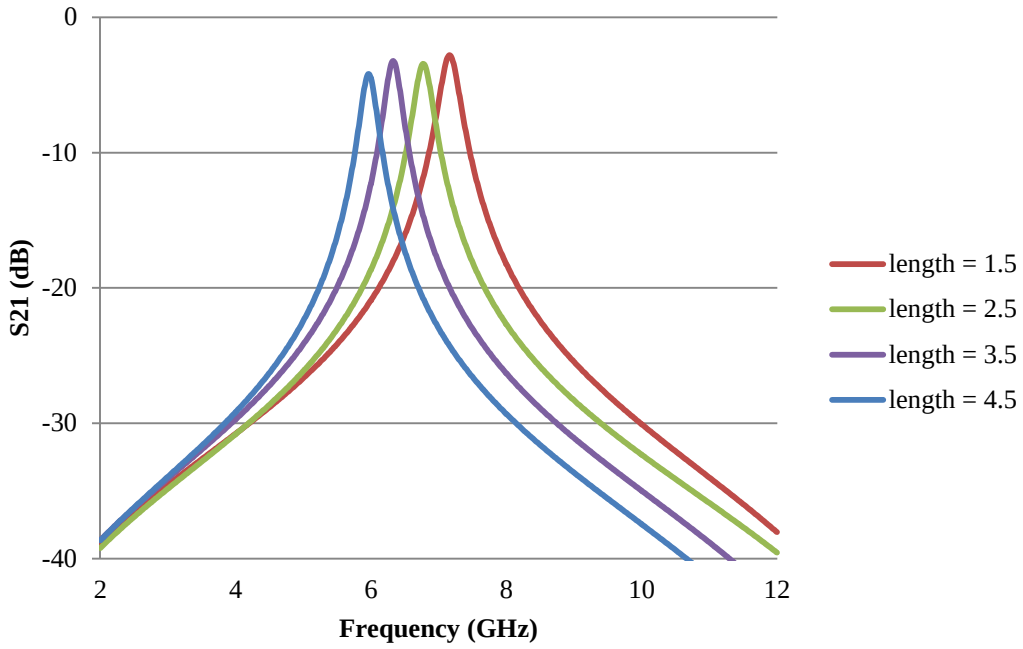

Figure 5-17*: The simulated effect of changing the length of the added dipole (mm) on the transmission characteristics of the dipole-slot-dipole metasurface.*

5.5 Experimental Verification of Dipole-slot-dipole Metasurface

The dipole-slot metasurface samples were fabricated by etching the designs onto a thin GTS laminate with metal cladding on both sides. The thickness of the dielectric was 44 microns and the relative permittivity of GTS is equal to 3 [25]. The sample size was designed to be 260 by 260 mm. This size allowed an array of 52 by 52 elements. In order to construct a dipole-slot-dipole metasurface, another layer of dipoles, backed by the same 44microns thick GTS material was also fabricated. The dipoles were etched on its one side while metal was completely removed from the other. Figure 5-18 shows the fabricated samples.

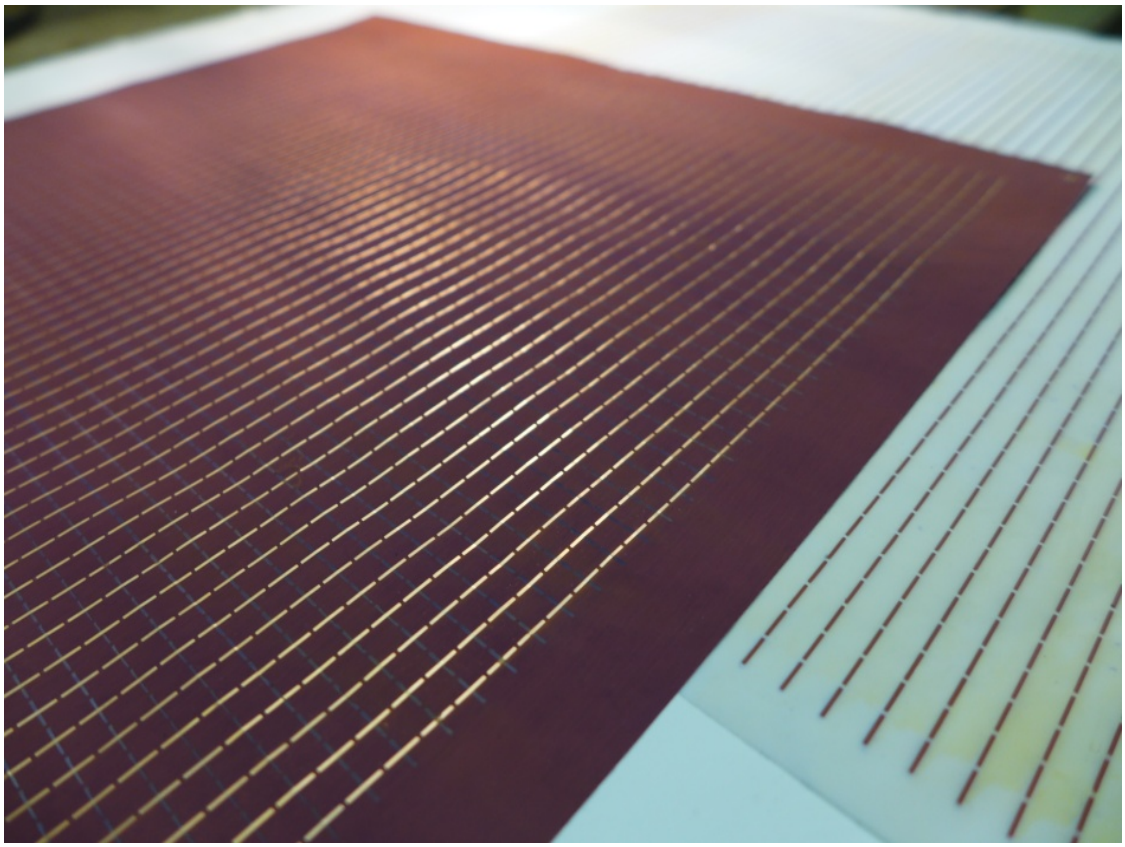

Figure 5-18*: Fabricated samples showing a dipole-slot metasurface and an additional layer of dipoles (third layer). The added dipole layer is shifted to make it visible. The dipoles and slots are 4.5mm long and 0.5mm wide with a periodicity of 5mm*

The pass band and the stop band were measured in a semi-anechoic chamber. Two horn antennas operating from 2 to 12 GHz with vertical polarisation were placed 3.5 m apart. They were placed in a 250mm by 250mm square aperture in the radar absorbing material wall.

The dipole-slot-dipole metasurface was constructed by placing the GTS backed dipole layer on the top of the dipole-slot metasurface. As shown in section 5.2.1, the dipole-slot-dipole metasurface is sensitive to the alignment of the dipoles so careful consideration was given to aligning the two (dipole and dipole-slot) layers. Both these layers were sandwiched between two sheets of Rohacell (dielectric constant = 1.05; loss tangent = 0.0003) [26] and were tightly pressed against each other in order to avoid any air gap as that can lead to a reduction in the added capacitance which manifests itself in increasing the resonant frequency of the dipole-slot-dipole metasurface. No glue was used. The samples were positioned in the far field of the horn antennas. The results shown are normalised compared to the received power without the samples. Note, the samples are polarisation sensitive and the dipoles were orientated vertically so as to be parallel with the polarisation of the horn antennas. The comparison between the measured and simulated results for the dipole-slot-dipole metasurface is shown in Figure 5-19. A good agreement between the simulated and the measured results was observed considering the sensitivity for the layer alignments.

Slight differences between the measured and simulated values for the dipole-slot-dipole metasurface can be attributed to the misalignment of the sample (as discussed in Section 5.2.1). The comparison between the measured transmission response of the dipole-slot metasurface and the dipole-slot-dipole metasurface is shown in Figure 5-20. This comparison shows that by adding a layer of dipoles to the dipole-slot metasurface, the resonant frequency of the structure has been decreased. (A slot-dipole-slot configuration was also considered and it has been presented in Appendix C)

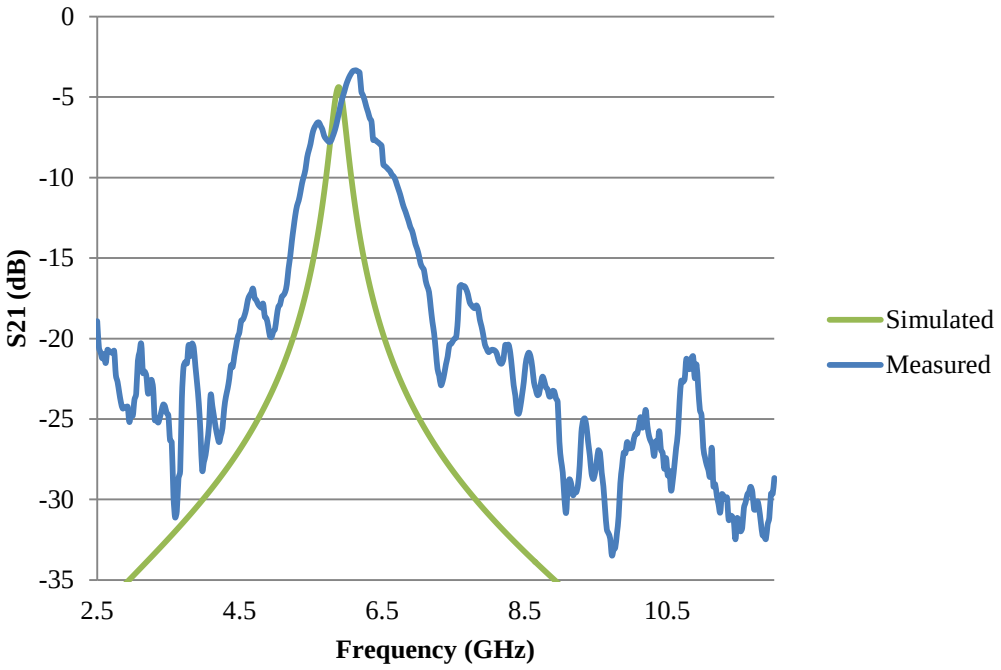

Figure 5-19*: Measured and simulated response of dipole-slot-dipole metasurface*

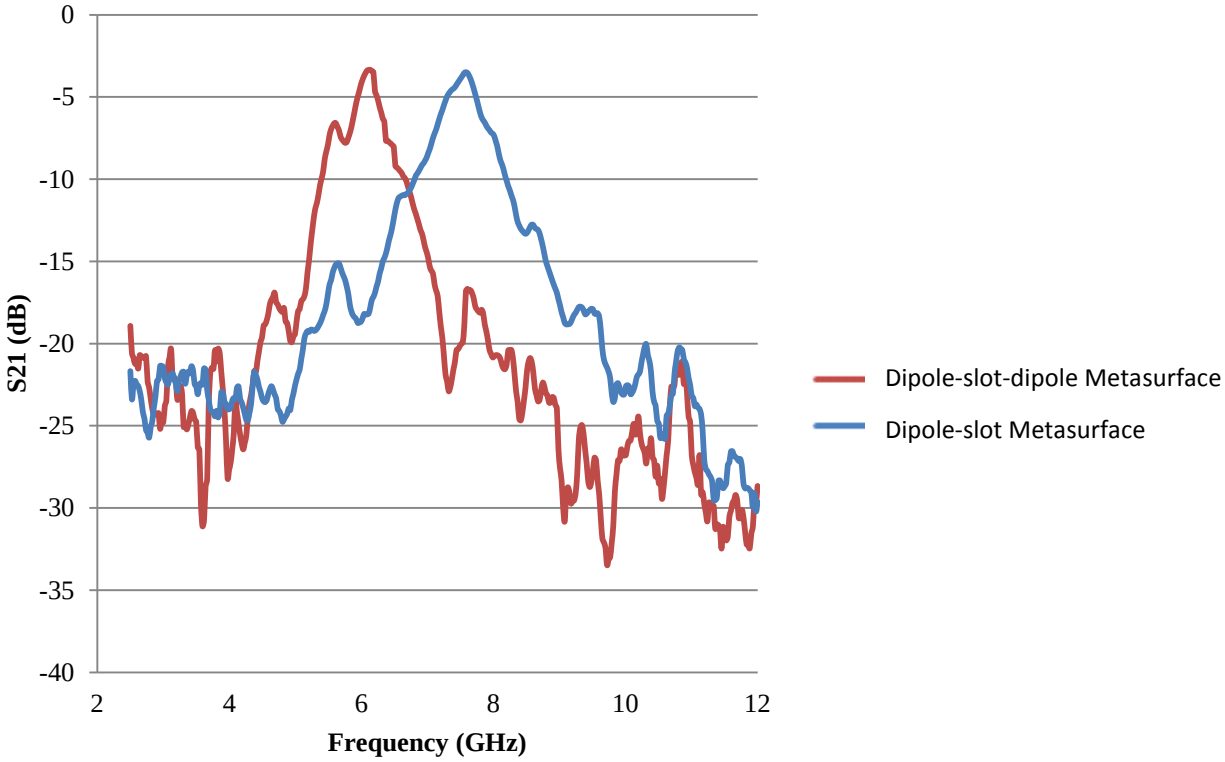

Figure 5-20*: Comparison of measured S21 of dipole-slot-dipole metasurface and dipole- slot metasurface*

5.6 Conclusions

It has been shown that for rotationally symmetric Babinet's complement geometries, maximum coupling occurs when one layer is shifted by half the periodicity (along both x- and y-axis) with respect to the other layer. This is due to the reason that inter-layer coupling is maximal when the electric fields maxima of one layer is placed adjacent to the electric fields minima of its complementary layer. This has been demonstrated with the help of square loops. The size of the structure was considerably minimized when one layer was shifted by half the periodicity. After shifting the layer, the structure has been classified as a square loop metasurface and it had dimensions of $\lambda/13.5$. Both structures (aligned and offset) however, resonated at a much lower frequency than a single layer band pass square loop FSS. The effect of increasing the dielectric thickness for the square loop metasurface has been studied and it has been shown that increasing the dielectric thickness causes an increase in the pass band resonance. The samples for both geometries were fabricated and their transmission response was measured in a semi anechoic chamber. A good agreement between the measurements and the simulations has been reported. The square loop metasurface is a miniaturized structure which is also polarisation independent.

The behaviour of the dipole-slot metasurface is controlled by the strong coupling among its layers. This property allows the miniaturization of this structure by adding extra capacitance. Further capacitance was added to the dipole-slot metasurface by adjacently placing a layer of dipoles. This resulted in decreasing the pass band resonant frequency of the structure from 7.5 to 6.1GHz. This new structure is called a dipole-slot-dipole metasurface. A qualitative equivalent circuit model has been developed. This model qualitatively explains the behaviour of dipole-slot-dipole metasurface and also illustrates its comparison with the dipole-slot metasurface. It should be noted that due to very strong coupling between the layers, the

absorption loss in both structures is closely related to the properties of the dielectric material. The new structure has a period of one-tenth of the free space wavelength at the resonant frequency. Since the miniaturization is the result of adding extra capacitance, it was shown that increasing the relative permittivity of the material supporting the dipoles array led to a decrease in the resonant frequency. Decreasing the length of the added dipoles caused a decrease in this capacitance therefore increasing the resonant frequency of the dipole-slot-dipole metasurface. It was demonstrated that the maximum coupling between the dipole-slot metasurface and the dielectric backed dipole layer occurs when the centre of the dipoles overlap the centre of the slots (since the electric fields of the slot are maximal at its centre). A lack of alignment decreased the coupling and caused an increase in the pass band resonance. The experimental validation was carried out by fabricating both, the dipole-slot metasurface and dipole-slot-dipole metasurface, and their response to an incoming plane wave was measured in a semi- anechoic chamber. A very good agreement was found between the simulations and the measured results.

References

[1] H. G. Booker, “Slot Aerials and Their Relation to Complementary Wire Aerials (Babinet’s Principle),” *J. Inst. Electr. Eng. - Part IIIA Radiolocation*, vol. 93, no. 4, pp. 620–626, 1946.

[2] D. Ferreira, R. F. S. Caldeirinha, I. Cuiñas, and T. R. Fernandes, “Square Loop and Slot Frequency Selective Surfaces Study for Equivalent Circuit Model Optimization,” *IEEE Trans. Antennas Propag.*, vol. 63, no. 9, pp. 3947–3955, 2015.

[3] M. A. R. Barrera and W. P. Carpes, “Numerical Model of the Effective Permittivity for Square-Loop Frequency Selective Surfaces,” *IEEE Trans. Magn.*, vol. 51, no. 3, pp. 3–6, 2015.

[4] R. J. Langley and E. A. Parker, “Equivalent Circuit Model For Arrays Of Square Loops,” *Electrnoics Lett.*, vol. 18, no. 7, pp. 1–3, 1982.

[5] A. D. Chuprin, E. A. Parker, and J. C. Batchelor, “Resonant frequencies of open and closed loop frequency selective surface arrays,” *Electron. Lett.*, vol. 36, no. 79, pp. 1601–1603, 2000.

[6] E. A. Parker, J. Robertson, B. Sanz-Izquierdo, and J. C. Batchelor, “Minimal size FSS for long wavelength operation,” *Electrnoics Lett.*, vol. 44, no. 6, pp. 6–7, 2008.

[7] Y. Shang, Z. Shen, and S. Xiao, “Frequency-Selective Rasorber Based on Square Loop and Cross Dipole Arrays,” *IEEE Trans. Antennas Propag.*, vol. 62, no. 11, pp. 5581–5589, 2014.

[8] S. Keyrouz, G. Perotto, and H. J. Visser, “Frequency selective surface for radio frequency energy harvesting applications,” *IET Microwaves, Antennas Propag.*, vol. 8, no. October 2013, pp. 523–531, 2014.

[9] B. Sanz-Izquierdo, E. A. Parker, and J. C. Batchelor, “Switchable Frequency Selective Slot Arrays,” *IEEE Trans. Antennas Propag.*, vol. 59, no. 7, pp. 2728–2731, 2011.

[10] A. Pal, A. Mehta, D. Mirshekar-Syahkal, P. Deo, and H. Nakano, “Dual-Band Low-Profile Capacitively Coupled Beam-Steerable Square-Loop Antenna,” *IEEE Trans. Antennas Propag.*, vol. 62, no. 3, pp. 1204–1211, 2014.

[11] S. J. Wu and J. H. Tarng, “Planar band-notched ultra-wideband antenna with square-looped and end-coupled resonator,” *IET Microwaves, Antennas Propag.*, no. March, pp. 1227–1233, 2011.

[12] P. Deo, M. Pant, A. Mehta, and H. Nakano, “Implementation and simulation of commercial RF switch integration with steerable square loop antenna,” *Electron. Lett.*, vol. 47, no. 12, pp. 3–4, 2011.

[13] P. Deo, A. Mehta, P. J. Massey, and H. Nakano, “Beam steerable square loop antenna over hybrid high impedance surface,” *Electron. Lett.*, vol. 45, no. 19, pp. 18–19, 2009.

[14] J. C. Vardaxoglou, *Frequency Selective Surfaces - Analysis and Design*. John Wiley & Sons, 1997.

[15] C. Antonopuloulos, R. Cahill, E. A. Parker, and I. M. Sturland, “Multilayer frequency-selective surfaces for millimetre and submillimetre wave applications,” *IEE Proc.*, vol. 144, no. 6, pp. 415–420, 1997.

[16] F. Bayatpur and K. Sarabandi, “Single-Layer High-Order Miniaturized-Element,” *IEEE Trans. Microw. Theory Tech.*, vol. 56, no. 4, pp. 774–781, 2008.

[17] N. Wang, Q. Liu, C. Wu, and L. Talbi, “Wideband Fabry-Perot Resonator Antenna With Two Complementary FSS Layers,” *IEEE Trans. Antennas Propag.*vol. 62, no. 5, pp. 2463–2471, 2014.

[18] A. Monorchio, G. Manara, and L. Lanuzza, “Synthesis of Artificial Magnetic Conductors by Using Multilayered Frequency Selective Surfaces,” *IEEE Trans. Antennas Propag.*, vol. 1, pp. 196–199, 2002.

[19] C. Pfeiffer and A. Grbic, “Metamaterial Huygens ’ Surfaces: Tailoring Wave Fronts with Reflectionless Sheets,” *Phys. Rev. Lett.*, vol. 197401, no. May, pp. 1–5, 2013.

[20] X. Wan, S. L. Jia, T. J. Cui, and Y. J. Zhao, “Independent modulations of the transmission amplitudes and phases by using Huygens metasurfaces,” *Nat. Publ. Gr.*, no. April, pp. 1–7, 2016.

[21] A. Epstein and G. V Eleftheriades, “Passive Lossless Huygens Metasurfaces for Conversion of Arbitrary Source Field to Directive Radiation,” *IEEE Trans. Antennas Propag.*, vol. 62, no. 11, pp. 5680–5695, 2014.

[22] A. Epstein, J. P. S. Wong, and G. V Eleftheriades, “Cavity-excited Huygens’ metasurface antennas for near-unity aperture illumination efficiency from arbitrarily large apertures,” *Nat. Commun.*, vol. 7, pp. 1–10, 2016.

[23] A. Epstein and G. V Eleftheriades, “Arbitrary Power-Conserving Field Transformations With Passive Lossless Omega-Type Bianisotropic Metasurfaces,” *IEEE Trans. Antennas Propag.*, vol. 64, no. 9, pp. 3880–3895, 2016.

[24] “Microwave Office.” http://www.awrcorp.com/products/microwave-office.

[25] C. C. Njoku, W. G. Whittow, and J. C. Vardaxoglou, “Effective permittivity of heterogeneous substrates with cubes in a 3-D Lattice,” *IEEE Antennas Wirel. Propag. Lett. (Special Issue Metamaterials)*, vol. 10, pp. 1480–1483, 2011.

[26] http://www.rohacell.com/sites/lists/PP-HP/Documents/ROHACELL-Dielectric-Properties-EN.pdf

Chapter 6 : Width-Optimization and Analytical Circuit Modelling of a Complementary Metasurface

Abstract

Chapter 4 explained the behaviour of the dipole-slot metasurfaces using a qualitative circuit model. This circuit model was then used to describe the response of a dipole-slot-dipole metasurface in Chapter 5. This chapter starts with exploring the effects of varying the width of the individual elements on the pass band resonance. Section 6.1 optimizes the value of the width in order to achieve maximum miniaturization of a dipole-slot metasurface. An analytical expression is derived by maximising the coupling co-efficient. This equation is then solved using Newton's method in order to obtain the optimum ratio between the length and the width of the individual elements (for maximum miniaturization). Section 6.2 shows that the optimized width is independent of the properties of the in-between dielectric. Section 6.3 reports that by maximising the coupling co-efficient, the ratio between the pass band and stop band resonance can be varied while keeping the pass band resonance nearly constant. This effect has also been demonstrated by fabricating three different metasurfaces and measuring their transmission response in a semi-anechoic chamber in Section 6.4. Section 6.5 presents the derivation of an analytical equivalent circuit model of a generalised Babinet

complementary metasurface using the electric and magnetic field integral equations. The analytical equivalent circuit model also reveals the reason behind the pass band nature of a complementary Babinet metasurface. Two integral equations are reduced to a single equation by approximating the thickness to equal zero in the Electric field integral equation. The resulting equation is solved using the method of moments and in Section 6.5.3, its results are compared with a full wave analysis using CST. Section 6.6 presents the conclusions drawn from this chapter. The key novelties presented in this chapter are: (i) Deriving an expression for the optimum width of the individual elements by maximising the coupling co-efficient which has been validated with simulations and measurements; and (ii) developing a generalised analytical circuit model of a Babinet complementary metasurface. This model has been developed from integral equations by making an appropriate assumption. The analytical equivalent circuit model has been compared with CST simulations (for a dipole-slot metasurface) and a very good agreement is found.

6.1 Width-Optimization of a Dipole-Slot Metasurface

Chapter 4 established that the capacitive coupling among the complementary dipole and slot layers (of the dipole-slot metasurface) is responsible for the compactness of this structure. A qualitative equivalent circuit model was also utilised to explain this behaviour. A dipole is a thin element with $l >> w$, where l is the length of the dipole and slots, and w is their width. In this section, this constraint on the width of the dipoles and the slots is relaxed in order to optimize the performance of the dipole-slot metasurface. The optimization was performed in order to achieve the maximum coupling of the two layers for a fixed length. The rationale governing this idea is that for maximum coupling, the resonant frequency of the dipole-slot metasurface would be at its lowest, thus the maximum degree of compactness can be achieved. The basic structure demonstrating the length and the width of the dipoles and the

slots, and the relationship between them, is shown in Figure 6-1. The dipoles and the slots are placed in the xy-plane.

It is intuitive that for the dipole to be able to add capacitance to the slot layer, it requires metal on the opposite side of the metasurface. This can also be clearly inferred from Figure 6-2. Figure 6-2 demonstrates a comparison between the S21 values for the two distinct dipole-slot complimentary geometries. Both structures are simulated in CST Microwave Studio. The dielectric for both structures has a relative permittivity of 3 and a loss tangent of 0.003. The dielectric is 0.05mm thick. Both structures have lengths equal to 4mm and a periodicity of 4.5mm. The distinction lies in their width. One structure has a width w equal to 0.4mm while the other structure has $l = w = 4$mm, thus making both, the dipoles and the slots, square for the latter geometry.

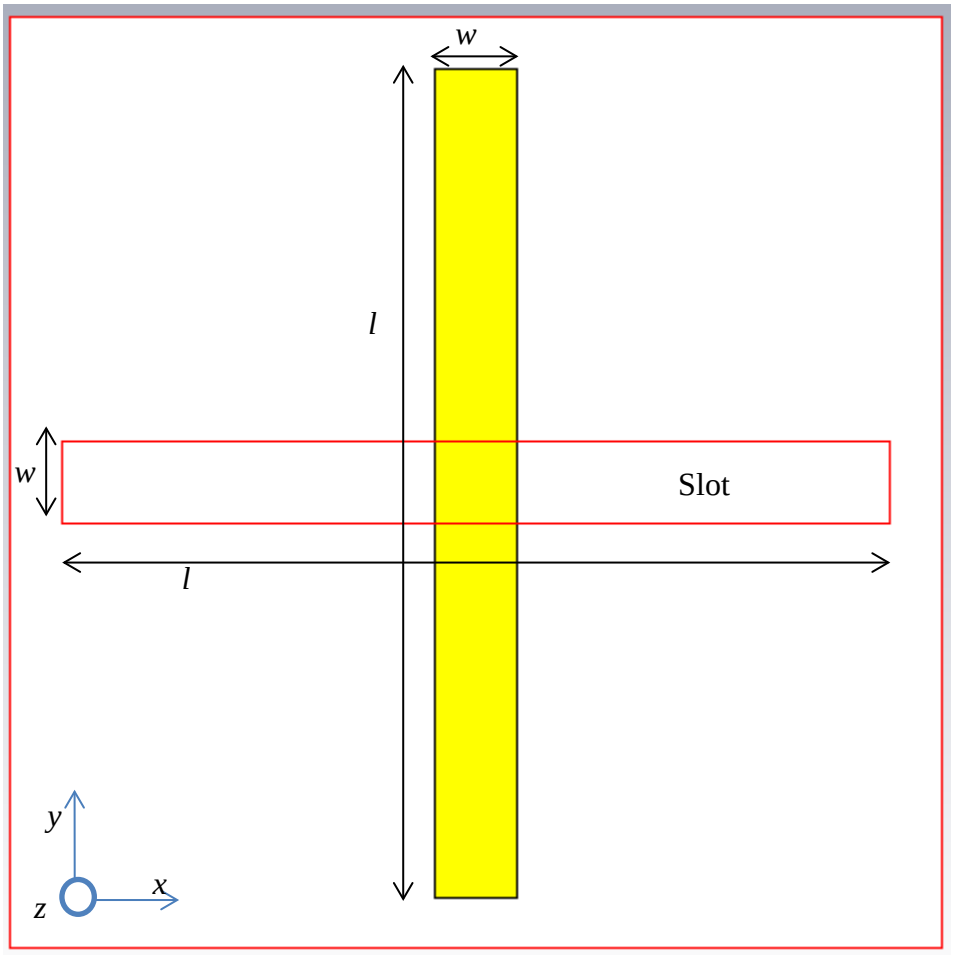

Figure 6-1: *The red outline shows the location of the slot on the other side of the dielectric. The length 'l' and the width w of the dipole and the slot is shown. The yellow colour shows the dipole.*

The square geometry of the building blocks ensures that there is no metal present directly behind the dipoles therefore it can only couple (or add capacitance) to the aperture layers across its edges. Since the added capacitance would be small for the square geometry (in comparison to the geometry with a smaller width where the dipole has metal on the other side of the dielectric) it should resonate at a much higher frequency. This is in agreement with the simulation results shown in Figure 6-2. The structure with width equal to 0.4mm exhibited a resonant frequency of 9.9 GHz while the 'square geometry' with width equal to 4mm showed a resonance at 14.1 GHz.

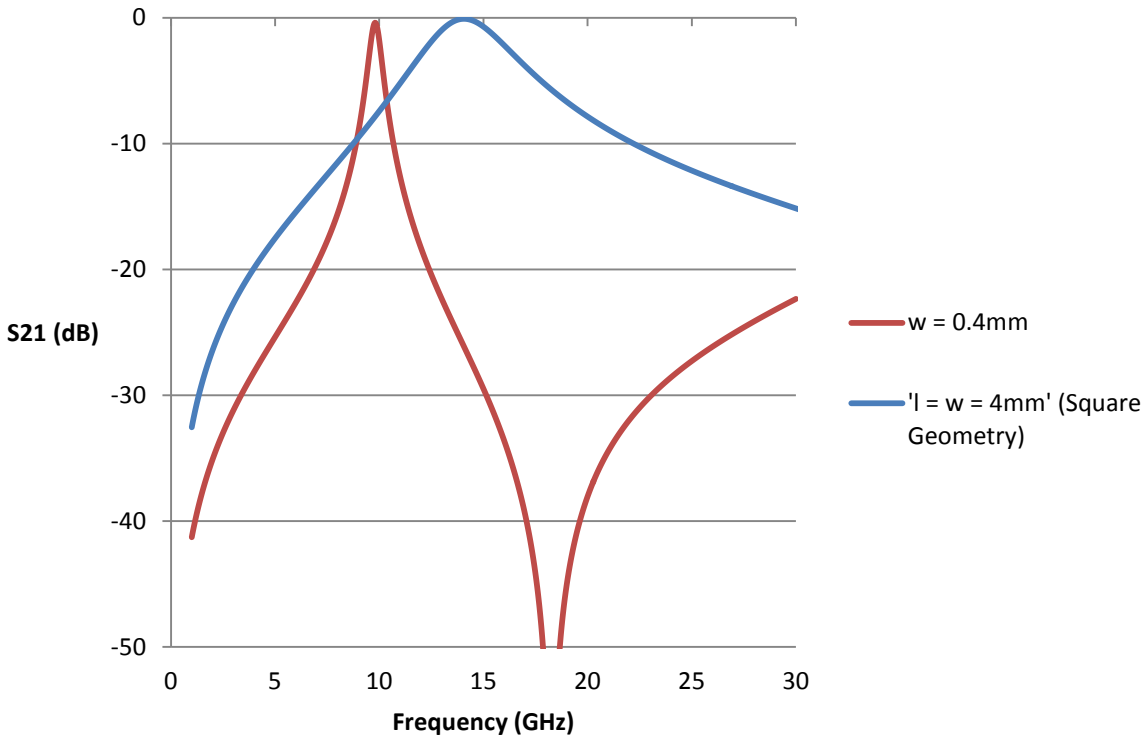

Figure 6-2: *Simulated transmission co-efficient (S21) comparison between two dipole-slot geometries with different widths*

This effect has also been illustrated with the electric fields magnitude plot of the 'square geometry' dipole-slot metasurface in Figure 6-3. Since the dipoles and slots are placed in the xy-plane, the electric fields are plotted along the z-axis (perpendicular to the plane and the dielectric). Figure 6-3 (a) shows a slanted view of the electric fields with four unit cells. It clearly shows that the electric fields are negligible in the region where there is an absence of metal on the other side of the dipole. Figure 6-3 (a) shows that the presence of the electric fields is at the edges of the dipoles. Similarly, Figure 6-3 (b) shows a side view of the magnitude of the electric fields along the z-axis. It contains two unit cells and clearly shows that the fields are maximal at the edges while they are minimal at the centre of the dipoles.

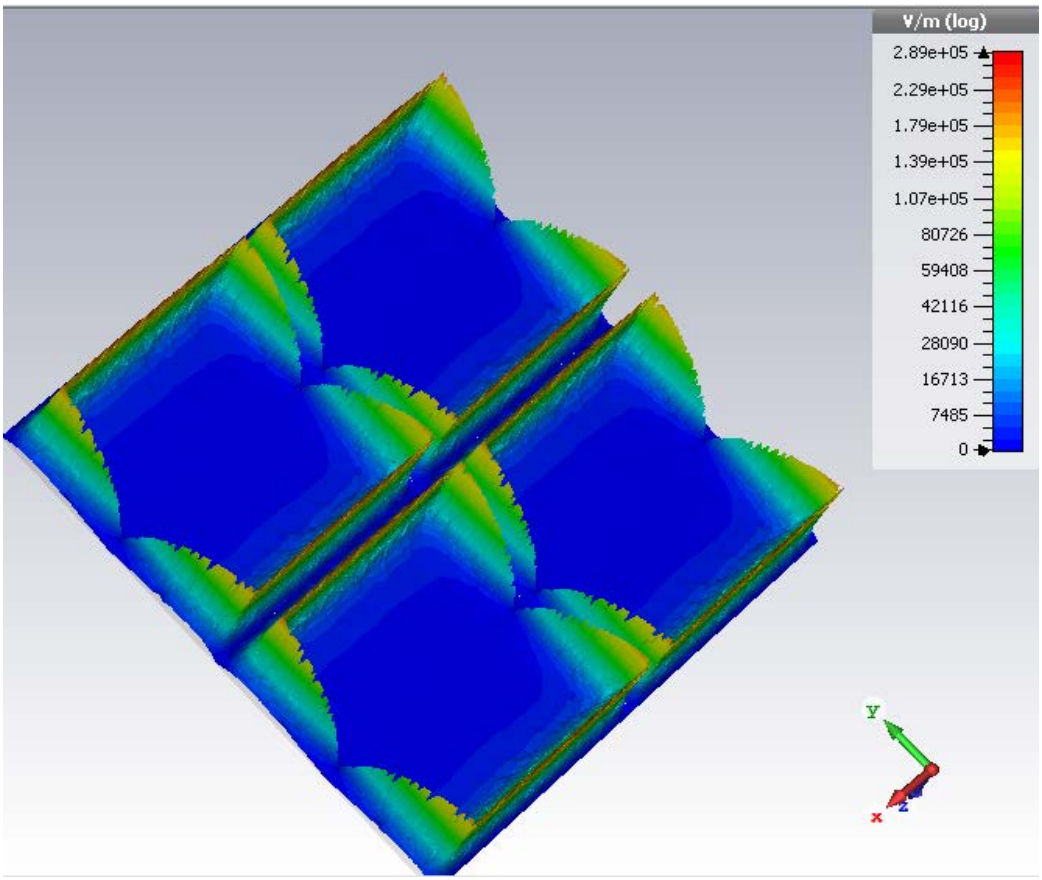

(a)

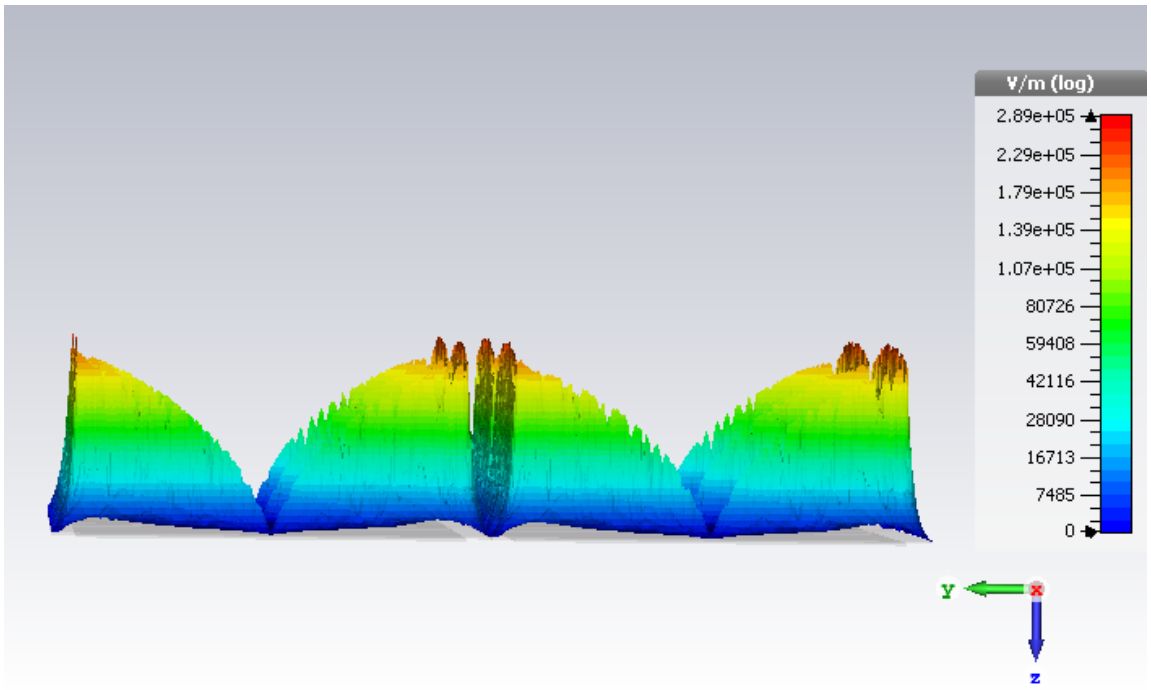

(b)

Figure 6-3: *Electric fields (magnitude) plot of a square geometry dipole-slot metasurface* ***(a)*** *slanted view;* ***(b)*** *side view (14.1 GHz)*

The maximum coupling among the two complimentary layers can be determined by finding the critical values for the "coupling co-efficient". The coupling co-efficient is equal to $w(\sin\left(\frac{\pi}{2}\frac{l-w}{l}\right)$), where *w* and *l* are shown in Figure 6-1. Two key assumptions form the basis of this coupling co-efficient:

i. The electric fields are constant along the width of the dipole

ii. $0 < w < l$

The term $\sin\left(\frac{\pi}{2}\frac{l-w}{l}\right)$ is due to the sinusoidal nature of the electric fields of the dipole. They are maximum at its edges and minimum at its centre. The argument of the sine function contains $\frac{l-w}{l}$ as the slot has to be placed the centre of the dipole. As width *w* of the slots increases, it decreases the area of the metal available to the dipole for the coupling; however for the two structures to be complimentary the width of the dipole also increases which causes an increase in the coupling area. Therefore the optimization can be achieved by maximising the coupling co-efficient. This is done by equating the derivative (rate of change) of the coupling co-efficient (with respect to the width) equal to zero, see Equation 6.1.

$$\frac{d}{dw}(wsin\left(\frac{\pi}{2}\frac{l-w}{l}\right)) = 0 \tag{6.1}$$

$$\frac{d}{dw}(wsin(\frac{\pi}{2}\left(1-\frac{w}{l}\right)) = 0$$

$$\frac{d}{dw}(wcos(\frac{\pi}{2}\left(\frac{w}{l}\right)) = 0$$

Taking the derivative with respect to *w*

$$cos\left(\frac{\pi}{2}\left(\frac{w}{l}\right)\right) - \frac{\pi}{2}\frac{w}{l}sin(\frac{\pi}{2}\left(\frac{w}{l}\right)) = 0 \tag{6.2}$$

By putting $\frac{\pi}{2}\left(\frac{w}{l}\right) = q$, the equation 6.2 can be written simply as

$$cos(q) - qsin(q) = 0 \tag{6.3}$$

Or

$$tan(q) = 1/q$$

These equations are transcendental equations and therefore they need to be solved numerically. The Newton Raphson method (based on linear approximation) follows the tangent of the curve and locates the point where it crosses the independent variable axis. This value is used to locate the next point on the curve and this is performed recursively until the solution converges (provided the initial guess lies in the basin of attraction). Equation 6.3 is solved for q using Newton's method and the answer converges to 0.86. Since $\frac{\pi}{2}\left(\frac{w}{l}\right) = q$, we can use this value to find the ratio between the width and the length of the dipoles. By substituting the value for q, we get a relation between w and l,

$$w = 0.55l \tag{6.4}$$

This relation shows that in order to achieve maximum coupling among the two layers, the value of the width needs to be 0.55 times the length of the dipoles and slots. This value of width will ensure maximum coupling between the two complementary layers and (for a constant length) maximum miniaturization will be achieved.

6.2 Simulation Experiments and Parametric Analysis on the Optimized Dipole-Slot Metasurface

In this Section, the miniaturization of the dipole-slot metasurface using the theory developed in Section 6.1 has been verified via CST simulations. A dipole-slot metasurface with length of 3mm is illuminated by a TE-polarised wave. This wave strikes the dipole-slot metasurface at normal incidence. The periodicity of the structure is 4mm. The dielectric placed between the two layers had a relative permittivity of 3 and a loss tangent of 0.025. The thickness of this dielectric was 0.07mm. The width of the dipoles and the slots was varied from 0.5mm to 2.9mm with an increment of 0.4mm. The purpose of varying the width is to find the value for which the resonant frequency of the dipole-slot metasurface is minimum thus causing maximum miniaturization. This will demonstrate that the coupling between the two layers is maximal. The results of this experiment are shown in Figure 6-4.

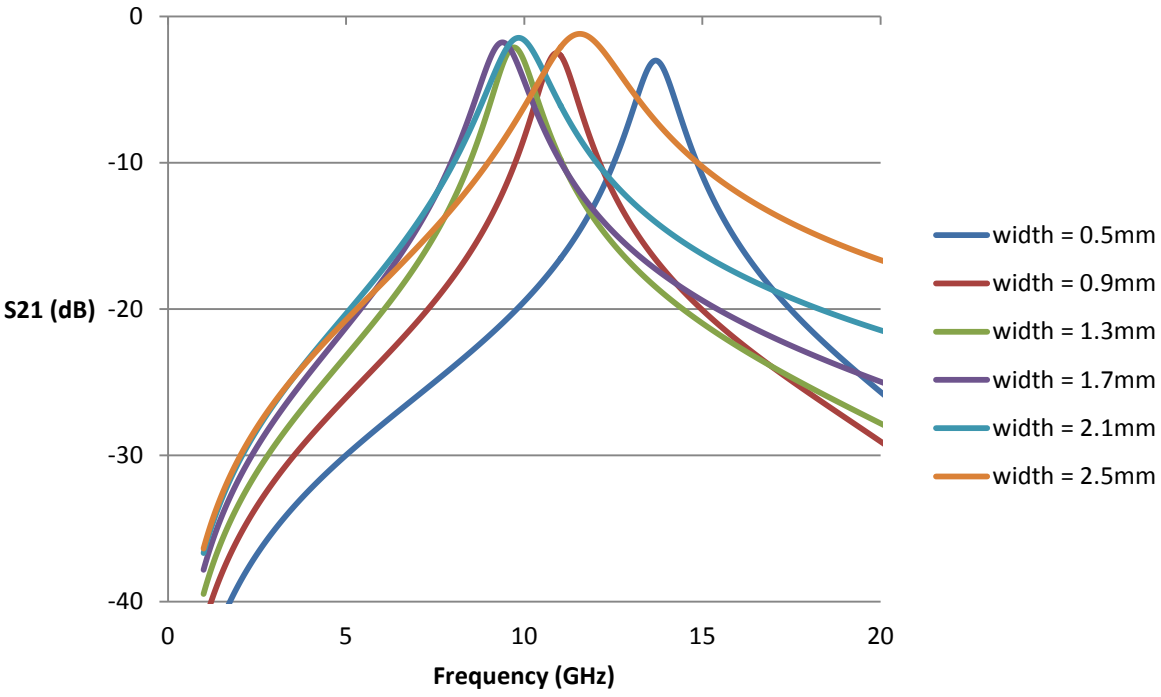

Figure 6-4: *Simulated effect of the variation in the width of the dipoles and the slots on the resonance of dipole-slot metasurfaces – length = 3mm*

Figure 6-4 shows that increasing the width from 0.5mm to 0.9, 1.3, and 1.7mm decreases the resonant frequency from 13.7 GHz to 10.9, 9.7 and 9.4 GHz respectively. Further increasing the width from 1.7 to 2.1 and 2.5mm causes an increase in the resonance from 9.4 to 9.9 GHz and 11.6 GHz respectively. This shows that the maximum coupling between the two layers occurs when the width is 1.7mm since the resonant frequency of the dipole-slot metasurface is lowest for this width. The value of the width (for the maximum coupling) of a dipole-slot metasurface, having a length (equal to) 3mm, predicted by the Equation 6.4 is 1.65mm. The two values of the width are extremely close to each other showing a strong agreement between theory and simulations. The absorption loss (1.5 – 3 dB) is due to the relatively higher value of the loss tangent of the dielectric.

Since the length is assumed to be constant in the derivation of the relation (between the length and the width for maximum coupling) in Equation 6.4, another set of simulations was performed by changing the length of the dipoles and the slots to 3.5mm while all other parameters are identical as used for the simulation results in Figure 6-4. The width of the dipoles and the slots is varied from 1.3mm to 1.9, 2, 2.1 and 2.7mm. The value of the optimum width for the maximum coupling according to Equation 6.4 is 1.92mm. The results of these simulations are shown in Figure 6-5.

The simulations show that the maximum coupling occurs when the width is equal to 2mm. This value is extremely close to the one given by the relation in Equation 6.4. The resonant frequency of the dipole-slot metasurface for this width is 7 GHz. As the length was increased to 2.7mm, the resonant frequency increased to 8 GHz while the decrease in the width to 1.3mm caused the resonance to increase to 7.8 GHz. For the width of 1.9mm and 2.1mm, the resonant frequency increased only slightly (< 0.1 GHz) and is extremely close to 7 GHz.

These simulation experiments show that the relation given in Equation 6.4 stands valid with changing the length (constant) of the dipole-slot metasurface.

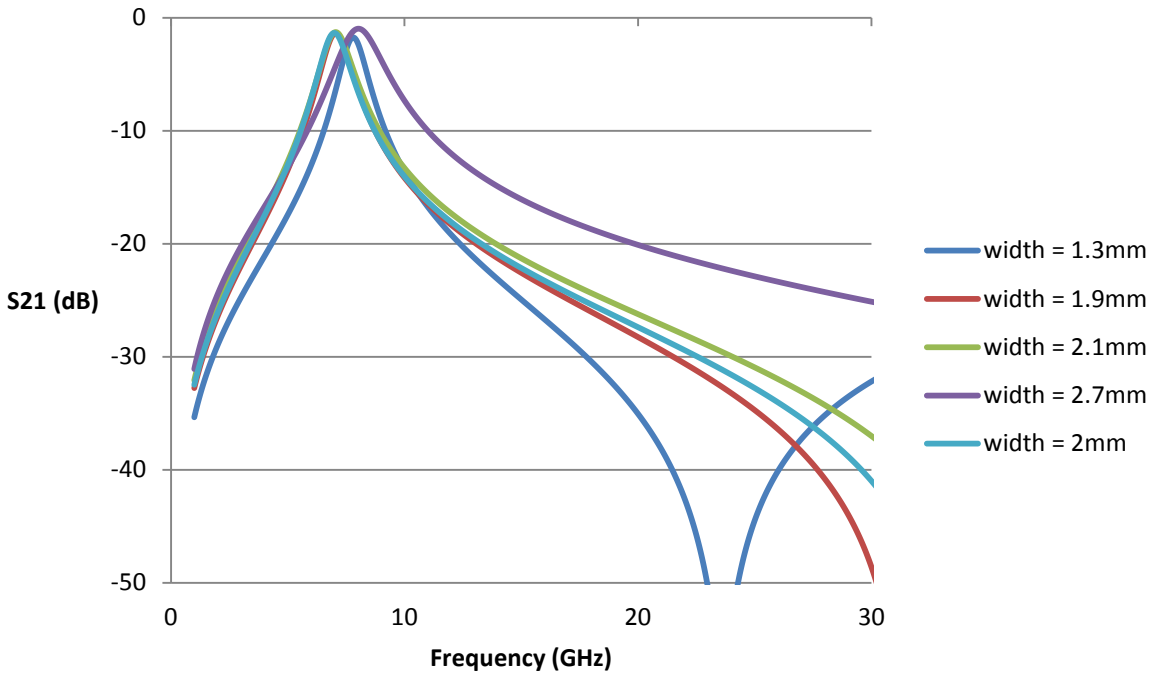

Figure 6-5: *Effect of variation of width on a dipole-slot metasurface resonance with the lengths of individual elements being 3.5mm (Simulated)*

6.2.1 Effect of the Relative Permittivity of the Dielectric on the Optimum Width

The relation between the optimum width and the length is derived by maximising the coupling co-efficient $w(\sin\left(\frac{\pi}{2}\frac{l-w}{l}\right)$. Since this coupling co-efficient is independent of the relative permittivity of the dielectric placed between the two complimentary layers, the optimum width of a dipole-slot metasurface is not effected by a change in the relative permittivity of the dielectric. This has been shown by simulating a dipole-slot metasurface with free space being employed as the dielectric which was 0.07mm thick. The length of the individual elements was 3mm and their width was varied from 1.1mm to 1.7mm and 2.3mm. The results are presented in Figure 6-6.

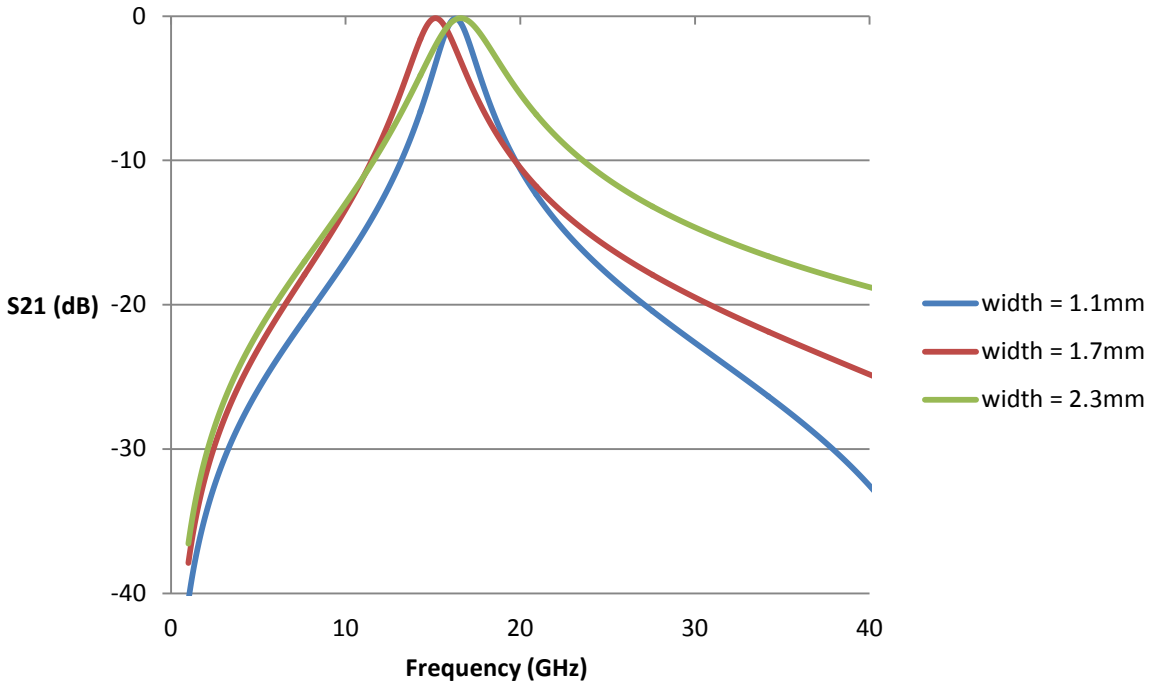

Figure 6-6: *Simulated effects of varying the width of a dipole-slot metasurface with free space being used as the dielectric (length of the individual elements is 3mm), optimized width = 1.7mm*

The results show that the maximum coupling between the two layers occurs when the width is 1.7mm (equation 6.4 predicts the width to be 1.65mm). For this width, the resonance occurred at 15.1 GHz. The transmission loss has been considerably minimised since free space is a loss-less material. The resonant frequency increased to 16.3 GHz and 16.6 GHz for the width of 1.1mm and 2.3mm respectively.

This allows to conclude that even though a decrease in the dielectric constant leads to a decrease in the coupling between the two complimentary layers (thus a higher resonant frequency in comparison with $\varepsilon_r = 3$), the width to length ratio for the maximum coupling remains unaffected. This is because of the fact that a lower dielectric index causes a decrease in coupling for all the widths; however the relative change between the inter-layer coupling for different widths is negligible.

6.2.2 Effect of Dielectric Thickness on the Optimum Width of a Dipole-Slot Metasurface

The coupling co-efficient $w(\sin\left(\frac{\pi}{2}\frac{l-w}{l}\right))$ is not related to the thickness of the dielectric however it has been shown in Section 4.2 that increasing the thickness leads to a decrease in the coupling between the two layers. This indicates that increasing the thickness should increase the resonant frequency of the dipole-slot metasurface however the optimum width should still remain unaffected. Since the length of the dipole-slot metasurface is still 3mm, the optimum width should still be close to 1.65mm according to the relation given in Equation 6.4. This is shown by varying the width of the individual elements from 1.1mm to 1.7mm and 2.3mm. The dielectric is still free space (same as in Section 6.2.1) but now its thickness has been increased to 0.1mm (from 0.07mm). The simulation results are shown in Figure 6-7.

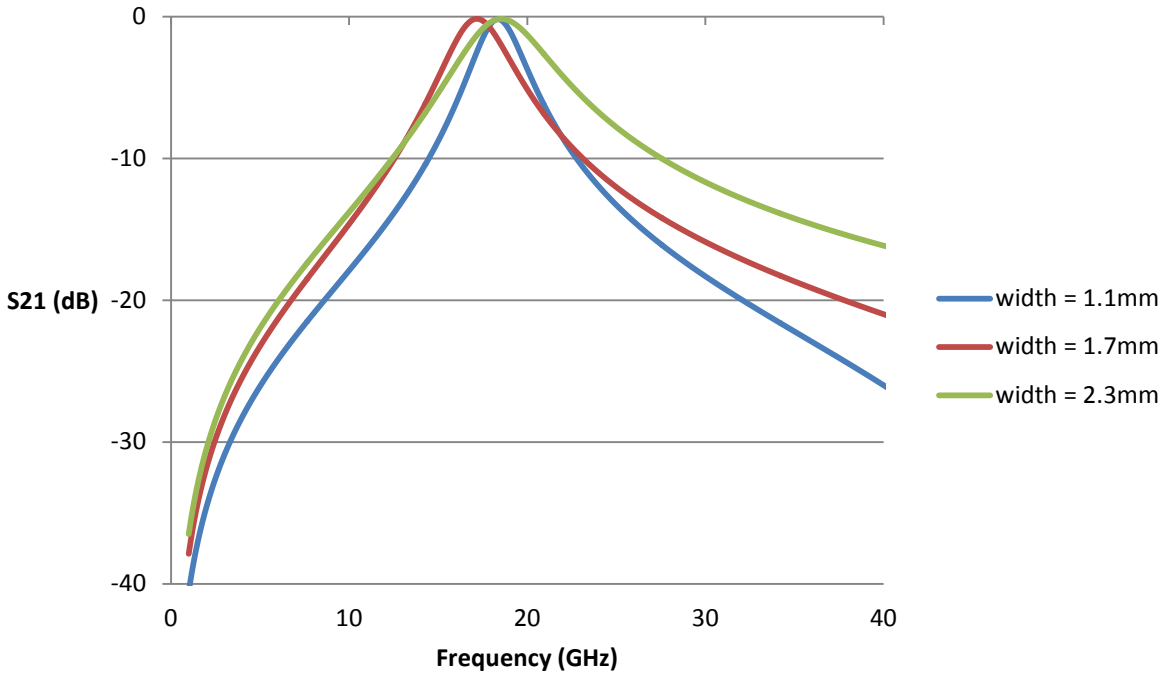

Figure 6-7: *Comparison between the resonant frequency of the dipole-slot metasurface for optimized and non-optimized widths (dielectric: free space, dielectric thickness: 0.1mm) (simulated)*

The optimum width was recorded to be 1.7mm. The structure exhibited a resonance at 17.1 GHz at this width (for the dielectric thickness equal to 0.07mm, the resonant frequency, for the same width, was 15.1 GHz). By changing the width to 1.1mm and 2.3mm, the resonant frequency increases to 18.3 GHz and 18.5 GHz respectively. This shows that the coupling co-efficient is indeed independent of the thickness of the dielectric and even though the increase in the thickness decreased the coupling, the optimum width for the maximum coupling remains unaffected.

6.3 Dipole-Slot Metasurfaces and Control of Pass band and Stop band Ratio

The optimization of the dipole-slot metasurface can be used to control the pass band and stop band ratio of such a scatterer. Since at the optimized width, the coupling between the two layers is maximal, its derivative or the rate of change (with respect to width) is equal to zero. As the width is altered this rate of change also increases; however near the optimized width (for a constant length), the rate of change remains closer to zero. This means that the change in the coupling between the two layers is also very small. As the coupling only changes slightly the deviation in the resonant frequency (from the optimized width) is also small. This has been shown via CST simulations in the Figure 6-8. For Figure 6-8, the dipole-slot metasurface has the periodicity of 4mm. The length of the individual elements is 3.5mm therefore using Equation 6.4 the optimized width is 1.92mm. The two layers are separated by a 0.07mm thick dielectric having a relative permittivity of 3 and a loss tangent of 0.025. The basic structure of this metasurface is identical to Figure 6-1. This metasurface is illuminated by a TE polarised wave at normal incidence.

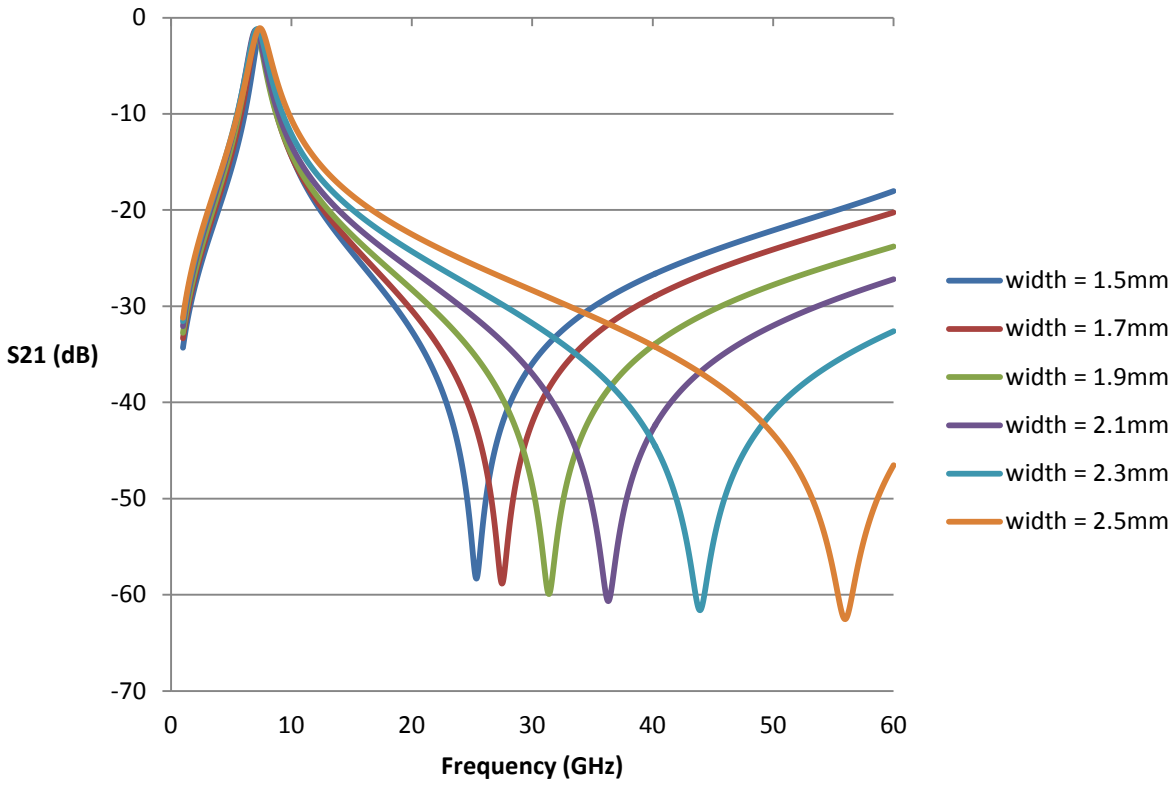

Figure 6-8: *Simulated effect of change in the width of the individual on elements on the pass band and the stop band of a dipole-slot metasurface*

It has been observed that increasing the width from 1.7mm to 2.3mm led to a consistent increase in the band stop resonant frequency; however the pass band resonant frequency marginally decreased until the width reached 2mm and started to increase after this value. The pass band resonant frequency for the width of 2mm was observed to be 7.02 GHz while the stop band resonant frequency was found to be 33.8 GHz. It is worth mentioning that even though the width is varied from 1.7mm to 2.3mm, the increase in the pass band resonant frequency is below 2.5% with respect to its minimum value. The effect of the change in the width on both resonant frequencies and its effect on the ratio between the pass band and the stop band resonance are shown in Table 6-1. A good transmission loss (less than 1.5dB) for the pass band of has been shown. The transmission loss can be further improved by using a dielectric of lower loss tangent. It was also observed that decreasing the width below 1.7mm

or increasing it beyond 2.3mm led to a more pronounced change in the pass band resonant frequency. The values for the pass band for the width of 1.3 and 2.7mm are 7.43 and 8.01 GHz respectively. This larger change is due to the reason that as the value of the width is now very different from its optimized value; therefore the rate of change of the inter-layer coupling has increased. This higher rate of change produced a much larger change in the inter-layer coupling thus causing a significant shift in the pass band resonance.

Table 6-1: *The ratio between the pass band (GHz) and the stop band (GHz) of a dipole-slot metasurface with respect to the change in the optimized width. The optimized width (showing the lowest resonance) is in* ***bold***

Width (mm)	**Pass band Resonant Frequency (GHz)**	**Stop band Resonant Frequency (GHz)**	**Frequency Ratio between Stop band and Pass band**
1.5	*7.43*	*25.36*	-
1.7	7.19	27.49	3.82
1.9	7.08	31.08	4.39
2.0	**7.02**	**33.80**	**4.81**
2.1	7.08	36.28	5.12
2.3	7.19	43.95	6.11
2.5	*7.37*	*55.99*	-

Another advantage of designing the dipole-slot metasurface at its optimized value is the increased manufacturing tolerance. Since the rate of change is zero at the optimized value and it remains closer to zero for small changes in dimensions of the individual elements therefore making the optimized structure much more tolerant to the dimensional changes afflicted by the fabrication process. For example, consider a fabrication process having an accuracy of 0.2mm. The designer expects the dipole-slot metasurface to be 0.3mm wide; however the

actual fabricated value of the width could easily be 0.5mm (due to the fabrication accuracy of 0.2mm). This change in the width will shift the resonant frequency of the dipole-slot metasurface by 2.7 GHz (the resonance for a 0.3mm wide dipole-slot metasurface is 11.6 GHz while that of a 0.5mm wide structure is 14.3 GHz). Comparing it to the design at the optimized width of 1.9mm (by Equation 6.4) – the structure should have a pass band resonance of 7.08 GHz; however, for the similar 0.2mm deviation between the expected and the fabricated width (which can now be 1.7mm), the shift in the resonance will be only 0.11 GHz clearly showing that the dipole-slot metasurface designed at the optimized width is much more tolerant to manufacturing inaccuracies/irregularities.

6.4 Experimental Verification of Optimizing the Width of a Dipole-Slot Metasurface

In this section, the optimization of a dipole-slot metasurface with respect to the width of the individual elements has been experimentally verified. Three different dipole-slot metasurfaces have been fabricated. All these metasurfaces have a periodicity of 6mm and the individual element length equal to 5mm. These structures are shown in Figure 6-9. By using equation 6.4, the optimized width for this length is equal to 2.75mm. The structure shown in Figure 6-9 (c) has the width of individual elements equal to 2.7mm. The structures shown in Figure 6-9 (a) and (b) have widths equal to 1mm and 3.9mm respectively. The purpose of three different widths is to show that the dipole-slot metasurface with the optimized width offers the maximum miniaturization by resonating at the lowest frequency. By decreasing or increasing the width (as for the samples in shown Figure 6-9 (a) and (b)), the resonant frequency increased thus causing an increase in the size of the individual unit cell with respect to resonant wavelength. The transmission response of all three metasurfaces has been

measured in a semi-anechoic chamber. The measurement setup has been described in Section 5.2.1.

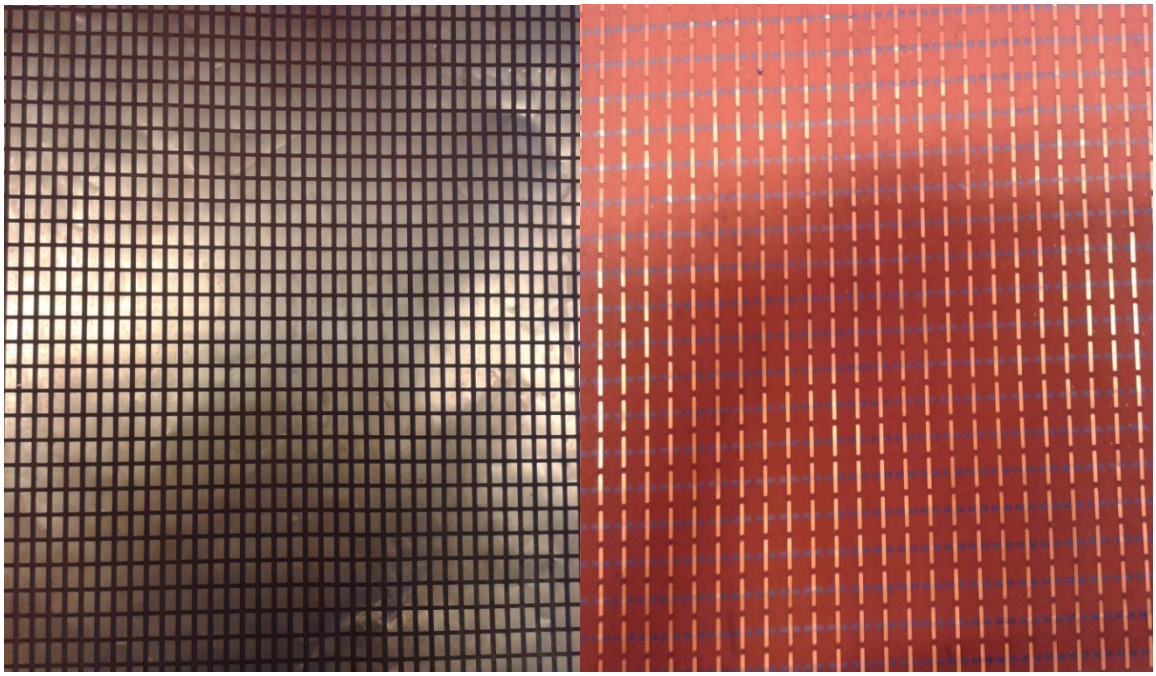

(a) (b)

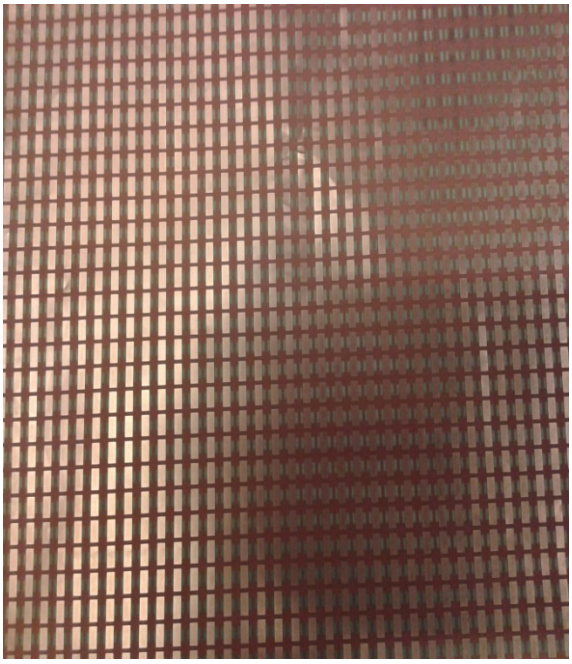

(c)

Figure 6-9: *Fabricated samples of dipole-slot metasurfaces having a periodicity of 6mm and individual lengths of elements 5mm (a) width = 3.9mm (b) width = 1mm (c) width = 2.7mm*

6.4.1 Measured Results

The three metasurfaces shown in Figure 6-9 are 264mm × 264mm thus each fabricated sheet has 44 × 44 samples and completely covers the square aperture. An excellent agreement has been found between the measured and the simulated CST values. The GTS material used for fabricating the samples was 0.044mm thick and it had a relative permittivity of 3. The measured and the simulated results, for the samples with individual elements having a width of 1mm, are shown in Figure 6-10. The measured and simulated results show a resonance at 4.78 and 4.81 GHz respectively. The measured and simulated transmission loss is 3.2 and 3.7dB respectively.

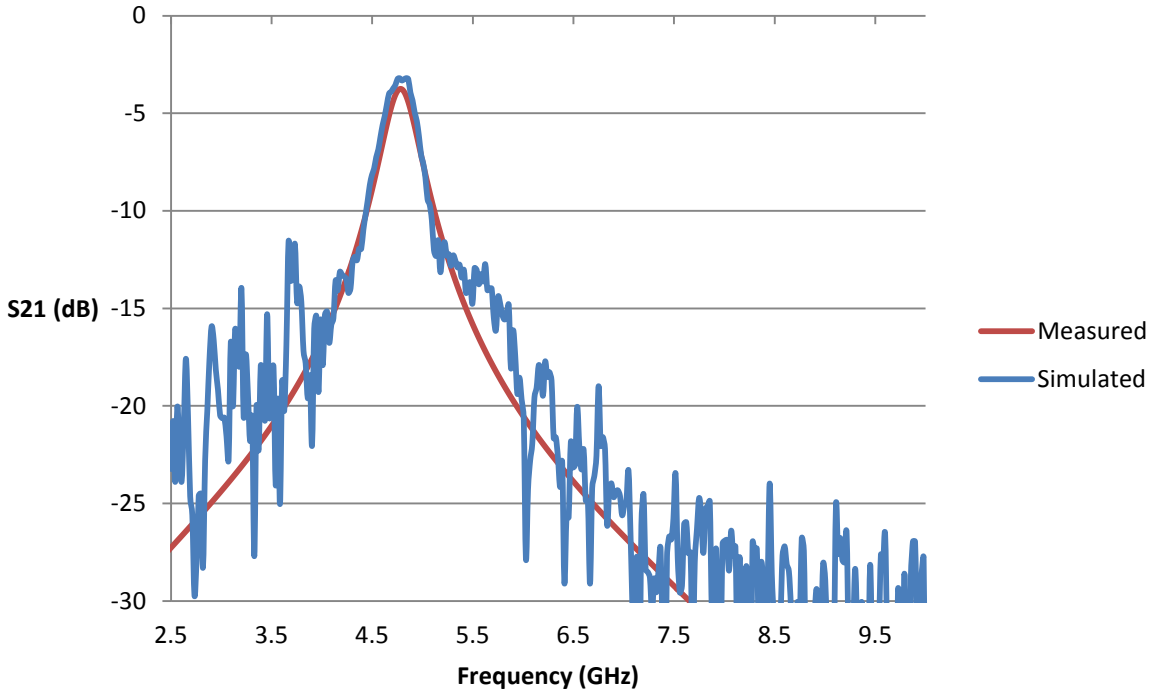

Figure 6-10: *Comparison between the simulated and measured results for the dipole-slot metasurface having a width of 1mm (shown in Figure 6-9(a))*

For the samples with width equal to 3.9mm (shown in Figure 6-9 (b)), the simulated and the measured results are shown in Figure 6-11. The simulated resonance for this structure occurred at 4 GHz while the measurements show a pass band resonance at 3.96 GHz thereby indicating an excellent agreement between the measured and the simulated values.

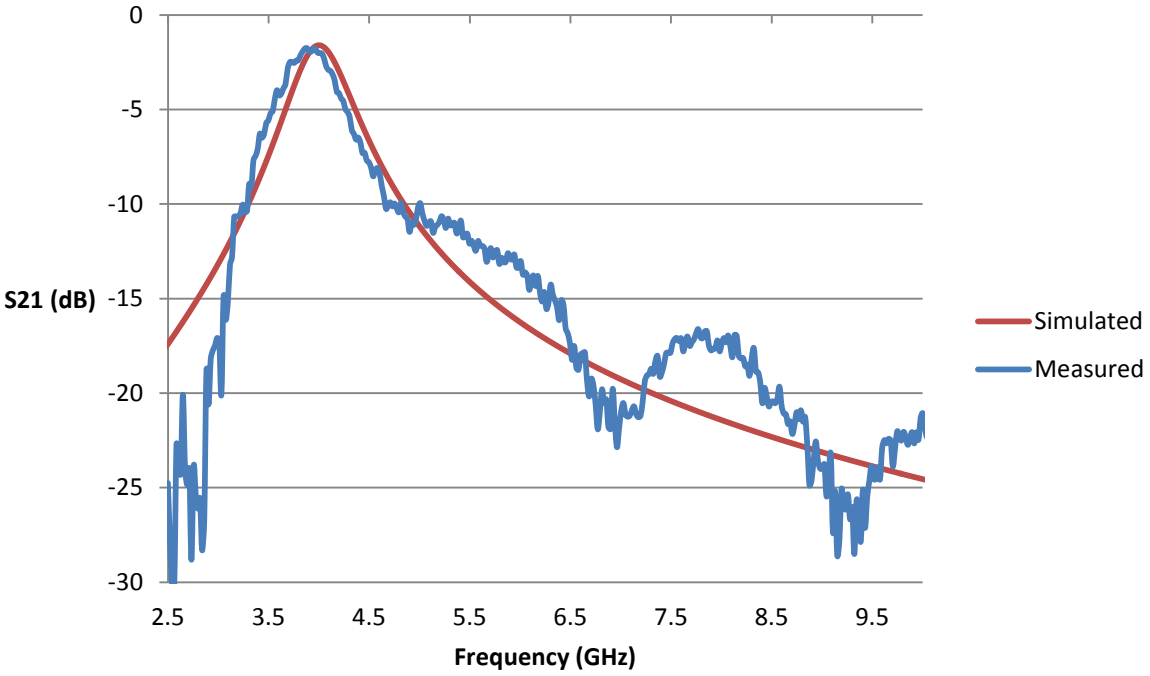

Figure 6-11: *Simulated and Measured results for a dipole-slot metasurface with the width of the individual elements being 3.9mm (shown in Figure 6-9(b))*

The optimized width for the length 5mm is 2.75mm. The samples with the optimized width (2.7mm) are shown in Figure 6-9 (c). The simulated and the measured results for this sample are shown in Figure 6-12. A good agreement between both results was recorded. The simulated resonance occurred at 3.37 GHz while the measured value was at 3.28 GHz. The case of small deviation in the measured results for this metasurface above 5 GHz is uncertain, but the response never rises above -15dB..

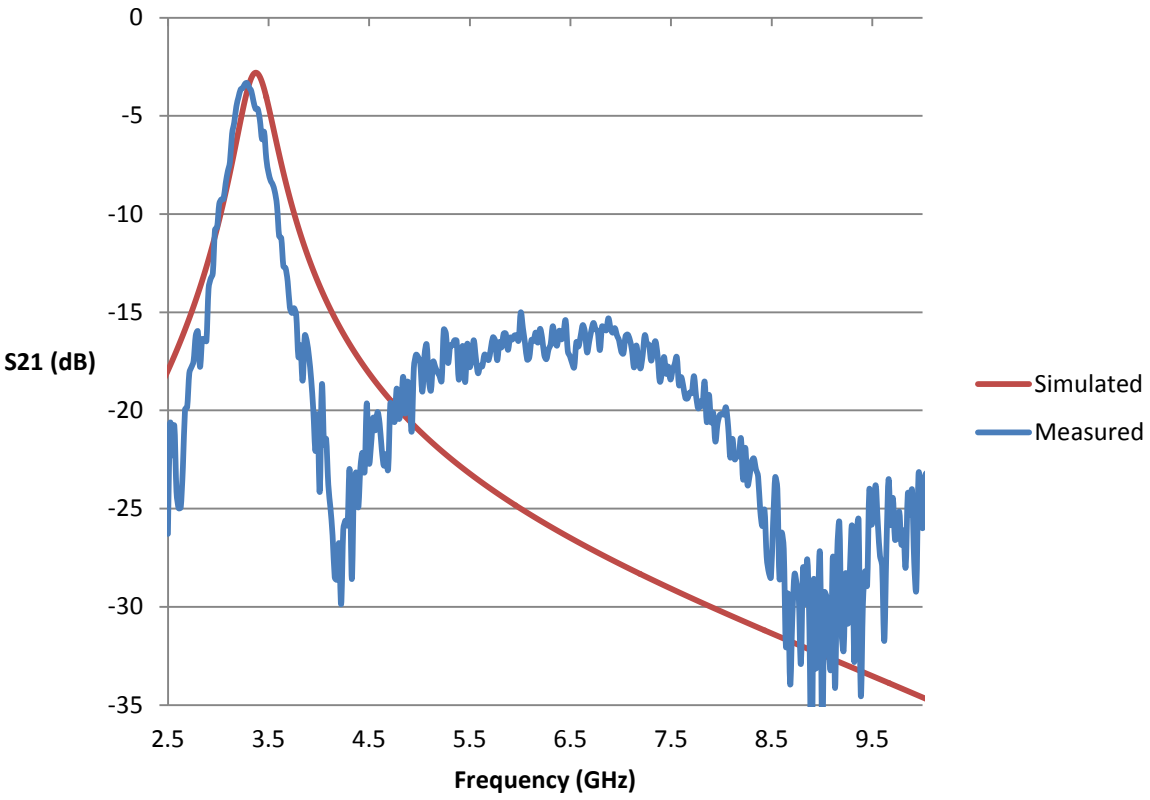

Figure 6-12: *Simulated and measured results for the optimized width equal to 2.7mm (shown in Figure 6-b (c))*

The measured resonant frequency for all three widths (1, 2.7 and 3.9mm) is 4.78, 3.28 and 3.96 GHz respectively. The comparison between the measured transmission responses of all three fabricated samples is shown in Figure 6-13. The measured results therefore validate the theory of maximising the coupling co-efficient. Figure 6-13 clearly indicates that the resonant frequency of the dipole-slot metasurface is minimum for the optimized width hence maximum miniaturization was achieved; any deviation from this optimized value (by either increasing or decreasing the width) causes the resonant frequency to increase (as the inter-layer coupling decreases) and the unit cell size to shrink with respect to the resonant wavelength.

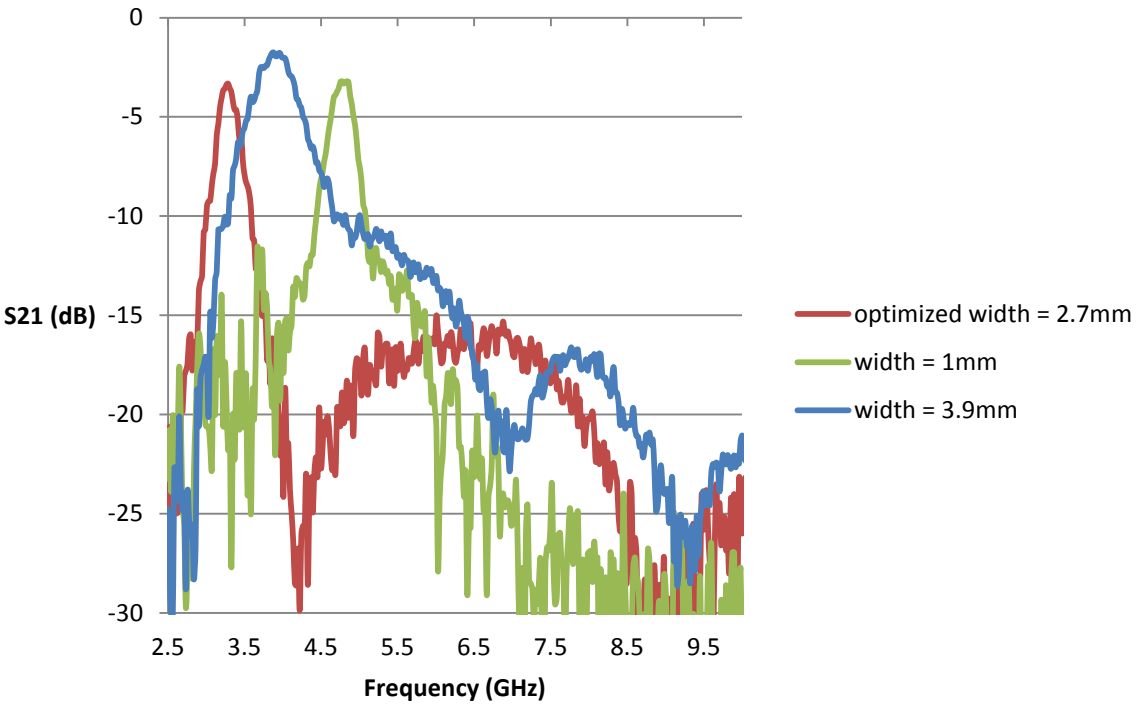

Figure 6-13: *Comparison between the measured results of all three metasurfaces. This figure clearly shows that the resonant frequency is lowest for the optimized width and it increases if the width is either increased or decreased (from the optimized value)*

6.5 Analytical Circuit Modelling of a Complementary Metasurface

A dipole-slot metasurface consists of two complementary periodic layers, an apertures array which is inherently band pass and an array of metallic scatterers who are naturally band stop. However, when combined together the resulting metasurface exhibits a pass band behaviour (which is the natural response of a periodic apertures layer). This section analytically explains the reason for this behaviour. The electric and magnetic field integral equations are derived for a Babinet complementary metasurface. These equations are then used to derive a generalised analytical circuit model for any complementary metasurface. Although any dielectric could be employed between the two layers of the complementary metasurface, for mathematical simplicity it is assumed that the dielectric between the two layers is identical to the one surrounding this metasurface. This has been illustrated in Figure 6-14. The equivalent circuit modelling of a periodic structure to explain its behaviour has been a very potent approach. Since FSS is a periodic structure, its behaviour has been often explained with equivalent circuit modelling [1]–[5]. A similar approach has been applied to metamaterials and metasurfaces [6]–[8]. A circuit model to characterise the behaviour of Huygen's metasurfaces and checkerboard metasurfaces has been presented in [9], [10]. An equivalent circuit modelling approach has also been employed to design a tuneable absorbing graphene metasurface in the terahertz region [11].

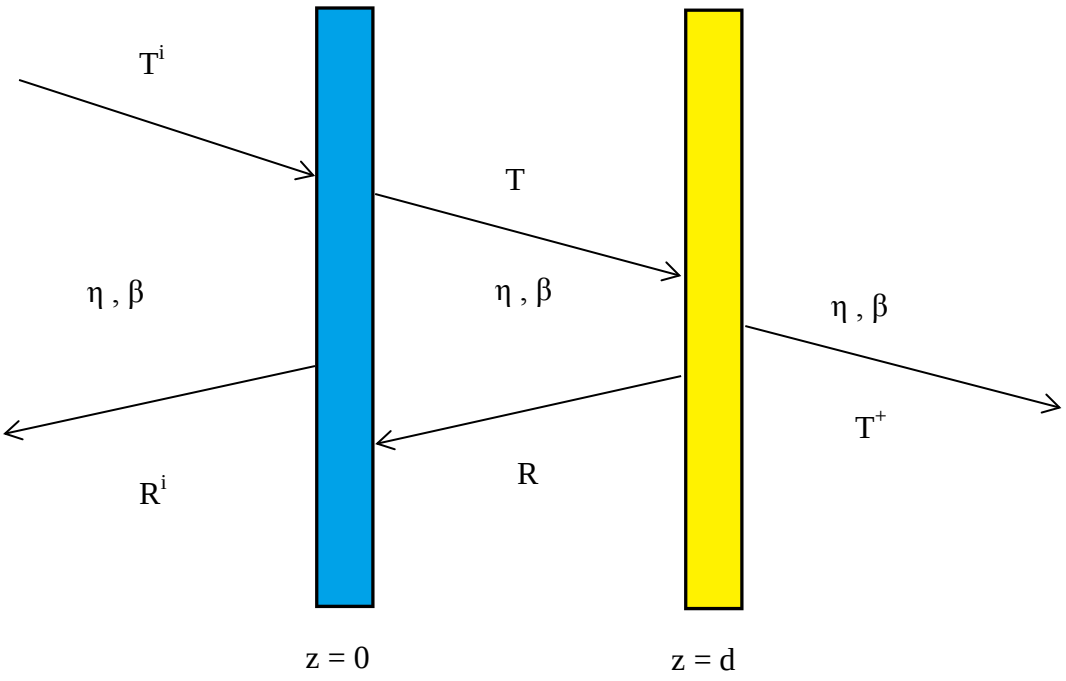

Figure 6-14: *The cross section of a complementary metasurface with the wave travelling along positive z-axis. Blue shows the layer of metallic scatterers while yellow is the array of apertures (their Babinet's complement)*

6.5.1 Integral Equations

This subsection (6.5.1) is based on the work presented in [1] and [12] (The integral equations derived are based on the concepts presented in [12] and the Floquet mode theory for periodic structures is covered in detail in [1]). Consider a complementary metasurface placed in the xy-plane. The periodicity of the structure is *a* along both x- and y-axes. The incoming electromagnetic wave is travelling in the direction of the positive z-axis. The array of metallic scatterers has been placed at z = 0. The thickness of the dielectric placed between the two layers is *d*. Assuming that the thickness of the metallic and the apertures layer is negligible, the aperture layer is therefore placed at $z = d$. This has been shown in Figure 6-14. It is assumed that the medium present between the two layers is free space. Since a complementary metasurface is a periodic structure therefore it's electric and magnetic fields

can be defined by using Floquet expansion [1]. The Floquet modes (over a unit cell) ψ_{pq} are defined such that [1]

$$\iint \psi_{pq}\,\psi_{rs}^{*} = \begin{cases} A & if\ p = r, q = s \\ 0 & if\ p \neq r, q \neq s \end{cases}$$

where ψ^* is the complex conjugate of ψ and A is the area of the unit cell equal to a^2.

The electric and magnetic fields for the three regions, shown in Figure 6-14, can be written in terms of Floquet modes as follows

For, $z \leq 0$

$$\vec{E}^{-} = \vec{E}^{i} + \sum_{mpq} R_{mpq}^{i} e^{j\beta_{pq}z} \psi_{pq} \vec{K}_{mpq}$$

$$\vec{H}^{-} = \vec{H}^{i} - \sum_{mpq} \eta_{mpq} R_{mpq}^{i} e^{j\beta_{pq}z} \psi_{pq} \vec{z} \times \vec{K}_{mpq}$$

(6.5)

For, $0 \leq z \leq d$

$$\vec{E}' = \sum_{mpq} (T_{mpq} e^{-j\beta_{pq}z} + R_{mpq} e^{j\beta_{pq}z}) \psi_{pq} \vec{K}_{mpq}$$

$$\vec{H}' = \sum_{mpq} \eta_{mpq} (T_{mpq} e^{-j\beta_{pq}z} - R_{mpq} e^{j\beta_{pq}z}) \psi_{pq} \vec{z} \times \vec{K}_{mpq}$$

(6.6)

For, $z \geq d$

$$\vec{E}^{+} = \sum_{mpq} T^{+}_{mpq} e^{-j\beta_{pq}z} \psi_{\mathrm{pq}} \vec{K}_{mpq}$$

$$\vec{H}^{+} = \sum_{mpq} \eta_{mpq} T^{+}_{mpq} e^{-j\beta_{pq}z} \psi_{\mathrm{pq}} \vec{\mathrm{z}} \times \vec{K}_{mpq}$$

(6.7)

where E^{i} is given by

$$\vec{E}^{i} = \sum_{mpq} T^{i}_{m00} e^{-j\beta_{00}z} \psi_{00} \vec{K}_{m00}$$

(6.8)

The subscript m is used to signify the transverse mode and $\vec{\mathrm{z}}$ is the unit vector along the z-axis. η_{mpq} is the modal admittance such that for TM mode [1]

$$\eta_{1pq} = \frac{k\eta}{\beta_{pq}}$$

(6.9)

For the TE mode [1]

$$\eta_{2pq} = \frac{\beta_{pq}\eta}{k}$$

(6.10)

η is free space admittance given by $\eta = \sqrt{\varepsilon_0 / \mu_0}$, ε_0 and μ_0 are the permittivity and permeability of free space, p and q represent the Floquet mode number and $\eta_{m00} = \eta$.

β_{pq} is the propagation constant such that

$$\beta_{pq} = \sqrt{k^2 - k_x^2 - k_y^2}$$

(6.11)

For pure TM/TE incidence, the relationship between k_x and k_y is given by [1]

$$\vec{k}_{tpq} = \overrightarrow{k_t} + p\vec{k}_1 + q\vec{k}_2 = k_x\vec{\mathrm{x}} + k_y\vec{\mathrm{y}} \tag{6.12}$$

$$\vec{k}_1 = \frac{2\pi}{a}\vec{\mathrm{y}} \tag{6.13}$$

$$\vec{k}_2 = \frac{2\pi}{a}\vec{\mathrm{x}} \tag{6.14}$$

$\vec{K}_{mpq}$ is the unit vector and is given by equations 6.15a and 6.15b

For TM mode [1]:

$$\vec{K}_{1pq} = \frac{\vec{k}_{tpq}}{|\vec{k}_{tpq}|} \tag{6.15a}$$

For TE mode [1]:

$$\vec{K}_{2pq} = \vec{\mathrm{z}} \times \vec{K}_{1pq} \tag{6.15b}$$

By applying appropriate boundary conditions at *z = 0* and *z = d*, the coupled integral equations can be derived for the complementary metasurface. At *z = 0*, across the metallic scatterers array, the electric field is continuous and equal to zero therefore this can be used to formulate the Electric field integral equation (EFIE).

At z = 0,

$$T^i_{m00} + R^i_{mpq} = T_{mpq} + R_{mpq} \tag{6.16}$$

Since the tangential magnetic field is discontinuous at *z = 0*, therefore

$$\eta_{m00}T^{i}_{m00} - \eta_{mpq}R^{i}_{mpq} = \eta_{mpq}T_{mpq} - \eta_{mpq}R_{mpq} + {\boldsymbol{J_{mpq}}}/{A} \tag{6.17}$$

where $\boldsymbol{J_{mpq}}$ is the Floquet spectrum of the current density.

Since tangential electric field is continuous at z = d, across the apertures, therefore

$$T_{mpq}e^{-j\beta_{pq}d} + R_{mpq}e^{j\beta_{pq}d} = T^{+}_{mpq}e^{-j\beta_{pq}d} = \boldsymbol{E_{mpq}}/A \tag{6.18}$$

where $\boldsymbol{E_{mpq}}$ represent the Floquet spectrum of the electric field.

Substituting R^{i}_{mpq} from equation 6.16 in to 6.17 yields

$$2\eta_{m00}T^{i}_{m00} = 2\eta_{mpq}T_{mpq} - {\boldsymbol{J_{mpq}}}/{A} \tag{6.19a}$$

$$T_{mpq} = T^{i}_{m00} - {\boldsymbol{J_{mpq}}}/{2\eta_{mpq}A} \tag{6.19b}$$

Similarly equation 6.18 can be rewritten as

$$R_{mpq} = \boldsymbol{E_{mpq}}e^{-j\beta_{pq}d}/A - T_{mpq}e^{-2j\beta_{pq}d} \tag{6.20}$$

By applying the boundary condition that the tangential electric field is zero on the surface of the conductor, we can write EFIE as

$$\sum_{mpq}(T_{mpq} + R_{mpq})\psi_{\mathrm{pq}}\vec{K}_{mpq} = 0$$

By substituting the values of R_{mpq} and T_{mpq} from equations 6.20 and 6.19b respectively, EFIE can be written as

$$\sum_{mpq} T^{i}_{m00} - \frac{\boldsymbol{J_{mpq}}}{2\eta_{mpq}A} + \frac{\boldsymbol{E_{mpq}}e^{-j\beta_{pq}d}}{A} - T^{i}_{m00}e^{-2j\beta_{oo}d} + \frac{\boldsymbol{J_{mpq}}e^{-2j\beta_{pq}d}}{2\eta_{mpq}A})\psi_{\mathrm{pq}}\vec{K}_{mpq} = 0$$

$$\sum_{m} T^{i}_{m00}\left(1 - e^{-2j\beta_{00}d}\right)\psi_{pq}\vec{K}_{m00} = \sum_{mpq}\left(\frac{\boldsymbol{J_{mpq}}}{2\eta_{mpq}A}\left(1 - e^{-2j\beta_{pq}d}\right) - \frac{\boldsymbol{E_{mpq}}e^{-j\beta_{pq}d}}{A}\right)\psi_{pq}\vec{K}_{mpq}$$

(6.21)

The magnetic field integral equation (MFIE) can be written by applying boundary condition at $z = d$, since the magnetic field is continuous across the apertures therefore

$$\sum_{mpq}\left(\eta_{mpq}T_{mpq}e^{-j\beta_{pq}d} - \eta_{mpq}R_{mpq}e^{j\beta_{pq}d} - \frac{\eta_{mpq}\boldsymbol{E_{mpq}}}{A}\right)\psi_{pq}\vec{z} \times \vec{K}_{mpq} = 0$$

By substituting T_{mpq} and R_{mpq} from equations 6.19b and 6.20, MFIE can be rewritten as

$$\sum_{mpq}\eta_{mpq}\left(\left(T^{i}_{m00} - \boldsymbol{J_{mpq}}\Big/2\eta_{mpq}A\right)e^{-j\beta_{pq}d} - \left(\boldsymbol{E_{mpq}}e^{-j\beta_{pq}d}/A - T^{i}_{m00}e^{-2j\beta_{pq}d}\right.\right.$$

$$\left.\left. - \boldsymbol{J_{mpq}}e^{-2j\beta_{pq}d}\Big/2\eta_{mpq}A\right)e^{j\beta_{pq}d} - \frac{\boldsymbol{E_{mpq}}}{A}\right)\psi_{pq}\vec{z} \times \vec{K}_{mpq} = 0$$

$$\sum_{m}\left(2\eta_{m00}T^{i}_{m00}e^{-j\beta_{00}d}\right)\psi_{00}\vec{z} \times \vec{K}_{m00} = \sum_{mpq}\left(\left(\frac{\boldsymbol{J_{mpq}}}{A}e^{-j\beta_{pq}d}\right) + \frac{2\eta_{mpq}\boldsymbol{E_{mpq}}}{A}\right)\psi_{pq}\vec{z} \times \vec{K}_{mpq}$$

(6.22)

6.5.2 Method of Moments Solution and Circuit Modelling using Integral Equations

The integral equations, 6.21 and 6.22, can be solved by using the method of moments (MoM) [13]. MoM converts the two integral equations in to a matrix equation *(AX = B)* which can be solved by using Lower Upper matrix decomposition and matrix inversion [13]. This conversion is achieved by writing the currents and the fields (in the EFIE and MFIE) as a sum of basis function(s). The number of basis functions is approximated to be finite and a non-trivial solution is obtained when these functions are orthonormal (and linearly independent) [1]. Before matrix inversion the dot product of the matrices is taken with the testing functions. In this chapter, the Galerkin approach was used and the testing functions are the same as the basis functions [1], [13]. After taking the dot product with the testing function, the EFIE and MFIE given by equations 6.21 and 6.22 respectively are reduced to the matrix equation 6.23.

$$\begin{aligned} Z_d I - bV &= V_i \\ bI + Y_s V &= I_i \end{aligned} \tag{6.23}$$

where the first is EFIE and the second is MFIE; $\boldsymbol{h}$ and $\boldsymbol{e}$ are the basis and testing functions for the arrays of the metallic and the aperture elements respectively

$$Z_d = \sum_{mpq} \left(\frac{\left(1 - e^{-2j\beta_{pq}d}\right)}{2\eta_{mpq}A}\right) \boldsymbol{h}\boldsymbol{h}^*$$

$$b = \sum_{mpq} \frac{e^{-j\beta_{pq}d}}{A} \boldsymbol{h}\boldsymbol{e}^*$$

$$Y_s = \sum_{mpq} \frac{2\eta_{mpq} e^{-j\beta_{pq} d}}{A} \boldsymbol{e}\boldsymbol{e}^*$$

$$V_i = \left(1 - e^{-2j\beta_{00} d}\right) \boldsymbol{h} \begin{cases} E_{TM}^i \\ E_{TE}^i \end{cases}$$

$$I_i = \left(2e^{-j\beta_{00} d}\right) \boldsymbol{e} \begin{cases} \frac{\eta k}{\beta_{00}} E_{TM}^i \\ \frac{\eta \beta_{00}}{k} E_{TE}^i \end{cases}$$

The term Z_d represents the impedance of the periodic metallic array of elements which are placed in the close proximity of the apertures layer. The two layers are separated by a distance *d*. The term *b* in EFIE takes into account the effects of the radiation of the apertures array on the periodic metallic array. Similarly the Y_s term in the MFIE (equation 6.23b) is the free space admittance of the apertures array, radiating under an incident tangential magnetic field; while the term *b* represents the effects of the periodic metallic layer on the apertures array.

Since the distance between the two complementary layers is extremely small when compared with the resonant frequency wavelength of the metasurface, hence the thickness can be thought of as approaching to zero. This can be approximated in the driving term, such that *d = 0*. This leads to the driving term in the EFIE (equation 6.23a) going to zero. Therefore the equation 6.23 can be re-written as

$$Z_d I - bV = 0$$

$$bI + Y_s V = I_i \tag{6.24}$$

And since the distance between the two complementary layers is extremely small; a single equivalent impedance, placed in parallel to the transmission line, can be used to model the behaviour of this metasurface as shown in Figure 6-15. From the circuit in Figure 6-15

$$\begin{bmatrix} Z_d & -b \\ b & Y_s \end{bmatrix} \begin{bmatrix} I \\ V \end{bmatrix} = \begin{bmatrix} 0 \\ I_i \end{bmatrix}$$

$$\begin{bmatrix} I \\ V \end{bmatrix} = \frac{1}{Z_d Y_s + b^2} \begin{bmatrix} Y_s & b \\ -b & Z_d \end{bmatrix} \begin{bmatrix} 0 \\ I_i \end{bmatrix}$$

$$I = \frac{bI_i}{Z_d Y_s + b^2}$$

$$V = \frac{Z_d I_i}{Z_d Y_s + b^2}$$

$$\frac{I}{V} = \frac{b}{Z_d}$$

$$\frac{V}{I_i} = \frac{Z_d Z_s}{Z_d + b^2 Z_s}$$

$$\frac{I_i}{V} = Y_s + b^2 Y_d$$

(6.25)

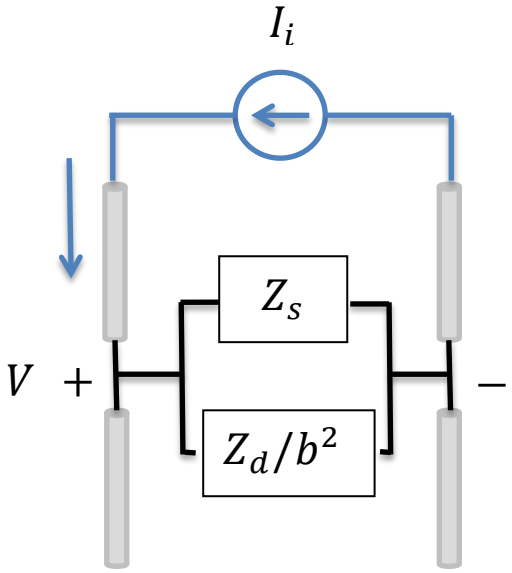

Figure 6-15: *Equivalent circuit model of a Babinet complementary coupled metasurface*

Equation 6.25 shows that the equivalent impedance of two Babinet's complementary layers (in a coupled metasurface) is the parallel configuration between the two admittances Y_s and $b^2 Y_d$. This also shows that by making an appropriate substitution the two integral equations are replaced by a single equation with one variable which can be used to determine the response of any coupled complementary metasurface.

The equivalent circuit model, shown in Figure 6-15, also gives insight into the behaviour of a complementary metasurface. The complementary metasurface has a layer of a metallic array which has a natural band stop response while the second layer consists of apertures and its natural response is that of a band pass filter. From equation 6.25, the equivalent impedance of the complementary metasurface is parallel between the impedance of the apertures and the impedance of the metallic array (divided by the square of coupling factor *b*). The response of a circuit is always band pass when its individual circuit elements (capacitors/inductors) are

placed in parallel. This is exactly the case for a Babinet complementary metasurface therefore its response mimics that of an aperture layer albeit at a much lower frequency (for a circuit transmission response to be band stop, its circuit elements need to be in series with each other). The lower frequency resonance behaviour can also be explained using the analytical circuit model. Since the two impedances are parallel and the dominant element of the metallic layer is capacitance therefore when such an element is placed in parallel to a band pass structure, it causes a resultant increase in the capacitance of the entire structure thus leading to a decrease in the resonant frequency.

A different way to explain the same phenomenon can be explained via integral equations. The right hand side term of the equation 6.24 is 0, which shows that the response of the metallic layer after taking into account the effects of the complementary layer is essentially cancelled. However this is not the case for the MFIE since its forcing term does not approach zero. Therefore the response of the complementary metasurface can be completely characterised by a single MFIE equation. As the MFIE accounts for the behaviour of the apertures, hence the resulting response of the complementary metasurface also resembles that of a periodic apertures layer; therefore a complementary metasurface will always have a band pass response (even though one of its two building blocks is a band stop element).

6.6 Comparison of Analytical Equivalent Circuit Model with Simulations

To compare the generalised equivalent circuit of the complementary metasurface, the first step was to define a particular Babinet complementary metasurface. Since a periodic layer of dipoles is a Babinet's complement of a periodic slots array, a dipole-slot metasurface was utilised to compare the equivalent circuit with the full wave simulations using CST

Microwave Studio. The method of moments analysis requires modelling the integral equation with basis functions. For accurate modelling, multiple basis functions are used. This also affects the terms in equation 6.24. Since more than one basis function was used for the both layers of the metasurface, each term of the equation namely Z_d, b, Y_s, V, I and I_i also becomes a matrix. The equation 6.24 is then re-written as

$$Z_d I - bV = 0$$

$$bI + Y_s V = I_i$$

$$Z_d I = bV$$

$$I = (Z_d)^{-1} bV$$

$$b(Z_d)^{-1} bV + Y_s V = I_i$$

$$V = (b(Z_d)^{-1} b + Y_s)^{-1} I_i$$

For $(Z_d)^{-1} = Y_d$, this can be written as

$$V = (bY_d b + Y_s)^{-1} I_i$$

If *n* is the number of basis functions used for the both layers then Y_d, b, Y_s are $n \times n$ matrices while V and I_i are matrices of order $n \times 1$. The dipole and slots used to construct the dipole-slot metasurface have a length equal to 9.5mm. Both are 0.3mm wide and are separated by a distance of 0.07mm. The material present between the two layers is free space. The periodicity of the structure is 10mm. The length of the dipoles is oriented along the x-axis while the slots are placed along the y-axis. The basis functions used to model the metallic (dipole) layers are $\sin(\frac{\pi x}{ld})$, $\sin(\frac{3\pi x}{ld})$ and $\sin(\frac{5\pi x}{ld})$, while *ld* is the length of the dipoles. Since the fields on the dipoles are a function of sine therefore entire domain basis functions are utilised. These basis functions are also orthogonal to each other. Similarly for the slots layer, the basis and testing functions used are also $\sin(\frac{\pi y}{ls})$, $\sin(\frac{3\pi y}{ls})$ and $\sin(\frac{5\pi y}{ls})$ where *ls* is the

length of the slots. The slots are rotated by 90 degrees with respect to the dipoles therefore they are placed along the y-axis. The number of Floquet modes used for both layers in order to obtain a converged solution for the transmission response (and cover the spectra of all the basis functions) is found to be 37. This structure was then also simulated in CST by using periodic boundary conditions. A TM polarised wave was incident at the normal on the dipole-slot metasurface. The comparison between the transmission response of the equivalent circuit model and the full wave simulations using CST is shown in Figure 6-16.

The equivalent circuit model exhibits a resonance at 8.4 GHz while CST simulations show a resonance at 8.3 GHz. The transmission loss simulated in CST is 0.02dB while that observed in the equivalent circuit model is 0.39dB. Thus an excellent agreement between the equivalent circuit model and the full wave simulations was observed. This also shows that the approximation made in the EFIE to simplify the model and effectively explain the behaviour of a general complementary metasurface, without compromising the accuracy of the results is valid.

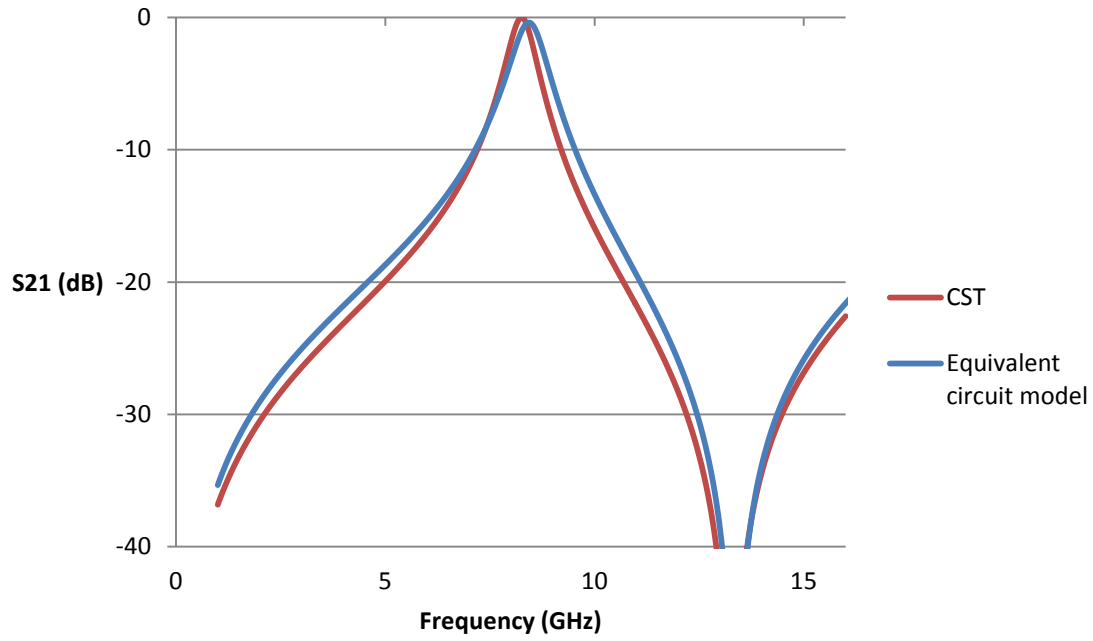

Figure 6-16: *Comparison between the transmission response of a dipole-slot metasurface between the analytical equivalent circuit model and CST*

6.7 Conclusions

It has been shown that the width of the dipoles and the slots in a Babinet complementary dipole-slot metasurface has a significant effect on the coupling between the two complementary layers; therefore the resonant frequency of the dipole-slot metasurface is dependent on the length to width ratio of these elements. By maximising the coupling co-efficient of the two layers (for a fixed length), an optimized value of the width can be obtained which results in achieving the maximum compactness for a dipole-slot metasurface. This optimised value of width is equal to 0.55*l*, where *l* is the length of the individual element. It has been shown that increasing or decreasing the width beyond this value leads to an increase in the resonant frequency of the structure. This has been verified using measurements. Three dipole-slot metasurfaces on a dielectric of thickness 0.044mm and a relative permittivity of 3 were fabricated. The length of the individual elements was kept at 5mm for all these metasurfaces. It has been demonstrated that the maximum compactness (minimum pass band resonance) was achieved with the optimized width of 2.7mm for this length. The pass band resonant frequency measured for this width was 3.28 GHz. Increasing the width to 3.9mm or decreasing it to 1mm resulted in the structure resonating at much higher frequency. These measured pass band resonant frequencies are 4.0 and 4.78 GHz respectively. It has also been shown that the optimized value of the width is independent of the thickness and the relative permittivity of the dielectric.

The pass band nature of the Babinet complementary metasurface has been explained by using an analytical equivalent circuit model. Since the analytical equivalent circuit is composed of the impedance of the apertures layer placed in parallel to the metallic layer's impedance (multiplied by the square of the coupling factor), the resultant response of any Babinet complementary metasurface is naturally band pass. The equivalent circuit was designed with

the help of the electric and magnetic field integral equations. It has been shown that by approximating the thickness of the dielectric approaching zero in the EFIE, the two integral equations can be reduced to a single equation. The analytical equivalent circuit model has been verified by a dipole-slot metasurface. The transmission response of a dipole-slot metasurface using the equivalent circuit model has been compared with its response simulated using the full wave simulations in CST. An excellent agreement has been observed between the two responses. This also shows that approximating the thickness of the dielectric equal to zero in the EFIE simplifies the calculations without compromising the numerical accuracy.

References

[1] J. C. Vardaxoglou, *Frequency Selective Surfaces - Analysis and Design*. John Wiley & Sons, 1997.

[2] A. N. A. El-Sheikh and R. J. Langley, "Multiport network analysis of frequency-selective surfaces," *IEE Proc -Microw Antennas Propag*, vol. 141, no. 3, pp. 7–9, 1994.

[3] Z. L. Wang, K. Hashimoto, N. Shinohara, and H. Matsumoto, "Frequency-Selective Surface for Microwave Power Transmission," *IEEE Trans. Microw. Theory Tech.*, vol. 47, no. 10, pp. 2039–2042, 1999.

[4] S. B. Savia and E. A. Parker, "Equivalent circuit model for superdense linear dipole FSS," *IEE Proc -Microw Antennas Propag*, vol. 150, no. I, pp. 37–42, 2003.

[5] D. S. Wang, P. Zhao, and C. H. Chan, "Design and Analysis of a High-Selectivity," vol. 64, no. 6, pp. 1694–1703, 2016.

[6] N. Engheta and R. Ziolkowski, *Metamaterials: Physics and Engineering Explorations*. Wiley-IEEE Press, 2006.

[7] E. Erfani, M. Niroo-jazi, and S. Tatu, "A High-Gain Broadband Gradient Refractive Index Metasurface Lens Antenna," *IEEE Trans. Antennas Propag.*, vol. 64, no. 5, pp. 1968–1973, 2016.

[8] S. Saadat, M. Adnan, and H. Mosallaei, "Composite Metamaterial and Metasurface Integrated With Non-Foster Active Circuit Elements: A Bandwidth-Enhancement Investigation," *IEEE Trans. Antennas Propag.*, vol. 61, no. 3, pp. 1210–1218, 2013.

[9] M. Selvanayagam and G. V. Eleftheriades, "Circuit modeling of Huygens surfaces," *IEEE Antennas Wirel. Propag. Lett.*, vol. 12, no. 2, pp. 1642–1645, 2013.

[10] D. González-ovejero, E. Martini, B. Loiseaux, C. Tripon-Canseliet, M. Mencagli, J.

Chazelas, and S. Maci, “Basic Properties of Checkerboard Metasurfaces,” *IEEE Antennas Wirel. Propag. Lett.*, vol. 14, pp. 406–409, 2015.

[11] X. Huang, X. Zhang, Z. Hu, M. Aqeeli, and A. Alburaikan, “Design of broadband and tunable terahertz absorbers based on graphene metasurface: equivalent circuit model approach,” *IET Microwaves, Antennas Propag.*, vol. 9, no. August 2014, pp. 307–312, 2015.

[12] D. S. Lockyer, J. C. Vardaxoglou, and R. A. Simpkin, “Complementary Frequency Selective Surfaces,” *IEE Proc. - Microwaves, Antennas Propag.*, vol. 147, no. 6, pp. 501–507, 2000.

[13] C. Balanis, *Advanced Engineering Electromagnetics*. John Wiley & Sons, 1989.

Chapter 7 : Conclusions and Future Work

This thesis has discussed the advantages, fabrication and properties of artificial (man-made) materials. These materials can be divided in to two categories. (i) When the individual building blocks are non-resonant – such materials have a wideband nature as their behaviour remains quasi-static over a wide range of frequencies. In this thesis, they are referred to as heterogeneous composite materials since they are made from two or more constituents with distinct electromagnetic properties. (ii) When the individual unit cell is resonant – these two dimensional materials are called metasurfaces. Due to their small size and phase discontinuity (across their surface), they offer various advantages like wavefront shaping, ultra-thin lenses and compact spatial filters. In this thesis, metasurfaces are designed based on Babinet's principle (in which strong coupling between the complementary layers is responsible for their compact and pass band characteristics). The measured results for both these types of materials have been presented in this thesis and showed good agreement with simulations. Furthermore, analytical models have been developed.

7.1 Summary of Research Novelty

In Chapter 2, it was shown that heterogeneous materials can be used to improve the performance of a patch antenna with a 3D printed flexible substrate. The heterogeneous substrate was prepared by placing two sub-wavelength slots at the edges of the patch. Since the 3D printed substrate was lossy therefore the homogeneous patch antenna suffered from low radiation efficiency. By incorporating these slots in the heterogeneous substrate, it has been shown that the radiation efficiency of such an antenna can be increased.

Chapter 3 showed that heterogeneous composite materials can be prepared by using 3D printing. 3D printing is a simple, yet very powerful manufacturing process which holds the potential of not only making the design of RF devices monolithic but is also capable of making ‘on demand’ dielectrics. Such heterogeneous composite materials (whose properties can be controlled by the designer) have been fabricated and measured. It has been shown that by combining 3D printed structures with commercially available laminates, a large near continuous and range of relative permittivities was manufactured. A design equation for these structures had been derived on the basis of the Weiner bounds. The engineering tolerance of 3D printing as a manufacturing process has been reported.

For metasurfaces (which have individual resonant unit cells), the focus of this thesis has been on Babinet complementary metasurfaces. Chapter 4 has explained the compact nature and pass-band response of a dipole-slot metasurface by developing a qualitative equivalent circuit model. The coupling between the two complementary layers was explained by a parallel capacitance added to the slots layer due to the close proximity of the dipoles layer. This capacitance was used to explain the down shifting of resonant frequency. It was shown that adding an additional layer of dipoles to the other side of slots caused further miniaturization. This structure was named a dipole-slot-dipole metasurface. The qualitative equivalent circuit

was extended by adding another coupling capacitance and a series LC branch, in order to explain the behaviour of the dipole-slot-dipole metasurface. The response of both, the dipole-slot and dipole-slot-dipole metasurfaces were measured in a semi-anechoic chamber and a clear downshifting of the resonant frequency by adding an additional layer of dipoles was reported.

An extremely miniaturized ($\lambda/13.5$) metasurface was constructed with complementary square loops as its individual building blocks. The square loops are symmetric with respect to 90˚ rotation and it was observed that in order for maximum coupling to occur, one layer must be shifted along both axes by half the periodicity. This was required so that the maxima of electric fields of one layer are placed adjacent to the minima of electric fields of the complementary layer. This condition is necessary for strong coupling between the Babinet complementary layers and has been explained using Babinet's principle.

An expression for optimising the width of the dipole-slot metasurface has been derived in Chapter 6. By maximising the coupling co-efficient, an optimized width to length ratio has been derived which leads to the smallest unit cell size for a fixed element length. This ratio was then verified by both CST simulations and measurements. A large pass band to stop band ratio was obtained when the dipole-slot metasurface was designed at its optimized width. The design of a dipole-slot metasurface at this optimized width was also found to be tolerant to fabrication inconsistencies.

At the end of this thesis, a generalised equivalent circuit model has been developed for a Babinet complementary metasurface. This model was derived by using the integral equations for both layers. The major approximation for developing this model was based around the sub-wavelength thickness of this structure. Since the thickness between the two layers for a Babinet complementary metasurface is extremely small as compared to wavelength hence it was approximated as approaching to zero. The model is applicable to any combination of

metallic and apertures layer as long as they are Babinet complement of each other and are separated by an extremely small (sub-wavelength) thickness. The model was compared with CST simulations and an excellent agreement was recorded.

7.2 Summary of Results

In Chapter 2, heterogeneous substrates were prepared by incorporating air filled slots at the edges of a microstrip patch antenna. This approach was applied to a flexible 3D printed substrate antenna using DM9760 as the base material. The high loss tangent value of DM9760 caused the antenna to have low radiation efficiency. By the using heterogeneous substrate, radiation efficiency of this flexible antenna was significantly improved. The measured radiation efficiency for the homogeneous substrate antenna at 2.4 GHz was 44% while the measured radiation efficiency for the heterogeneous substrate antenna was 60% and 74% at the first and second resonant (2.52 and 2.74 GHz) respectively. For the heterogeneous substrate, the bandwidth of the patch antenna was also increased (from 160 MHz to 380 MHz) by combining the two TM modes.

In Chapter 3, heterogeneous composite materials covering a wide range of relative permittivity were prepared. These materials were manufactured by using commercial laminates and 3D printing. Bi-phase composites used two distinct materials as their constituents. These constituents were Arlon AD-1000, Taconic RF-60, Taconic RF-45 and PLA. The effective relative permittivity of these composites was determined by using them as a substrate for a microstrip patch antenna. By using different ratios of constituents, composites with effective relative permittivity ranging from 3.6 to 8.7 were engineered. Three-phase composite materials (having three different constituents air, PLA and RF-60A)

were manufactured by directly printing on RF-60A. By varying the constituents volumetric ratios, composite materials with a relative permittivity from 1.47 to 6.0 were manufactured. A design equation for estimating the relative permittivity of three-phase materials was derived. A good agreement between the estimated and measured values was reported. The repeatability of 3D printing as a manufacturing technique for 'on demand' dielectrics was investigated by manufacturing structures with different lattices. Every lattice had different volumetric ratios of PLA and air, and at least four different samples were manufactured for each lattice. A minute deviation of less than 0.1 was observed, across the measured relative permittivity for each lattice, showing the reliability of 3D printing as a manufacturing technique for 'on demand' dielectrics.

The focus of Chapters 4, 5 and 6 was on Babinet complementary metasurfaces. In Chapter 4, the compact nature and transmission loss of the dipole-slot metasurface has been investigated. Simulation investigations were performed on dipole-slot metasurfaces with individual elements of dimensions 4×0.4 mm^2 with a periodicity of 4.5×4.5 mm^2. It was shown that increasing the dielectric constant from 1 to 5 decreased the resonance from 15.5 to 8.1 GHz; similarly decreasing the inter-layer coupling by increasing the thickness of dielectric (0.03 to 0.11 mm) led to a decrease in the resonant frequency (8.1 to 13.8 GHz). It was also shown that by increasing the loss tangent of the dielectric from 0.005 to 0.1 lead to an increase in transmission loss from 0.5dB to 7.3dB. The behaviour of the dipole-slot metasurface was also described by developing an equivalent circuit model. A series LC branch was used for dipoles while a parallel LC circuit was used for slots. The inter-layer coupling was represented by a coupling capacitor. The measured results of a fabricated dipole-slot were presented. This structure had a periodicity of 5×5 mm^2 with individual elements being 4.5×0.5 mm^2. The thickness of the in-between dielectric was 0.044 mm. This measured resonance

of this dipole-slot metasurface was 7.8 GHz which makes it a ~λ/7 structure. The measured and simulated values showed good agreement.

Chapter 5 has shown further miniaturization (beyond λ/7) for Babinet complementary metasurfaces. It was shown that by using square loops as the building blocks of such a metasurface, a structure as compact as λ/17 was designed. This metasurface had one of its complementary layers shifted by half the periodicity (along both axes) with respect to each other. This polarisation independent metasurface had a periodicity of 4×4 mm^2 with the length of each side of square being 3.5 mm. The fabricated structure transmission response was measured in a semi-anechoic chamber. The measured values agreed with the simulated results. The measured resonant frequency for this metasurface was 4.4 GHz with the dielectric of thickness 0.044 mm (making this structure λ/17).

It was also shown that polarisation dependant dipole-slot metasurfaces can be further miniaturizated by adding an additional layer of dipoles to the dipole-slot metasurface, making the structure a dipole-slot-dipole metasurface. A dipole-slot-dipole metasurface was a λ/10 structure. This compact nature of the dipole-slot-dipole metasurface was explained by using a qualitative equivalent circuit model. An extra coupling capacitor and a series LC circuit branch were added to the qualitative circuit model of the dipole-slot metasurface (shown in Chapter 4). A dipole-slot-dipole metasurface with a periodicity of 5×5 mm^2 and the length and width of individual elements being 4.5 mm and 0.5 mm respectively, exhibited a resonant frequency of 6.1 GHz. This fabricated metasurface showed good agreement with simulations. The comparison between the measured and simulated results was shown in Section 5.5.

In Chapter 6, the width of a dipole-slot metasurface was optimized in order to achieve the maximum miniaturization for a fixed length. The optimized width to length ratio of 0.55 was derived by maximising the coupling co-efficient. It was shown that this ratio was independent of the thickness and the relative permittivity of the dielectric. Three metasurfaces with a

periodicity of 6 mm and length of individual constituents being 5 mm were fabricated. The dielectric was 0.044 mm thick. The three widths of these dipole-slot metasurfaces were 1 mm, 2.7 mm (optimized) and 3.9 mm. The measured resonant frequency for the metasurface with the optimized width was 3.28 GHz. The metasurface with width 1 mm and 3.9 mm resonated at 4.78 GHz and 3.96 GHz respectively.

The second half of Chapter 6 contained a generalised analytical equivalent circuit model for a Babinet complementary metasurface. This model explained the pass band nature and the compact structure of any Babinet complementary metasurface. Two integral equations were reduced to a single equation by approximating the thickness of the dielectric approaching zero. The model was tested for a dipole-slot complementary metasurface and the results were compared to CST simulations. This dipole-slot metasurface had the periodicity of 10×10 mm^2. The length and width of each individual element was 9.5 mm and 0.3 mm respectively. The resonant frequency predicted by CST for this metasurface was 8.4 GHz. The resonant frequency predicted by the analytical circuit model was found to be 8.3 GHz.

7.3 Future Work

This thesis has shown that ‘on demand’ dielectrics can be manufactured using 3D printing. However, the commercial laminates were combined with 3D printing in order to obtain a large range of relative permittivity. In future, the whole process can become monolithic if high permittivity materials can be 3D printed. By combining such materials with PLA and controlling the ratio of the constituent materials, the whole process to manufacture ‘on demand’ dielectrics can be simplified. The design would although require further studies on how the two materials interact with each other when printed as a single process; and what are the manufacturing limits of the printer in terms of resolution and accuracy. Since 3D printing

offers various techniques which include fused deposition modelling, laser sintering, stereolithography etc. it would be advantageous to structure the dielectrics using different techniques to find out which technique works better for a certain type(s) of designs.

On the other end of spectrum if 3D printers can combine printing of dielectrics (plastic) and metals in a single process, a different way to manufacture 'on demand' dielectrics can be realised. The dielectric constant of such a composite material can be controlled by the orientation of the metallic inclusions and the volumetric ratio between metal and plastic. Such printers could also be used to fabricate metasurfaces with high precision. This can be extremely useful for designing multi-layered metasurfaces. A dipole-slot-dipole metasurface was shown in this thesis and it was found to be very difficult to align. Such practical difficulties would be eliminated by using precise mechanical control offered by 3D printing. One would also be able to go beyond the dipole-slot couple and look at other geometrically complicated Babinet complementary structures for making multi-layered metasurfaces.

This thesis has focussed on explaining the physics behind the compact and pass band nature of Babinet complementary metasurfaces. Further work should be focussed on how to take advantage of these structures for practical applications. Due to their compact and pass band nature, a Babinet complementary metasurface can be designed to focus energy. This can be achieved by controlling the response of individual scatterers. By tailoring the phase discontinuity due to each scatterer, such metasurfaces can theoretically be used to design ultra-thin lenses.

The resonant frequency of the dipole-slot metasurface changes when it is placed adjacent to a slab of any dielectric material. This shift in the resonant frequency is sensitive to dielectric constant of the material and the thickness of the slab. This sensitivity can be utilised to ascertain the relative permittivity of the dielectric material. Since the metasurface unit cell is

compact and sub-wavelength therefore this can be used to perform dielectric measurements in a waveguide environment.

Appendix A

This Appendix describes heterogeneous substrate antennas whose bandwidth is enhanced by combining the two modes. The first heterogeneous substrate as shown in Figure A-1 is made from three different dielectrics. This Appendix is related to Section 2.2. By carefully controlling the permittivity and location of the introduced dielectric inside the substrate, the first and second resonances of a rectangular microstrip antenna are combined leading to an increase in the overall bandwidth of the structure.

The patch is placed on a 76 x 76mm^2, 3.5mm thick Rogers RU-3003 substrate, having a loss tangent of 0.013 and relative permittivity of 3. Heterogeneous substrate has been prepared by cutting slots (inside the substrate). These slots are symmetrical along the edges of the patch. Slots along y-axis are have a length of 38mm, a width of 6mm and are filled with Rogers-RT/Duroid-5880, a material having a relative permittivity of 2.2 and a loss tangent of 0.0009.

Along x-axis the slots are 46mm long, 9mm wide and air-filled. Figure A-1 illustrates the substrate and the embedded slots along with their dimensions and local relative permittivity.

The impedance matching is dependent on the feed position for a probe feed. The two resonances are from the perpendicular edges of the patch so the feed is off-set with respect to both axes. The patch is 47mm in length (along y-axis) and 40mm in width (along x-axis) and is shown in Figure A-2 along with the position of the feed.

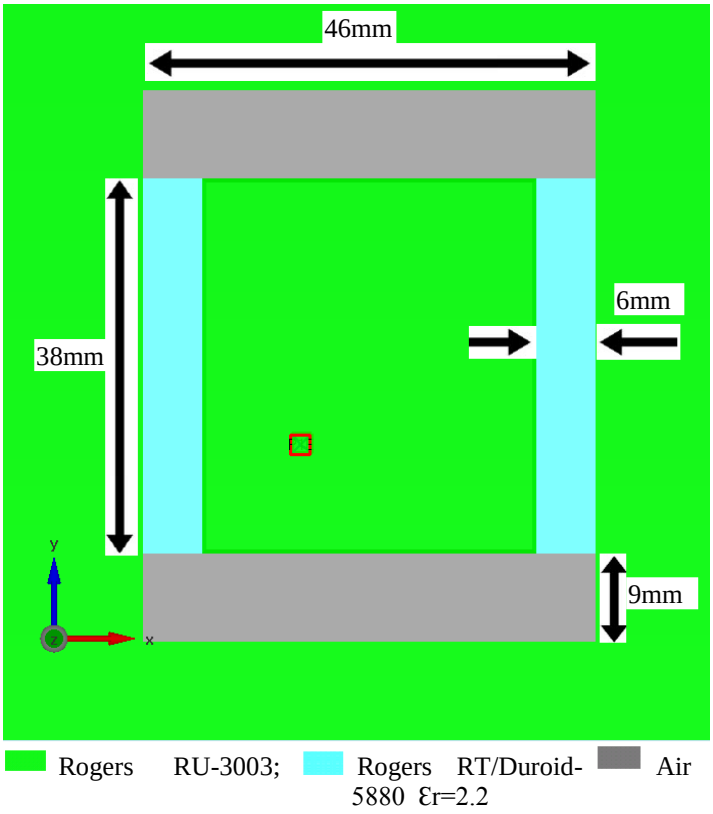

Figure A-1: Heterogeneous substrate synthesized by cutting slots. The dimensions and local relative permittivity of the slots are indicated.

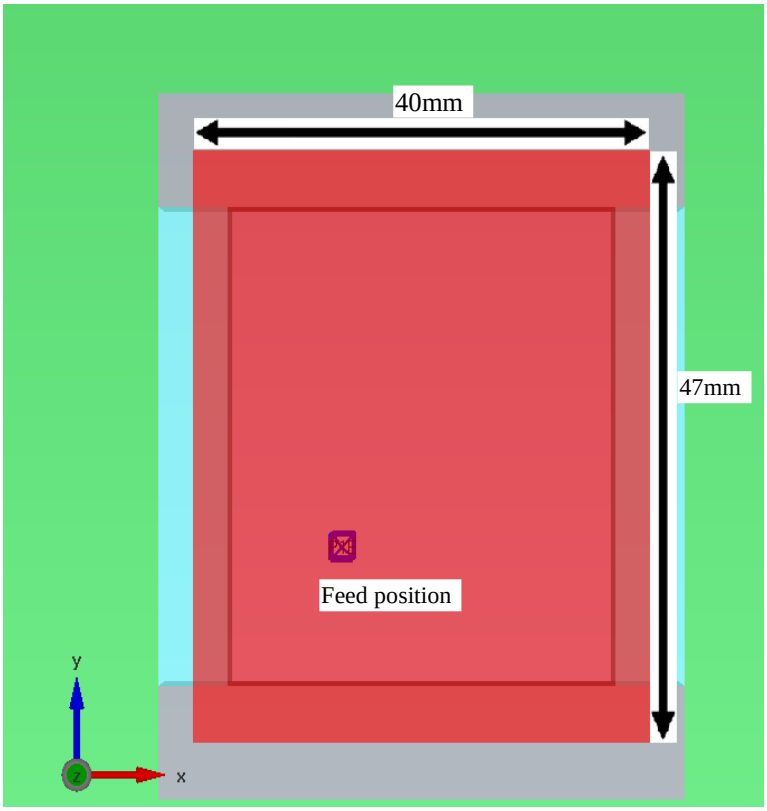

Figure A-2: Patch antenna on heterogeneous substrates showing patch dimensions and feed position.

Results and Discussion

The bandwidth of a microstrip patch is improved by using heterogeneous substrates. These substrates are prepared by cutting slots of different size and relative permittivity in the substrate. The underlying principle is similar as described in Section 2.2. The Rogers RT/Duroid-5880 filled slots along y-axis affect the second resonance the most whereas the air filled slots along the x-axis have a larger impact on the second resonance. The sizes of both slots are optimized to combine the resonances due to the perpendicular edges of the patch and have a larger bandwidth. Low loss materials have been used for preparing this heterogeneous substrate. The total bandwidth for heterogeneous substrate antenna is approximately 0.19GHz and is shown in Figure A-3. The radiation patterns for both resonances in theta and phi planes are shown in Figure A-4 and Figure A-5.

This antenna is then compared with another antenna which has the exact same physical attributes except for having a homogeneous Rogers RU-3003 substrate. The homogeneous substrate antenna has a 10-dB impedance bandwidth of 0.03GHz, with its first resonance occurring at 1.77GHz. Its second resonance is at 2.02GHz and the antenna has a 10-dB impedance bandwidth of 0.06 GHz for the second resonance. In order to keep the resonant frequency of the antenna on a 3.5mm thick Rogers RU-3003 substrate the same, the length and width of the homogeneous antenna was reduced to 38mm and 32mm respectively. This antenna had a resonant frequency of 2.15 GHz and a bandwidth of 0.05GHz. The feed position of this antenna was optimized in order to achieve a better impedance match at the resonant frequency. All antennas are simulated in EMPIRE XCcEL software which uses finite difference time domain (FDTD) algorithm.

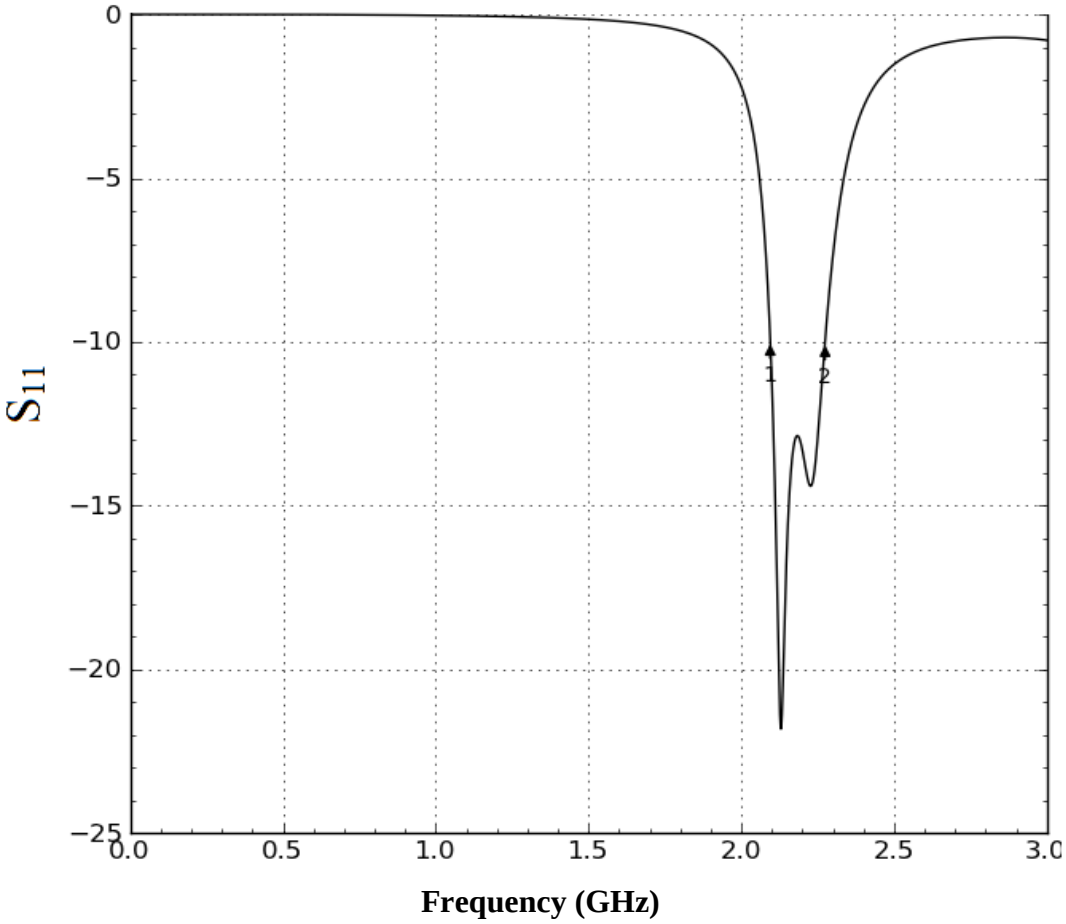

Figure A-3: S_{11} for the heterogeneous substrate patch antenna with three dielectric materials

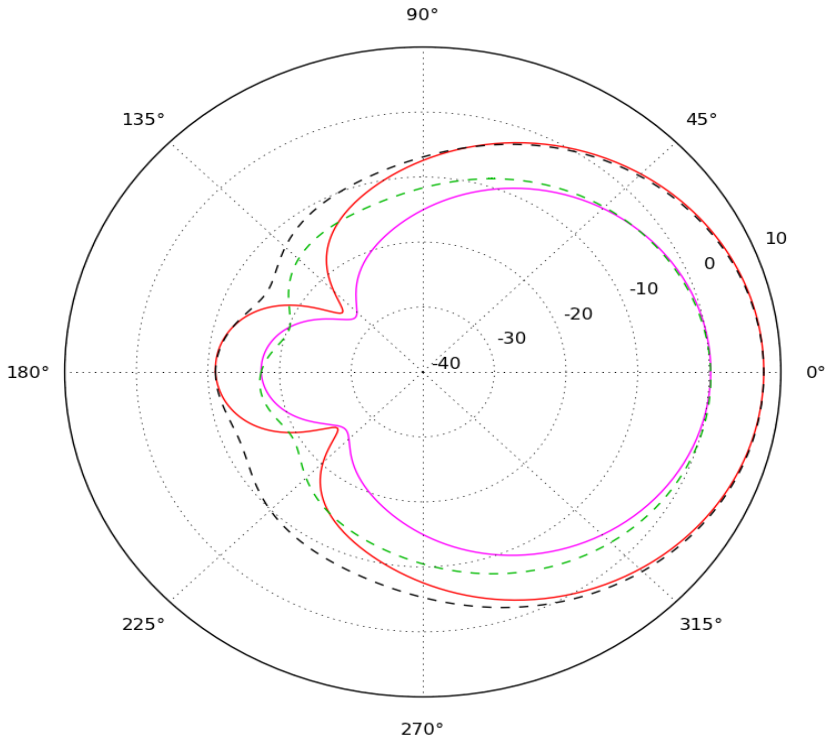

Figure A-4: Radiation patterns in both theta and phi planes for heterogeneous substrate patch at 2.12GHz (first resonance). Dotted lines are for the phi-plane. (Polar plot on dB scale)

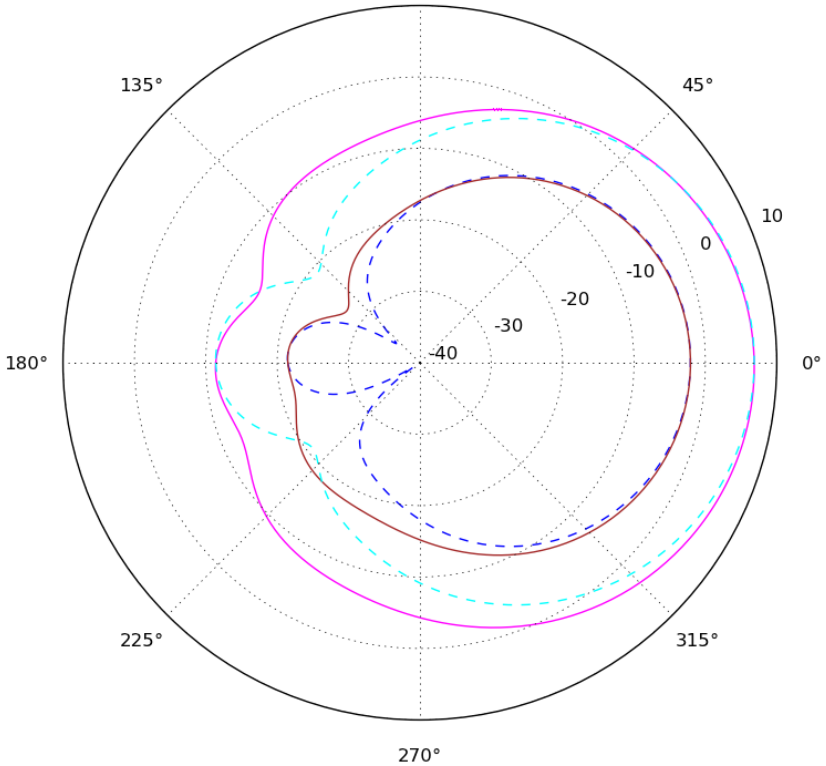

Figure A-5: Radiation patterns in both theta and phi planes for heterogeneous substrate patch at 2.22GHz (first resonance). Dotted lines are for the phi-plane. (Polar plot on dB scale)

Heterogeneous Substrate Antennas with Commercial Laminates

Two antennas with the same anatomy, as shown in Figure A-6 were manufactured using Taconic TLY (εr = 2.2; loss tangent = 0.0009) and Taconic RF-45 (εr = 4.5; loss tangent = 0.0037) as the base materials (for heterogeneous substrates). Heterogeneous substrates were prepared by cutting slots in the substrates for both materials. These slots were 6mm wide and were placed at the edges of the both patches. The patch had a length of 34mm long and a width of 28mm, for the Taconic TLY laminate. The patch using RF-45 as the base material was 33mm long and 27.5mm wide. The presence of the slots brought the first resonant frequency closer to the second resonant frequency therefore causing an increase in the resultant bandwidth of the antennas. The fabricated antennas are shown in Figure A-7.

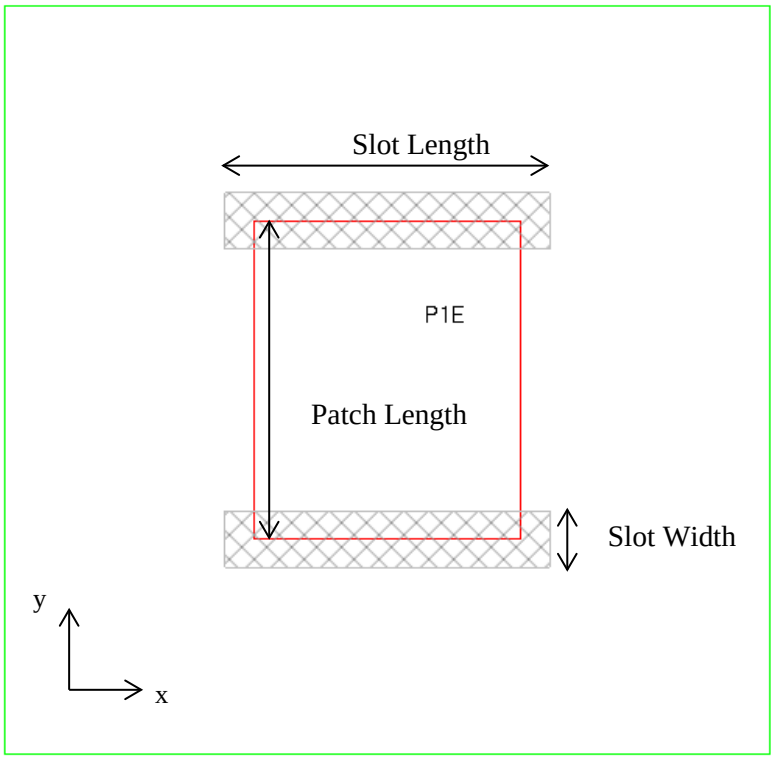

Figure A-6: Basic design for Taconic RF-45 and Taconic TLY heterogeneous substrate antennas. Red line indicates the boundary of the patch; slots are shown by the grey area

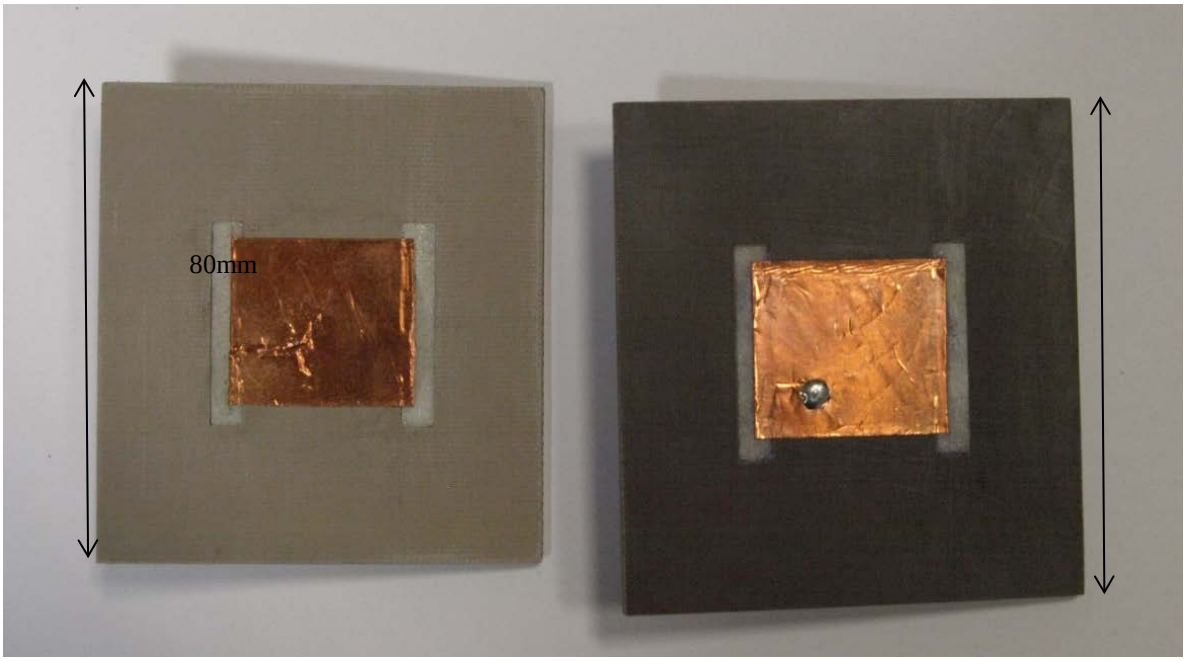

Figure A-7: Fabricated heterogeneous substrate antennas for enhanced bandwidth; the left one uses Taconic RF-45 as a substrate and the right one uses Taconic-TLY

Measured Results

Typically a microstrip antenna is fed along the central line perpendicular to the radiating edges. Such placement of the feed does not excite both TM10 and TM01 modes. It was found that by feeding the patch antenna diagonally (i.e. offsetting the feed from the centre of both principle axes), both modes can be excited. A good impedance match has been obtained for both the modes and causing the antennas to have a comparatively larger bandwidth.

The comparison between the measured and simulated results for both antennas is shown in Figure A-8 and Figure A-9. The measured results show a very good agreement with the simulated results. For Taconic RF-45, the antenna showed a bandwidth of 0.17 GHz which is 6.8% with the first resonance at 2.44 GHz and second resonance at 2.53 GHz. For Taconic TLY, the first resonance occurred at 3.18 GHz and second resonance was at 3.43 GHz; the antenna had a bandwidth of 0.43 GHz which is 12.7%. The higher percentage of bandwidth

for second design is because Taconic-TLY has a lower permittivity than Taconic RF-45. The antennas were simulated in both EMPIRE XCcEL and CST.

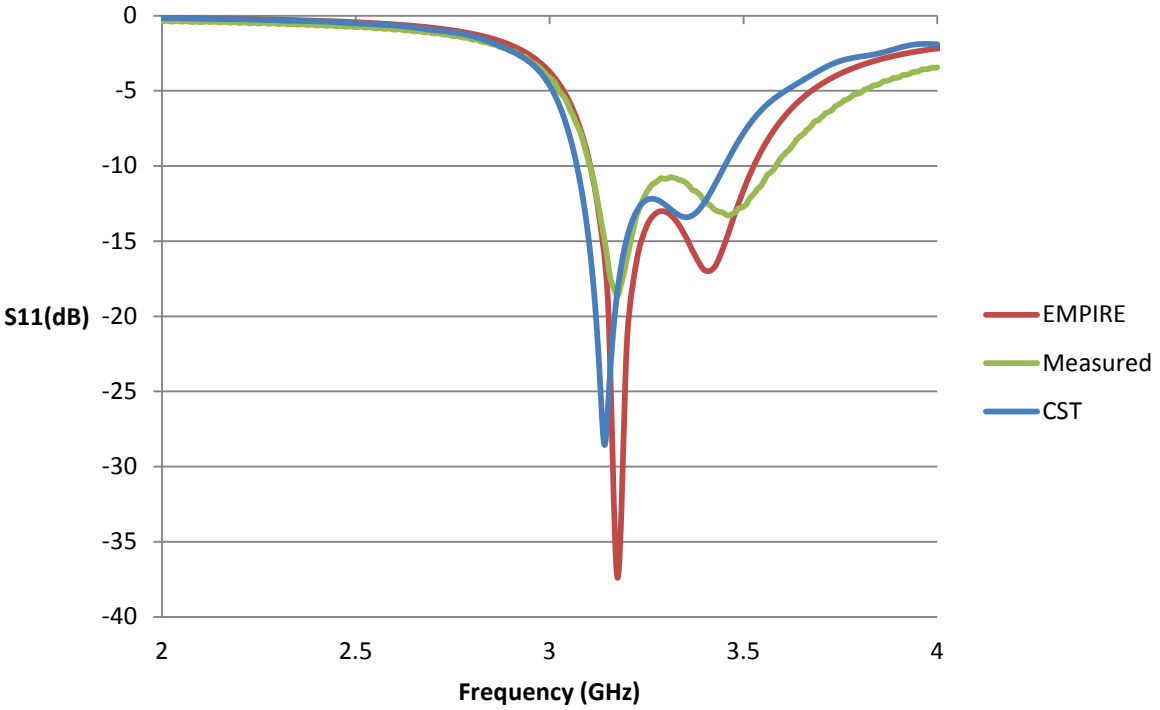

Figure A-8: S11 parameter for heterogeneous substrate antenna on Taconic-TLY

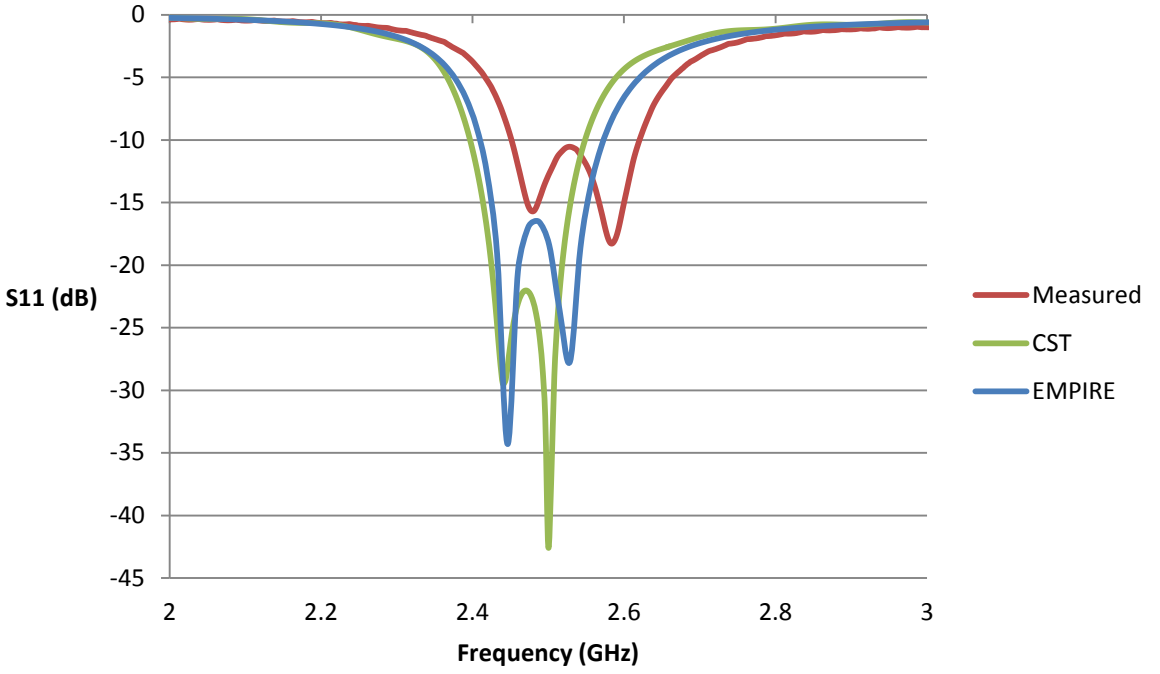

Figure A-9: S11 parameter for heterogeneous substrate antenna on RF-45

Appendix B

This Appendix shows the comparison between stratified and squared lattice composite materials and is linked to Chapter 3. Since 3D printing uses layer by layer structuring of the material, the proposed stratified structures introduce air in the parent material in the form of layers as shown in Figure B-1. This method leads to a sharper decrease in the relative permittivity in comparison to the material shown in Figure B-2, where air is introduced inside the parent material in the form of square shaped holes; whose thickness is the same as that of the substrate.

Figure B-1: A layered substrate is shown. Green indicates the parent material and air introduced in the form of layers is shown in red

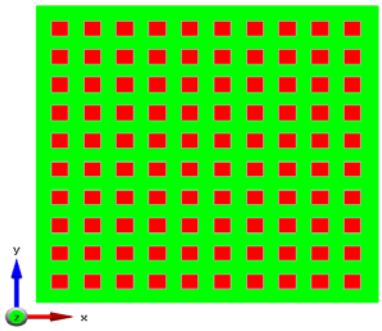

Figure B-2: A checkered substrate is shown. Green indicates the parent material and air introduced in the form cuboid holes is shown in red

Simulation Results

To calculate the effective permittivity of both types of materials, they are used as a substrate for a conventional microstrip patch antenna. The simulations for these patches are carried out in EMPIRE XCcEL. The parent material used for simulations is DM9760 (ε_r = 3; loss tangent = 0.051) which can be easily printer by a Connex 500 3D printer. The thickness of the

substrate is 3mm for all simulations. The length of the patch is 36mm and its width is 26mm for these simulations. The effective relative permittivity is then calculated from the following equation [1].

$$f = \frac{c}{2L\sqrt{\varepsilon_{eff}}}$$

Where *f* is the resonant frequency, *L* is the length of the antenna; *c* is speed of light and ε_{eff} is the effective relative permittivity of the composite material (substrate).

The results are presented in Table B-1. The results clearly indicate that increasing the volumetric ratio of air leads to a decrease in the effective permittivity and that the decrease in the permittivity is larger for the layered structure in comparison to the checkered one for the same volumetric ratio, the resonant frequency of the patch is higher in the case of the layered substrate indicating a lower value for the permittivity.

Table B-1: Simulated Results

Substrate	Volumetric Ratio of air (%)	Resonant Frequency (GHz)	Effective Permittivity
Homogeneous	0	2.42	2.965
Checkered	25	2.65	2.472
Checkered	50	2.90	2.064
Checkered	75	3.23	1.664
Layered	25	2.82	2.183
Layered	50	3.13	1.772
Layered	75	3.42	1.476

References

[1] K.-L. Wong, *Compact and Broadband Microstrip Antennas*. John Wiley & Sons, 2004.